Time-Delayed Control of Quantum Phase Transitions

vorgelegt von Physiker
Wassilij Kopylov
geb. in Perm

Von der Fakultät II – Mathematik und Naturwissenschaften
der Technischen Universität Berlin
zur Erlangung des akademischen Grades
Doktor der Naturwissenschaften
Dr. rer. nat.

genehmigte Dissertation

Promotionsausschuss:

Vorsitzender: Prof. Dr. rer. nat. Mario Dähne
1. Gutachter: Prof. Dr. rer. nat. Tobias Brandes, TU Berlin
2. Gutachter: Dr. rer. nat. Clive Emary, University of Hull

Tag der wissenschaftlichen Aussprache: 13. November 2015

Berlin 2015

Zusammenfassung

In der vorliegenden Arbeit stellen wir eine relativ neue theoretische Methode vor, die es erlaubt verschiede Vielteilchen-Quantensysteme zu kontrollieren und neue Phasen zu erzeugen. Dazu übertragen wir das Konzept eine zeitverzögerten Pyragas - Rückkopplungsschleife auf Vielteichen-Quantensysteme wie das Dicke Model, das Lipkin-Meshkov-Glick (LMG) Model und ein zwei-Moden Laser mit Tavis-Cummings (TC) Wechselwirkung. Alle Systeme befinden sich in einer dissipativen Umgebung. Die anschließende Untersuchung basiert auf der Annahme eines mittleren Feldes, die wir im thermodynamischen Grenzfall für berechtigt halten.

In dem dissipativen Dicke System wird die Atom-Feld-Kopplungskonstante mit der Differenz der zu zwei verschieden Zeitpunkten abgestrahlten Photonenzahl gewichtet. Die gewählte Kontrollmethode erzeugt neue Quantenphasen zusätzlich zu der superradianten Phase in dem Dicke Modell. Diese erscheinen als eine unendliche Sequenz von super- und subkritischen Hopf-Bifurkationen von dem stationären Zustand. Dadurch werden stabile und instabile Grenzzyklen generiert. Wir analysieren die auftretenden Bifurkationen in Abhängigkeit von der zeitlichen Verzögerung und Rückkopplungsstärke und geben einen analytischen Ausdruck für die Phasengrenze an. Wir argumentieren zusätzlich, dass der benutzte Feedbacktyp sich leicht in bestehende experimentelle Bauten integrieren lässt, da dort die Kopplungskonstante von der Laserintensität abhängt.

In dem dissipativen LMG Model untersuchen wir die Auswirkung der Dissipation auf den Quantenphasenübergang von angeregten Zuständen (ESQPT). Wir zeigen, dass das ESQPT Signal sogar im Spektrum und nicht nur in dem Dichtespektrum des effektiven Hamiltonian sichtbar ist. Die Mittelwerte der Observablen zeigen jedoch nur ein gedämpftes ESQPT Signal. Wir benutzen nun die Pyragas kontrolle um neue Phasen in dem LMG Model zu generieren und dadurch das ESQPT Signal in den Observablen wiederherzustellen. Wir analysieren und diskutieren ausführlich das Systemverhalten unter dem Einfluss zeitverzögerter Kontrolle. Außerdem argumentieren wir, dass diese Methode das ESQPT Signal experimentell leichter zu messen erlaubt.

Anschließend analysieren wir einen zwei-moden Laser, der auf einer Erweiterung des TC Models mit zusätzlichen Pump- und Zerfallskanälen basiert. Wir lösen die entsprechenden stationären Gleichungen fürs mittlere Feld analytisch und bekommen ein komplexes Phasendiagramm mit bis zu vier stabilen Fixpunkten. Nun wenden wir verschiedene einfache Pyragas Rückkopplungsschleifen an, um die Laserdynamik zu beeinflussen. Wir zeigen, wie man die Frequenz von dem emittierten Licht kontrollieren und nicht stabile Systemkonfigurationen stabilisieren kann.

Damit verknüpft unsere Arbeit die Bereiche Kontrolle, Phasenübergänge und Dissipation und zeigt interessante und unerwartete Dynamik in den Quanten-Vielteichen Systemen.

Abstract

In this theoretical thesis we apply the time-delayed Pyragas feedback scheme to several many-body quantum systems in order to control the quantum phases in a rather new way. The systems are the dissipative Dicke model, the dissipative Lipkin-Meshkov-Glick (LMG) model and a two-mode Tavis-Cummings laser.

In the dissipative Dicke model our chosen way of feedback control, namely the modulation of the atom-field coupling by a difference of emitted photon numbers at different times, creates additional new quantum phases. These show up as an infinite sequence of super- and subcritical Hopf bifurcations of the stationary state by generation of stable and unstable limit cycles. We analyze and discuss the appearing bifurcations as a function of time delay and feedback strength and calculate an analytical expression for the phase boundaries. On top of this, we argue that our scheme is easy to implement within existing experimental setups, as in experiments the coupling is tuned by laser intensity.

In the dissipative LMG model we investigate how the dissipation affects the excited state quantum phase transition (ESQPT). We show that with dissipative effects the ESQPT is directly visible in the spectrum of the effective Hamiltonian and not only in the density of states. Moreover, the ESQPT signal in the system observables gets smoothed. Then we use time delayed feedback control to restore the ESQPT signal by creation of new phases. We analyze and discuss the behavior of the system for different time delays. We argue that using our feedback scheme it is easier to measure ESQPT in the open LMG system than without it in the closed one.

Then we use a 2-mode laser based on the Tavis-Cummings model with additional incoherent pumping and decay channels. Instead of the usually used rate-equation model, we describe the two-mode laser starting from a quantum mechanical description and present an analytical solution of the corresponding stationary mean-field equations in thermodynamic limit. We analyze the stationary solutions and their stability and obtain a complex phase diagram with up to 4 fixed points. In addition to this, we apply different time delayed Pyragas feedback control schemes, which allow us to influence the laser dynamic. The frequency of the emitted laser light can be controlled then or an unstable fixed point stabilized.

In this way, our thesis links the topics of control, phase transitions and dissipation together which induce an interesting and unexpected dynamics in quantum many-body systems. Although all final calculations are at the mean-field level, we hold them to be valid in thermodynamic limit.

Contents

1. Introduction **1**

2. Theory **3**

2.1. Time Delayed Control . . . 3
2.1.1. Pyragas Control . . . 4
2.1.2. One Example of Pyragas Control Type . . . 4
2.2. Phase Transitions . . . 6
2.2.1. Quantum Phase Transition . . . 7
2.2.2. Excited Quantum Phase Transition . . . 7
2.2.3. Condensation and Lasing . . . 8
2.3. LMG Model . . . 8
2.3.1. Spectrum, QPT and ESQPT . . . 9
2.3.2. Averaged Observables . . . 9
2.3.3. Semiclassical Energy . . . 11
2.4. Dicke Model . . . 12
2.4.1. Spectral Properties, QPT and ESQPT . . . 13
2.4.2. Tavis-Cummings Model . . . 13
2.5. Dissipation in Quantum Systems . . . 15
2.6. Quantum Regressions Theorem . . . 15
2.7. Experimental Setups . . . 16
2.7.1. Dicke Phase Transition . . . 16
2.7.2. Tavis-Cummings Model . . . 17
2.7.3. Lipkin-Meshkov-Glick . . . 18

3. Time-Delayed Feedback Control of the Dicke-Hepp-Lieb Superradiant Quantum Phase Transition **21**

3.1. Introduction . . . 21
3.2. Non-equilibrium Dissipative Dicke Model with Time-Delayed Feedback. 22
3.2.1. General Model . . . 22
3.2.2. Implementation of Pyragas Feedback . . . 23
3.2.3. Semiclassical equations. . . . 24
3.2.4. Fixed Points and Stability . . . 28
3.3. Dicke System without Time Delay . . . 31
3.3.1. Stability . . . 31
3.3.2. Dynamics . . . 34
3.4. Dicke System with Time Delayed Pyragas Control . . . 35
3.4.1. Phase Diagram in the (g_0, ω) Plane . . . 35

3.4.2. Dynamical Evolution . . . 36
3.4.3. Analysis of Zone Boundaries . . . 39
3.4.4. Phase Diagram in the (τ, λ)-Plane . . . 42
3.4.5. Limit Cycle Properties . . . 42
3.4.6. Result Robustness . . . 47
3.4.7. Numerical Methods . . . 50
3.5. Discussion and Outlook . . . 51
3.5.1. Experimental Realisation . . . 51
3.5.2. Aspects of Pyragas Control . . . 52
3.6. Summary . . . 53

4. Time-Delayed Control of Excited State Quantum Phase Transitions in the Lipkin-Meshkov-Glick model 55
4.1. Introduction . . . 55
4.2. LMG Model with Dissipation and Feedback . . . 56
4.3. Dissipative ESQPT at Quantum Level . . . 56
4.3.1. Spectral Signatures of Dissipative ESQPTs . . . 57
4.3.2. Correlation Functions . . . 59
4.4. Dissipative ESQPT Signal at Mean-Field Level . . . 63
4.4.1. Mean-field Equations . . . 64
4.4.2. Dissipative Damping of the ESQPT . . . 65
4.5. Pyragas Control of the ESQPT Signal . . . 67
4.5.1. Linear Stability Analysis with Time Delay . . . 67
4.5.2. Feedback Compensates Dissipation . . . 71
4.5.3. Chaotic Behaviour . . . 73
4.6. Discussion . . . 75
4.7. Summary . . . 77

5. Dissipative Two-Mode Tavis-Cummings Model with Time-Delayed Feedback Control 79
5.1. Introduction . . . 79
5.2. Model . . . 80
5.3. Dynamics without Feedback . . . 83
5.3.1. Steady States . . . 83
5.3.2. Stability of Steady States . . . 84
5.4. Dynamics with Feedback . . . 87
5.4.1. Stabilization of Fixed Points . . . 87
5.4.2. Selection of the Dominantly Occupied Mode . . . 90
5.5. Discussion . . . 93
5.6. Summary . . . 94

6. Conclusion 97

Appendix **101**

A. Overview of Used Symbols and Abbreviations **103**

B. Time Delayed Control of Photon Condensation **105**
B.1. Introduction . . . 105
B.2. Model of Photon Condensation . . . 105
B.3. Re-derivation of the Master Equation . . . 105
B.3.1. General Form of the Master Equation with Born-Markov Approximation . . . 106
B.3.2. Polaron Transformation and System-Bath Identification . . . 107
B.3.3. Determination of the Bath Correlation Functions . . . 107
B.3.4. Putting the Master Equation together . . . 110
B.3.5. Comparison of Derived $K(\omega)$ With Ref. [Kir13] . . . 114
B.3.6. Master Equation with Linear Coupling Term . . . 114
B.4. Semiclassical Rate Equation . . . 115
B.4.1. Equation for $\langle \hat{n}_m \rangle \equiv a_m^\dagger a_m$ . . . 115
B.4.2. Equation for $p_1(t) \equiv \langle \sigma_i^+ \sigma_i^- \rangle$ . . . 116
B.4.3. Adiabatic Elimination . . . 118
B.4.4. Contribution of Linear Term in the Master Equation . . . 118
B.4.5. Solution of the Mean-Field Equation . . . 119
B.5. Time-Delayed Feedback Control Applied to Photon Condensation Model 119
B.5.1. Feedback Types . . . 119
B.5.2. Coupling of Type B . . . 121
B.5.3. Coupling of Type A . . . 123
B.5.4. Coupling of Type C . . . 124
B.6. Discussion . . . 125

C. ESQPT Signal from Periodic Dynamic in Dicke and Tavis-Cummings Models **127**
C.1. Dicke Model . . . 127
C.1.1. Semiclassical Equations . . . 127
C.1.2. Energy Landscape . . . 127
C.1.3. Averaged Dynamics . . . 128
C.2. Tavis-Cummings model . . . 129
C.2.1. Mean-Field Equations . . . 130
C.2.2. Numerical Procedure . . . 131
C.2.3. Averages and ESQPT Signal . . . 132
C.2.4. ESQPT Signal from Coherent State Dynamics . . . 135
C.2.5. Discussion/Conclusion . . . 137

Acknowledgement **139**

1. Introduction

The development and application of control strategies is an important know-how in our world. Its direct purpose is to affect the behavior of different systems like machines, engineering or experimental setups in any desired way. The first control scheme - the centrifugal governor - was applied to an engine more than a century ago to regulate the amount of fuel usage by the engine and thereby to control its speed. Since then control and regulation has played a key role in (classical) engineering science. Control strategies perform their job usually unseen for people, nevertheless almost everyone is in touch with it. Let us look at some examples present in almost every day life. First is a fan regulation in the computer whose speed depends on the temperature inside the computer box. Second example is an electronic amplifier where the output signal modulates the input signal, which improves the performance of the amplifier. A third - and a rather different - example is washing machine whose washing time is set only by the chosen program and doesn't depend on the cleanness of clothes. In contrast to the last example where the control signal was given from the outside, the first both examples have in common that their control signal depends on the sate of the systems itself. Such schemes are called feedback schemes, since they fed their state back into the system. This state can be taken from the previous time, the feedback scheme is then time-delayed. A one special, rather simple but very successful time-delayed scheme is of Pyragas type, the feedback signal depends then on a difference of the system states at two different times [Pyr92].

The applications of feedback schemes are not only restricted to engineering science, since they spread out to other (more) diverse research areas and can be found even in neuromedicine to prevent diseases like epilepsy [Ros04, Der03]. Nowadays it has become a contemporary and increasingly important topic, especially in quantum physics [Wis09]. Here especially interacting many-body quantum systems in or beyond equilibrium conditions has triggered great interest for many decades. Even completely without feedback they offer a very rich, exciting and at first sight often unexpected physical behavior. Interestingly different kinds of phase transitions play a major role in such systems and are the origin of many occurring effects. Of particular interest in this context is quantum phase transition (QPT). At a quantum level, the QPT is visible as a non-analyticity of the ground state at some point in the parameter space [Sac07].

The merging of such systems and feedback opens a wide area of additional possibilities. Of particular interest is then the control of quantum properties like coherences [PÏ1], laser statics [Mac86], entanglement [Hei15], quantum phases and phase transitions [Wis09, Gri14, Kop15b]. The expanding experimental possibilities to realize a complex quantum system offer a test-bed for new theories, applications and effects and

increase the scientific curiosity of a feedback application to quantum systems. This is for instance true for cold atoms and laser systems. Nowadays it is possible to create optical traps for the atoms in a high finesse optical resonator, to set the atom-atom and atom-field interaction in order to realize collective phenomena, to monitor the cavity field in real-time, to induce different transitions between system states via additional laser fields, and all of this with high precision [Rit13a].

Our key idea for this thesis is to generate new non-equilibrium phases or to stabilize the unstable one in several many-body quantum system applying time delayed Pyragas feedback control. As a test-bed for time-delayed control application we choose the Dicke model, Lipkin-Meshkov-Glick (LMG) model and an extended lasing version of Tavis-Cummings (TC) model, all of them coupled to a dissipative environment. In the first two cases we use the feedback loop to change one internal system parameter - the system interaction strength. Unexpectedly, even a small modification can create new non-equilibrium phases which can even undo the dissipative effects. The last case is a two-mode lasing model with a very complex - previously unknown - phase diagram. Here the application of different feedback schemes can be used to select the mode with a macroscopically occupation. In all cases we perform a deep numerical analysis of appearing bifurcations and an analytical analysis of appearing new phase boundaries in the presence of time delayed control.

The structure of the thesis is as follows. In chapter 2 we provide general information about the used models, Pyragas control and different phase transitions - topics which build the foundation of this thesis. In the following chapters we discuss the application of Pyragas control to the models. Thus in chapter 3 we generate new non-equilibrium limit-cycle phases in the Dicke model. In chapter 4 we investigate the dissipative effects on the ESQPT and use Pyragas control to cancel them. In chapter 5 we show the complex phase diagram of a 2-mode laser system with up to 4 different steady states and use Pyragas control to select the lasing mode or to stabilize the unstable steady state. In the Appendix B we discuss the results of feedback application to a model for photon condensation based on [Kir13] and in Appendix C show that the ESQPT signal is hidden in the periodic dynamic of a closed Dicke system.

2. Theory

Here we sum up the main properties of a quantum phase transition, Pyragas feedback and the Dicke, Lipkin-Meshkov-Glick (LMG) and Tavis-Cummings (TC) models.

2.1. Time Delayed Control

Feedback control is a promising tool to change the system dynamics in a desired way. Influence of the laser statistics [Mac86], neurosystems [Sch09] or even control at a quantum level [Wis09, Bas12, PÏ1, Kab15, Gri15] are only some examples of its power.

A system control can be designed in different ways. One usually distinguishes between an open and closed control loop. In the closed version the properties of the system of interest affect the feedback, in contrast, the open feedback type is fully determined from the outside, see Fig. 2.1.

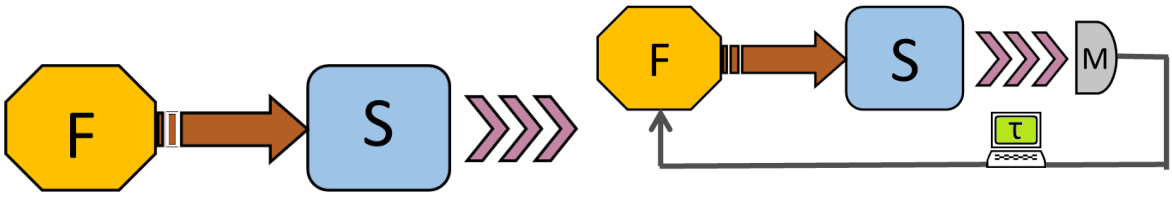

(a) open loop (b) closed loop

Figure 2.1.: A scheme for a open (a) and closed (b) control loops applied to a system S. Whereas in the open version the feedback signal F is determined from the outside, in the closed version the feedback is the depends on a systems state which is determined by a device M. Additional modification of the signal, i.e. adding time delay τ, is possible.

As the closed feedback needs some system property, there are in a quantum version of feedback at least two ways how to use the signal for a control. Either a property is measured and the result influences the control or the control machine is directly coupled to the system and influences it without direct measurements. In the first case it is an incoherent, in the second a coherent type. The main difference is then that a measurement influences in general the quantum mechanical state of a system of interest. Thus the separation in coherent and incoherent feedback types is a specificity of quantum mechanic. Fig. 2.2 visualizes both versions of closed loop control marking quantum system by the dashed or dotted rectangle. A delay in the feedback function, for example due to a final signal velocity, can play a major role in system controlling [Jus09].

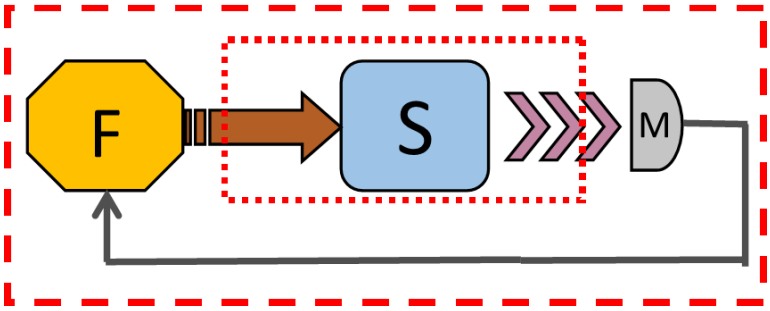

Figure 2.2.: Figure shows two possible applications of a closed loop control for a quantum system S. Either the state of the system is measured and the signal is put back in a quantum system incoherently, or the systems state influences the system coherently without measurement, e.g. by a mirror. In the first case only the dotted part is quantum, in the last case it can be the dashed part in general.

2.1.1. Pyragas Control

Pyragas feedback type is one special but very successful kind of a closed feedback loop and was originally designed to prevent chaos by stabilizing an unstable periodic orbit [Pyr92]. Its key idea is to feedback the difference of a system observable at two different times $t - \tau$ and t. Pyragas power is hidden in its simplicity. Due to the difference structure the feedback control term vanishes in the stationary state or for a periodic solution for fixed τ-value since it is proportional to the difference of the system observable. Thus Pyragas feedback can modify the fixed point or limit cycle stability without changing them [HÖ5].

2.1.2. One Example of Pyragas Control Type

We demostrate the action of Pyragas Control on a simple model of a damped harmonic oscillator of unit mass [HÖ5]. In the position-momentum space its dynamic is desribed by

$$\dot{\vec{v}}(t) = \mathbf{M}\vec{v}(t) \tag{2.1}$$

with

$$\vec{v} = (x, p)^T \tag{2.2}$$

and

$$\mathbf{M} = \begin{pmatrix} 0 & 1 \\ -\omega^2 & -2\gamma \end{pmatrix}, \tag{2.3}$$

where x and p are position and momentum coordinates, ω is the frequency and γ the damping rate. In the following we assume $\omega > \gamma$, thus we have an oscillating solution. Eq. 2.1 has a stable fixed point $(x_0, p_0) = (0, 0)$, it is the end state of harmonic oscillator due to damping. In the following we want to prevent the oscillator

of going into this state. Therefore, we introduce time-delayed Pyragas feedback control modifying Eq. (2.1) as

$$\dot{\vec{v}}(t) = \mathbf{M}\vec{v}(t) + K\mathbf{1}(\vec{v}(t-\tau) - \vec{v}(t)). \tag{2.4}$$

This corresponds to measure the position x and momentum p of a harmonic oscillator at time t and $t-\tau$ and feedback the difference weighted by a factor K to modify $\dot{x}$ and $\dot{p}$ of a harmonic oscillator. These are still linear equations with time delay and can be exactly solved by a Laplace transformation or using the formalism of Lambert function [Yi06b, Yi06a]. However, at this step we are interested whenever the trivial fixed point still attracts the solution. Therefore we insert the exponential ansatz $\vec{v} = \vec{v}_0 \cdot e^{\Lambda t}, \Lambda \in \mathcal{C}$ into Eq. (2.4), yielding the condition for Λ

$$\det\left[\Lambda\mathbf{1} - (\mathbf{M} - K\mathbf{1}) - K\mathbf{1}e^{-\Lambda\tau}\right] = 0. \tag{2.5}$$

Without feedback $\tau = 0$ this equation can immediately solved for Λ (note the made $\omega > \gamma$ assumption)

$$\Lambda = -\gamma \pm i\sqrt{\omega^2 - \gamma^2}. \tag{2.6}$$

The solution $\vec{v}$ is then a harmonic damped oscillation around origin. The frequency is given by $\sqrt{\omega^2 - \gamma^2}$ and γ is the exponential damping factor of the oscillation amplitude.

The question is how feedback changes the real part of Λ. For $\Re(\Lambda) = 0$ the solution will be undamped, for $\Re(\Lambda) > 0$ actually diverge. However with feedback Eq. (2.5) is much harder to solve, as it is now transcendent and has an infinite number of solutions. In this case one succeeds using the Lambert-W function [HÖ5]. Lambert-W function W is defined as an inverse of a complex function we^w and has different solution branches.

Eq. (2.5) can be rewritten as

$$\begin{aligned}
\left[K\left(1 - e^{-\Lambda\tau}\right) + \gamma + \Lambda\right]^2 &= -(\omega^2 - \gamma^2) \\
\Rightarrow \pm i\sqrt{\omega^2 - \gamma^2} &= K\left(1 - e^{-\Lambda\tau}\right) + \gamma + \Lambda \\
\Rightarrow \left[K + \Lambda + \gamma \mp i\sqrt{\omega^2 - \gamma^2}\right]\tau &= K\tau e^{-\Lambda\tau}.
\end{aligned}$$

Defining $z \equiv \left[K + \Lambda + \gamma \mp i\sqrt{\omega^2 - \gamma^2}\right]\tau$ we can express

$$ze^z = K\tau e^{-\Lambda\tau}\exp\left[K + \Lambda + \gamma \mp i\sqrt{\omega^2 - \gamma^2}\right]\tau = K\tau\exp\left[K + \gamma \mp i\sqrt{\omega^2 - \gamma^2}\right]\tau.$$

Applying the W function on both sides we obtain

$$z = W\left(K\tau\exp\left[K + \gamma \mp i\sqrt{\omega^2 - \gamma^2}\right]\tau\right),$$

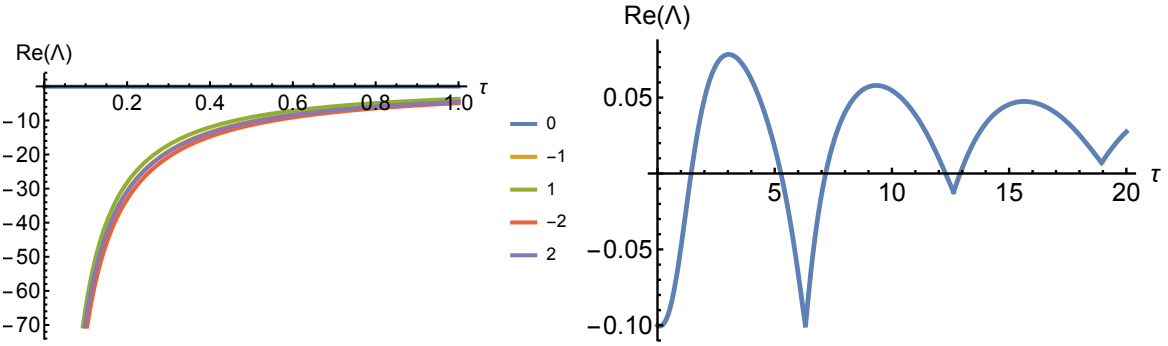

Figure 2.3.: (left) Real part of Eq. (2.7) for some branches and the zoom (right) for the zero branch with the biggest real part. Vanishing real part at $\tau = 1.4345$ corresponds to Fig. 2.4 (c). Parameters: $\gamma = 0.1\omega$

and use of z definition results in

$$\begin{aligned} \Lambda\tau &= W\left(K\tau \exp\left[K + \gamma \mp i\sqrt{\omega^2 - \gamma^2}\right]\tau\right) - K\tau - \left[\gamma \mp i\sqrt{\omega^2 - \gamma^2}\right]\tau \\ \Rightarrow \Lambda &= \frac{1}{\tau}W\left(K\tau \exp\left[K + \gamma \mp i\sqrt{\omega^2 - \gamma^2}\right]\tau\right) - K - \left[\gamma \mp i\sqrt{\omega^2 - \gamma^2}\right]. \end{aligned} \tag{2.7}$$

The last equation Eq. (2.7) describes the dependency of the eigenvalue Λ on time delay τ. For every fixed τ value it has an infinite number of solutions due to an infinite number of branches of the Lambert-W function. Fig. 2.3 shows the real part of Λ as a function of τ for some branches and a zoom around the zero-branch with the biggest real part. As the equations (2.4) are linear, the whole solution for $\vec{v}$ is then a superposition of all possible Λ values. However, the eigenvalue with the biggest real part determines the dominant dynamic of the system for $t \gg 0$. For $\tau \to 0$ all solutions diverge, except one. The zero branch converges to the eigenvalue without time delay $\lim_{\tau\to 0}\Lambda = -\gamma \pm i\sqrt{\omega^2 - \gamma^2}$. We see that the maximum real part changes as a function of τ (left). This change mirrors the attraction strength of the fixed point. For negative values the fixed point is stable and the oscillator ends up in a $(x_0, p_0) = (0, 0)$ state, see Fig. 2.4(a,b). For positive values the fixed point is unstable and the system diverges, see Fig. 2.4(d). In between, there is a critical τ value, where the fixed point attraction is zero and the system ends up forever oscillating, a state which is known in absence of dissipation.

Thus, this example visualizes how Pyragas feedback can manipulate the stability of the system, driving it into new states.

2.2. Phase Transitions

A phase transition describes in general a dramatic change in a physical system, i.e. the system goes into another phase state which can have very different properties to the previous one. Usually it occurs if some system parameter g overgrows some critical value g_c. Phase transitions are a universal physical effect and can appear everywhere:

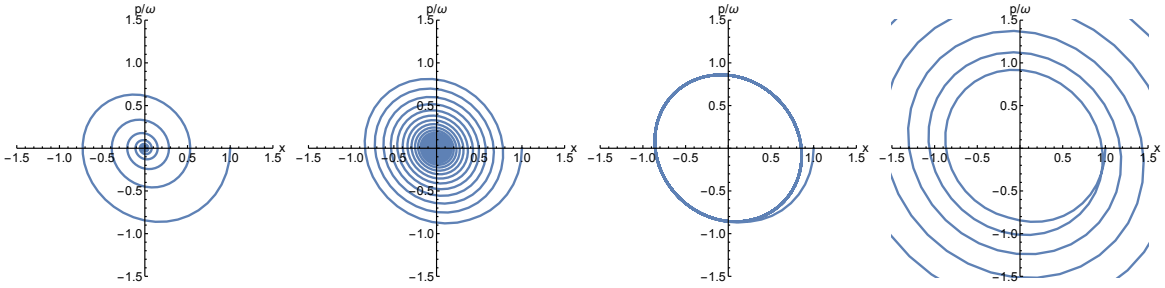

(a) $\tau = 0$ (b) $\tau = 1/\omega$ (c) $\tau = 1.4345/\omega$ (d) $\tau = 1.8/\omega$

Figure 2.4.: Harmonic oscillator in phase space with applied Pyragas feedback. Increase of time delay τ increase first the convergence time toward the fixed point (b). For special values of τ the real part of Eq. (2.7) vanishes and the solution ends up in an orbit (c). Further increase of τ destabilize the system (d). Initial condition $(x_0, p_0) = (1, 0)$. Parameters: $\gamma = 0.1\omega$

In classical physics as a transition from solid to liquid according to the function of temperature [LL70], in cosmology as a splitting of the electro-nuclear force as a function of energy [Gut81], in quantum mechanics as a transition to a ferromagnetic state as a function of magnetic field at zero temperature [Sac07]. The last example is one special kind of a phase transition, a quantum phase transition (QPT).

2.2.1. Quantum Phase Transition

A QPT occurs often for interacting spin-systems at zero temperature T and infinite number of spins. Its indicator is a non-analyticity of a ground state energy as a function of g at a critical point g_c [Sac07]. As $T = 0$ only quantum fluctuations are present, which diverge at a critical g_c value. Thus one says that a QPT is driven by quantum fluctuations in contrast to a phase transition for $T > 0$, which is then driven by thermal fluctuations. The type of the non-analyticity determines the order of a QPT.

For some famous models like Dicke superradiance [Dic54, Hep73b, Wan73, Ema03b] or Lipkin-Meshkov-Glick (LMG) [Lip65], the main properties of QPT can be explained and understood at a semiclassical level in the thermodynamic limit. The QPT is then visible as a bifurcation of an averaged system observable as a function of g at point g_c.

QPT can appear as in a equilibrium as in a non-equilibrium context [Val13]. In the last case the system can be driven by a time dependent field or has losses. Whereas the QPT in equilibrium context are well understood [LL70, Sac07], the QPT in non-equilibrium are even today a big research area, especially as the transition signatures known from an equilibrium context cannot be applied in every non-equilibrium case.

2.2.2. Excited Quantum Phase Transition

Non-analyticity can also appear for excited states hidden as a level clustering [Cap08] in the energy spectrum. An excited state quantum phase transition (ESQPT) appears

then which has become a growing community in recent years [Cap08, Str14, San15]. The ESQPT becomes then visible in the system spectrum density as discontinuities or divergence [Cap08, Bra13], which induce a non-analyticity for some system observables, e.g. for the average over the corresponding eigenstates [PF11a]. Moreover, the eigenstate structure contains the ESQPT signatures, too [San15].

ESQPT can be well visualized and understood at a semiclassical level as it is connected to a saddle point in the semi-classical energy potential as a function of system observables [Cap08]. A critical path with an energy of the saddle point - the so called separatrix - can then be defined in the semiclassical configuration space. The paths which are close to the separatrix constructs then the ESQPT signal: For both models, the ESQPT manifests itself in the observable average as a peak at a certain energy [PF11b, PF09, Bra13]. Furthermore, a semiclassical treatment allows the analytical calculation of the density of states [Bra13, Rib08]. ESQPT was for example studied in connection with quenches [PF11a, San15] or chaos [PF11a] and was already observed in molecular systems [Win05] or microwave Dirac billiards [Die13].

2.2.3. Condensation and Lasing

Condensation and lasing are two additional examples of a phase transition. Condensation appears for example in a Bose-Einstein condensate. Typical for condensation is a macroscopic occupation of the ground mode with massive particles and the system is in equilibrium [Pit03]. In contrast, lasing transition is a non-equilibrium phase transition due to the coupling with the environment and additional pumping, although it has a macroscopic mode population with massless particles in the condensed phase [Hak84]. Interestingly, despite this big difference both transitions are appearing together in dye filled cavities, which was demonstrated as experimentally [Kla10, Mar15] as theoretically [Kir13]. In the condensed phase the ground mode becomes macroscopically populated and the corresponding statistics is Bose-Einstein, in the lasing phase and for higher cavity losses one of the upper modes is macroscopically occupied with non-common statistics [Kir15].

2.3. LMG Model

The LMG Model was originally developed as a test-bed of different approximation in nuclear physics [Lip65]. Nowadays it offers a test-bed to study the properties of an interacting many-body quantum system, especially as it can be experimentally realized with trapped cold atoms [Zib10]. Due to effectively only two degrees of freedom the LMG model lends itself for explanation and visualization of different phase transitions and their connection to the expectation values of observables.

The LMG Hamiltonian reads,

$$\hat{H} = -h\hat{J}_z - \frac{\gamma_x}{N}\hat{J}_x^2 - \frac{\gamma_y}{N}\hat{J}_y^2, \tag{2.8}$$

where $\hat{J}_i = \frac{1}{2}\sum_{j=1}^{N} \hat{\sigma}_i^j, i \in \{x, y, z\}$ are collective angular momentum operators, N is the number of two-level atoms, h is an effective parameter for external magnetic field in z-direction and γ_x or γ_y describes the spin-spin interaction strength, which is the same for all spins in the LMG model. The Hamiltonian preserves the total angular momentum j as it commutes with $J^2 = J_x^2 + J_y^2 + J_z^2$. The Hamiltonian dynamic can be restricted to fixed total angular momentum j. Additionally, the Hamiltonian is invariant under the operations $\hat{J}_x \to -\hat{J}_x$ or $\hat{J}_y \to -\hat{J}_y$. However, an analytical solution of the eigenvalue problem is difficult [Pan99] but is simplified in thermodynamic limit $N \to \infty$ [Rib08, Dus05] or in the special case $\gamma_x = \gamma_y$.

2.3.1. Spectrum, QPT and ESQPT

Here we show the numerically obtained spectrum of Eq. (2.8) and the corresponding density of states which indicates the quantum criticality of the LMG model, the QPT and the ESQPT.

Figure 2.5 shows the spectral properties of the LMG Hamiltonian Eq. (2.8). Increasing the γ_x coupling, the pairs of neighbouring energy levels with different parity approach each other and become degenerated after a critical value of γ_c

$$\gamma_c = h. \tag{2.9}$$

Starting from this point the ground state energy decreases, see Fig. 2.5(a) and its second derivative has a jump at a critical γ_x value, see Fig. 2.5(b). This is the property of a QPT. The corresponding density of states (Fig. 2.5(c)) for a fixed γ_x value shows in the so called symmetry broken phase for $\gamma_x > \gamma_c$ a non-analytic behavior [Rib08] which is a signature of an ESQPT [Cap08]. Whereas for $\gamma_y = 0$ there is only one logarithmic divergence (arrow), there is an additional jump in the density of states (dashed arrow) for $\gamma_y > \gamma_x$ and the ESQPT is shifted to lower energies (arrow). The corresponding phase diagram is well known [Rib08], see Fig. 2.5(d) . In the region A is the normal phase, whereas in the regions B and C is the symmetry broken phase with one or two ESQPTs, respectively.

2.3.2. Averaged Observables

The observable averages like $\langle J_z \rangle$ or $\langle J_x^2 \rangle$ calculated for example either in the ground state for different γ_x values or in the eigenstates for a constant γ_x value show the QPT and ESQPT signatures, respectively. They are depicted in Fig. 2.6. In part (a) the $\left\langle \hat{J}_z \right\rangle$ and $\left\langle \hat{J}_x^2 \right\rangle$ are shown as a function of spin coupling γ_x in the ground state. The quantum phase transition occurs at $\gamma_x = \gamma_c = h$. Whereas in the normal phase the $\left\langle \hat{J}_x^2 \right\rangle / N$ average is always zero, in the symmetry broken phase it becomes positive. Moreover, a stability check would show a pitchfork bifurcation at γ_c. Part (b) shows the signature of the ESQPT in the expectation values of observables for fixed coupling γ_x as a function of energy. The expectation values are evaluated in different eigenstates of the LMG Hamiltonian H with the energy E. Whereas in the normal phase (dashed

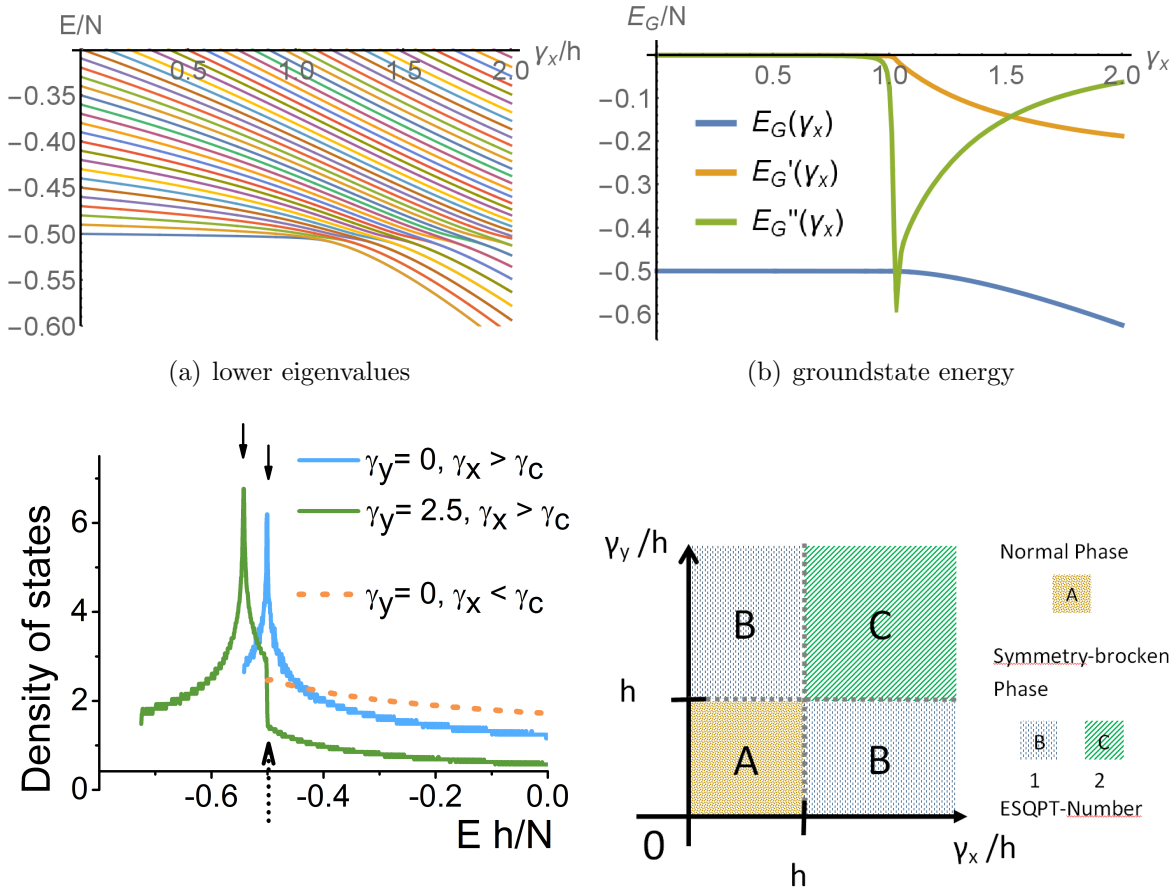

(a) lower eigenvalues

(b) groundstate energy

(c) density of states

(d) Phase Diagram

Figure 2.5.: Spectral properties of the LMG Hamiltonian Eq. (2.8). (a) The spectrum as a function of γ_x for $N = 100$ (b) The ground state energy and its derivatives for $N = 1000$. The second derivative has a jump at a critical γ_x value which marks the QPT (c) Density of states for different γ_y values for $N = 10000$. The logarithmic divergence is due to the ESQPT (arrow). On top for $\gamma_y = -2.5h$ the density of states has a jump (dotted arrow). Such behaviour is absent in the normal phase for $\gamma_x < \gamma_c$ (dashed line). (d) A sketch of a phase diagram in the (γ_x, γ_y) space. The normal phase is only in the region A. The regions B and C have one and two ESQPTs, respectively, as shown in part (c). Parameters: (a) $\gamma_y = 0$, $N = 100$ (b) $\gamma_y = 0, N = 1000$ (c) $\gamma_x = 1.5$ (solid), $\gamma_x = 0.5$ (dashed), $N = 10000$.

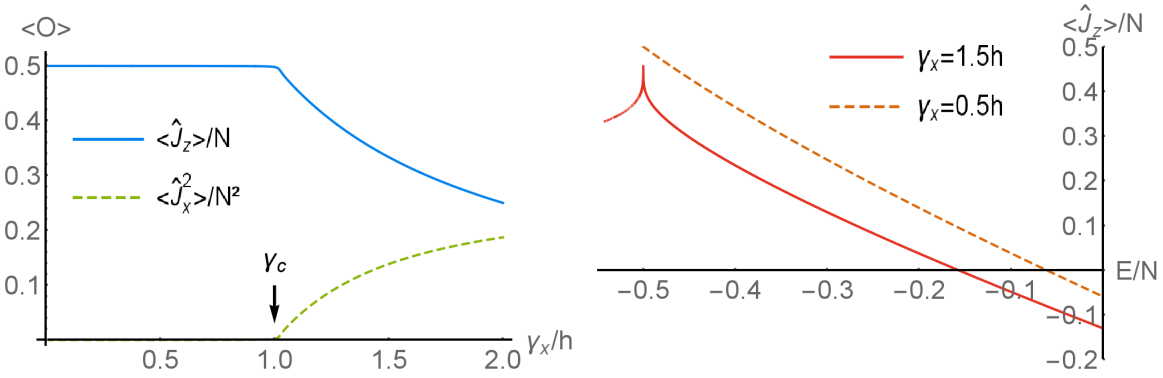

(a) ground state (b) excited states

Figure 2.6.: Averaged observable in different eigenstates. a) In the ground state the $\hat{J}_z$ expectation values are non-analytic at a critical value of γ. b) Crossing the energy of the ESQPT at -0.5 h/N the $\langle J_z \rangle$ has peak. Parameters: $\gamma_y = 0, N = 1000$.

orange line) the $\hat{J}_z$ expectation value decreases approximately linear, in the symmetry broken phase (solid red line) we see a (power law) peak at a critical energy $E/N = 0.5$ in the excited states. This is the energy, where the density of states diverges, see Fig. 2.5(c).

2.3.3. Semiclassical Energy

The properties of both quantum phase transitions can be explained as special points in the semiclassical energy landscape. Replacing the operators in Eq. (2.8) by averaged variables and rescaling by N ,e.g. $\hat{J}_i/N \to J_i$ we obtain a semiclassical rescaled LMG Hamiltonian H_{LMG} which we can directly use to calculate the energy for every system configuration (J_x, J_y, J_z) [Dus05]

$$H_{LMG} = -hJ_z - \gamma_x J_x^2 - \gamma_y J_y^2. \tag{2.10}$$

Under the restriction that the spin length J^2 is conserved, we can plot the corresponding energies H_{LMG} on the rescaled Bloch sphere with radius 1/2. In Fig. 2.7 we plot an energy landscape in the configuration space for different γ_x and γ_y values. The white lines show the paths with the same energy which the classical system would take. In the energetic landscape we see several points which we can classify as local minima (Min), local maxima (Max) and saddle points (S). First, in the normal phase Fig. 2.7(a) we see only one local minimum on top of the Bloch sphere with energy $-0.5h/N$ which corresponds to the energy of the ground state in Fig. 2.5(b) and a maximal value of J_z, see Fig. 2.6(a). Second, in the symmetry broken phase a bifurcation occurs. There are two local minima with decreased energy which are shifted to the lower J_z values, see Figs. 2.5(b) and 2.6(a) for comparison. Third, the energy of the ESQPT peak in Fig. 2.5(c) is equivalent to the energy at the saddle point (S) on the energy

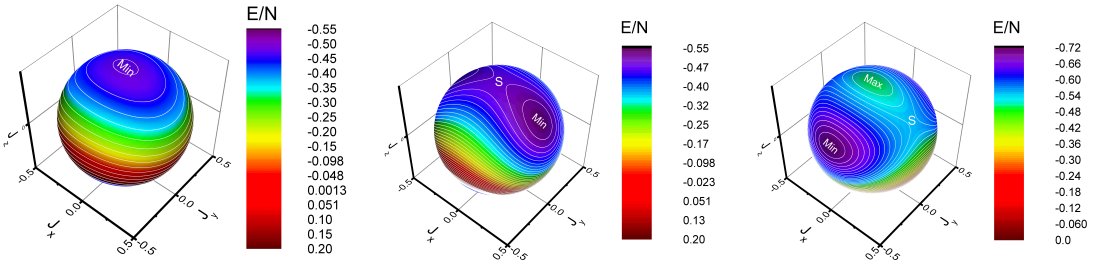

(a) $\gamma_x = 0.5h < \gamma_c, \gamma_y = 0$ (b) $\gamma_x = 1.5h > \gamma_c, \gamma_y = 0$ (c) $\gamma_x = 1.5h > \gamma_c, \gamma_y = 2.5h$

Figure 2.7.: Energetic manifold H_{LMG} for different γ_x, γ_y values. Whereas in the normal phase (part a) there is only one local minimum (Min) on the top of the sphere, it bifurcates in two (part b) for $\gamma_x > \gamma_c$ which are separated by a saddle point (S). For $\gamma_y > \gamma_x$ this saddle point moves to lower J_z values and a local maximum occurs instead (part c).

sphere. Last, but not least, for $\gamma_y > \gamma_x$ the position of the saddle point is shifted, see Fig. 2.7(c) and a local maximum occurs on top which corresponds to a jump in the density of states. Reference [Eng14, BM14a] shows that the density of states can be calculated directly from the periodic Bloch sphere dynamics. The divergence is then connected to the divergence of the period duration of paths closed to the (S) point and the jump is connected to a sudden change of paths number with some special energy.

The connection to the quantum mechanical version is the following. On the Bloch sphere each position can be fixed in spherical coordinates by two angels ϕ and θ. To perform a thermodynamic limit we use coherent states $|\theta, \phi\rangle = \sum_{m=-N/2}^{m=N/2} t_{\theta,\phi,N/2}(m) |m\rangle$ where $t_{\theta,\phi,N/2}(m)$ are the corresponding coefficients [Zha90]. The coherent states are the closest ones to the classical and are fixed by two spherical angels and the particle number N. In the thermodynamic limit the energy $\langle\theta, \phi| \hat{H} |\theta, \phi\rangle$ is equivalent to H_{LMG} for a given point on the Bloch sphere.

Interestingly, we have checked, that in the LMG case the following connection is true, too. Each Hamiltonian eigenstate with the energy E leads to some system state (J_x, J_y, J_z) on average. Inserting this state into the semiclassical LMG Hamiltonian H_{LMG}, we obtain the same energy E from the used eigenstate [1]. The origin of this could be explained with the connection of eigenstates and coherent states in the thermodynamic limit [Pau93].

2.4. Dicke Model

The Dicke model was originally introduced in 1954 by Dicke [Dic54] to study the spontaneous collective decay of the N atomic system. This resulted in a flash which scales with N^2. Later the partition function in thermal equilibrium was calculated

[1] Due to the symmetry of Eq. (2.8) the averages like $\langle J_x \rangle$ or $\langle J_y \rangle$ will be always zero. Therefore, to obtain $\langle J_x \rangle$ we calculate $\pm\sqrt{\langle J_x^2 \rangle}$ which we identify with $\langle J_x \rangle$ neglecting the fluctuations in thermodynamic limit

and the so called Hepp-Lieb QPT from a normal to superradiant phase introduced [Hep73b, Hep73a, Wan73].

The Dicke Hamiltonian reads

$$H = \omega \hat{a}^\dagger \hat{a} + \omega_0 \hat{J}_z + \frac{g}{\sqrt{2j}}(\hat{a}^\dagger + \hat{a})(\hat{J}_+ + \hat{J}_-), \tag{2.11}$$

where $a^{(\dagger)}$ is the algebra of the bosonic cavity field and $\hat{J}_{z,x,z,\pm}$ are collective bosonic operators which are defined over the sum of N two-level atoms, i.e. $J_{x,y,z} = \frac{1}{2}\sum_{j=1}^{N} \sigma_j^{x,y,z}$ and $J_\pm = \sum_{j=1}^{N} \sigma_j^\pm$. The frequencies ω and $\frac{\omega_0}{2}$ are of the cavity mode and the two-level atom, respectively. The constant g describes the interaction between the bosonic mode and the atomic system. This constant is scaled with the spin length j, this is necessary to have a defined thermodynamic limit. In the following we set $j \equiv \frac{N}{2}$ [Ema03a] assuming the maximum spin length. The Dicke Hamiltonian commutes with with $\hat{J}^2$ operator and is invariant under the transformation $\hat{a} \to -\hat{a}, \hat{J}_+ \to -.\hat{J}_+$.

2.4.1. Spectral Properties, QPT and ESQPT

Due to the bosonic mode with infinite Hilbert space, the Dicke model is much harder to treat numerically that the LMG model. However, for the numerical treatment one usually truncates the Hilbert space of the cavity mode at N_n. The truncation is dependent on the properties of interest. We use the representation of Hamiltonian Eq. (2.11) in the Dicke basis $|n\rangle \otimes |lm\rangle$, where $|n\rangle$ is an eigenstate of a bosonic system and $|lm\rangle$ is an eigenstate of J^2 and J_z. This allows us numerically to calculate the energy spectrum of the Dicke model for a finite N, see Fig. 2.8. For $N \to \infty$ this model exhibits a second order QPT, the ground state (orange line) is not analytical at a critical value of $g = g_c$ with [Hep73a, Ema03a]

$$g_c = \sqrt{\frac{\omega\omega_0}{4}}. \tag{2.12}$$

Its second derivative has a jump (blue line). For $g > g_c$ the optical mode becomes macroscopically occupied in thermodynamic limit, see Fig. 2.8(b). This indicates the result of a superradiant phase transition.

Fig. 2.9 shows that the ESQPT is present in the Dicke model, too [PF11a, Bra13]. In contrast to the LMG model, it becomes first visible in the derivative of the spectral density as a discontinuity. Note that the decrease of density for positive energy values is due to the truncation N_n.

2.4.2. Tavis-Cummings Model

Tavis-Cummings Model [Tav68] can be seen as a Dicke model with a rotating wave approximation. Keeping only the counter rotating terms Eq. (2.11) simplifies to

$$H = \omega \hat{a}^\dagger \hat{a} + \omega_0 \hat{J}_z + \frac{g}{\sqrt{2j}}(\hat{a}^\dagger \hat{J}_- + \hat{a}\hat{J}_+). \tag{2.13}$$

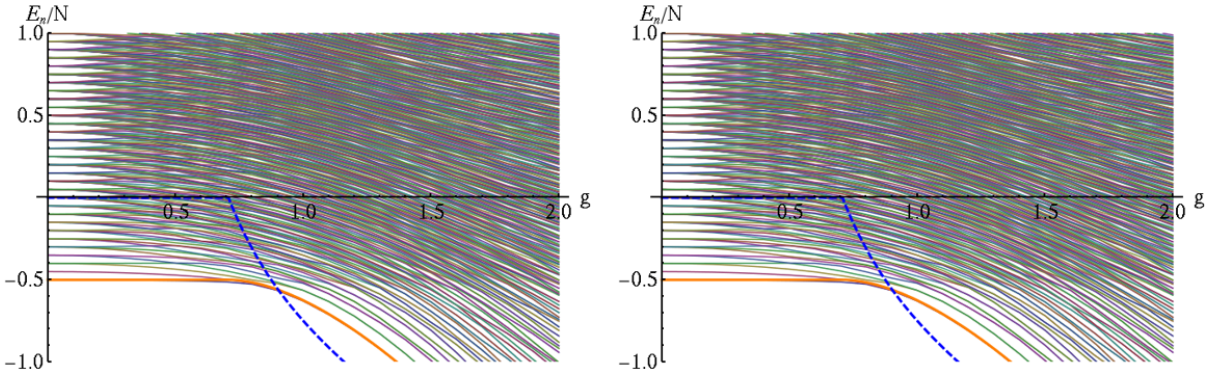

(a) Dicke - lower spectrum (b) mode occupation

Figure 2.8.: (a) Dicke spectrum calculated for $N =$ and the ground energy (orange) and its second derivative (blue) calculated in the thermodynamic limit [Ema03a] as a function of . (b) Occupation of a bosonic mode in ground state as a function of coupling constant.

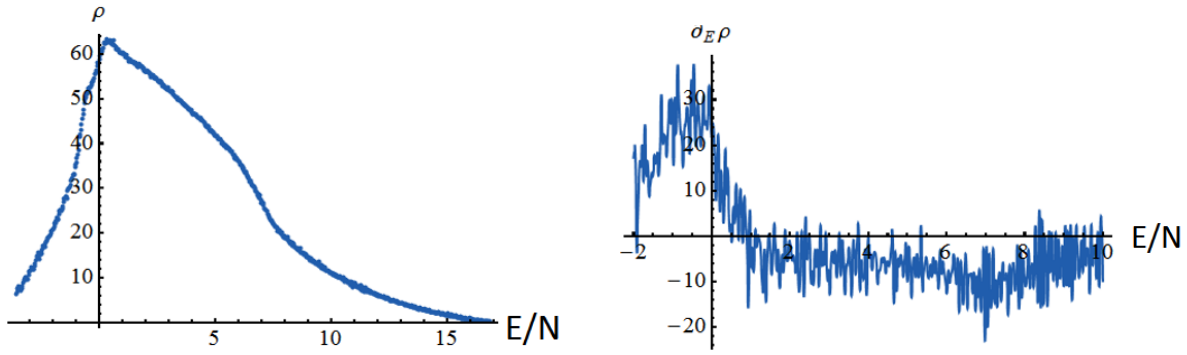

(a) Energy density (b) Energy derivative

Figure 2.9.: Spectral density (a) and its derivative (b) in the superradiant case. The ESQPT is here becomes visible first in the derivative as a (smoothed) jump. Parameters: $g = 2\omega, N_n = 350, N = 50$.

This Hamiltonian is integrable and has an additional conservation of excitation number $\hat{M} = \hat{J}_z + \hat{a}^\dagger \hat{a}$. It has also a phase transition at

$$g_c = \sqrt{\omega \omega_0}. \tag{2.14}$$

2.5. Dissipation in Quantum Systems

The dissipative effects in a quantum system which is described by a Hamiltonian H can be handled at the level of the master equation. In the Born-Markov-Secular approximation the dissipative and effects of incoherent pumping can be treated in a common way by adding to the master equation terms of Lindblad type [Scu97]. The master equation becomes then

$$\dot{\hat{\rho}} = -i \left[\hat{H}, \hat{\rho}\right] - \sum_k \frac{\kappa_k}{2} \mathcal{D}[O_k]\hat{\rho}, \tag{2.15}$$

with a Lindblad operator $\mathcal{D}[O_k]\rho = \hat{O}_k^\dagger \hat{O}_k \hat{\rho} + \hat{\rho}\hat{O}_k^\dagger \hat{O}_k - 2\hat{O}_k \hat{\rho} \hat{O}_k^\dagger$ and a dissipation rate κ_k. $\hat{O}_k$ is a system operator which is damped. Note that in general such assumption requires a microscopic re-derivation.

2.6. Quantum Regressions Theorem

The quantum regression theorem [Lax68] allows to calculate two point correlation functions based on evolution of one point correlation function for a dissipative system which dynamic is described by a Born-Markov-Secular master equation of Lindblad type, see Eq. (2.15).

A system operator average can be calculated as [Sch14a]

$$\begin{aligned}
\partial_t \left\langle \hat{O} \right\rangle &= \mathrm{Tr}\left\{ \hat{O} \dot{\hat{\rho}} \right\} \overset{\text{Eq. (2.15)}}{=} \mathrm{Tr}\left\{ -i\, \hat{O} \left[\hat{H}, \hat{\rho}\right] - \kappa\, \hat{O}\, \mathcal{D}[\hat{a}]\hat{\rho} \right\} \\
&= \mathrm{Tr}\left\{ -i\hat{O} \left(\hat{H}\hat{\rho} - \hat{\rho}\hat{H} \right) - \kappa \hat{O} \left(\hat{a}^\dagger \hat{a} \rho + \rho \hat{a}^\dagger \hat{a} - 2\hat{a}\rho\hat{a}^\dagger \right) \right\} \\
&= -i\, \mathrm{Tr}\left\{ \left(\hat{O}\hat{H} - \hat{H}\hat{O} \right) \rho \right\} - \kappa\, \mathrm{Tr}\left\{ \left(\hat{O}\hat{a}^\dagger \hat{a} + \hat{a}^\dagger \hat{a} \hat{O} - 2\hat{a}^\dagger \hat{O} \hat{a} \right) \rho \right\} \\
&= i \left\langle \left[\hat{H}, \hat{O}\right] \right\rangle - \kappa \left\langle \left[\hat{O}, \hat{a}^\dagger \hat{a}\right]_+ - 2\hat{a}^\dagger \hat{O} \hat{a} \right\rangle .
\end{aligned} \tag{2.16}$$

Let the system $\hat{O}_1, \hat{O}_2 .. \hat{O}_j .. \hat{O}_F$ be the set of all possible linear independent operators on the system Hilbert-space, then we can rewrite the Eq. (2.16) $\hat{O}_j$ as [Sch14a]

$$\partial_t \left\langle \hat{O}_j \right\rangle (t) = \mathrm{Tr}\left\{ \sum_k \left[G_{jk} \hat{O}_k \right] \hat{\rho}(t) \right\}, \tag{2.17}$$

there G_{jk} are entries of a matrix $\mathbf{G}$ chosen in a way to fulfill the equality.

Switching to Heisenberg picture with time-dependent Operators $\hat{O}_k(t)$ and a constant density matrix ρ Eq. (2.17) can be formulated as a differential equation for an operator evolution

$$\partial_t \hat{O}_j(t) = \sum_k G_{jk} \hat{O}_k(t). \tag{2.18}$$

The quantum regressions theorem states that a two-point correlation function obeys

$$\partial_t \left\langle \hat{O}_j(t+z)\hat{O}_l(t) \right\rangle = \mathrm{Tr}\left\{ \sum_k \left[G_{jk}\hat{O}_k(t+z)\hat{O}_l(t) \right] \hat{\rho}(t) \right\} = \sum_k G_{jk} \left\langle \hat{O}_k(t+z)\hat{O}_l(t) \right\rangle \tag{2.19}$$

with the same matrix $\mathbf{G}$.

2.7. Experimental Setups

2.7.1. Dicke Phase Transition

The Dicke quantum phase transition was realized in the ingenious experimental setup by Baumann et al. [Bau10, Bau11] using a pure Bose-Einstein condensate (BEC) with 10^5 ^{87}Rb atoms trapped inside an ultrahigh-finesse optical cavity. The whole system gets additionally pumped with a laser which creates a standing-wave potential perpendicular to the cavity direction, see Fig. 2.10(a). The pump laser plays a key role for the obtained results. First, if its pump power exceeds a critical value, a self organization process was observed where an atomic momentum-state, the cavity mode become macroscopically occupied, see Fig. 2.10(b). Interestingly, the system can be mapped to a Dicke model, where the momentum states of the Bose-Einstein condensate build the two-level atomic system (after adiabatic elimination of higher states). Thus, the observed self-organization process corresponds to the Dicke quantum phase transition. The interaction of the BEC with the pump field is then set by the intensity of a pump laser and the scattering of the cavity and pump laser fields generate the non-RWA interaction in the Dicke model

$$g(\hat{a}^\dagger + \hat{a})(\hat{J}_+ + \hat{J}_-).$$

Here, $\hat{a}^\dagger \hat{J}_+$ describes an absorption of a photon from a pumped field and its emission into the cavity field. Essential is now the momentum conservation. As the pump and cavity fields are perpendicular to each other, the momentum of photons is carried by the atom. The ground state of a BEC is a zero momentum state $|0_x, 0_z\rangle$. A photon absorption from a pump laser field excites the atomic system to the $|0_x, 0_z\rangle$ state and the following emission into the cavity field excites the atomic system to the $|k_x, k_z\rangle$ state, see Fig. 2.10(c). In the same way, aJ^- describes a complementary process,

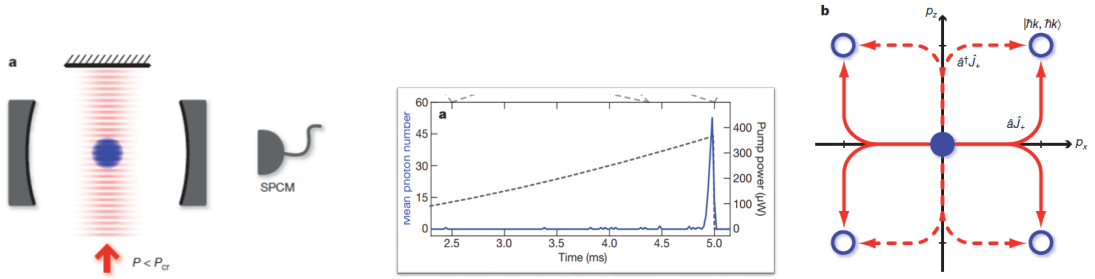

(a) Experimental setup (b) Experimental setup (c) Momentum space

Figure 2.10.: Taken from Ref. [Bau10], ©(2010) Nature Publishing Group, reprinted by permission from Macmillan Publishers Ltd: Nature. (a) Experimental setup of the Dicke model with a pumping field (b)and the observation of the QPT when the pumping power overgrows the critical threshold. (c) scattering between the pumping and cavity fields generate an atomic two-level transition from the BEC ground state with zero momentum state to a excited BEC.

where the cavity photon is absorbed and emitted into the pump field. The remaining momenta carries the atomic system. In this way the atomic system can populate a higher momentum state, which corresponds to an excited level of the two-level atomic system in the Dicke model.

Note that the described setup was realized for a rather big dissipation rate κ. Reference [Kli15] describes the implementation of the Dicke model with a weak dissipation channel. A Dicke model can be experimentally realized using Raman transitions [Bad14], too. With the last it is possible to realize the rotated-wave version of the Dicke – the Tavis-Cummings model.

2.7.2. Tavis-Cummings Model

The Dicke model was even realized by Baden et al. [Bad14] using the cavity-assisted Raman transitions in ultra-cold atoms which are coupled to an optical cavity mode [Dim07]. The advantage of the setup is, that it is possible to tune the counter and non-counter rotated terms of the Hamiltonian interaction part Eq. (2.11) independently. Thus, it is possible to switch between the full Dicke and the Tavis-Cummings models. For the realization of the Dicke or TC interaction the interplay between two laser beams with frequencies Ω_s and Ω_r, the hyperfine states of atoms which are additionally split by an applied magnetic field and the Raman states. The atoms are trapped in the cavity. Figure 2.11 shows a scheme of the setup. The hyperfine ground states $|F = 1, m = 1\rangle$, $|F = 2, m = 2\rangle$ are coupled to each other via two Raman transitions. The first transition takes the atom from the state $|F = 1, m = 1\rangle$ to the state $|F = 2, m = 2\rangle$ via absorption of a photon from the laser beam with the frequency Ω_s and emission of a photon into the cavity, and vice versa. The second transition takes the atom from the state $|F = 1, m = 1\rangle$ to the state $|F = 2, m = 2\rangle$ by absorption of

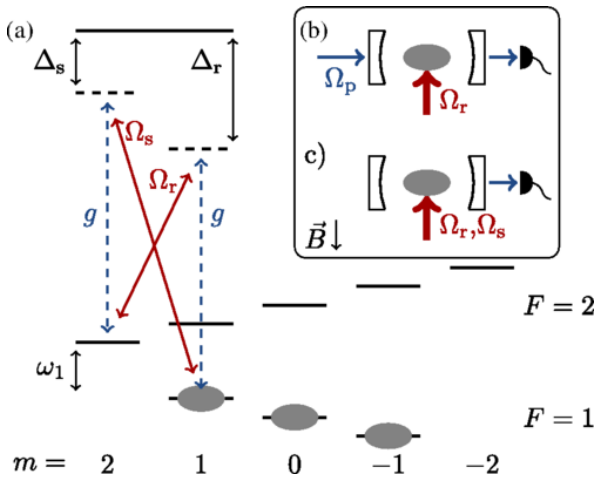

Figure 2.11.: Taken (and reprinted with permission) from Ref. [Bad14], ©(2014) American Physical Society. Experimental scheme of the Dicke and TC models. (a) Schematic energy representation of hyperfine states of the atoms, coupling to the Raman states and the laser beams. Setup for implementation of the Dicke (b) and TC (c) models.

a photon from a cavity field and emission into the laser beam field with the frequency Ω_r, and vice versa. Both processes describe the realization of the non-counter and counter rotated terms in the Dicke Hamiltonian, respectively. Thus, without the first laser beam Fig. 2.11(c) this is a realization of a TC model.

2.7.3. Lipkin-Meshkov-Glick

The Lipkin-Meshkov-Glick model was implemented by Oberthaler et al. using a ^{87}Rb Bose-Einstein condensate [Zib10, Gro10]. Therefore they prepare the system in two hyperfine states $|a\rangle$ and $|b\rangle$ of the Rb, see Fig. 2.12(a) for a schematic setup. A two-photon transition with a frequency Ω induce a linear coupling between these states. Additionally, they use a Fashbach resonance to manipulate the interparticle interaction χ. The dynamics is then effectively described by the LMG Hamiltonian

$$\hat{H} = \chi \hat{J}_z^2 - \Omega \hat{J}_x.$$

The system is designed in a such way that the accessible parameter regime lies around the bifurcation point of the LMG Hamiltonian, i.e. $\Omega \approx \chi N$. Thus the system can be driven from the Rabi to Josephson regime which correspond to the normal and the symmetry brocken phase in the LMG model. Oberthaler et al. use $N = 300 - 1000$ atoms, thus a semiclassical approach can be used. Figure 2.12(b) shows the measured results for the inversion $\left\langle \hat{J}_z \right\rangle$ which bifurcates at a critical coupling $\Lambda = \frac{\chi N}{\Omega}$ which matches pretty good to the corresponding mean-field calculation.

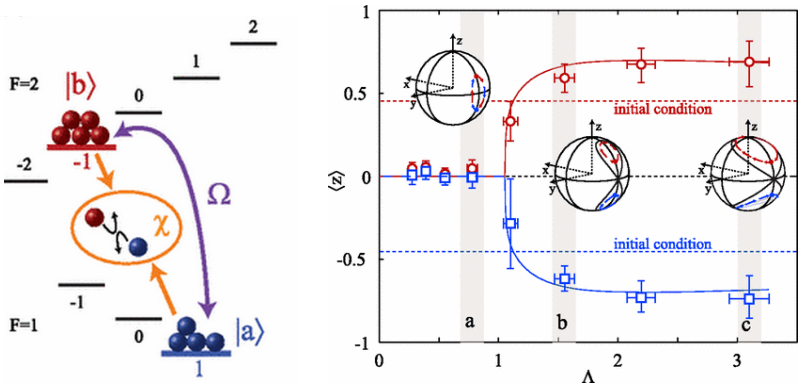

(a) energetic configuration (b) Bifurcation Observation

Figure 2.12.: Taken (and reprinted with permission) from Ref. [Zib10], ©American Physical Society. Experimental implementation of the LMG model in a BEC using Fashbach resonance. (a) Schematic energy levels in the experimental setup. (b) Experimental observation of the bifurcation and comparison with a semiclassical prediction.

3. Time-Delayed Feedback Control of the Dicke-Hepp-Lieb Superradiant Quantum Phase Transition

This chapter is mainly based on the results published in Ref. [Kop15a].

3.1. Introduction

Interacting quantum systems with time-dependent Hamiltonians offer rich and exciting possibilities to study many-body physics beyond equilibrium conditions. There has be a recent surge in generating correlated non-equilibrium dynamics in a controlled way by changing the interaction parameters as a function of time, for example by periodically modulating the coupling constants, or by abruptly quenching them. In this chapter we show we show another and conceptually very different option for driving quantum systems out of equilibrium, by modulating interaction parameters via a measurement-based feedback loop.

Our key idea is to generate new non-equilibrium phases via Pyragas control of the interaction between the single bosonic cavity mode and the collection of quantum two-level systems [Dic54, Hep73b, Wan73] in Dicke-Hepp-Lieb superradiance. The superradiant transition without control, which has been observed only recently in cold atoms within a photonic cavity [Bau10, Bau11, Rit13b, Nag10], also with applied quenches [Kli15] or using cavity-assisted Raman transitions [Bad14], has an underlying semi-classical bifurcation, which makes it an ideal candidate to study feedback at the boundary between non-linear (classical) dynamics and quantum many-body systems [Ema03b, Ema03a].

Open loop control of the Dicke model has been studied in the past, for example in the form of periodic modulations [Bas12, Bau11] or linear increase of the atom-field-coupling constants [Ace15] or the level splitting modulation [Vac12, DL09]. Last but not least, Grimsmo et al. [Gri14] found a speed-up towards the stationary state and qualitative changes of the phase diagram when applying Pyragas-feedback to the cavity mode alone incoherently. In our model, we condition the effective coupling strength between the cavity and the atoms of the Dicke system - in the experiment just proportional to the laser intensity [Bau10] - on a difference of photon numbers emitted from the cavity at different times. We use a mean field approach and linear stability analysis in order to show that closed loop control dramatically affects the states in the primary superradiant regime, creating a new phase with an infinite sequence of Hopf

bifurcations between stable fixed points and limit cycles. We also derive analytical results in the form of a single transcendental equation that determined the boundaries between the different zones in the phase diagrams.

The structure of this chapter is as follows: In Sec. 3.2 we introduce the model with the conditioned coupling constant $g(t)$, and perform the linearized stability analysis based on semiclassical equations of motion; in Sec. 3.3 we recapitulate the main results without feedback whereas in Sec. 3.4 we visualize and discuss the results in presence of feedback and also go beyond the linear stability analysis and give more details on the numerical procedure; in Sec. 3.5 we summarize our findings, discussing them in a more general context.

3.2. Non-equilibrium Dissipative Dicke Model with Time-Delayed Feedback.

3.2.1. General Model

The Hamiltonian of the Dicke model

$$\hat{H} = \omega \hat{a}^\dagger \hat{a} + \omega_0 \hat{J}_z + \frac{g}{\sqrt{2j}}(\hat{a}^\dagger + \hat{a})(\hat{J}_+ + \hat{J}_-) \tag{3.1}$$

describes the interaction between a single bosonic mode with frequency ω and annihilation operator $\hat{a}$, and N two level systems with level splitting ω_0 and collective angular momentum operators $\hat{J}_{z,\pm}$ [Ema03b]. The latter are defined as a sum over the two level system $\hat{J}_z = \frac{1}{2}\sum_{k=1}^{N} \sigma_{z,\pm}^k$ and $\hat{J}_\pm = \sum_{k=1}^{N} \sigma_\pm^k$, where $\sigma_k^{\pm,z}$ are the Pauli matrices of the k-th atom. The total angular momentum is the pseudo-spin j, and we set it to its maximum value, i.e., $j = N/2$. The last summand of the Hamiltonian $\hat{H}$ is the interaction between the bosonic mode and the collective angular momentum in its full form and is the essence of the Dicke model. The interaction parameter g is often assumed constant and even then leads to a huge amount of fascinating effects [Ema03a, Nag11]. The factor $\frac{1}{\sqrt{2j}}$ is necessary to have a physical and well defined thermodynamic limit. See Sec. 2.4 for more information. For our feedback scheme we use an open realization of the Dicke model, coupling the optical mode to a zero-temperature bath. The corresponding density matrix $\hat{\rho}$ of the Dicke system in the common Born-Markov approximation is [Scu97, Bre02, Kop13].

$$\dot{\hat{\rho}}(t) = -i[\hat{H}, \hat{\rho}] - \kappa \mathcal{D}[\hat{a}]\hat{\rho}, \tag{3.2}$$

where $\mathcal{D}[\hat{a}]\rho = \hat{a}^\dagger \hat{a}\rho + \rho \hat{a}^\dagger \hat{a} - 2\hat{a}\rho\hat{a}^\dagger$ and κ is decay rate. Fig. 3.1 visualizes the Dicke system with the main parameters. Note that the form of the master equation (3.2) assumes that the system Hamiltonian is in the rotated frame at the frequency of a pump laser [Kop13]. Thus the system gets pumped, which prevents it from going to thermal equilibrium.

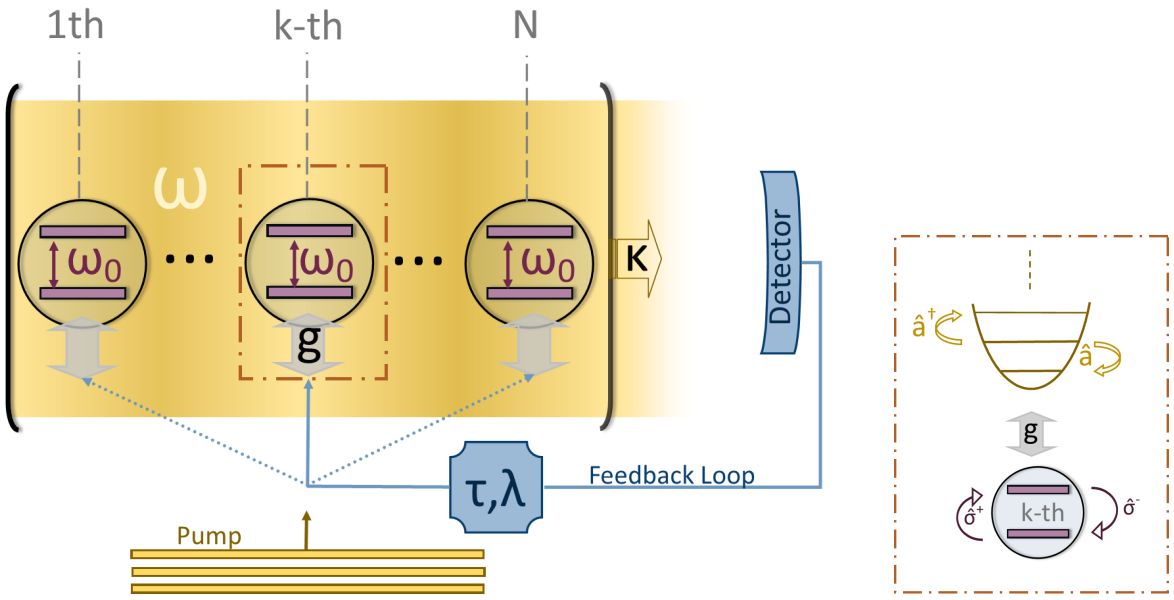

Figure 3.1.: Visualization of dissipative Dicke model with feedback. (left) Cavity light mode with the frequency ω interacts with the strength g with each of N two-level atoms. The bosonic mode decays with the rate κ to the environment. The time-delayed feedback loop modifies the coupling strength g based on the photon measurement results, τ and λ are the delay and the amplification of the feedback signal, respectively. Additionally the bosonic mode is pumped by a pumping laser. (right) A simple visualization of light-atom interaction with corresponding algebra.

3.2.2. Implementation of Pyragas Feedback

In contrast to a constant g coupling, we assume here a time-dependent coupling $g(t)$ that is modulated by a time-delayed feedback loop. Among various models for $g(t)$, the Pyragas form [Pyr92]

$$g \to g(t) = g_0 + \frac{\lambda}{N}\left[\left\langle \hat{a}^\dagger \hat{a}\right\rangle (t-\tau) - \left\langle \hat{a}^\dagger \hat{a}\right\rangle (t)\right] \tag{3.3}$$

with the time-delayed feedback of the boson number at two different times t and $t-\tau$ and feedback strength λ turns out to lead to the richest phase diagrams.

As the averaged photon flux is proportional to the mean cavity photon occupation number [Özt12, Kop13], the form of the Eq. (3.3) would correspond to measured, average photon fluxes coupled back to the interaction parameter g, see Fig. 3.1. Moreover, in the pioneering experiments for the Dicke-Hepp-Lieb phase transition in open photonic cavities [Bau10] this coupling constant is set by intensity of a pump laser, which, in general, offers high degree of control. Apart from the Pyragas delay form, this scheme is in fact close to the original feedback loops used for modulating the photon counting statistics in lasers [Mac86].

We note that by using mean (expectation) values in equation (3.3) instead of operators (and additional noise terms in a stochastic master equation [Wis09]) for the boson occupations, we already assume a mean field description that we expect to hold for $N \to \infty$ and that we formalize in the following.

3.2.3. Semiclassical equations.

In analogy with semiclassical laser theory, phase transitions in the Dicke model for $N \to \infty$ are well described by mean-field equations for (factorized) operator expectation values [Bon70, Bha12, Arm06, Kop13].

3.2.3.1. Results: Sum-up

In this part we sum up the results from section 3.2.3. Auxiliary calculations and additional comments can be found after this part. The semiclassical mean-field equations in thermodynamic limit read

$$\begin{aligned} \dot{x} &= -\kappa x + \omega y, \quad \dot{y} = -\kappa y - \omega x - 2\frac{g(t)}{\sqrt{2j}} J_x, \\ \dot{J}_x &= -\omega_0 J_y, \quad \dot{J}_y = \omega_0 J_x - 4\frac{g(t)}{\sqrt{2j}} \cdot x \cdot J_z, \dot{J}_z = 4\frac{g(t)}{\sqrt{2j}} \cdot x \cdot J_y, \end{aligned} \tag{3.4}$$

where we have split a and $J_\pm$ into real and imaginary parts, $a = x + iy$ and $J_\pm = J_x \pm i J_y$ and denoted operator averages by corresponding symbols without hat. Bosonic mode is damped by the decay rate κ, and the coupling $g(t)$ takes the form $g(t) = g_0 + \lambda\left(x_\tau^2 - x^2 + y_\tau^2 - y^2\right)$ with the shortcut $f_\tau \equiv f(t-\tau)$.

Note that the length of the pseudo-spin j is a conserved quantity even for time dependent $g(t)$. Therefore, the time development of the spin subsystem takes place on the surface of a Bloch sphere with the radius $N/2$.

3.2.3.2. Derivation

To derive the mean-field equations we use a standard formula for an averaged value of a system operator $\hat{O}$ based on the density matrix ρ.

$$\left\langle \hat{O} \right\rangle = \mathrm{Tr}\left(\hat{O}\hat{\rho}\right) \quad \Rightarrow \quad \partial_t \left\langle \hat{O} \right\rangle = \mathrm{Tr}\left(\hat{O}\dot{\hat{\rho}}\right). \tag{3.5}$$

Note that as we are in the Schrödinger picture, the system operators are time independent that is why only ρ depends on time. As the given density matrix ρ has a Lindblad form Eq. (3.2), we can rewrite Eq. (3.5) using trace properties as

$$\partial_t \left\langle \hat{O} \right\rangle = \mathrm{Tr}\left\{\hat{O}\dot{\hat{\rho}}\right\} \overset{\text{Eq. (3.2)}}{=} = i\left\langle \left[\hat{H}, \hat{O}\right] \right\rangle - \kappa \left\langle \left[\hat{O}, \hat{a}^\dagger \hat{a}\right]_+ - 2\hat{a}^\dagger \hat{O} \hat{a} \right\rangle, \tag{3.6}$$

see Sec. 2.6 for a derivation. Now we can determine the equation of motion for the averages over the $\hat{a}, \hat{a}^\dagger, \hat{J}_\pm, \hat{J}_z$ operators. For the field mode, by using the Hamiltonian

Eq. (3.1) with time dependent coupling constant $g(t)$ and knowing bosonic commutator relations $\left[\hat{a}, \hat{a}^\dagger\right] = 1 \Rightarrow \left[\hat{a}, \hat{a}^\dagger\hat{a}\right] = \hat{a}$, we obtain

$$\begin{aligned}\partial_t \langle\hat{a}\rangle &= i\left\langle\left[\hat{H}, \hat{a}\right]\right\rangle - \kappa\left\langle\hat{a}\hat{a}^\dagger\hat{a} + \hat{a}^\dagger\hat{a}\hat{a} - 2\hat{a}^\dagger\hat{a}\hat{a}\right\rangle \qquad (3.7)\\ &= i\left\langle\omega\hat{a} + \frac{g(t)}{\sqrt{2j}}\hat{J}_- + \frac{g(t)}{\sqrt{2j}}\hat{J}_+\right\rangle - \kappa\left\langle\left[\hat{a}, \hat{a}^\dagger\right]\hat{a}\right\rangle\\ &= (i\omega - \kappa)\langle\hat{a}\rangle + i\frac{g(t)}{\sqrt{2j}}\left(\left\langle\hat{J}_+\right\rangle + \left\langle\hat{J}_-\right\rangle\right). \qquad (3.8)\end{aligned}$$

The equation of motion for the atomic system can be derived in an analogous manner. First, by use [1] of $\left[\hat{J}_x, \hat{J}_y\right] = i\hat{J}_z$ we get

$$\begin{aligned}\left[\hat{J}_-, \hat{J}_z\right] &= \left[\hat{J}_x, \hat{J}_z\right] - i\left[\hat{J}_y, \hat{J}_z\right] = -i\hat{J}_y + \hat{J}_x = \hat{J}_-, \qquad (3.9)\\ \left[\hat{J}_z, \hat{J}_+\right] &= \hat{J}_+,\\ \left[\hat{J}_+, \hat{J}_-\right] &= 2\hat{J}_z.\end{aligned}$$

Then using Eq. (3.6) we note that the dissipative κ term vanishes as $\left[a^{(\dagger)}, J_{\pm,z}\right] = 0$. With the Hamiltonian Eq. (3.1) we obtain

$$\partial_t \langle J_-\rangle = i\left\langle\left[H, \hat{J}_-\right]\right\rangle = -i\omega_0\left\langle\hat{J}_-\right\rangle + 2i\frac{g(t)}{\sqrt{2j}}\left\langle(\hat{a} + \hat{a}^\dagger)\hat{J}_z\right\rangle, \qquad (3.10)$$

$$\partial_t \langle J_z\rangle = i\left\langle\left[H, \hat{J}_z\right]\right\rangle = i\frac{g(t)}{\sqrt{2j}}\left\langle(\hat{a} + \hat{a}^\dagger)\left[\hat{J}_+ + \hat{J}_-, \hat{J}_z\right]\right\rangle = i\frac{g(t)}{\sqrt{2j}}\left\langle(\hat{a}^\dagger + \hat{a})(\hat{J}_- - \hat{J}_+)\right\rangle.$$

Other equations can be obtained by adjunction. As we see, the equation of motion for a single operator average couples to an average of two operator products, for example $\left\langle\hat{J}_-\right\rangle$ couples to $\left\langle\hat{a}\hat{J}_z\right\rangle$. One could now derive the equation for the average over two operator products, but they would couple to an average over three operators etc. This is the well known hierarchy problem. A common way to handle it is a truncation of the mean-field equations at certain level.

Splitting an arbitrary operator $\hat{O}$ in two contributions: the mean-field part $\left\langle\hat{O}\right\rangle \equiv O$, which is an average, and the fluctuations around it $\delta\hat{O}$, i.e., $\hat{O} = O + \delta\hat{O}$ the average of two operator values becomes

$$\left\langle\hat{O}_1\hat{O}_2\right\rangle = O_1O_2 + \delta\hat{O}_1O_2 + \delta\hat{O}_2O_1 + \delta\hat{O}_1\delta\hat{O}_2.$$

In the thermodynamic limit, i.e., $N \to \infty$, it is known for different models including the Dicke model, too, that regardless of the quantum fluctuations, the point of the phase

[1] this follows from the definition of the collective spin operator and the well known commutator relation for Pauli matrices $[\sigma_x, \sigma_y] = 2i\sigma_z$.

transition or averaged operator values are the same [Bon70, Bha12, Arm06, Kop13]. The big advantages of this approximation is a closed set of the differential equations.

Thus, applying the mean-field approximation to our equations for the operator averages Eqs. (3.7), (3.10) we obtain a closed set of semiclassical equations for the Dicke model with time dependent coupling strength g

$$\begin{aligned}
&\partial_t a = -(i\omega+\kappa)a + i\frac{g(t)}{\sqrt{N}}\left(J_+ + J_-\right), \quad \partial_t a^* = (i\omega-\kappa)a^* - i\frac{g(t)}{\sqrt{N}}\left(J_+ + J_-\right), \\
&\partial_t J_- = -i\omega_0 J_- + 2i\frac{g(t)}{\sqrt{N}}(aJ_z + a^* J_z), \quad \partial_t J_+ = i\omega_0 J_+ - 2i\frac{g(t)}{\sqrt{N}}(aJ_z + a^* J_z), \\
&\partial_t J_z = i\frac{g(t)}{\sqrt{N}}(a^* + a)(J_- - J_+).
\end{aligned} \tag{3.11}$$

Here we used a shortcut O instead of an operator average $\left\langle \hat{O} \right\rangle$, derived adjunct equations using the definition $\left\langle \hat{O}^\dagger \right\rangle = O^*$ and replaced $2j$ by the number of atoms N according to our assumption of maximum spin in the introduction part.

For the numerical purpose it is useful to have real valued equations instead of the complex ones. Thus, we make an alternative formulation of Eqs. (3.11) in terms of real-valued functions $\Re(a) \equiv x$, $\Im(a) \equiv y$ and use the connections $J_\pm = \frac{1}{2}\left(J_x + iJ_y\right) \Leftrightarrow J_x = \frac{1}{2}\left(J_+ + J_-\right)$, $J_y = -\frac{i}{2}\left(J_+ - J_-\right)$. Evaluating real and imaginary parts from Eqs. (3.11), it is straightforward to obtain the following set of real-valued equations in thermodynamic limit

$$\begin{aligned}
&\dot{x} = -\kappa x + \omega y, \quad \dot{y} = -\kappa y - \omega x - 2\frac{g(t)}{\sqrt{N}} J_x, \\
&\dot{J}_x = -\omega_0 J_y, \quad \dot{J}_y = \omega_0 J_x - 4\frac{g(t)}{\sqrt{N}} \cdot x \cdot J_z, \quad \dot{J}_z = 4\frac{g(t)}{\sqrt{N}} \cdot x \cdot J_y.
\end{aligned} \tag{3.12}$$

The time dependent coupling $g(t)$ has then the following form

$$\begin{aligned}
g(t) &= g_0 + \frac{\lambda}{N}\left[\left\langle \hat{a}^\dagger \hat{a} \right\rangle (t-\tau) - \left\langle \hat{a}^\dagger \hat{a} \right\rangle (t)\right] = g_0 + \frac{\lambda}{N}\left[(a^* a)(t-\tau) - (a^* a)(t)\right] \\
&= g_0 + \frac{\lambda}{N}\left[x^2(t-\tau) + y^2(t-\tau) - x^2(t) - y^2(t)\right].
\end{aligned} \tag{3.13}$$

3.2.3.3. Rescaling

Analysing Eqs. (3.12) one has to pay attention that not only $N \to \infty$, but also the spin components scale with the number of particles N, as the spin expectation values J_i are the sum over all spins. This fact prohibits the vanishing of all terms of order $\frac{1}{\sqrt{N}}$. As the mean field equations are only valid in the thermodynamic limit ($N \to \infty$), we can only operate with rescaled observables to avoid infinities. Indeed, the whole

equations set (3.12) can be rescaled by factorizing each equation with N^{-1} or $N^{-1/2}$ in the following way

$$\begin{aligned} \frac{\dot{x}}{\sqrt{N}} &= -\kappa\frac{x}{\sqrt{N}} + \omega\frac{y}{\sqrt{N}}, \qquad \frac{\dot{y}}{\sqrt{N}} = -\kappa\frac{y}{\sqrt{N}} - \omega\frac{x}{\sqrt{N}} - 2g(t)\frac{J_x}{N}, \\ \frac{\dot{J}_x}{N} &= -\omega_0\frac{J_y}{N}, \qquad \frac{\dot{J}_y}{N} = \omega_0\frac{J_x}{N} - 4g(t)\frac{x}{\sqrt{N}}\cdot\frac{J_z}{N}, \qquad \frac{\dot{J}_z}{N} = 4g(t)\frac{x}{\sqrt{N}}\cdot\frac{J_y}{N}. \end{aligned} \tag{3.14}$$

From this rescaling we also see that atomic observables x and y scale with $1/\sqrt{N}$, thus the photon number $\left\langle \hat{a}^\dagger\hat{a}\right\rangle = a^*a = x^2 + y^2$ scales with the number of particles N. At this point we also see the usefulness of the coupling constant rescaling. Without the $\frac{1}{\sqrt{N}}$ factor, it would be also necessary to rescale the coupling constant g to keep the scaling properties of the mean-field equations.

3.2.3.4. Spin Length Conservation

Like in the closed version ($\kappa = 0$) of the Dicke model, the spin length $\hat{J}^2$ is a conserved quantity even for time dependent $g(t)$ [Ema03a, Bha12]. Whereas in the closed case this means that $\hat{J}^2$ commutes with the system Hamiltonian $\hat{H}$, in the open ($\kappa \neq 0$) case one has additionally to take care of the dissipative term and prove that $\partial_t\hat{J}^2 = 0$. We check the first property using $\left[\hat{J}^2, \hat{J}_{x,y,z}\right] = 0$,

$$\begin{aligned} \left[\hat{H}, \hat{J}^2\right] &= \omega_0\left[\hat{J}_z, \hat{J}^2\right] + \frac{g(t)}{\sqrt{2j}}(\hat{a}^\dagger + \hat{a})\left[\hat{J}_+ + \hat{J}_-, \hat{J}^2\right] \\ &= 2\frac{g(t)}{\sqrt{2j}}(\hat{a}^\dagger + \hat{a})\left[\hat{J}_x, \hat{J}^2\right] = 0. \end{aligned} \tag{3.15}$$

With this result we show that $\partial_t\hat{J}^2 = 0$. Using Eq. (3.6) we see that its second part $[\hat{J}^2, \hat{a}^\dagger\hat{a}]_+ - 2\hat{a}^\dagger\hat{J}^2\hat{a}$ vanishes as the atomic operators commute with the optical ones. Its first part is zero because of the previous calculation. Thus the dissipation does not affect the spin length even for time dependent g values. Moreover, as it should be, the derived mean-field equations (3.4) conserve the spin length in spite of truncation

$$\partial_t J^2 = 2J\dot{J} = 2(J_x\dot{J}_x + J_y\dot{J}_y + J_z\dot{J}_z) = 0, \tag{3.16}$$

which means that the spin length is constant and we fix it at the maximum value,

$$J^2 = \frac{N}{2} = \text{const.} \tag{3.17}$$

3.2.4. Fixed Points and Stability

The long-time dynamics of a non-linear equation is given by attractors of the system. Due to the dissipation to the environment the Dicke system has a non-equilibrium steady state – a fixed point. The fixed points of Eq. (3.4) are well known [Bha12] and do not depend on τ since the feedback term Eq. (3.3) vanishes in the steady state due to the Pyragas form. To calculate them, we set all time derivatives in the corresponding equation to zero and solve it for optical and atomic expectation values. There are two different solutions which corresponds to two different phases.

- The trivial solution

$$J_x^0 = J_y^0 = x^0 = y^0 = 0, \quad J_z^0 = \pm N/2 \tag{3.18}$$

  corresponds to the normal phase and exists for all parameter values. Note that the value for J_z is fixed by the constrain (3.17).

- The non-trivial solution

$$J_x^0 = \pm\sqrt{\frac{N^2}{4} - J_z^{0^2}}, \qquad J_y^0 = 0, \qquad J_z^0 = \frac{-N\omega_0(\kappa^2+\omega^2)}{8g_0^2\omega}, \tag{3.19}$$
$$x^0 = -J_x^0\frac{2g_0\omega}{\sqrt{N}(\kappa^2+\omega^2)}, \qquad y^0 = \frac{\kappa x_0}{\omega}$$

  corresponds to the superradiant phase that exists only if $g \geq g_c$.

The critical coupling g_c is given by

$$g_c \equiv \sqrt{\omega_0(\kappa^2+\omega^2)/4\omega}. \tag{3.20}$$

3.2.4.1. Linearization

The environment around a fixed point acts either attractive or repulsive. In the first case the solution would converge to the fixed point and the latter would be stable, in the other case not. For two dimensional system described by first order differential equations without time delay this property can be described and visualized by a vector field that gives the direction of the system motion. This vector field can be calculated at every point in configuration space [Str01]. However, for a more complicated system this is not possible any more. Instead the linearization procedure is used, which also holds for systems with time delay [Sch08]. The equations have to be linearized around the fixed point. The linearized equations can describe the dynamics of a system correctly if the initial condition is chosen close to the fixed point, so that the influence of other possible attractors is insignificant. As the resulted equations are linear, they can be solved by an exponential ansatz $\sim e^{\Lambda t}$, where Λ has to be determined. The value of Λ determines whether the fixed point is stable or not. Imaginary and real parts of Λ describe frequency of oscillations and the amplitude, respectively. Thus, the solution

converges if $e^{\Lambda t} \to 0$ for $t \to \infty$ which is the case for $\Re(\Lambda) < 0$. Only then the solution does not diverge for $t \to \infty$. In the case $\Re(\Lambda) > 0$ the ansatz diverges, the distance to the fixed point increases exponentially, thus the linearized equations are then not valid any more and the fixed point is unstable [Str01].

To find out how the time-delayed feedback affects the stability of the system, we have to study the fixed point stability. Therefore we linearize Eqs. (3.4) around a fixed point $(x^0, y^0, J^0_{x,y,z})$ paying attention to the time delay in the g coupling [Sch10, H05]. The linearization ansatz is then

$$x = x^0+\delta x, \quad x_\tau = x^0+\delta x_\tau, \qquad y = y^0+\delta y, \quad y_\tau = y^0+\delta y_\tau, \qquad J_{x,y,z} = J^0_{x,y,z}+\delta J_{x,y,z}. \tag{3.21}$$

Note that all fluctuations δO are time-dependent and the shortcut $\delta O_\tau \equiv \delta O(t-\tau)$ is used.

Inserting the ansatz Eq. (3.21) into the semiclassical equations (3.4), neglecting all products of fluctuations with each other, which should be considerably smaller than fluctuations themselves, the linearized equations yield

$$\delta\vec{v}\,'(t) = \mathbf{B}\cdot\delta\vec{v}(t) + \mathbf{A}\cdot\delta\vec{v}(t-\tau) \tag{3.22}$$

with $\delta\vec{v} = (\delta J_x, \delta J_y, \delta x, \delta y)^T$ describing the deviation from the fixed point and

$$\begin{aligned}
\mathbf{A} &= \frac{1}{N\sqrt{N}}\begin{pmatrix} 0 & 0 & 0 & 0 \\ 0 & 0 & -8J^0_z(x^0)^2\lambda & -8J^0_z x^0 y^0\lambda \\ 0 & 0 & 0 & 0 \\ 0 & 0 & -4J^0_x x^0\lambda & -4J^0_x y^0\lambda \end{pmatrix}, \\
\mathbf{B} &= \begin{pmatrix} 0 & -\omega_0 & 0 & 0 \\ \frac{4g_0 J^0_x x^0}{J^0_z\sqrt{N}} + \omega_0 & 0 & 8J^0_z(x^0)^2\frac{\lambda}{N\sqrt{N}} - 4\frac{g_0}{\sqrt{N}}J^0_z & 8J^0_z x^0 y^0\frac{\lambda}{N\sqrt{N}} \\ 0 & 0 & -\kappa & \omega \\ -2\frac{g_0}{\sqrt{N}} & 0 & 4J^0_x x^0\frac{\lambda}{N\sqrt{N}} - \omega & 4J^0_x y^0\frac{\lambda}{N\sqrt{N}} - \kappa \end{pmatrix}.
\end{aligned} \tag{3.23}$$

For the derivation we have used the spin-length conservation (3.17), which allows us to eliminate δJ_z dependency

$$\begin{aligned}
&\frac{N^2}{4} = J_x^2 + J_y^2 + J_z^2 \\
\overset{(3.21)}{\Rightarrow}\ &\frac{N^2}{4} = \sum_{k=x,y,z}\left(J^0_k + \delta J_k\right)^2 \overset{\delta J_j \delta J_k \approx 0}{\approx} \underbrace{\sum_{k=x,y,z} {J^0_k}^2}_{=J^2=\frac{N^2}{4}} + \sum_{k=x,y,z} 2J^0_k\cdot\delta J_k \\
&\Rightarrow 0 = J^0_x\delta J_x + J^0_y\delta J_y + J^0_z\delta J_z \Rightarrow \delta J_z = -\frac{J^0_x\delta J_x + J^0_y\delta J_y}{J^0_z}.
\end{aligned}$$

Summarizing, Eq. (3.22) describes the fluctuations behavior around the fixed point $\vec{v}$, i.e., it contains the information about the fixed point stability even for different time

delays τ. In the next subsection we derive the corresponding characteristic equation, which can be directly used to calculate the stability.

But first we show how to derive the linearized equation for the J_y. Inserting Eq. (3.21) into J_y equation (3.4), we obtain

$$
\begin{aligned}
\overbrace{(J_y^0)}^{=0} + \delta J_y' &= \omega_0 J_x^0 + \omega_0 \delta J_x - \frac{4}{\sqrt{N}} (x_0 + \delta x) \left(J_z^0 + \delta J_z\right) \\
&\quad \times \left\{ g_0 + \frac{\lambda}{N} \left[(x_0 - \delta x_\tau)^2 - (x_0 - \delta x)^2 + (y_0 - \delta y_\tau)^2 - (y_0 - \delta y)^2 \right] \right\} \\
\Rightarrow \delta J_y' &= \underbrace{\omega_0 J_x^0 - 4\frac{g_0}{\sqrt{N}} x_0 J_z^0}_{=0, \text{ condition for fixed point}} + \omega_0 \delta J_x - 4\frac{g_0}{\sqrt{N}} x_0 \delta J_z - 4\frac{g_0}{\sqrt{N}} J_z^0 \delta x \\
&\quad + 8\frac{\lambda}{N\sqrt{N}} x_0 J_z^0 \left[x_0(\delta x_\tau - \delta x) + y_0(\delta y_\tau - \delta y) \right] + O(\delta) \qquad (3.24) \\
&\overset{(3.24)}{=} \omega_0 \delta J_x + 4\frac{g_0}{\sqrt{N}} \frac{x_0}{J_z^0} \left(J_x^0 \delta J_x + J_y^0 \delta J_y \right) - 4\frac{g_0}{\sqrt{N}} J_z^0 \delta x \\
&\quad + 8\frac{\lambda}{N\sqrt{N}} x_0 J_z^0 \left[x_0(\delta x_\tau - \delta x) + y_0(\delta y_\tau - \delta y) \right] \\
&= \left(\omega_0 + 4\frac{g_0}{\sqrt{N}} \frac{J_x^0 x_0}{J_z^0} \right) \delta J_x + 4\frac{g_0}{\sqrt{N}} \frac{J_y^0 x_0}{J_z^0} \delta J_y - 4\frac{g_0}{\sqrt{N}} J_z^0 \delta x \\
&\quad + 8\frac{\lambda}{N\sqrt{N}} x_0 J_z^0 \left[x_0(\delta x_\tau - \delta x) + y_0(\delta y_\tau - \delta y) \right] + O(\delta) \\
&\approx \left(\frac{4 g_0 J_x^0 x^0}{J_z^0 \sqrt{N}} + \omega_0, \quad 0, \quad 8 J_z^0 (x^0)^2 \frac{\lambda}{N\sqrt{N}} - 4\frac{g_0}{\sqrt{N}} J_z^0, \quad 8 J_z^0 x^0 y^0 \frac{\lambda}{N\sqrt{N}} \right) \cdot \delta \vec{v} \\
&\quad + \frac{1}{N\sqrt{N}} \left(0, \quad 0, \quad -8 J_z^0 (x^0)^2 \lambda, \quad -8 J_z^0 x^0 y^0 \lambda \right) \cdot \delta \vec{v}_\tau . \qquad (3.25)
\end{aligned}
$$

Thus the resulted equation gives the second row of the matrices $\mathbf{A}$ and $\mathbf{B}$ (3.22). The calculation of other linearized equations is similar.

3.2.4.2. Characteristic Equation with Time Delay

Fluctuations behavior $\vec{v}(t)$ determines the fixed point stability. We solve Eq. (3.22) with the exponential ansatz: $\delta \vec{v} = \delta \vec{v}_1 \cdot e^{\Lambda t}$

$$
\begin{aligned}
\Lambda \vec{v}_1 \cdot e^{\Lambda t} &= \mathbf{B} \vec{v}_1 \cdot e^{\Lambda t} + \mathbf{A} \vec{v}_1 \cdot e^{\Lambda (t-\tau)}, \\
&\Rightarrow \left(\Lambda \mathbf{1} - \mathbf{B} - \mathbf{A} \cdot e^{-\Lambda \tau} \right) \cdot \delta \vec{v} = 0. \qquad (3.26)
\end{aligned}
$$

The non-trivial solution for $\delta \vec{v}$ is given by the following characteristic equation

$$
\det \left(\Lambda \cdot \mathbf{1} - \mathbf{B} - \mathbf{A} \cdot e^{-\Lambda \tau} \right) = 0 \,. \qquad (3.27)
$$

For $\tau \neq 0$ this transcendental equation has an infinite set of solutions for the eigenvalues $\Lambda \in \mathcal{C}$, which part in general can be found only numerically. The fixed point $\vec{v}^{\,0}$ is stable, if the real parts of all corresponding eigenvalues are negative. In this case the fluctuations $\delta\vec{v}$ become zero for $t \to \infty$ and the exponential ansatz is indeed a good approximation for the system dynamics close to the fixed point for arbitrary values of t. From the Eq. (3.27) it is obvious that the fixed point stability could be controlled by the time delay parameter τ. For $\tau = 0$ the equation has a finite number of solutions and the eigenvalues depend in this case only on the system parameters. Note that despite transcendental form of Eq. (3.27) it is often possible to find an analytical expression which determines the boundaries between a stable and an unstable configuration caused by time delay. Now we have all equations together to perform the stability analysis. Before analyzing the effects of Pyragas control onto the system, we will first shortly summarize the well-known behavior without time delay effects.

3.3. Dicke System without Time Delay

First, we recapitulate the results for the Dicke system without time-delay τ [Bha12], thus we can more easily understand the changes due to the time-delayed control in the next section. There are two different kinds of fixed points, the trivial one (Eq. (3.18)) and the non-trivial one (Eq. (3.19)) which correspond to a normal (NR) and superradiant (SR) phases, respectively. In the following we recapitulate the dynamical and stationary properties of both phases. The resulted phase diagram is well known [Bha12].

3.3.1. Stability

Using the linear stability analysis from the previous section we can check, whether the fixed points are stable. For $\tau = 0$ the characteristic equation (3.27) is not transcendental any more and the solution is equivalent to the eigenvalues of the matrix $\mathbf{B} + \mathbf{A}$.

3.3.1.1. Normal Phase

In the normal phase the field mode carries no macroscopic occupation. The atomic inversion has its maximal or minimal value $J_z^0 = \pm\frac{N}{2}$. The trivial solution exists for all parameter values. To check its stability, we insert the corresponding fixed point Eq. (3.18) of the Dicke Hamiltonian in to Eq. (3.27) ($\tau = 0$), yielding

$$\det\left[\Lambda\mathbf{1} - (\mathbf{B} + \mathbf{A})\right] = 0, \tag{3.28}$$

$$\mathbf{B} + \mathbf{A} = \begin{pmatrix} 0 & -\omega_0 & 0 & 0 \\ \omega_0 & 0 & -4\frac{g_0}{N}J_z^0 & 0 \\ 0 & 0 & -\kappa & \omega \\ -2\frac{g_0}{\sqrt{N}} & 0 & -\omega & -\kappa \end{pmatrix}.$$

Evaluation of the determinant gives the stability condition

$$0 = 4\frac{g_0^2}{N}\omega\omega_0 J_z^0 + (\Lambda^2 + \omega_0^2)[(\Lambda + \kappa)^2 + \omega^2], \tag{3.29}$$

which is then of the fourth order and can be in general exactly solved. As the full solution is hard to analyze in presence of the dissipation rate κ, we look for the occurrence of the normal phase stability switch. At that point Λ has to be purely imaginary $\Lambda = i\Omega$. This condition gives an equation for Ω, which is only real if

$$\frac{g_0}{\sqrt{N}} = \pm\sqrt{\frac{(\kappa^2 + \omega^2)\omega_0}{-2\omega J_z^0}}. \tag{3.30}$$

The coupling has to be positive for physical reasons, which is only the case for $J_z^0 = -\frac{N}{2}$. Thus the trivial fixed point with $J_z^0 = -\frac{N}{2}$ changes its stability if $g_0 > g_c$ where g_c is the critical coupling value

$$g_c = \sqrt{\frac{(\kappa^2 + \omega^2)\omega_0}{2\omega}}, \tag{3.31}$$

whereas the trivial fixed point with $J_z^0 = +\frac{N}{2}$ remains stable forever. Up till now we know only something about the stability change, but we do not know if the trivial fixed point is stable or unstable for $g < g_c$ and $g > g_c$. This can be easily checked for $g < g_c$ in a particular case $\omega_0 = \omega = \kappa$. Then the eigenvalue with the greatest real part reads

$$\Lambda_{max} = \frac{1}{2}\left(-\omega + \sqrt{-3\omega^2 + 4\sqrt{-8g_0^2\omega^2 J_z^0 - \omega}}\right). \tag{3.32}$$

For $J_z^0 = +\frac{N}{2}$ the inner root is purely imaginary, the outer root is then greater than ω and the real part of the eigenvalue is positive. Thus the solution is unstable. For $g_0 = g_c$ and $J_z^0 = -\frac{N}{2}$ the eigenvalue is zero as the outer root is ω_0. For $g_0 < g_c$ the outer root will be less than ω, as the inner root is smaller than that in $g_0 = g_c$ case. Thus the eigenvalue is negative and the fixed point is stable. Note that eigenvalues in all cases are either real or build complex-conjugate pairs.

Summarizing, normal phase solution with $J_z^0 = \frac{N}{2}$ is always unstable, whereas the solution with $J_z^0 = -\frac{N}{2}$ loses its stability for $g_0 \geq g_c$.

3.3.1.2. Superradiant Phase

In case of $g_0 > g_c$ both superradiant solutions Eq. (3.19) become stable, as can be expected from the bifurcation theory [Str01]. Thus the real parts of all eigenvalues Λ (Eq. (3.27)) are negative. However we do not provide the corresponding expressions as they are too long. An eigenvalue treatment can be found in [Dim07]. The main property of the superradiant regime is macroscopic occupation of the optical mode $a^*a = n > 0$. The J_x component of the spin system has two different orientations in a steady state, as the system Hamiltonian (3.1) and the master equation (3.2) are invariant under the parity transformation $a^{(\dagger)} \to -a^{(\dagger)}$, $J_\pm \to -J_\pm \Rightarrow J_x \to -J_x$ [Bha12].

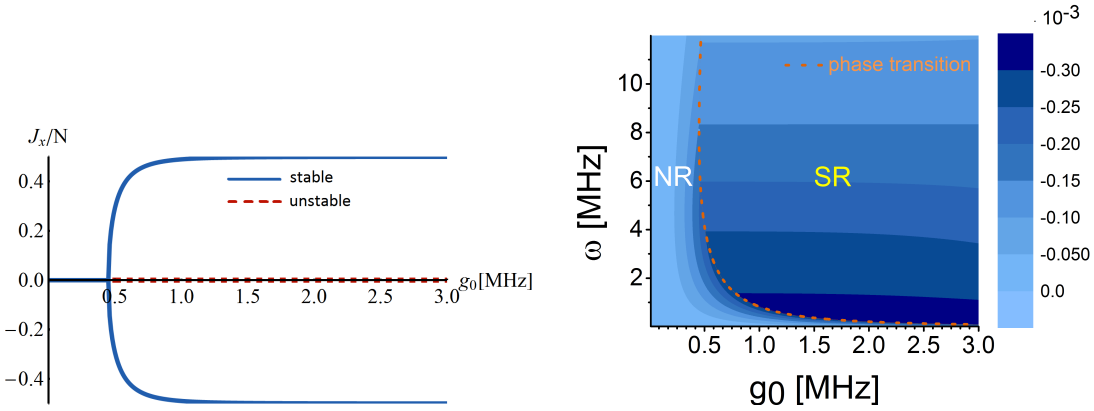

(a) Bifurcation

(b) Phase diagram for $\tau = 0$

Figure 3.2.: (a) J_x coordinate of the fixed point. For $g_0 < g_c$ only trivial solution with $J_x/N = 0$ exists and is stable (solid blue line). At $g_0 = g_c$ it becomes unstable (red dashed line) but two new stable solutions (solid blue line) split up, thus a Pitchfork bifurcation happens. Parameter: $\omega = 8$ MHz. (b) Phase diagram without time delay in the (ω, g_0)-space. The dashed orange line shows the critical value g_c. The normal phase (NR) is stable for $g_0 < g_c$, whereas the superradiant phase is stable for $g_0 > g_c$. The color encodes the largest real part of the eigenvalues. Note that it is always negative, because for calculation we use the fixed point which is stable in the given phase. Parameters: $\kappa = 8.1$ MHz, $\omega_0 = 0.05$ MHz, $\tau = 0$.

3.3.1.3. Phase and Bifurcation Diagrams

Fig. 3.2(a) shows the bifurcation diagram for the J_x component as a function of the coupling g_0 for fixed parameter values. The phase transition is visible as a Pitchfork bifurcation at $g_0 = g_c$, where the trivial solution becomes unstable and two stable solutions split up. This bifurcation corresponds directly to a quantum phase transition of the model without a mean-field approximation. Note that the quantum mechanical calculation gives the same results in the thermodynamic limit for the critical coupling value g_c as for the mode occupation a^*a or inversion J_z, comparing to the semiclassical approach [Bon70, Bha12, Arm06, Kop13, BM14b]. Fig. 3.2(b) shows the phase diagram in (g_0, ω)-plane. The orange-dashed line is a critical coupling g_c, see Eq. (3.20). For $g < g_c$ the normal phase is stable, whereas for $g > g_c$ the superradiant phase is stable. Color represents the maximum real part of all eigenvalues Λ (Eq. (3.27)) of the trivial fixed point Eq. (3.18) for $g_0 < g_c$ and of the superradiant fixed point Eq. (3.19) for $g_0 > g_c$.

3.3.2. Dynamics

In this section we replicate the dynamical evolution of the averaged Dicke system values [Bha12]. In the closed version the system has one eigenvalue in the normal phase and two degenerate eigenvalues in the superradiant phase with minimal energy, but the averaged dynamics of system observables is chaotic even at the mean-field level [Ema03a]. In our case the optical mode becomes damped and the system tends to a non-equilibrium steady state – the fixed point from the previous section. Solving Eqs. (3.4) numerically from randomly chosen initial conditions, we visualize a typical time development of the averaged system observables of the atomic part for both phases in Fig. 3.3. As the spin length is always conserved, we plot the evolution on a Bloch sphere with radius $N/2$. The red and blue dots represent the unstable and stable fixed point positions, respectively. We see that for $g_0 < g_c$ the solution tends to spiral toward the south pool of the Bloch sphere, see Fig. 3.3(a). In contrast, in the superradiant phase $g_0 > g_c$ this point is unstable. The solution converges then to one of the two fixed points with $J_x^0 \neq 0$, see Fig. 3.3(b). Note the flip of the J_z axis. Close to a fixed point, the solution spirals towards it. This is connected with the eigenvalues Λ Eq. (3.27), which contain a complex conjugate pair. Note that due to the small ω_0 value, the system takes a long time to approach the stable solution and the distance between two neighbouring trajectories is very small. The ω_0 value denotes the level splitting of the atomic system and characterizes the energy transfer rate to the environment by interacting with the bosonic mode.

These are the main results on the uncontrolled Dicke system, which we have to know in order to understand the changes in presence of the time-delayed Pyragas control.

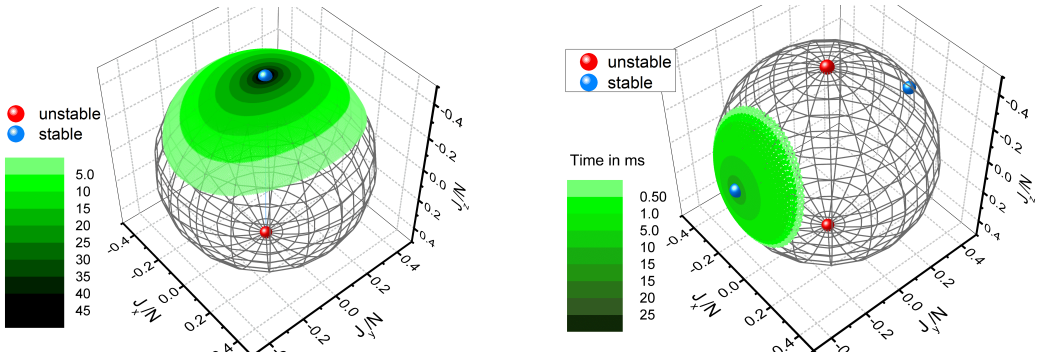

(a) Normal phase (b) Superradiant phase

Figure 3.3.: Typical evolution of atomic system in the normal and superradiant phase. The red (blue) points denote unstable (stable) fixed points of the system. Whereas in the normal phase the inversion approaches its minimal value $-N/2$, in the superradiant phase it is bigger. Note the flip of the J_z axis. The color encodes the dynamical time evolution. Parameters: $\kappa = 8.1$ MHz, $\omega_0 = 0.05$ MHz, $\omega = 8$ MHz, $g_0 = 0.3$ MHz(a), $g_0 = 1$ MHz (b), $\tau = 0$.

3.4. Dicke System with Time Delayed Pyragas Control

In this section we study new and unexpected effects caused by the Pyragas type of control applied to the atom-field coupling constant g Eq. (3.3) in the Dicke model. First, we determine its effect on the stability of the fixed points. Second, we visualize and explain the meaning of the corresponding new phase diagram. Third, we explore system behavior beyond the common linear stability analysis. In the plots we usually take the parameters close to the experimental realization [Bau10, Bha12], i.e. $\omega_0 = 0.05$ MHz, $\kappa = 8.1$ MHz. Thus the level splitting is very small compared to other values, whereas the dissipation rate κ is rather big. This case is rather close to the ultra-strong-coupling limit of the Dicke model [Alc12]. At the end of this section we look slightly for the $\omega_0 = \omega$ case.

3.4.1. Phase Diagram in the (g_0, ω) Plane

To study the stability of fixed points in presence of feedback, we insert the corresponding fixed points Eqs. (3.18),(3.19) into the characteristic equation Eq. (3.27) and solve it for Λ. For $\tau \neq 0$ this equation becomes transcendental and is non-linear on top, therefore we use the root-search algorithm starting with a initial condition for $\Lambda_0 = a_0 + ib_0$. As the equation has an infinite number of roots, we use 1600 different initial condition choosing $a_0, b_0 \in [-40, 40]$ to be sure that we have got all significant roots. We note that in some simple cases such equations can be treated analytically using Lambert function approach [HÖ5], see theory Sec. 2.1.

The real part of the resulting roots Λ is shown in Fig. 3.4 as a function of coupling τ for some fixed parameter values. The root-structure is typical for equations of type Eq. (3.27). We see several branches, where the solutions are located. For $\tau \to 0$ the exponential term in the characteristic equation vanishes and only four eigenvalues survives (arrows in the figure). Other eigenvalues diverge, as we can see in Fig. 3.4. The inset shows a zoom around the x-axis. Whereas most eigenvalues are negative, there are small areas, with one positive eigenvalue, which can be seen in the inset. Thus, the fixed point stability changes from stable to unstable.

Using the maximum real part of all eigenvalues for a Dicke system with a fixed time delay value τ and different ω and g_0 values, we obtain the phase diagram of our model in the ω–g_0–plane, see Fig. 3.5. The color in Fig. 3.5 encodes the maximum real part of all solutions Λ for a given system configuration. The orange-dashed line separates the normal from the superradiant phase. Left and right figures are plotted for two different τ values.

First, in the left part of the phase diagram (for $g_0 \leq g_c$) we recover the usual normal phase, where the boson occupation is zero, the $\mathbf{A}$ matrix Eq. (3.27) vanishes then and as a consequence the feedback scheme equation (3.3) remains without effect. Thus the used feedback scheme has no influence in the normal phase. In contrast, for $g_0 > g_c$ and positive τ, the superradiant phase splits up into an infinite sequence of tongue-like areas that alternate between zones with stable, superradiant fixed points (F), and - as we will see later - limit cycles (L) with periodically oscillating system observables. We

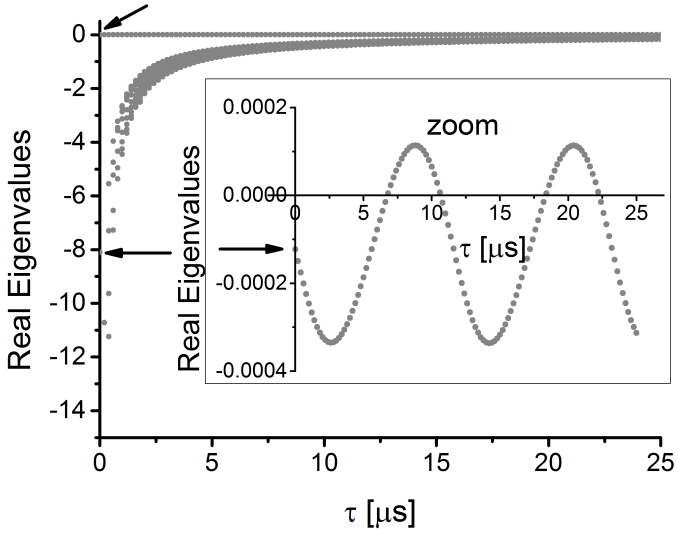

Figure 3.4.: A typical solution of Eq. (3.27). We see several eigenvalue branches. The inset shows a zoom around a x-axis. Parameters: $\tau = 20$ μs, $\lambda = 5$ MHz and $\omega_0 = 0.05$ MHz, $\kappa = 8.1$ MHz [Bha12, Bau10].

will devote the next sections to analyzing and interpreting this rather surprising effect. Comparing the right and left figures we see that the decreasing τ blows-up the (F) and (L) zones to bigger g values, thus one can expect that there is some lower bound for τ value where the new structure disappears and phase diagram converges to the old case without feedback, Fig. 3.2(b).

3.4.2. Dynamical Evolution

Figure 3.6 displays the two markedly different types of time evolution in the superradiant regime. In the fixed point zones (F), the only effect of the Pyragas scheme is to speed up the convergence of the spin-components and the mean boson occupation a^*a towards their fixed point values [Gri15] (left). This has to be contrasted with the limit-cycle zones (L), where the fixed point is unstable, and the observables end up oscillating with a single frequency (right). Therefore the system of coupled time-delayed differential equations (3.12) is solved numerically. We have to specify not only the initial conditions, but also the history for $t \in [-\tau, 0[$, keeping it constant at the initial condition values. In all simulations we keep the values for $x(0)$ and $y(0)$ fixed around $0.1/\sqrt{N}$, set $J_y(0) \cdot N = 0$ and change the initial conditions for $J_z(0)$ or $J_x(0)$ respectively.

Although the control does not change the fixed point stability in the (F)-zones, it changes its attraction power, which is visible as a convergence speed up in the Fig. 3.6. This behavior can be read from the eigenvalues Eq. (3.27). Comparing the maximum real part of all eigenvalues for $\tau = 0$ ms Fig. (3.2(a)) and $\tau = 20$ ms Fig. (3.5(b)) for the system configuration $P2$, we read out from the color code $-0.15 \cdot 10^{-3}$ and

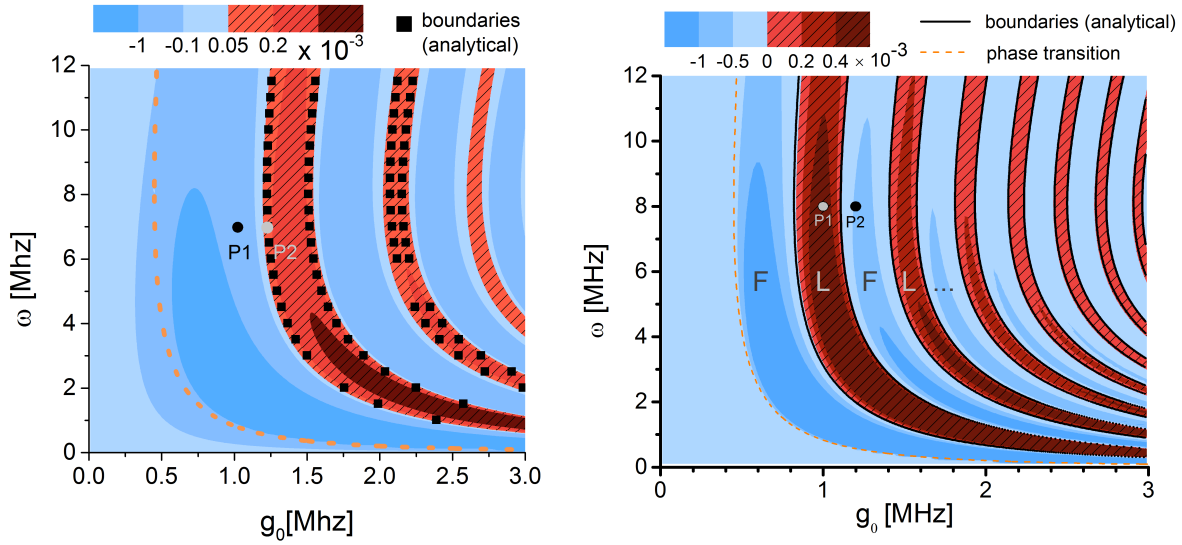

(a) Phase diagram for $\tau = 10\ \mu$s

(b) Phase diagram for $\tau = 20\ \mu$s

Figure 3.5.: Phase diagram for fixed time delay τ and feedback strength λ. The dashed (orange) line separates the normal from the superradiant phase. The superradiant regime is split by time-delayed control into zones with stable fixed points (F) and limit cycles (L) with boundaries (black curves(b) or squares (a)) determined from Eq. (3.46). Color encodes the largest real part of the eigenvalue. Parameters: $\lambda = 5$ MHz and $\omega_0 = 0.05$ MHz, $\kappa = 8.1$ MHz [Bha12, Bau10]. Part (b) is taken from Ref. [Kop15b].

$-0.5 \cdot 10^{-3}$, respectively. Thus, the maximum real part of all eigenvalues becomes more negative by time delay, which increases the attraction power of the corresponding fixed point and as consequence reduces the converges time scale. Note, this speed up is not valid in the whole phase space. Especially close to the boundaries between the (F) and (L) regions, the real part of all eigenvalues approaches zero and becomes bigger as in the $\tau = 0$ case. The dynamic becomes then very slow which increases the numerical effort to end into a steady state, because Eqs. (3.4) have to be integrated till much greater times.

Fig. 3.7 (left) shows mode occupation a^*a as a function of time for different τ values. For $\tau = 10\mu$s the fixed point P1 is stable as one can take from Fig. 3.5(a) and the system has a non-oscillating steady state. Increasing τ value the system ends up in the the (L)-region and the systems ends in the oscillating state, see P1 in Fig. 3.5(b). Moreover, Fig. 3.7 (left) shows that the time delay τ effects as the amplitude and the frequency of the oscillations. This effects we will study in detail later.

In the right part of Fig. 3.7 a time dependency due to feedback control of the atom-field coupling g(t) is shown. It behaves in the same manner, as the occupation of the optical mode. In the (F) zone the fixed point is stable and the coupling converges to the constant g_0 value, thus the feedback action vanishes in the steady state. However, in the (L) zone the atom-field coupling oscillates with a finite frequency, which is the same

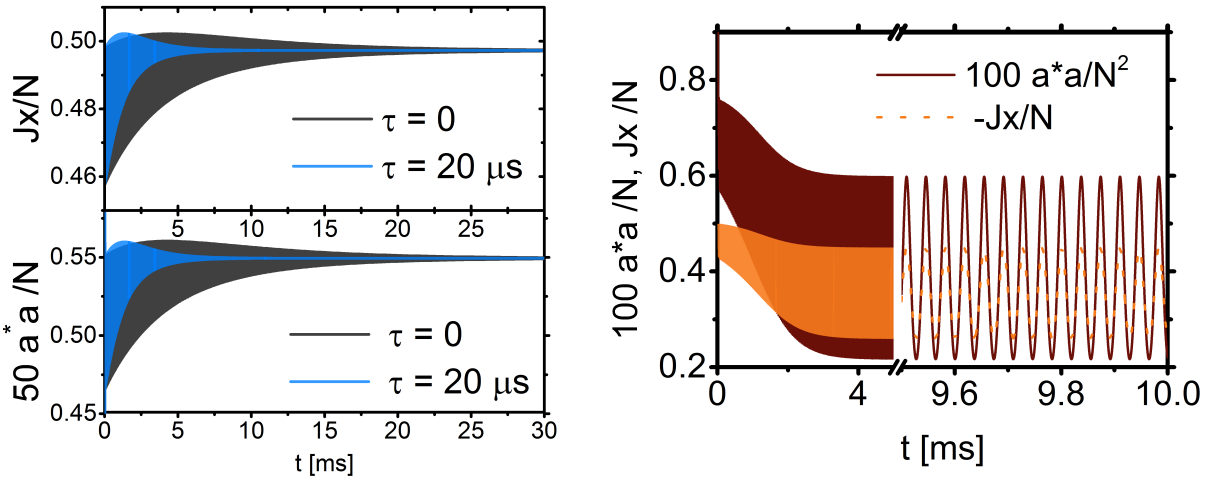

Figure 3.6.: Time evolution of mode occupation a^*a and angular momentum component J_x corresponding to stable fixed point P2 (left) and stable limit cycle P1 (right) in the phase diagram Fig. 3.5(b). Taken from Ref. [Kop15b].

as for other system observables, and amplitude around the g_0 value. The amplitude is rather small, especially $g(t)$ is bigger than g_c for all times. Thus, $g(t)$ remains in the superradiant regime and does not undergo the critical coupling in the (L) phase.

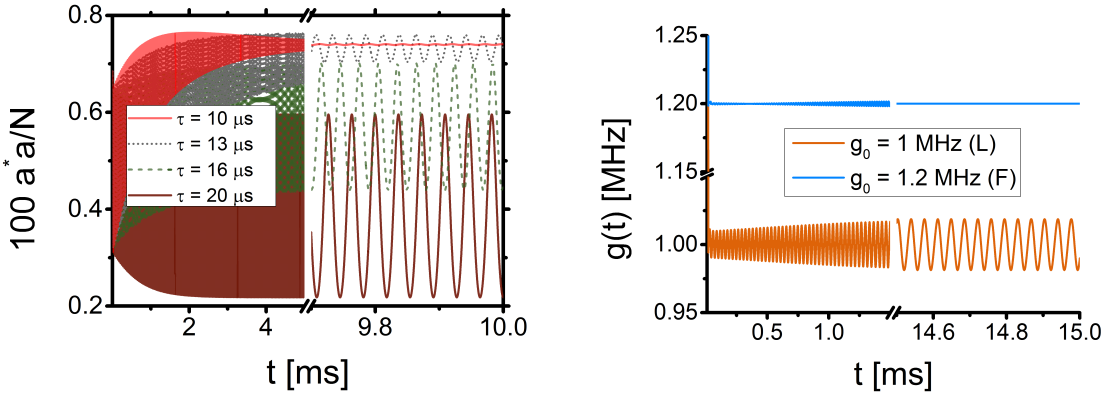

Figure 3.7.: (left) Time evolution of mode occupation a^*a for different time delay τ. Other parameter value are chosen corresponding to the point P1 in Fig. 3.5(b). For decreasing τ value, the oscillation amplitude of the steady state decreases. For $\tau = 10$ μs the fixed point is stable thus it has zero amplitude. (right) Controlled time evolution of the coupling $g(t)$ for the points P1 and P2 from Fig. 3.5(b).

3.4.3. Analysis of Zone Boundaries

An analytical expression can often be derived for the boundaries between stable and unstable zones in time-delayed systems: At the boundaries the biggest real part of all eigenvalues is zero. This condition allows to simplify the stability equation (3.27). In our case this simplification allows us to determine the boundaries between the (F) and (L) areas in the phase diagram Fig. 3.5.

3.4.3.1. Simplified Transcendental Equation

To obtain a simplified transcendental stability equation from Eq. (3.27) we additionally use the limit of very small level splitting $\omega_0 \ll \omega\,, g_0$, which describes the ultra-strong coupling limit of the Dicke model [Alc12] and corresponds to a feedback-controlled displaced harmonic oscillator. This assumption is justified in the existing experimental setups [Bau10, Bha12].
In the superradiant case (the normal phase stability is not affected by the assumed time delay control) the fixed point solution Eq. (3.19) is approximated in case $\omega \approx 0$ as

$$J_z^0 \to 0, \quad J_x^0 \to \pm\frac{1}{2}N, \qquad x^0\sqrt{N} \to -\frac{2g_0\omega}{k^2+\omega^2}J_x^0, \quad y^0\sqrt{N} \to -\frac{k}{\omega}\frac{2g_0\omega}{k^2+\omega^2}J_x^0. \tag{3.33}$$

The linearized equation for fluctuations Eq. (3.22) becomes then

$$\delta\vec{v}\,'(t) = \mathbf{B_0}\cdot\delta\vec{v}(t) + \mathbf{A_0}\cdot\delta\vec{v}(t-\tau), \tag{3.34}$$

$$\mathbf{A_0} = \begin{pmatrix} 0 & 0 & 0 & 0 \\ 0 & 0 & 0 & 0 \\ 0 & 0 & 0 & 0 \\ 0 & 0 & -4J_x^0x^0\frac{\lambda}{N\sqrt{N}} & -4J_x^0y^0\frac{\lambda}{N\sqrt{N}} \end{pmatrix},$$

$$\mathbf{B_0} = \begin{pmatrix} 0 & -\omega_0 & 0 & 0 \\ \Omega^2/\omega_0 & 0 & 0 & 0 \\ 0 & 0 & -\kappa & \omega \\ -2\frac{g_0}{\sqrt{N}} & 0 & 4J_x^0x^0\frac{\lambda}{N\sqrt{N}} - \omega & 4J_x^0y^0\frac{\lambda}{N\sqrt{N}} - \kappa \end{pmatrix} \tag{3.35}$$

with $\Omega^2 = \frac{4g_0J_x^0x^0\omega^0}{J_z^0\sqrt{N}}$.

In the first column of the $\mathbf{B_0}$ matrix we have additionally skipped ω_0 as it is much smaller than Ω^2/ω_0. Using $\delta\vec{v} = (\delta J_x, \delta J_y, \delta x, \delta y)^T$, we can derive an equation for fluctuations δJ_i

$$\left.\begin{array}{ll} \delta\dot{J}_x & = -\omega_0\delta J_y \\ \delta\dot{J}_y & = \frac{\Omega^2}{\omega_0}\delta J_x \end{array}\right\} \Rightarrow \delta\ddot{J}_x = -\Omega^2\delta J_x. \tag{3.36}$$

The differential equation for the angular momentum fluctuations around the mean-field solution can be solved as

$$\delta J_x = \mathrm{span}\{\sin(\Omega t), \cos(\Omega t)\} \tag{3.37}$$

and offers a simple interpretation for the introduced Ω parameter. Thus, in the considered limit $\omega_0 \to 0$, $\Re(\Lambda) = 0$ and linearization assumption the angular momentum averages $J_i^{(0)} + \delta J_i(t)$ are oscillating periodically around the fixed point $J_i^{(0)}$ with the frequency Ω. The fluctuations δJ_i are neither converging toward nor diverging from the fixed point for all parameter values, have no time delay dependency and therefore can not be directly used to determine the baseline of stability in a parameter space for a finite τ value.

Therefore we additionally derive the equation of motion for the fluctuations δx using following procedure. From the last two rows of Eq. (3.34) we read

$$\delta\dot{x} = -\kappa\delta x + \omega\delta y \quad \Rightarrow \quad \delta y = \frac{1}{\omega}\delta\dot{x} + \frac{k}{\omega}\delta x, \tag{3.38}$$

$$\delta\dot{y} = -2\frac{g_0}{\sqrt{N}}\delta J_x - \omega\delta x - \kappa\delta y - 4J_x^0 x^0 \frac{\lambda}{N\sqrt{N}}(\delta x_\tau - \delta x) - 4J_x^0 y^0 \frac{\lambda}{N\sqrt{N}}(\delta y_\tau - \delta y).$$

(3.39)

Differentiation of $\delta\dot{x}$ equation with respect to t and use of $\delta\dot{y}$ equation results in

$$\begin{aligned}
\delta\ddot{x} =& - k\delta\dot{x} + \omega\delta\dot{y} \\
=& - k\delta\dot{x} - 2\frac{g_0}{\sqrt{N}}\omega\delta J_x - \omega^2\delta x - \omega\kappa\delta y - 4\omega J_x^0 x^0 \frac{\lambda}{N\sqrt{N}}(\delta x_\tau - \delta x) \\
& - 4\omega J_x^0 y^0 \frac{\lambda}{N\sqrt{N}}(\delta y_\tau - \delta y) \\
=& - 2\kappa\delta\dot{x} - (\omega^2 + k^2)\delta x - 2\frac{g_0}{\sqrt{N}}\omega\delta J_x \\
& - 4\omega J_x^0 \frac{\lambda}{N\sqrt{N}}\left(x^0(\delta x_\tau - \delta x) + y^0\left(\frac{1}{\omega}(\delta\dot{x}_\tau - \delta\dot{x}) + \frac{\kappa}{\omega}(\delta x_\tau - \delta x)\right)\right). \\
\Rightarrow 0 =& \delta\ddot{x} + 2\kappa\delta\dot{x} + (\omega^2 + \kappa^2)\delta x + 2\frac{g_0}{\sqrt{N}}\omega\delta J_x \\
& + 4\frac{\lambda}{N\sqrt{N}}J_x^0\left((\omega x^0 + k y^0)(\delta x_\tau - \delta x) + y^0(\delta\dot{x}_\tau - \delta\dot{x})\right).
\end{aligned} \tag{3.40}$$

We use now the superradiant solution (3.33), so that we can express following parts of Eq. (3.39) by the equal expressions

$$\begin{aligned}
4\frac{\lambda}{N\sqrt{N}}J_x^0(\omega x^0 + k y^0) &= -4\frac{\lambda}{N\sqrt{N}}J_x^0(\omega x^0 + \frac{k^2}{\omega}x^0) \\
&= -4\frac{\lambda}{N\sqrt{N}}J_x^0\frac{\omega^2 + \kappa^2}{\omega}\cdot\frac{2g_0\omega}{\sqrt{N}(\kappa^2 + \omega^2)}J_x^0 \\
&= -8\lambda\sqrt{g_0}N^2 J_x^0 = -2\lambda g_0, \\
4\frac{\lambda}{N\sqrt{N}}J_x^0 y^0 &= 4\sqrt{\lambda}N^2\frac{1}{2}\frac{\kappa}{\omega}\cdot\frac{-2g_0\omega}{k^2 + \omega^2}\frac{1}{2} = -\frac{2g_0\lambda\kappa}{\kappa^2 + \omega^2}.
\end{aligned}$$

In addition,

$$\begin{aligned}\Omega^2 &= \frac{4g_0 J_x^0 x^0 \omega_0}{J_z^0\sqrt{N}} = \frac{4g_0 \frac{-2g_0\omega}{(\kappa^2+\omega^2)\sqrt{N}} \cdot \frac{1}{4}N^2 \cdot \omega_0}{-N\frac{\omega_0(\kappa^2+\omega^2)}{8\frac{g_0}{\sqrt{N}}^2\omega} \cdot \sqrt{N}} \\ &= \frac{2g_0^2\omega}{(\kappa^2+\omega^2)^2} \cdot 8g_0^2\omega = \frac{4^2 g_0^4 \omega^2}{(\kappa^2+\omega^2)^2} \\ \Rightarrow \Omega &= \frac{4g_0^2\omega}{(\kappa^2+\omega^2)}. \end{aligned} \tag{3.41}$$

Using it, Eq. (3.39) turns into

$$0 = \delta\ddot{x} + 2\kappa\delta\dot{x} + (\omega^2+\kappa^2)\delta x - 2g_0\lambda(\delta x_\tau - \delta x) - \frac{2\lambda\kappa g_0}{\omega^2+\kappa^2}(\delta\dot{x}_\tau - \delta\dot{x}) + 2\frac{g_0}{\sqrt{N}}\omega\delta J_x \tag{3.42}$$

and represents an equation for the fluctuation δx around the fixed point x^0. The upper differential equation is time-delayed due to dependence on δx_τ. The solution of such equation gives the boundary between the (F) and (L) phases for example for fixed τ values in the configuration space.

3.4.3.2. Boundary Equation

To solve the Eq. (3.42) we make an ansatz based on the known solution for the spin component J_x Eq. (3.37): $\delta J_x = E_1 \sin(\Omega t)$, $\delta x = E_2 \sin(\Omega t)$. Thus we ask, for which parameter values the undamped fluctuations solve the δx equation. The ansatz is at the baseline between the stable fixed point with damped fluctuations and an unstable fixed point with diverging fluctuations. Its validity gives the boundaries between the (F) and (L) zones in the phase diagram (Fig. (3.2)). Inserting the ansatz into (3.42) we obtain

$$\begin{aligned} 0 = \sin(\Omega t)&\left[-\Omega^2 + \omega^2 + \kappa^2 - 2g_0\lambda\left(\cos(\Omega\tau) - 1\right) - \frac{\lambda\kappa}{2g_0\omega}\Omega^2\sin(\Omega\tau) + 2g_0\omega\frac{E_1}{E_2}\right] \\ + \cos(\Omega t)&\left[2\kappa\Omega + 2g_0\lambda\sin(\Omega\tau) - \frac{\lambda\kappa}{2g_0\omega}\Omega^2\left(\cos(\Omega\tau) - 1\right)\right]. \end{aligned} \tag{3.43}$$

To fulfil the equation both square brackets have to be zero. The $\cos(\Omega t)$ bracket is zero, if

$$0 = C_1 + C_2 \cdot \sin(\Omega\tau) - C_3\cos(\Omega\tau) \tag{3.44}$$

with

$$\begin{aligned} C_1 &= 2\kappa\Omega + \frac{\lambda\kappa}{2g_0\omega}\Omega^2 \\ C_2 &= 2g_0\lambda \\ C_3 &= \frac{\lambda\kappa}{2g_0\omega}\Omega^2. \end{aligned}$$

Using the connections $\sin(x) = \frac{2\tan(x/2)}{1+\tan^2(x/2)}$, $\cos(x) = \frac{1-\tan^2(x/2)}{1+\tan^2(x/2)}$ we rewrite the upper expression as

$$C_1\left[1+\tan^2\left(\frac{\Omega\tau}{2}\right)\right]+2C_2\cdot\tan\left(\frac{\Omega\tau}{2}\right)-C_3\left[1-\tan^2\left(\frac{\Omega\tau}{2}\right)\right]. \tag{3.45}$$

This is a quadratic equation in $\tan\left(\frac{\Omega\tau}{2}\right)$, thus using the *pq*-relation we obtain

$$\tan\left(\frac{\Omega\tau}{2}\right)=\frac{-C_2\pm\sqrt{-C_1^2+C_2^2+C_3^2}}{C_1+C_3}, \tag{3.46}$$

which represents a root of the Eq. (3.37) with vanishing real part, i.e. $\Lambda = \pm i\Omega$.

Parameter configurations satisfying this equation mark the boundary between stable (F) and unstable (L) fixed points. The solution of Eq. (3.46) shown in Fig. 3.5(b) with black lines matches the boundaries given by the numerical data in case $\omega_0 = 0.05$ MHz very well.

3.4.4. Phase Diagram in the (τ, λ)-Plane

Fig. 3.7 shows that the time delay τ plays also an important role for the system phase. Just derived Eq. (3.46) allows us to elucidate the role of the delay time τ in the control scheme: to obtain real-valued results for the time delay τ, the root in Eq. (3.46) has to be positive. This condition is only satisfied if the feedback coupling λ is larger than some critical value λ_l, which we determine from the vanishing of the root in Eq. (3.46).

We corroborate these findings by plotting the largest real part of the eigenvalue numerically determined from Eq. (3.27) in the (λ, τ)-plane for fixed ω and g_0 values, see Fig. 3.8. We recognize tongue-like zones switching between stable fixed-point and limit cycle (L) zones upon modification of the time delay τ, and furthermore the existence of a critical feedback strength λ_l for entering in the (L) zones. The black lines represent the analytical results for the boundaries between two phases, obtain from Eq. (3.46).

In the next section we discuss the role of delay time τ as a control parameter, by exploring the (L) phase properties and by showing a corresponding bifurcation diagram as a function of τ.

3.4.5. Limit Cycle Properties

The phase diagram Fig. 3.8 shows that a continuous increase of τ drives the system periodically first from the (F) to (L) phase and then from (L) to (F) phase. At a first boundary the system switches from the (F) in to the (L) zone. This is accompanied by a stability swap: the fixed point becomes unstable and a stable limit cycle appears. Fig. 3.9 visualizes this behavior, showing the time evolution of the atom-subsystem on the Bloch sphere for two different τ-values obtained from Eq. (3.4). In the left figure $\tau = 5\mu$s, the system is prepared in the first (F) zone of the phase diagram Fig. 3.8. The (blue) fixed point is then stable and we see that the atomic subsystem converges to it. Whereas in the right figure $\tau = 9\mu$s and the system is then in the first (L) zone

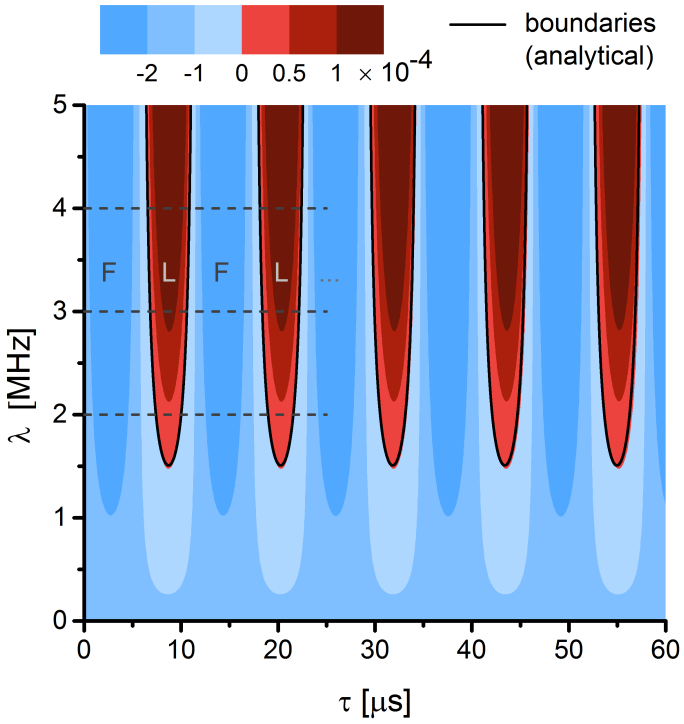

Figure 3.8.: Phase diagram with sequence of stable fixed point (F) and limit cycle (L) zones in the λ (coupling strength) vs. τ (delay time) plane. The black lines represent zone boundaries derived from the single transcendental equation (3.27). Dashed lines indicate cross-sections shown in Fig. 3.11. Color represents the largest real part of the eigenvalues. Parameters: $\omega = 10$ MHz, $g_0 = 1.5$ MHz, $\omega_0 = 0.05$ MHz, $\kappa = 8.1$ MHz. Taken from Ref. [Kop15b].

of the corresponding phase diagram. All fixed points (red) are unstable now and do not attract the solution any more. Instead, the solution converges to a stable limit cycle (dark brown ring on the Bloch sphere) with a certain size and period. Thus, a transition into the (L) zone is connected to a transition from stable fixed point to stable limit cycle. This behavior is known as a supercritical Hopf bifurcation.

The question is now, how does this Hopf bifurcation happens. Does the limit cycle appears continuous or suddenly by crossing the boundaries? How does its size depend upon τ? In the following we give answers to such questions, therefore we solve the equations of motion (3.4) keeping all parameters except τ at fixed value and construct from the solution a bifurcation diagram by plotting the size of the limit cycle. Fig. 3.10 (left) is a sketch of a typical Hopf bifurcation diagram. First the fixed point is stable and J_z component has a constant value in steady state. After the boundary crossing at some critical τ value a limit cycle appears and the J_z component starts to oscillate between two values. Here, instead of plotting the typical Hopf bifurcation diagram using absolute values (Fig. 3.10, left), we show the equivalent representation, by plotting

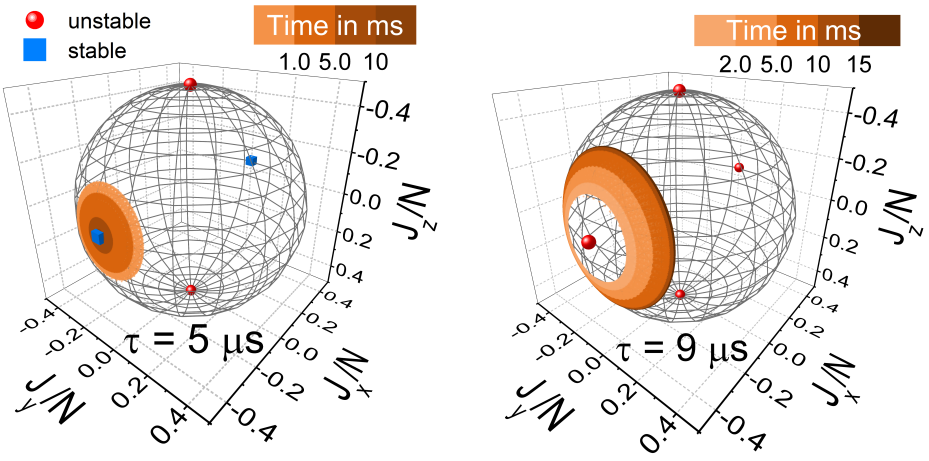

Figure 3.9.: Time evolution of the spin component for two different time delays τ corresponding to stable fixed point and stable limit cycle, respectively. Parameters: as in Fig. 3.8, $\lambda = 3$ MHz. Taken from Ref. [Kop15b].

only the radius (amplitude) of the emerging limit cycle as a function of time delay τ (Fig. 3.10, right). Zero amplitude would correspond to a stable fixed point.

Note that due to the parity invariance $x \to -x$, $y \to -y$, $J_x \to -J_x$, $J_y \to -J_y$ of Eq. (3.12) there are not only two fixed points in the superradiant regime, but also two stable limit cycles with the same amplitude if τ matches the (L) zone. This bifurcation diagram does not distinguish between the two limit cycles, as we plot only relative values and they are the same for both limit cycles.

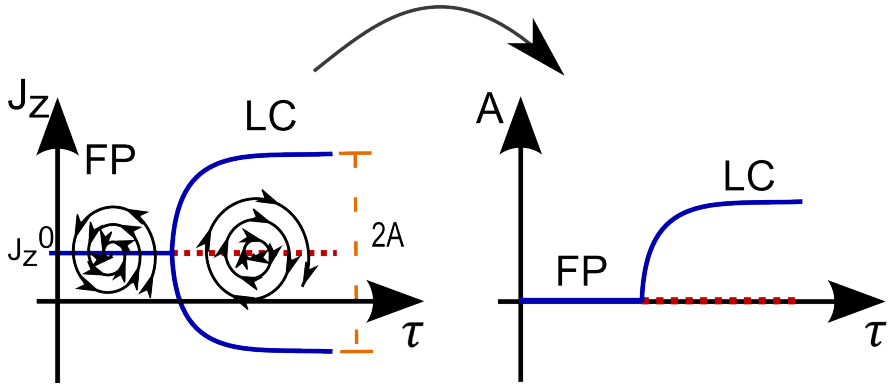

Figure 3.10.: A sketch of the Hopf bifurcation scenario by plotting the J_z values of fixed point (FP) and the max/min J_z-value of the limit cycle (LC) and the corresponding amplitude representation. Taken from Ref. [Kop15b].

Solving the equations of motion Eqs. (3.4) for parameter values along the dashed lines in Fig. 3.8, we find that the amplitude and period T of the limit cycles depend upon τ, as depicted in Fig. 3.11 for the J_z amplitude. To obtain the whole bifurcation diagram Fig. 3.11, it is necessary to go beyond the linear stability analysis, too, choosing

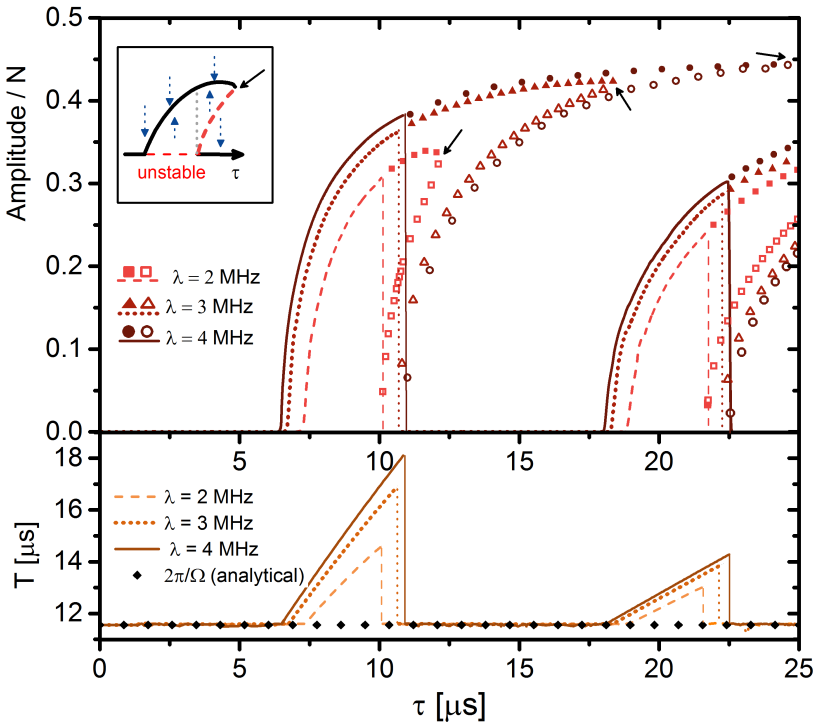

Figure 3.11.: Bifurcation scenario for limit cycle amplitudes (upper) and periods T (lower) of J_z as a function of delay time τ along the cross-sections (dashed lines at fixed λ) in Fig. 3.8. The filled symbols in the upper part describe the continuation of the limit cycle for initial value above the unstable limit cycle (unfilled symbols). The inset sketches the appearing saddle-node bifurcation of limit cycles and the dotted arrows show the direction of the phase flow for fixed tau. Taken from Ref. [Kop15b].

the initial condition farther away from the fixed point in sense of the linear stability analysis.

First, we recognize that for initial conditions close to the fixed point (typically we use $J_z(0) = 0$ or $(J_z(0) - J_z^0)/J_z^0 \approx 0.1\%$ as initial conditions) both the amplitude and the period show the same Hopf bifurcation scenario (connected lines) appearing for certain values of τ in Fig. 3.8. The non-zero slope of the curves marks the beginning of the L-zone and the Hopf bifurcation, the maxima of the curves mark the end of the L-zone. The amplitude or period slope at the begin of the (L)-zone is not continuous. As a particularly striking feature, we observe a drastic collapse of the limit cycle (vertical lines) for values of $\lambda > \lambda_l$ and the birth of an unstable limit cycle (disconnected unfilled symbols, shown only in the upper part of Fig. 3.11) by a subcritical Hopf bifurcation when the time delay τ reaches the end of the (L) zone. Our numerics show that this collapse occurs as a jump discontinuity. Furthermore, a stable limit cycle still exists behind the (L) zone (disconnected filled symbols) as a continuation of the previous one

but, because of bistability with the stable fixed point, it can only be reached if the initial amplitude lies above the amplitude of the unstable limit cycle, which marks the boundary between the basins of attraction of the fixed point and limit cycle attractors. Fig. 3.12 visualizes this rich behavior. The unstable limit cycle is marked by a red line. The system with the initial condition inside this unstable limit cycle converges to a stable fixed point. In contrast, the system with the initial condition outside the unstable limit cycle (but still in the same half sphere, cause of symmetry) has an stable limit cycle as a non-equilibrium steady state.

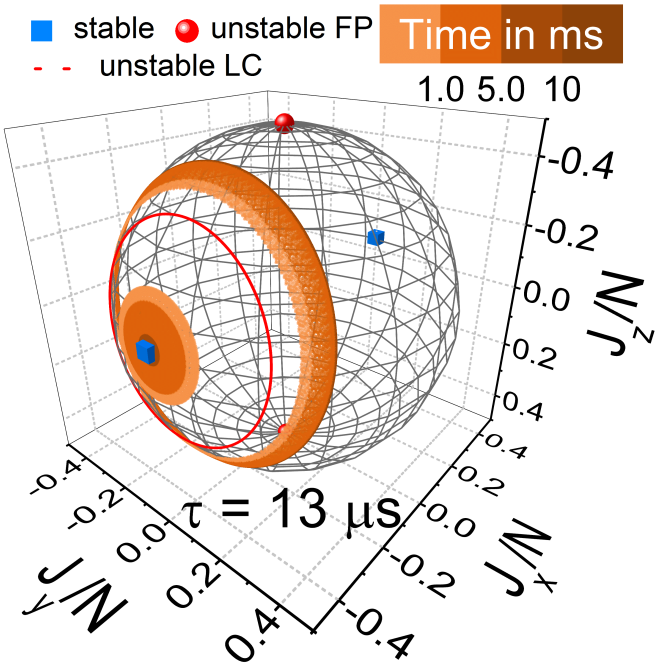

Figure 3.12.: Time evolution of the spin component for two different initial conditions leading to a to stable fixed point and stable limit cycle, respectively. Time delay is set in a way that the system has two different non-equilibrium steady states. The red dashed line marks the unstable limit cycle. Parameters: as in Fig. 3.8, $\lambda = 3$ MHz, $\tau = 13\mu$s.

Moreover, the branches of the stable and the unstable limit cycles in Fig. 3.11 merge in a saddle-node-bifurcation (arrows in Fig. 3.11). The inset shows this bifurcation schematically, the dotted arrows point to the stable solution (black solid line) the system will take for different initial conditions. The onset of the saddle-node-bifurcation is highly λ dependent, whereas the dashed/solid curves which are obtain close to the fixed point converges to a curve for increased λ value. Note that, to access the amplitude of the unstable limit cycle, we change the initial condition $J_z(0) \cdot N \in]0.5, -0.5[$ in small steps $\delta J_z(0)$ until the solution converges to the other attractor. Then we identify we initial amplitude of $J_z(t)$ with the amplitude of the unstable limit cycle, which is a good approximation for small $\delta J_z(0)$.

A combination of the periodical structure of the phase diagram Fig. 3.8 which mirrors in the bifurcation diagram Fig. 3.11 and the saddle-node bifurcations can generate a set of stable limit cycles for a fixed set of parameter values for bigger τ values. For example, for $\tau = 23\mu$s and $\lambda = 4$ MHz (Fig. 3.11) the system has two stable limit cycles and an fixed point on top.

In addition, limit cycle period increases linearly with time delay for the initial condition close to the fixed point, see Fig. 3.11 (lower). The theoretical prediction for the oscillating frequency Ω from the linear stability analysis of the fixed point Eq. (3.41) matches well with the damped oscillation period in the F-region. This seems surprising at first sight, as one would expect the matching only close to the boundaries due to the further made assumption for the derivation of this condition that the maximum real part of all eigenvalues Eq. (3.27) is zero. However, the maximum real part of all eigenvalues is rather close to zero in other cases, see the color code in Fig. 3.5(b), which explains the matching in other cases.

The mean occupation of the optical mode a^*a - as all $\vec{v}$ components - shows the same oscillating behaviour and bifurcation scenario. As a consequence of a^*a being proportional to the photon output, also the mean number of photons emitted from the system oscillates with a fixed frequency that can be externally controlled.

3.4.6. Result Robustness

In all previous sections we have used parameter values which are closed to the experimental realization [Bau10, Bha12], i.e. a small level splitting ω_0 and a dissipation rate κ of the order of the cavity mode frequency ω. In this section we emphasize that the new limit cycle phase and the complex phase diagram with unexpected bifurcation scenario are not restricted to this choice of parameters. Furthermore, our numerics show that they exist for all tested parameter values which points to its generality. In the following we assume the resonant case, thus $\omega_0 = \omega$.

3.4.6.1. Phase Diagram, Dynamics and Bifurcation

Fig. 3.13 shows the main results in the resonant case. The phase diagram Fig. 3.13(a) in the (τ, λ) space shows alternating (F) and (L) zones, similar as in the $\omega_0 \ll 1$ case Fig. 3.8, a lower bound for the feedback strength λ_l without the (L) phase is also present. The main difference is that for $\tau\omega > 20$ and $\lambda > 3\omega$ there are no (F) phases any more. The κ value influences the width of the (L) zones and the distance between them. If we choose this value smaller, then similar structure would appear at smaller dimensionless delay times $\tau\omega$. The green dots in this figure represent the analytic solution where the maximum real part of all eigenvalues vanishes.

The eigenvalue structure Fig. 3.13(b) of the stability matrix Eq. (3.27) looks more typical for time-delayed systems, than in case of $\omega \ll 1$: Different real parts of the roots rise to the positive values, crossing the x-axis and fall down again.

Fig. 3.13(c) shows the Hopf-bifurcation scenario along the dashed white line in Fig. 3.13(a). Here we plot the amplitude of the J_z system component in the steady

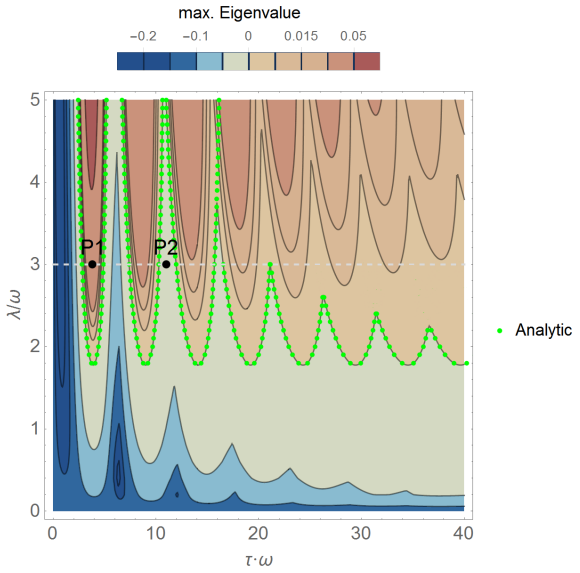

(a) Phase diagramm

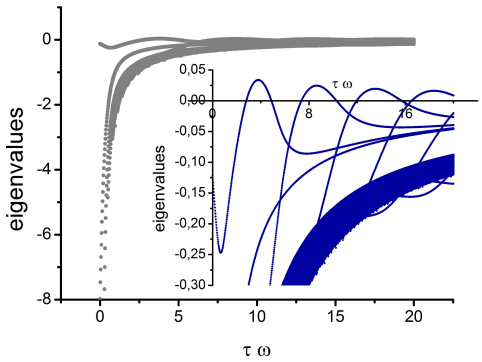

(b) Eigenvalue structure for $\lambda = 3$ MHz

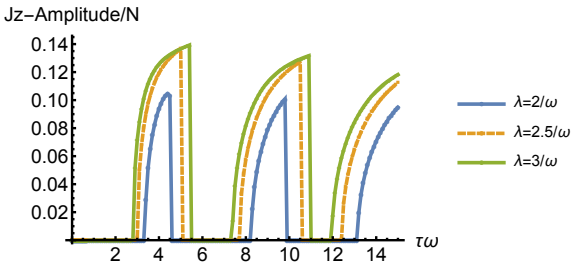

(c) Bifurcation diagram

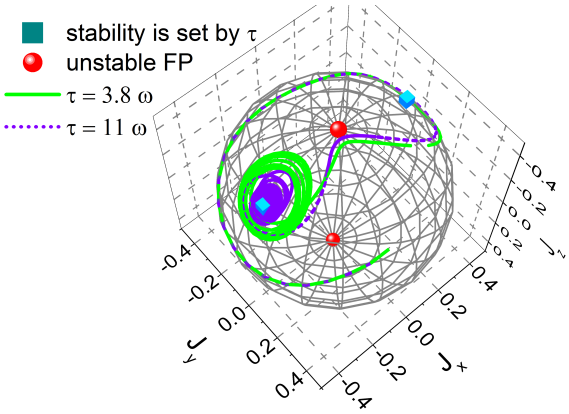

(d) Evolution of the atomic subsystem

Figure 3.13.: Properties of the Dicke system with feedback in resonant case. (a) Phase diagram in (τ, λ) space with the common superradiant phase (blue-like) and the new limit cycle phase (red-like). Green dots show the boundaries between the phases and were calculated analytically. Color code is the maximum real part of all eigenvalues Eq. (3.27) (b) A typical structure of the eigenvalues Eq. (3.27). (c) Bifurcation scenario across the white dashed line in (a) for initial conditions close to the fixed point. The non-zero amplitude shows the limit cycle zones. (d) Two representative time evolution of the atomic subsystem in the (F) and (L) zones. Parameters: $\omega = \omega_0$, $\kappa = 8.1\omega$, $g_0 = 5\omega$.

state. The non-zero amplitude marks the begin and the end of the (L) phase. This diagram is qualitatively the same as in $\omega_0 \ll 1$ case (Fig. 3.11). Note, we have not performed the analysis beyond the linearization assumption here.

Last but not least, Fig. 3.13(d) shows the time evolution of the atomic subsystem for the P1 and P2 points in Fig. 3.13(a). Thus, the non-equilibrium steady state is the limit cycle or a fixed point for P1 and P2, respectively. The main difference from the $\omega_0 \ll 1$ case is the convergence time scale which is smaller in the resonant case.

3.4.6.2. Analytic Calculation

A simplification of the transcendental equation (3.27) occurs in the resonant case $\omega = \omega_0 = 1$, which allow to obtain a closed form for the boundaries between the (F) and (L) zones in the phase diagram. Therefore, we proceed as follows

1. We calculate the determinant from the stability equation (3.27) and insert one of the superradiant solutions (3.19).

2. We want to have the boundary, thus the real part of the eigenvalue Λ should be zero. So assume that Λ is purely imaginary, i.e. $\Lambda = is$.

3. To fulfil the stability equation, its real and imaginary parts must be zero. So we split this equation into real and imaginary parts. The real part reads:

$$
\begin{aligned}
0 = \kappa s \sin\Big(\frac{s\tau}{2}\Big) \Big[& 128\big(\kappa^2+1\big)g_0^7 - 16\big(\kappa^2+1\big)^2 g_0^4 \lambda s^2 - 8\big(\kappa^2+1\big)^3 g_0^3 s^2 \\
& + \big(\kappa^2+1\big)^4 \lambda\big(s^2-1\big) + 256 g_0^8 \lambda \Big] + 4\big(\kappa^2+1\big) g_0^3 \Big[\kappa^6\big(s^2+1\big) + \kappa^4\big(-s^4+3s^2+3\big) \\
& + \kappa^2\big(-16g_0^4 - 2s^4 + 3s^2 + 3\big) + 16 g_0^4\big(s^2-1\big) - s^4 + s^2 + 1 \Big] \cos\Big(\frac{s\tau}{2}\Big)
\end{aligned}
$$

   The imaginary part reads

$$
\begin{aligned}
0 = -\big(\kappa^2+1\big) \Big\{ & \sin\Big(\frac{s\tau}{2}\Big) \Big[64 g_0^7\big(\kappa^2 - s^2 + 1\big) - 16\big(\kappa^2+1\big)^2 g_0^4 \lambda s^2 \\
& - 4\big(\kappa^2+1\big)^2 g_0^3\big(\kappa^2\big(s^2+1\big) - s^4 + s^2 + 1\big) + \big(\kappa^2+1\big)^4 \lambda\big(s^2-1\big) + 256 g_0^8 \lambda \Big] \\
& - 8\kappa g_0^3 s\big[\big(\kappa^2+1\big)^2 s^2 - 16 g_0^4\big] \cos\Big(\frac{s\tau}{2}\Big) \Big\}.
\end{aligned}
$$

4. Now we solve the imaginary part for τ. There are two main solutions and each solution has an additional parameter $n \in \mathbb{N}$ due to the periodicity of sine and cosine functions. The solution for τ depends on this stage also on the eigenvalue s. We denote the solutions as $\tau_{\pm,n}(s)$.

5. Now we can insert the $\tau_{\pm,n}(s)$ solution into the real part of the stability equation. Then we get the eigenvalues s as a function only of the system parameter. For each τ there are up to 8 solutions for s. But only 2 of them are leading to the real positive τ. Thus, inserting this solutions back in to $\tau_{\pm,n}(s)$ we get 4 different implicit equations for $\tau_{i\in\{+1,+2,-1,-2\},n}$ as a function of system parameters τ, κ, λ. Due to a very long equation we show only its form here: $\tau_{i,n} = f_i + g_i \cdot n$ where

the functions f and g depend on the fixed point and system parameters. We see now that the solutions for the same i have equal distances to each other and are lying on the same line. Each solution describes either an even or an odd number of unstable zones and distinguish between the left and the right side of this zone, see Fig. 3.13(a).

3.4.7. Numerical Methods

We are now going to provide more information about the way of getting results from our numerics showed in figures. Figs. 3.5, 3.8 and 3.13(a) contain the solution of the characteristic equation (Eq. (3.27)). Because of its transcendental form, it is impossible to find all the roots, but the roots are usually located in some branches and the most of them approach $-\infty$ for $\tau \to 0$ [Sch08]. The main task of the linear stability analysis is to exclude the branches with positive real part. To achieve it, we use 1600 different starting configurations for $\Lambda = a_0 + ib_0$ (chosen values $a_0, b_0 \in [-40, 40]$) in the root-search function for every system configuration and take then the eigenvalue with the biggest real part.
We continue now with Fig. 3.11. Therefore we solve the system of coupled time-delayed differential equations (3.4) numerically. We have to specify not only the initial conditions, but also the history for $t \in [-\tau, 0[$ and keep the history constant at the initial condition values. In the simulations we keep the values for $x(0)$ and $y(0)$ fixed around $0.1/\sqrt{N}$, set $J_y(0) \cdot N = 0$ and change the initial condition for $J_z(0)$ or $J_x(0)$. The choice of initial conditions is important in the zone with an unstable limit cycle. To be in the possible attraction area of the fixed point, we have to choose the initial condition in such a way that the amplitude of the oscillation for small t values lies under the amplitude of the limit cycle. Typically we choose $J_z(0) = 0$ or $(J_z(0) - J_z^0)/J_z^0 \approx 0.1\%$ to avoid the crossing with the unstable limit cycle. Solving the equation of motion till the oscillating behavior of $\vec{v}$ components remains unchanged, we determine the amplitude and the period of this oscillations, which we plot then as connected lines in Fig. 3.11. Note that results of both initial condition coincide, if the unstable limit cycle is unimportant for the dynamics. Respectively, we choose the initial value above the unstable limit cycle to get the limit cycle continuation (filled symbols in Fig. 3.11), determining again the oscillation properties of the solution for $t \gg 1$. Typically we set $J_z(0) \cdot N = 0.49$ to determine the limit cycle with the greatest amplitude.

To obtain the position of the unstable limit cycle we proceed as follows. We change the initial condition $J_z(0) \cdot N \in]0.5, -0.5[$ in small steps $\delta J_z(0)$ (Fig. 3.14, functions 1 - 4), and determine the initial condition $J_z(0)^{(u)}$, where the solution changes its behavior if compared to $J_z(0) = J_z(0)^{(u)} + \delta J_z(0)$ (Fig. 3.14, functions 2 and 3). The behavior change is identified by comparing the amplitudes of oscillations A at two different times $t_1 < t_2$ (typically $t_1 = 100\ \mu s$, $t_2 = 1000\ \mu s$). If $A(t_1) < A(t_2)$ that means that the solution develops to another attractor (Fig. 3.14, t-axis) as if $A(t_1) > A(t_2)$ (Fig. 3.14, thick blue horizontal lines). We then identify the amplitude of the unstable limit cycle with the amplitude just after the begin of time development for the initial condition, where this behavior change occurs (Fig. 3.14, function 2 or 3). It is a good

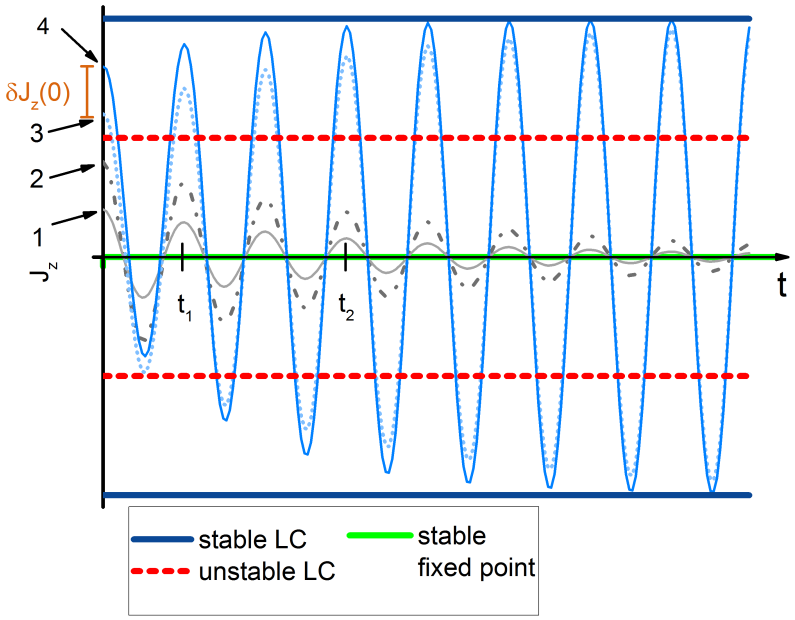

Figure 3.14.: A sketch for determination of an unstable limit cycle. Changing the initial condition (1,2,3,4) the function converges to the limit cycle (thick blue horizontal line), instead of the fixed point (green line at the t - axes). Making $\delta J_z(0)$ smaller, the initial amplitudes of the curves (here 2 and 3) give approximately the amplitude of the unstable limit cycle (thick red dashed horizontal line).

approximation, if $\delta J_z(0)$ is small enough. The obtained results are the unfilled symbols in Fig. 3.11. The procedure is visualized in Fig. 3.14. Note that the convergence is much slower that in this sketch.

3.5. Discussion and Outlook

The application of the Pyragas control to the coupling g of the Dicke model generates a complex phase diagram with stable fixed points (F) and limit cycles (L) in the superradiant regime. The alternations between (F) and (L) zones (Fig. 3.8) in fact constitute an infinite sequence of super- and subcritical Hopf bifurcations of the stationary state generating stable and unstable limit cycles, respectively. Furthermore the feedback generates bistable regions ending by a saddle-node bifurcation.

3.5.1. Experimental Realisation

In the experimental setup [Bau10], a Bose-Einstein condensate (BEC) is trapped inside an optical cavity and is additionally driven by a pump laser. The two-level atomic system is built of atoms with two different momentum states, where one is the BEC

ground state. Other momentum states have to be excluded by a two-mode-assumption, which is fulfilled if the pumping frequency is far detuned from the resonant atomic frequencies. The collective spin operators $J_\pm$ describe the atomic transitions in the collective momentum space. The interaction term in the Dicke-Hamiltonian Eq. (3.1) is an effect of the interplay between the photons of the pumping field and the cavity photons via the two-level system. Furthermore, Eq. (3.1) is given in the rotating frame at the pump laser frequency. In that way the Hamiltonian has no direct dependence on the pumping laser, its properties are already included in the parameters. Thus the coupling constant g, which becomes time dependent in our approach, is defined by the light intensity of the pumping field.
On the one hand, our approach modifies only this intensity and does not add additional frequencies to the cavity. The intensity increase/decrease is small compared to the uncontrolled system, because $g_0 \ll \lambda/Na^*a$ as we can conclude from Fig. 3.7 (right), and λ can be assumed to be unity to achieve the calculated effects (see Fig. 3.8). Thus, the two-mode approximation of the Dicke model in the atomic momentum space should remain valid and no other energy states except these two should be excited. On the other hand, it should be possible to restrict the feedback strength parameters such that the possible excitations are avoided.
Deviations due to photon loss between the measured mean photon number and its actual value can be compensated by time interval extension for calculating the mean value (because of rather slow dynamical evolution with fast oscillations) or by tuning the λ-coupling.

3.5.2. Aspects of Pyragas Control

The open loop control provided in [Bas12] creates new fixed points in the normal and superradiant regime, so a bifurcation is induced by periodic modulation of the coupling constant. In contrast, the closed loop control scheme used here completely changes the impact on the Dicke system and the bifurcation scenario. Although the Pyragas control performed by Grimsmo et al. [Gri14] is physically very different from our scheme, it creates similar phase diagrams with limit cycles. Furthermore, adding the back action of the cavity field $U\hat{J}_z\hat{a}^\dagger\hat{a}$ to the Dicke Hamiltonian H Eq. (3.1), there are some parameter regimes where the solution of the mean-field equation has persistent oscillations [Bha12]. This is linked to the absence of stable fixed points, the same happens in the LC-zone caused by time delay. These analogies indicate that the analyzed limit cycle phase is not something that is artificially added to the model by Pyragas control. Rather, this phase is hidden in the model and becomes visible by the control. We remark that the possibility of periodic dynamics in such systems was also observed in optomechanical BEC experiments [Rit09, Bre08].

We emphasize that the time dependence of $g(t \to \infty)$, equation (3.3), does not disappear in the L-regions in contrast to the F-regions, leading to the phase diagram discussed above. In the L-region $g(t)$ oscillates with the same period as the other system observables. This is a consequence of subtracting two oscillating functions $x(t-\tau)^2 + y(t-\tau)^2$ and $x(t)^2 + y(t)^2$ with the same period. Our feedback scheme here

switches between non-invasive and invasive behavior by crossing the boundaries within the phase diagram. Our results also demonstrate that the Pyragas form in equation (3.3) is essential to create a new stable phase. In contrast, for the direct feedback scheme $g(t) = g_0 + \lambda \left\langle \hat{a}^\dagger \hat{a} \right\rangle (t - \tau)$, depending on parameter values the occupation of the optical mode diverges and the control does not work well, or the time delay does not seriously modify the phase diagram at all (not shown here).

Finally, we also checked that the (experimentally less practical) Pyragas feedback for the angular momentum (instead of the photonic feedback) also leads to the creation of a limit cycle phase in the superradiant regime, but can also not influence the stability of the normal phase.

We expect that our feedback scheme can be implemented whenever semiclassical equations of motion provide an adequate description for the quantum bifurcation type phase transitions that govern models with collective degrees of freedom, such as the Dicke or the Lipkin-Meshkov-Glick model [Lip65].

An open and challenging problem is the implementation of time-delayed feedback control for quantum critical systems beyond the mean-field level, i.e., where quantum fluctuations are expected to play a major role [Nag11]. However, one possible way was recently published by Grimsmo [Gri15].

3.6. Summary

In this section we have theoretically studied a time-delayed control of Pyragas type of the dissipative Dicke model at the mean-field level. Therefore, we have assumed the modification of the coupling g according to

$$g(t) = g_0 + \frac{\lambda}{N\sqrt{N}}[n(t-\tau) - n(t)],$$

where $n(t)$ is the mean occupation of the optical mode at time t which is proportional to the mean flux out from the cavity. Thus the feedback is measurement-based and has a time delay τ. Using the mean-field approach, it is possible to derive a closed set of time-delayed differential equations for the system observables. The equations describe a quantum phase transition and have a non-trivial steady state solution in the superradiant phase, exactly as in the non-feedback case [Bha12]. First, we have used linear stability analysis to study the feedback influence on the fixed point. In a superradiant regime we found a new complex phase diagram Fig. 3.8 with an old superradiant phase where the fixed point is stable and a new limit cycle phase, where the fixed point is unstable and a stable limit cycle appears. Both phases are alternating periodically as a function of τ. For the boundaries we could provide analytical expression. Studying the Dicke system with control beyond the linear stability analysis, we found out that several stable limit cycle phases and a common superradiant phase can be present for the same system configuration at larger time delays. The corresponding bifurcation diagram Fig. 3.11 has Hopf and saddle-node bifurcation. We show that the in the limit cycle phase the controlled coupling g oscillates periodically but only slightly deviates

from the stationary value g_0. Therefore we argue that the existing experimental setup and the theoretical basement for the Dicke model should remain valid even in the new phase.

4. Time-Delayed Control of Excited State Quantum Phase Transitions in the Lipkin-Meshkov-Glick model

This chapter is mainly based on the results published in Ref. [Kop15b].

4.1. Introduction

In this section we use Pyragas control to influence the excited state quantum phase transition (ESQPT) in the open LMG model [Lip65]. ESQPT is - in contrast to the QPT - a criticality in the excited states of a system [Cap08], see Sec. 2.2 for more information. On the one hand the ESQPT is directly visible in the density of states as a divergence or a non-analyticity, on the other hand its imprint is visible in the system averaged observables which are in general easier to determine experimentally. Additional, for the models which are investigated in this thesis, a semiclassical correspondence to the ESQPT exist, see Sec. 2.2.2.

In the previous chapter, we applied time-delayed Pyragas control to a Dicke model [Dic54] to create new non-equilibrium phases [Kop15b]. In Ref. [Eng15] we suggested a new method to extract the ESQPT signal from the time evolution in the closed LMG system and used an energy-independent representation to detect the ESQPT signal. Closed loop control was already applied to the LMG model to induce new phases or to modify the divergence in the density of states [Bas14a, Bas14b, Eng13]. Moreover, Oberthaler et al. implemented the LMG model using the existing ingenious experimental setup based on ^{87}Rb Bose-Einstein condensates [Zib10], which offers a high degree of control for system preparation, providing a possibility to test new insights about the (ES)QTP. Surprisingly, the effects of a dissipative environment on the ESQPT seems not to be well studied in contrast to the QPT [Mor08b], though they are always present in experimental realizations.

Inspired by this, we study the effects of dissipation on the ESQPT signal in the LMG model and apply a time-delayed feedback scheme to cancel them by the creation of new phases. In our model, we condition the atomic coupling on the difference of a spin observable average at two different times and perform the calculation at a mean-field-level. On top we show that in dissipative systems the ESQPT is directly visible in a complex spectrum of effective system Hamiltonian.

This chapter is organized as follows. In Sec. 4.2 we introduce the dissipative LMG model and the feedback. In section 4.3 we study the dissipative effects on a ESQPT

at a quantum level evaluating the complex spectrum of an effective Hamiltonian and calculating two different correlation functions. In Sec. 4.4 we show the smoothing effects of the ESQPT signal due to dissipation at a mean-field level and show in Sec. 4.5 how to compensate them using time-delayed Pyragas control. In the last Sec. 4.6 we discuss the results.

4.2. LMG Model with Dissipation and Feedback

The LMG model [Lip65] describes an interaction between N spins and represents a special case of a Heisenberg Model. In general, the LMG Hamiltonian reads

$$\hat{H} = -h\hat{J}_z - \frac{\gamma_x}{N}\hat{J}_x^2 - \frac{\gamma_y}{N}\hat{J}_y^2, \tag{4.1}$$

where $\hat{J}_i = \frac{1}{2}\sum_{j=1}^{N}\hat{\sigma}_i^j, i \in \{x, y, z\}$ are collective angular momentum operators, h is an effective parameter for the external magnetic field in z-direction and γ_x or γ_y describes the spin-spin interaction strength, which is the same for all pairs of spins in the LMG model. In the following, we will tacitly use the fully anisotropic $\gamma_y = 0$ case, if we do not explicitly point to $\gamma_y \neq 0$ case.
Especially in experimental realizations, the LMG system is always coupled to an environment which cause the damping and thermalization of the system and can be modeled by a master equation [Mor08b, Mor08a] with collective decay [Lee14]

$$\dot{\hat{\rho}} = -i[\hat{H}, \hat{\rho}] - \frac{\kappa}{2N}\mathcal{D}[\hat{J}^+]\hat{\rho}, \tag{4.2}$$

where $\mathcal{D}[\hat{J}^+]\hat{\rho} = \hat{J}^-\hat{J}^+\hat{\rho} + \hat{\rho}\hat{J}^-\hat{J}^+ - 2\hat{J}^+\rho\hat{J}^-$ is the Lindblad-dissipator and $\hat{J}^\pm = \hat{J}_x \pm i\hat{J}_y$.
To compensate the dissipative effects we assume a time-dependent coupling γ_x of Pyragas form [Pyr92]. Therefore we condition γ_x to depend on the difference of $\hat{J}_z$ averages at two different times with time delay τ as

$$\gamma_x = \gamma_x(t) = \gamma + \frac{\lambda}{N^2}\left[\left\langle \hat{J}_z(t-\tau)\right\rangle^2 - \left\langle \hat{J}_z(t)\right\rangle^2\right], \tag{4.3}$$

In the following, we investigate the ESQPT signal at the quantum level using the effective Hamiltonian approach or calculating correlation function. At a semiclassical level we use the solution of mean-field equations in thermodynamic limit. In the second case we show the unique effect of the feedback loop especially in context of the ESQPT.

4.3. Dissipative ESQPT at Quantum Level

The fate of the ESQPT signal in presence of dissipation is still not studied well. In closed systems the ESQPT is hidden in the energy spectrum or is visible in observable averages as a function of energy [PF11b] as a non-analyticity, which can be obtained by quantum mechanical or semi-classical calculations. Its origin can be understood at

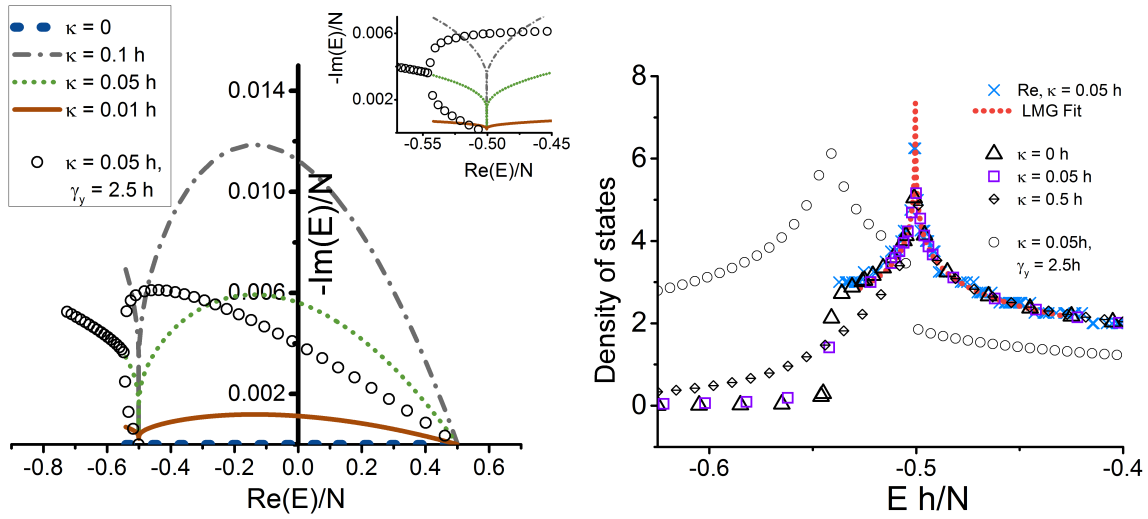

Figure 4.1.: (left) The complex spectrum for different values of γ. The Υ-structure indicates the position of the ESQPT. The inset shows the zoom around the ESQPT energy. (right) The density of states of the effective LMG Hamiltonian shows a logarithmic divergence at $E = -0.5N$. Crosses and empty symbols are obtained using only the real part of the spectrum or the whole spectrum with Eq. (4.7), respectively. For comparison, the $\gamma_y \neq 0$ case is additionally shown in both figures (open circles). Parameters: $(\gamma = 1.5h), N = 10000$ (blue crosses), $N = 1000$ (other cases), $\lambda = 0$. Taken from Ref. [Kop15a].

a semi-classical level as critical points from the energy surface, see Sec. 2.3 for more informations. In the following we show that complex spectrum of the non-hermitian Hamiltonian still contains the information about the ESQPT and analyze whether a correlation function contains the ESQPT signal.

4.3.1. Spectral Signatures of Dissipative ESQPTs

In dissipative systems described by a Lindblad master equation an effective non-hermitian Hamiltonian can be defined in a standard way. Rewriting the master equation (4.2) as

$$\dot{\hat{\rho}} = -i[\hat{H}_{eff}, \hat{\rho}] + \frac{\kappa}{N}\hat{\mathcal{J}}\hat{\rho}, \tag{4.4}$$

with the jump operator

$$\hat{\mathcal{J}}\hat{\rho} = \hat{J}^{+}\rho\hat{J}^{-}, \tag{4.5}$$

we obtain the effective non-hermitian Hamiltonian

$$\hat{H}_{eff} = \hat{H} - i\frac{\kappa}{2N}\hat{J}^{-}\hat{J}^{+} \tag{4.6}$$

with complex spectrum, which is shown in the Fig. 4.1 (left) for different values of κ in the symmetry broken phase. For $\kappa \neq 0$ the spectrum has an imaginary part which

scales with κ. The imaginary part can be interpreted as a decay rate at a certain energy level [Jun99, Kle85]. To complete the spectral information we show in the right part of figure 4.1 the corresponding density of states. For example, open triangles show the density of states along the blue dashed line in the left figure in the known $\kappa = 0$-case [Rib08], where a logarithmic divergence at $E = -0.5N$ is due to the ESQPT. We note that in some references like [Eng15] the normalization of the system observables is performed by $j \equiv N/2$ instead of here used N normalization, the ESQPT is then located at $E = -1j$.

How does the dissipation affect the ESQPT? The ESQPT survives and, somewhat surprisingly, it becomes visible not only in the density of states of the non-hermitian Hamiltonian H_{eff}, but can be also directly seen from its complex eigenvalues, see figure 4.1 (left). The ESQPT is hidden in this representation in a Υ-form at the energy of $E = -0.5N$. Another feature (due to the assumed Lindblad operator (4.2)) is the vanishing of the imaginary part of H_{eff} at the north and south poles of the corresponding Bloch sphere, which leads to zero imaginary part at the corresponding energies of $\mp 0.5N$. Thus the decay rate is zero there and the dissipative effects disappear at this points. Note, this effect is also present at the level of the mean-field equations (4.13), where dissipative terms do not contribute at the poles for arbitrary κ values due to conservation of the spin length.

We use two different methods to calculate the density of states in the $\kappa > 0$ case. First, we use only the real part of the eigenvalues and count their number in a certain energetic window, see blue crosses in Fig. 4.1 (right). To get clear results for the peak, we use $N = 10000$ atoms. For a too small number of atoms the peak can be smoothed or slightly shifted. The peak can be well fitted by a logarithmic function (red dotted curve) with a divergence at the energy $E = -0.5N$, which matches to the closed system (open triangles).

For the second method we use the definition

$$\nu(E) = -1/\pi \Im \mathrm{Tr}\left(\frac{1}{E - H_{eff}}\right) \tag{4.7}$$

with the non-hermitian Hamiltonian (open symbols). We emphasize that the results agree and have still a logarithmic divergence at the energy $E = -0.5N$, see the log-fit (red dotted curve). Especially for $E > -0.5N$ there is no visible deviation for different κ values from the $\kappa = 0$ case (open triangles). Only for $E < -0.5N$, there is a deviation from the non-dissipative result, which can be better seen for the curve with a bigger dissipation rate $\kappa = 0.5$ (diamond with a line). The origin of Eq. 4.7 is a combination of a Sokhotsky-Weierstrauss theorem

$$\lim_{\varepsilon \to 0^+} \frac{1}{x \pm i\varepsilon} = PV\frac{1}{x} \mp i\pi\delta(x),$$

where PV is principal value with a representation of the density states as

$$\rho = \sum_n \delta(E - E_n) = Tr\delta(E - \hat{H}).$$

We emphasize that the ESQPT signature is only the Υ-structure and not the zero imaginary part in the complex spectrum. For $\gamma_y = 0$ both effects are at the energy $E = -0.5$, though they can be easily separated for an anisotropic LMG Hamiltonian ($\gamma_y \neq 0$), where the ESQPT can be shifted to other energies and a jump in a density of states can occur on top [Rib08]. Setting $\gamma_y = 2.5h$, we observe a shift of the Υ-signal to the corresponding energy of ESQPT in this case (open circles in the left part of figure 4.1). The corresponding density of states (open circles in the right part of the figure) calculated with Eq. (4.7) has a peak at the ESQPT energy $E \approx -0.54N$ and a jump at $E = -0.5N$ [Rib08]. Note that the finite size effects smooths the peak and the jump in this case.

4.3.2. Correlation Functions

Experimentally, measuring of the correlation function [Car09] represents a common but powerful tool to determine the spectral properties of the system. Therefore we question ourselves as to whether the ESQPT signal is clearly printed in such a correlation function. Among various types of correlation functions we pick up two cases, a two-point correlation function and a waiting time distribution.

4.3.2.1. Two-Point Correlation Function

To determine a correlation function experimentally, one usually measures the leaking photon current at two different times t and $t + z$ (and or places). Theoretically, due to the system-environment interaction such correlation function can be expressed with system operators [Car09]. Therefore, we take

$$C_t(z) \equiv \left\langle \hat{J}^+(t+z)\hat{J}^-(t) \right\rangle \Theta(z)$$

as a typical two-point correlation function which we calculate using the quantum regression theorem [Sch14a] for finite size N, see Sec. 2.6 for more information. The operators are depicted in the Heisenberg picture and have therefore time dependency. The spectral signatures are usually encoded as maxima of the correlation function in the Fourier space.

In the following, we show and interpret the results for the correlation function $C_t(z)$ of the LMG model, calculating it for different system sizes N. The result of the quantum regression theorem strongly depends on the used initial condition of the system. We assume that our system starts either in an eigenstate of the closed LMG Hamiltonian or in a non-equilibrium steady state of the master equation Eq. (4.2).

Figure 4.2 shows the correlation function in the Fourier space

$$FT[C_t(z)](\omega) = \int_0^\infty C_t(z) e^{-i\omega z} dz$$

for two different decay rates κ and different initial conditions. The calculation is performed for $N = 8$ particles. The lower part of each subfigure shows the spectrum of

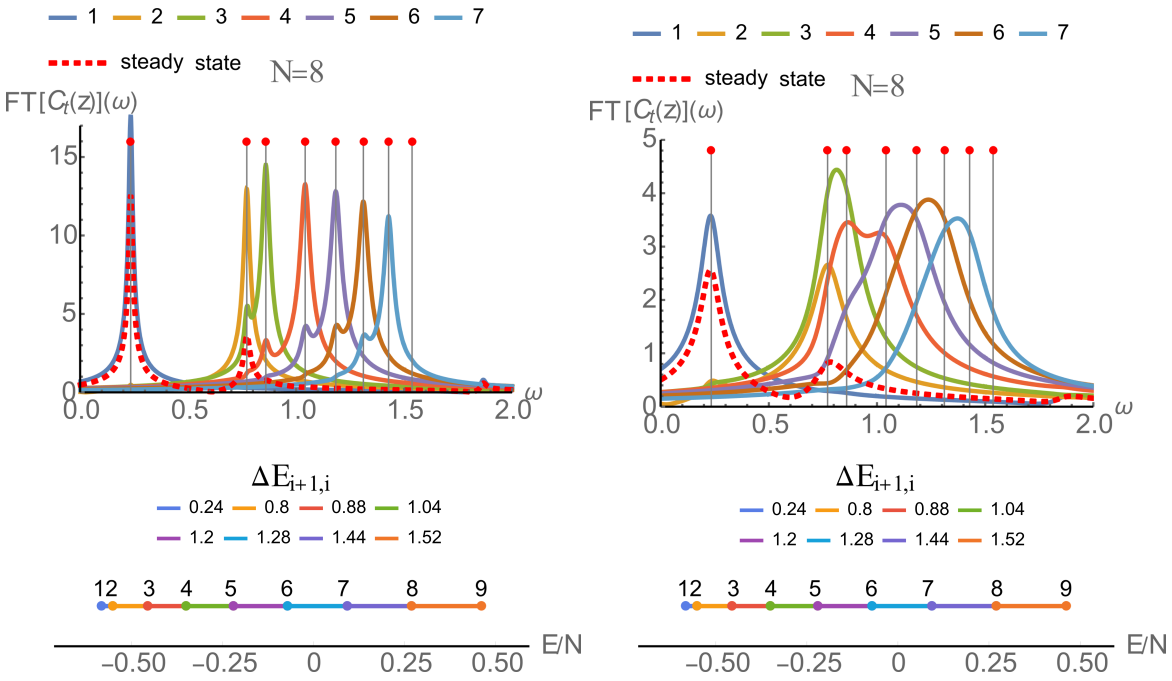

Figure 4.2.: (upper) Correlation function in the Fourier space for different initial condition which are chosen as eigenstates (solid lines) and stationary state (dashed line). Vertical lines with red point shows the energy difference of neighbouring levels. (lower) Spectrum of the LMG model, legend shows the energy distance of neighbouring levels. Integer counts the eigenstates and corresponds to the initial condition in the upper part. Parameters: $\kappa = 0.01h$ (left),$\kappa = 0.05h$(right),$\gamma = 1.5h, N = 8$.

the closed Hamiltonian. The eigenstates are numbered, e.g. the lower state corresponds to the state "1". The lower legend shows the distance between nearby energetic levels. This level distance of neighbouring energy levels is shown in the form of vertical lines with red points in the upper part of the diagram. The connected and dash-dotted lines show the correlation function behavior in the Fourier space. The initial condition is chosen as an eigenstate Nr. i and a steady state of the master equation, respectively. In the left part of Fig. 4.2 we see that the position of the local maxima corresponds to the neighbouring level distance in the energy space. Moreover, if the system is located in the kth eigenstate with energy E_k, then the peaks with the biggest amplitude show the level distance to the nearest levels, e.g. they are at the positions $\Delta E_{k,k\pm1} = |E_k - E_{k\pm1}|$. The stationary state is a superposition of eigenstates, thus the corresponding correlation function (red dashed line) should show this superposition behavior. As we can see, the stationary state correlation function has mainly two peaks which shows the energy distances $E_{1,2}$ and $E_{2,3}$. The right part of Fig. 4.2 shows that the width of the correlation function becomes larger with greater decay rate κ, thus the peaks merge together to one local maximum which is not located at the position of the energy gap any more, e.g. the green curve with an eigenstate no. 3.

Level clustering is an ESQPT signature, thus the correlation function should have then a peak at zero frequency, especially for large N values. Indeed, some corresponding correlation functions for $N = 50$, see Fig. 4.3, diverge at $\omega = 0$. However, this peak is not only due to the ESQPT, rather it is usually overlayed with two additional peaks. The macroscopic occupation always leads to an offset of a correlation function $C_t(z)$ as a function of z which results in a peak at the origin in the Fourier space. Second, the energies below the ESQPT energy $E < -0.5N$ are degenerated, see lower part of Fig. 4.3, the zero gap is always present in the spectrum in the symmetry broken phase. Thus, if the initial condition contains mostly such states, then the corresponding correlation function will have a peak at the origin. For example this is the case for the stationary state, see dashed line in the Figure. Indeed, our calculation shows that the steady state of the master equation Eq. (4.2) contains mostly only the two states with the lowest energy. This is energetically insufficient for the ESQPT, see red points in the lower figure.

Summarizing, a peak in the correlation function at the origin cannot allow to be interpreted as the ESQPT signal. Furthermore - and depending on the initial condition - it is a combination of several properties in the symmetry broken phase in the LMG model. By contrast, such a peak is completely absent in the normal phase, thus it can be seen as a phase transition signature in the LMG model.

4.3.2.2. Waiting Time Distribution

Waiting times characterize the probability that two (different) jumps occur after a time z [Bra08]. In the master equation formalism it is defined as

$$w_{kl}(z) = \frac{1}{N} \frac{\mathrm{Tr}\left(\hat{\mathcal{J}}_k e^{\hat{\mathcal{L}}_0 z} \hat{\mathcal{J}}_l \hat{\rho}_0\right)}{\mathrm{Tr}\left(\hat{\mathcal{J}}_l \hat{\rho}_0\right)}, \tag{4.8}$$

where the indices k and l label the jump type. Here $\hat{\rho}_0$ is a steady state density matrix and $\hat{\mathcal{L}}_0$ is the free Liouvillian which describes the evolution of the density matrix without jumps, e.g.,

$$\hat{\mathcal{L}}_0 \hat{\rho} = -i \left[\hat{H}_{eff}, \hat{\rho}\right]. \tag{4.9}$$

The numerator in Eq. (4.8) can be interpreted as follows. Starting from a steady state a jump of type l happens, then the system is developed under the free evolution for the time duration z, then again a jump of type k happens. The denominator is a normalization.

Numerically, it is easier to handle system operators than super-operators as $\hat{\mathcal{L}}_0$ and $\hat{\mathcal{J}}$. Here it is possible to rewrite Eq. (4.8) on the operator level using the following connection

$$e^{\hat{\mathcal{L}}_0 z} \hat{\rho} = e^{-i\hat{H}_{eff} z} \hat{\rho} e^{i\hat{H}^\dagger_{eff} z}. \tag{4.10}$$

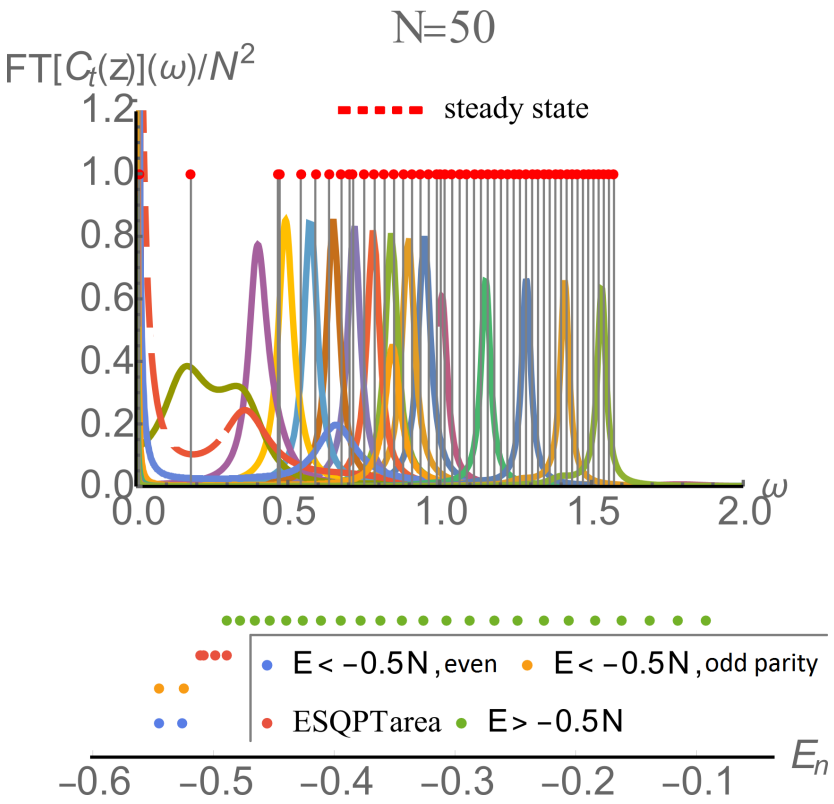

Figure 4.3.: (upper) Same as in Fig. 4.2 but for a larger particle number N. (lower) Spectrum of the closed Hamiltonian is divided in different areas, the degenerated part (blue and orange, $E < -0.5N$), the ESQPT part (red,especially for $N \gg 1$) and the rest (green). Parameters: $\kappa = 0.05h$,$\gamma = 1.5h$, $N = 8$.

This is possible due to the definition of the free Liouvillian Eq. (4.9). Using the Baker-Campbell-Hausdorff formula for non-hermitian operators we can see that

$$e^{\hat{\mathcal{L}}_0 z}\hat{\rho} = \sum_n \frac{(\hat{\mathcal{L}}_0 z)^n}{n!}\hat{\rho} = \hat{\rho} + \frac{(-iz)}{1!}\left[\hat{H}_{eff},\hat{\rho}\right] + \frac{(-iz)^2}{2!}\left[\hat{H}_{eff},\left[\hat{H}_{eff},\hat{\rho}\right]\right] + \ldots$$
$$= e^{-i\hat{H}_{eff}z}\hat{\rho}e^{i\hat{H}^\dagger_{eff}z}. \tag{4.11}$$

Thus, using Eq. (4.10) and Eq. (4.4) we can rewrite Eq. (4.8) as

$$w(z) = \frac{1}{N}\frac{\mathrm{Tr}\left(\hat{J}^+ e^{-i\hat{H}_{eff}z}\hat{J}^+\hat{\rho}_0\hat{J}^- e^{i\hat{H}^\dagger_{eff}z}\hat{J}^-\right)}{\mathrm{Tr}\left(\hat{J}^+\hat{\rho}_0\hat{J}^-\right)}, \tag{4.12}$$

where we neglect the jump labels as we have assumed only one jump type Eq. (4.4).

For the further numerical procedure we find a stationary solution of the density matrix equation and calculate then the waiting time distribution for different parameters.

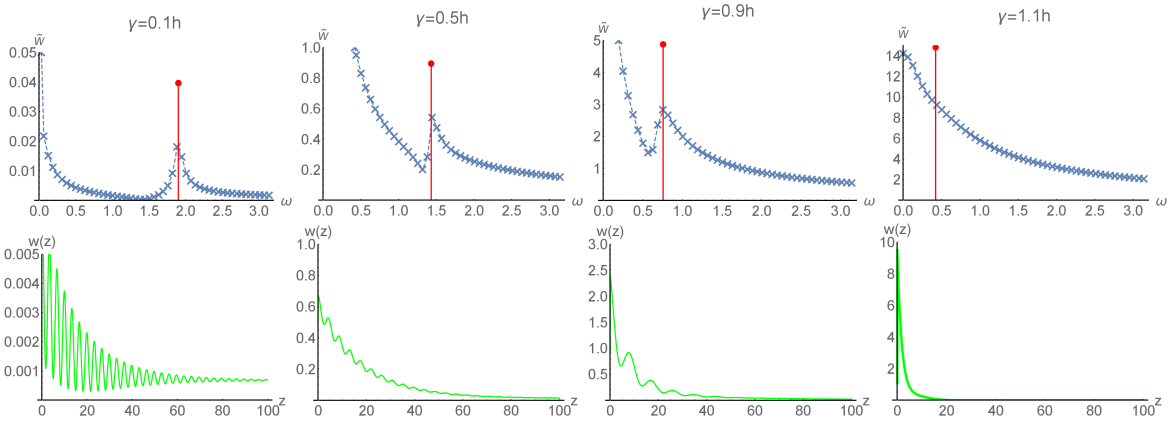

Figure 4.4.: Waiting time distribution in the time (lower) and frequency (upper) domain. In the symmetry broken phase $\gamma > \gamma_h$ the oscillations are absent. The vertical gray line shows the energy difference between the 4th and 2th level of the closed LMG Hamiltonian Eq. (4.1). $\kappa = 0.05h$,$N = 200$.

For our numerics we represent all operators with respect to the usual used $|lm\rangle$ Dicke basis.

Figure 4.4 shows the waiting time distribution in the time (lower) and frequency (upper) space for different atom coupling γ. First we see that in the normal phase for $\gamma < \gamma_c$ the waiting time distribution $w(z)$ oscillates and the oscillation amplitude increases with γ (lower). These oscillations induce a peak in the Fourier space (upper). We could identify the peak position with the energy difference between the 4th and 2th level of the closed Hamiltonian, see horizontal line with red point. Surprisingly, this peak is absent in the symmetry broken phase for $\gamma > \gamma_c$ and the waiting times behavior becomes approximately exponential.

Summarizing, we have not found any ESQPT signatures in the waiting time distribution of the LMG model. We subscribe the absence of signatures to different properties of the model. The steady state ρ_0 contains mostly two system states with the lowest energy, which are not connected with the ESQPT. The jump operators in the waiting time distribution change the state, but apparently only slightly: it induces a transition between the 4th and 2th level, but still far away from the ESQPT energy. However, the waiting time method allows us to distinguish between the normal and the symmetry broken phase by the presence or absence of the peak for $\omega > 0$ in the Fourier space, respectively.

4.4. Dissipative ESQPT Signal at Mean-Field Level

In this section we show how the damped dynamical evolution of the system affects the ESQPT signal and how does the Pyragas control helps to cancel dissipative effects.

4.4.1. Mean-field Equations

To derive a mean-field equation for the dissipative LMG system, we use $\left\langle \hat{O} \right\rangle = \mathrm{Tr}(\hat{O}\hat{\rho})$, assume the factorization assumptions $\left\langle \hat{O}_1\hat{O}_2 \right\rangle \approx \left\langle \hat{O}_1 \right\rangle \left\langle \hat{O}_2 \right\rangle$ which is known to hold in the thermodynamic limit and to forecast the same observable averages and the phase transition as the quantum mechanical calculations [Dus05, Eng15]. We then obtain a following set of closed semiclassical equations of motion [Mor08b]

$$\begin{aligned} \dot{J}_x(t) &= hJ_y(t) - \kappa J_x(t)J_z(t), \\ \dot{J}_y(t) &= -hJ_x(t) + 2\gamma_x(t)J_x(t)J_z(t) - \kappa J_y(t)J_z(t), \\ \dot{J}_z(t) &= -2\gamma_x(t)J_x(t)J_y(t) + \kappa\left(J_x(t)^2 + J_y(t)^2\right), \end{aligned} \tag{4.13}$$

with rescaled averages $J_i = \frac{1}{N}\left\langle \hat{J}_i \right\rangle$. Without time delay ($\lambda = 0$) the QPT, which is one important property in this system, corresponds at this semi-classical level to a pitchfork bifurcation [Mor08a]: Eq. (4.13) has two stationary states J_i^0, corresponding to a normal phase with $(J_x^0, J_y^0, J_z^0) = (0, 0, 1/2)$ and a symmetry broken phase

$$\begin{aligned} J_x^0 &= \pm\sqrt{\frac{-4h^2(\gamma - \sqrt{\gamma^2-\kappa^2}) + \kappa^2(\gamma + \sqrt{\gamma^2-\kappa^2})}{8\gamma\kappa^2}}, \\ J_y^0 &= \frac{\gamma - \sqrt{\gamma^2-\kappa^2}}{\kappa} \cdot J_x^0, \quad J_z^0 = h \cdot \frac{\gamma - \sqrt{\gamma^2-\kappa^2}}{\kappa^2}, \end{aligned} \tag{4.14}$$

whose stability swaps at a critical coupling

$$\gamma_c = h + \frac{\kappa^2}{4h}. \tag{4.15}$$

Note that even the dissipative model still fulfills the conservation law $J_x^2 + J_y^2 + J_z^2 = 1/4$, thus the dynamical evolution is restricted to a sphere. Furthermore, even with time delay ($\lambda > 0$) the fixed points remain the same, as the Pyragas term vanishes in the steady state.

In the next section, we investigate the ESQPT signal in presence of damping with and without control. Later we show that the time-delayed coupling $\gamma(t)$ may affect the linear stability of fixed points and the dynamical evolution of the system in a completely unexpected way, particular in its acting against the dissipation.

4.4.1.1. Auxiliary Calculations

But first, we want to give an example, how to obtain one of the equations from Eq. (4.13). Using $\partial_t \left\langle \hat{O} \right\rangle = \mathrm{Tr}(\hat{O}\dot{\hat{\rho}})$, trance-invariance under cyclic permutation and the commutator relation $\left[\hat{J}_x, \hat{J}_y\right] = i\hat{J}_z$ as Eq. (3.9), we obtain

$$\begin{aligned}\partial_t \left\langle \hat{J}_z \right\rangle &= \mathrm{Tr}\left\{ \hat{J}_z \dot{\rho} \right\} \overset{(4.2)}{=} \mathrm{Tr}\left\{ i\left[\hat{H}, \hat{J}_z\right]\hat{\rho} - \frac{\kappa}{2N}\left(\hat{J}_z\hat{J}^-\hat{J}^+ + \hat{J}^-\hat{J}^+\hat{J}^z - 2\hat{J}^-\hat{J}_z\hat{J}^+\right)\hat{\rho}\right\} \\ &= -\frac{\gamma_x}{N}\mathrm{Tr}\left\{(\hat{J}_x\hat{J}_y + \hat{J}_y\hat{J}_x)\hat{\rho}\right\} - \frac{\kappa}{2N}\mathrm{Tr}\left\{\left(\left[\hat{J}_z, \hat{J}^-\right]\hat{J}^+ + \hat{J}^-\left[\hat{J}^+, \hat{J}_z\right]\right)\hat{\rho}\right\} \\ &= -\frac{\gamma_x}{N}\mathrm{Tr}\left[(\hat{J}_x\hat{J}_y + \hat{J}_y\hat{J}_x)\hat{\rho}\right] + \frac{\kappa}{N}\mathrm{Tr}\left[(\hat{J}^-\hat{J}^+)\hat{\rho}\right].\end{aligned}$$

In the thermodynamic limit $N \to \infty$ the fluctuations are neglected and we split an average over an operator product in separate averages. Introducing the rescaling $J_i = \frac{1}{N}\left\langle \hat{\hat{J}}_i \right\rangle$ we end by the form shown in Eq. (4.13)

$$\begin{aligned}\partial_t \frac{\left\langle \hat{J}_z \right\rangle}{N} &= -\gamma_x \frac{\left\langle \hat{J} \right\rangle_x \left\langle \hat{J} \right\rangle_y + \left\langle \hat{J} \right\rangle_y \left\langle \hat{J} \right\rangle_x}{N^2} + \kappa \frac{\left\langle \hat{J}^- \right\rangle \left\langle \hat{J}^+ \right\rangle}{N^2} \\ \Rightarrow \partial_t J_z &= -2\gamma_x J_x J_y + \kappa\left(J^- J^+\right) = -2\gamma_x J_x J_y + \kappa\left(J_x^2 + J_y^2\right).\end{aligned}$$

The obtained mean field equations Eq. (4.13) fulfil the conservation law for the length of the angular momentum, too

$$\begin{aligned}\partial_t J^2 &= 2J_x\dot{J}_x + 2J_y\dot{J}_y + 2J_z\dot{J}_z == 2hJ_xJ_y - 2\kappa J_x^2 J_z - 2hJ_xJ_y \\ &= +2\gamma_x J_x J_y J_z - 2\kappa J_y^2 J_z - 2\gamma_x J_x J_y J_z + 2\kappa J_x^2 J_z + 2\kappa J_y^2 J_z \\ &= 0.\end{aligned}$$

4.4.2. Dissipative Damping of the ESQPT

Using the semiclassical equation of motion Eq. (4.13) we now study the action of dissipation on the ESQPT at this level. Therefore we first look at a dynamical evolution of the LMG system. The spin averages of the system are restricted to the Bloch sphere which is shown in Fig. 4.5 (inset). The sphere color represents the energy for a given system configuration for $\kappa = 0$ in the symmetry broken phase, the white lines represent the paths with the same energy. Without dissipation the system follows one of this paths keeping the energy fixed, i.e. staying in the eigenstate. For each eigenstate with an energy E one can compute an averaged value for $(J_x^2(E), J_z(E))$ by averaging over one or multiple periods. The black (dotted) curve (Fig. 4.5) shows this values for multiple eigenstates where each point has its own energy E. This is a novel representation of two observable averages which was recently suggested to visualize the energy independent ESQPT signal [Eng15], which is visible again as a peak. The the peak ends by $(0, 1/2)$. In the upper half of a Bloch sphere we see a separatrix, a (white) path which goes through the north pole of the sphere. Due to the symmetry of the path, its averaged values for J_x^2 and J_y^2 should be zero, whereas the J_z average is $1/2$. Thus, paths close to the separatrix are responsible for the ESQPT peak in (J_x^2, J_z) diagram. Without dissipation ($\kappa = 0$) the period length for fixed energy diverges at the

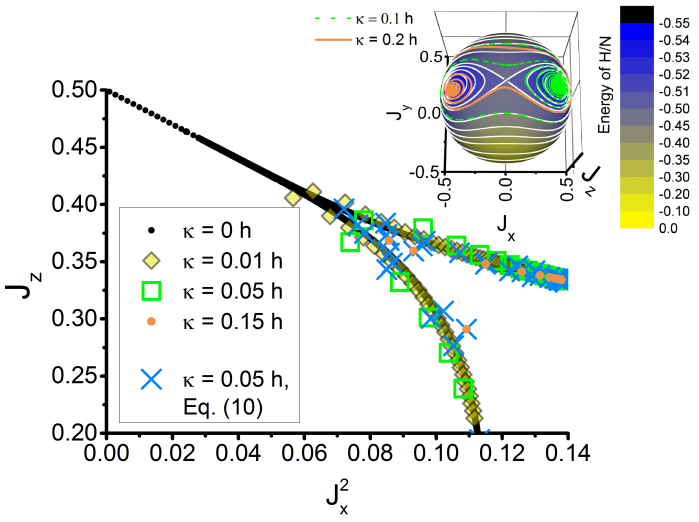

Figure 4.5.: The figure shows the smoothing impact of damping on the ESQPT signal for different κ values. The (blue) crosses show the averaging results using the integration method for $\Delta t = 20$. The ESQPT-signal under influence of damping gets smoothed. (Inset) Trajectories on the Bloch sphere visualize the system evolution, equation (4.13), for $\kappa = 0.1h$ (dashed green), $\kappa = 0.2h$ (orange) and $\kappa = 0$ (white contours). The color shows the rescaled energy in $\kappa = 0$ case. Parameters: $\gamma = 1.5h, \lambda = 0$. Taken from Ref. [Kop15a].

separatrix energy $E = -1/2N$ [Cap08], see gray line in Fig. 4.6. The period divergence is due to the saddle point in the energy landscape and is comparable with a movement of a particle in a double-well potential. If the particle has exact the energy of a local maximum, it need an infinity amount of time to reach it.

For $\kappa \neq 0$ the energy is not conserved any more and the system tends oscillating around the J_z-axis to a steady state Eq. (4.14). Fig. 4.5 (inset) shows two examples of the system state evolution $(J_x, J_y, J_z)(t)$ for two different κ values, which where obtained by solving semiclassical Eqs. (4.13) numerically. The ESQPT signal is now hidden in the dynamical evolution of the system. But, as we can see in Fig. 4.5, especially for big κ values there are only less paths, which are close to the separatrix, thus the ESQPT signal will be damped especially for big dissipation rates κ. The impact of damping to the ESQPT signal in the (J_z, J_x^2) plane can be obtained by calculating the mean values of $J_x^2(t), J_z(t)$-evolution for a period or by finding some optimal effective period Δt, in a way that the mean values calculated using the definition

$$\bar{O}(t) = \frac{1}{\Delta t} \int_{t=a}^{a+\Delta t} O(t)dt, \quad a \in \{0, T_{max}\}, \tag{4.16}$$

matches to the closed case as good as possible. In the first case, the results for different damping rates κ are shown in Fig. 4.5 by colored circles/diamonds and unfilled squares.

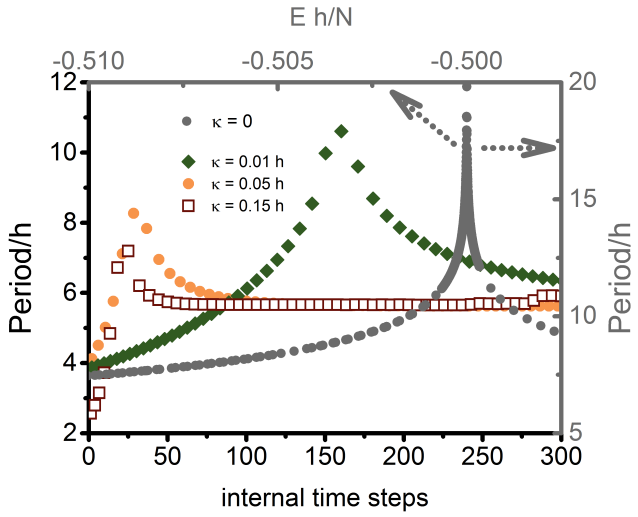

Figure 4.6.: A period as a function of energy or system evolution time for $\kappa = 0$ and $\kappa > 0$, respectively. Whereas without dissipation the period length diverge at the ESQPT energy, it has a local maximum for dissipative systems. Parameters: $\gamma = 1.5h, \lambda = 0$.

We see that the peak is now smoothed, but still visible especially for small damping rates. The blue crosses show the second case with effective period which lead to a much better ESQPT signal. Note, as a period length in the first case we take the time for one full rotation around the J_z-axis, which changes with time, see Fig. 4.6. Even for finite κ values (colored symbols), the period has a local maximum which smooths with increased dissipation. We have checked that the local maximum appears when the system crosses the separatrix line.

4.5. Pyragas Control of the ESQPT Signal

Now we set $\lambda \neq 0$ in $\gamma_x(t)$, Eq. (4.3) and investigate the impact of time-delayed control on the system.

4.5.1. Linear Stability Analysis with Time Delay

4.5.1.1. Characteristic Equation

A usual approach to analyze the effects of time-delayed feedback is first to check the stability of fixed points in the presence of control [HÖ5], a procedure is similar as in chapter 3. Therefore we linearize Eq. (4.13) around the fixed points $J_i(t) = J_i^0 + \delta J_i$, obtaining the following system of linearized equations with $\delta \mathbf{v} \equiv (\delta J_x, \delta J_y)^T$,

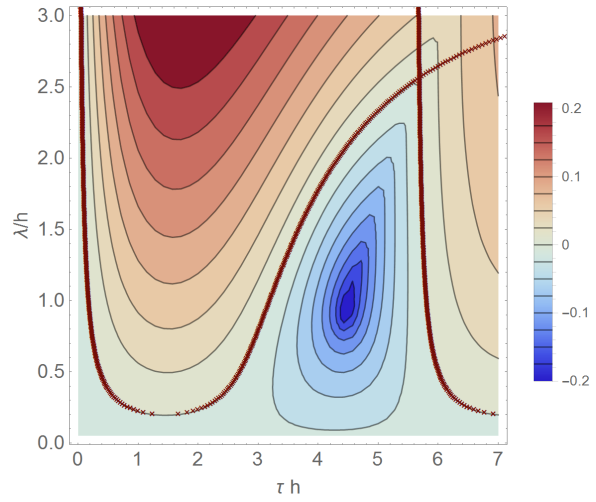

Figure 4.7.: Stability diagram in the $\tau - \lambda$-plane. The color represents the stability robustness of fixed points in the symmetry broken phase, which are not stable for positive values (red colored area). The brown line defines a boundary condition and has an analytical expression. Parameters: $\gamma = 1.5h, \kappa = 0.05h$. Taken from Ref. [Kop15a].

$$\partial_t \delta\mathbf{v}(t) = \mathbf{B} \cdot \delta\mathbf{v}(t) + \mathbf{A} \cdot \delta\mathbf{v}(t-\tau), \tag{4.17}$$

with

$$\mathbf{A} \equiv -4\lambda J_z^0 \begin{pmatrix} 0 & 0 \\ (J_x^0)^2 & J_x^0 J_y^0 \end{pmatrix},$$

$$\mathbf{B} \equiv \begin{pmatrix} \kappa\frac{(J_x^0)^2}{J_z^0} - \kappa J_z^0 & h + \kappa\frac{J_x^0 J_y^0}{J_z^0} \\ 4\lambda J_z^0 (J_x^0)^2 - 2\gamma\frac{(J_x^0)^2}{J_z^0} + \kappa\frac{J_y^0 J_x^0}{J_z^0} - h + 2\gamma J_z^0 & \kappa\frac{(J_y^0)^2}{J_z^0} + 4\lambda J_x^0 J_z^0 J_y^0 - 2\gamma\frac{J_x^0 J_y^0}{J_z^0} - \kappa J_z^0 \end{pmatrix},$$

with eliminated J_z component by use of the spin-length conservation law. The roots of the corresponding characteristic equation

$$\det(\Lambda\mathbf{1} - \mathbf{B} - \mathbf{A}\exp(-\Lambda\tau)) = 0 \tag{4.18}$$

determines the stability of a fixed point, which is stable if all real parts of all solutions Λ are negative [Sch08]. The main properties of this equation type were summarized in the previous chapter, see Sec. 3.2.4.2 for more details.

4.5.1.2. Stability Diagram

In Fig. 4.7 we plot the biggest real part of eigenvalues in the $\tau - \lambda-$ domain. We see that there is a window for λ -values, where the stability of fixed points oscillates from stable to unstable and from unstable to stable while increasing the time delay. Outside this window, the fixed points remains either stable ($\lambda \ll 1h$) or lose their stability

forever ($\lambda \gtrsim 2.5h$). In the stability window $3 \lesssim \tau \lesssim 6$ the eigenvalues are much more negative (dark blue color) than in case without control ($\tau \to 0$ or $\lambda = 0$, light blue color). The negativity of the eigenvalues mirrors the attraction power of fixed points, thus in the dark blue region the system converges faster to a fixed point in presence of control than without it - a feature which was also found in the previous chapter. Note that the boundaries between stable and unstable zones (brown line) can be calculated from an analytical expression, see next paragraph. In the next section we analyze the system properties in the unstable regime, use them to obtain a sharp ESQPT signal and show chaotic behavior for larger time delays τ.

4.5.1.3. Boundaries

To determine the boundaries in Fig. 4.7 we choose only imaginary Λ values in Eq. (4.18), thus $\Lambda \equiv i \cdot s, s \in \mathbb{R}$. Zero real part of the eigenvalue implicit that the the fixed point neither attract no push the linearized solution, which oscillates undamped then. Splitting then the Eq. (4.18) in an imaginary and real part, we obtain the correspondingly conditions

$$\begin{aligned}
0 &= G_0 + G_1 \cdot \cos(s\tau) + G_2 \cdot \sin(s\tau), \\
0 &= G_3 + G_4 \cdot \cos(s\tau) + G_5 \cdot \sin(s\tau), \\
G_0 &= -\frac{\kappa (J_x^0)^2 s}{J_z^0} + \frac{2\gamma J_x^0 J_y^0 s}{J_z^0} - 4J_x^0 J_y^0 J_z^0 \lambda s - \frac{\kappa (J_y^0)^2 s}{J_z^0} + 2\kappa J_z^0 s, \\
G_1 &= 4J_x^0 J_y^0 J_z^0 \lambda s, \quad G_2 = -4h(J_x^0)^2 J_z^0 \lambda - 4\kappa J_x^0 J_y^0 (J_z^0)^2 \lambda,
\end{aligned} \tag{4.19}$$

$$\begin{aligned}
G_3 &= h^2 - s^2 + \frac{2\gamma h (J_x^0)^2}{J_z^0} - 2\gamma h J_z^0 - \kappa^2 (J_x^0)^2 - \kappa^2 (J_y^0)^2 \\
&\quad + \kappa^2 (J_z^0)^2 - 4h(J_x^0)^2 J_z^0 \lambda - 4\kappa J_x^0 J_y^0 (J_z^0)^2 \lambda, \\
G_4 &= 4h(J_x^0)^2 J_z^0 \lambda + 4\kappa J_x^0 J_y^0 (J_z^0)^2 \lambda, \quad G_5 = 4J_x^0 J_y^0 J_z^0 \lambda s.
\end{aligned} \tag{4.20}$$

Bringing all sin and cos terms in both equations to one side, squaring them and adding together, we eliminate the τ-dependence and obtain the following equation

$$0 = s^4 + F_1 s^2 + F_0, \tag{4.21}$$

with

$$
\begin{aligned}
F_0 = \frac{1}{(J_z^0)^2}\Bigg\{ & \left(h^2 J_z^0 + 2\gamma h\left((J_x^0)^2 - (J_z^0)^2\right) + \kappa^2 J_z^0\left(-(J_x^0)^2 - (J_y^0)^2 + (J_z^0)^2\right)\right)\cdot \\
& \left(h^2 J_z^0 + 2h\left((J_x^0)^2\left(\gamma - 4(J_z^0)^2\lambda\right) - \gamma(J_z^0)^2\right)\right. \\
& \left. + \kappa J_z^0\left(-\kappa(J_x^0)^2 - 8J_x^0 J_y^0 (J_z^0)^2\lambda + \kappa\left((J_z^0)^2 - (J_y^0)^2\right)\right)\right)\Bigg\}, \\
F_1 = \frac{1}{(J_z^0)^2}\Bigg\{ & -2h^2(J_z^0)^2 + 4h\left((J_x^0)^2\left(2(J_z^0)^3\lambda - \gamma J_z^0\right) + \gamma(J_z^0)^3\right) \\
& + \kappa^2(J_x^0)^4 - 4\kappa(J_x^0)^3 J_y^0\left(\gamma - 2(J_z^0)^2\lambda\right) \\
& + 2(J_x^0)^2\left((J_y^0)^2\left(\kappa^2 + 2\gamma\left(\gamma - 4(J_z^0)^2\lambda\right)\right) - \kappa^2(J_z^0)^2\right) \\
& - 4\kappa J_x^0 J_y^0\left((J_y^0)^2\left(\gamma - 2(J_z^0)^2\lambda\right) + 2J_z^{0^4}\lambda - 2\gamma(J_z^0)^2\right) \\
& + \kappa^2\left((J_y^0)^4 - 2(J_y^0)^2(J_z^0)^2 + 2(J_z^0)^4\right)\Bigg\},
\end{aligned}
$$

which can be solved for s and has then in general 4 different solutions

$$
s = \pm\frac{1}{\sqrt{2}}\sqrt{-F_1 \pm \sqrt{F_1^2 - 4\cdot F_0}}. \tag{4.22}
$$

The equation (4.22) fixes now the eigenvalue $\Lambda = is$ for a given fixed point and feedback strength λ. Eq. (4.19) gives for every fixed s-value the corresponding time-delay τ, solving for example the imaginary part for τ we obtain

$$
\tau = \frac{1}{s}\arctan\left(\frac{\frac{\pm\frac{G_1\sqrt{-G_2^2\left(G_0^2-G_1^2-G_2^2\right)}}{G_1^2+G_2^2} + \frac{G_0 G_1^2}{G_1^2+G_2^2} - G_0}{G_2}}{\frac{\pm\sqrt{-G_0^2G_2^2+G_1^2G_2^2+G_2^4} - G_0G_1}{G_1^2+G_2^2}}\right) + \frac{2\pi}{s}\cdot z, \tag{4.23}
$$

where $z \in \mathbb{Z}$. The choice of z is necessary to get boundary conditions at higher time delays τ. Note that the s dependence is also hidden in G_i. At this step we have still to much solutions. A lot of them are non-physical (if $\tau < 0$ or $\tau \in \mathbb{C}$) or do not fulfill the real part equation (4.19) and have to be sorted out. The remaining solutions are plotted as a brown line in Fig. 4.7.

4.5.1.4. Auxiliary Remarks

The linearization procedure is similar as in the previous chapter, see Sec. 3.2.4. Nevertheless, we want to give some additional comments regarding the derivation of Eq. (4.17).

- The coupling γ_x contains the time-delayed $J_z(t-\tau)$ value. The linearization ansatz has in this case time-delayed fluctuation, e.g. $J_z(t-\tau) = J_z^0 + \delta J_z(t-\tau)$. Note, the fixed point J_z^0 is time delay independent.
- The products of fluctuations are neglected by the linearization assumption.
- The conservation of the spin length j allows to eliminate one of the fluctuations terms, in Eq. (4.17) δJ_z is eliminated, see Sec. 3.2.4 for more details.
- The characteristic equation is derived by an exponential ansatz for the fluctuations $\delta\mathbf{v}(t) \sim e^{-\Lambda t}, \Lambda \in \mathcal{C}$.
- The linearization assumption is valid close the fixed point in a sense that the impact of other system attractors can be neglected.
- The characteristic equation has in general infinite many number of roots Λ. We solve this equation numerically for a big amount of different initial condition in order to determine the root with the biggest real part. This is usually possible, despite the infinite number of the roots, as they are located at branches, see Chapter 3 for more information.

4.5.2. Feedback Compensates Dissipation

Our feedback scheme (Eq. (4.3)) modifies the system dynamics in an interesting and unexpected way. Increasing the time delay τ, we cross the boundary and make the fixed point unstable. Figure 4.8 demonstrates the feedback action, showing the trajectory evolution for different values of τ. The red (thick) curve shows the stationary state. For smaller τ values the trajectory ends in a new stable state in form of a limit cycle, thus a Hopf bifurcation occurs. Moreover the trajectory of the limit cycle has only small deviations from paths with fixed energy, which the LMG system would take without dissipation. As we can take from Fig. 4.8, the size of trajectories can be changed by τ, thus tuning the time delay value corresponds to a change of energy in a closed LMG system. In Fig. 4.8 we used initial condition close to the fixed point which is in the left part of the separatrix. Due to the symmetry of Eq. (4.13) $J_x \to -J_x$, another limit cycle exists in the right part of the separatrix which attracts if we choose the initial condition close to the second fixed point. Note, starting in the region outside the separatrix leads to the same stationary state or to the correspondent stationary state in the other Bloch half sphere for the considered τ values.

Thus, using the stationary limit cycle states for fixed τ values offers a possibility to obtain an ESQPT-Signal again, by calculating the

$$\bar{J}_z = \frac{1}{t_2 - t_1} \int_{t_1}^{t_2} J_z(t) dt \tag{4.24}$$

and

$$\bar{J}_x^2 = \frac{1}{t_2 - t_1} \int_{t_1}^{t_2} J_x(t)^2 dt \tag{4.25}$$

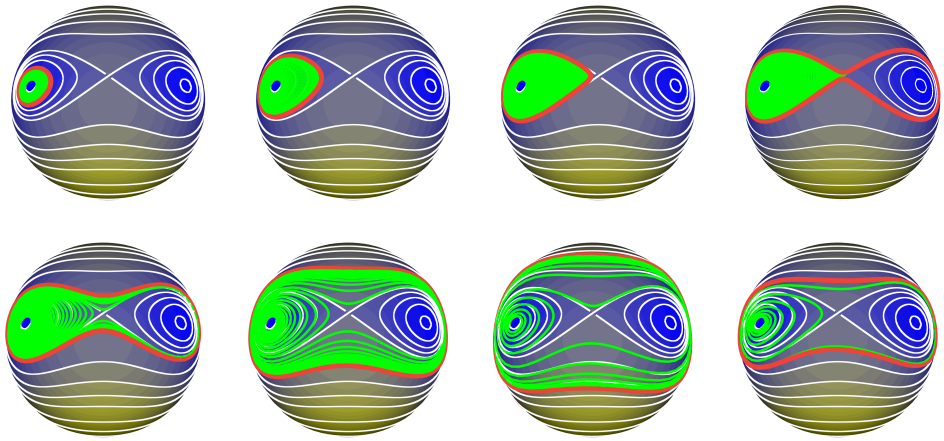

Figure 4.8.: Dynamical evolution of the controlled LMG system on the Bloch sphere for the following τ-values (from left to right): $\tau h = 0.2; 0.25; 0.3; 0.31$ (upper); 0.35; 0.5; 1; 2.5 (lower); The red thick path represents the stationary state. Increase of τ forces the solution to cross the separatrix. In this way the ESQPT signal (Fig. 4.9) is restored from stationary solutions with different τ values. Note, the axes and scaling are as in the inset of figure 4.5 but are not visible due to breakdown. Parameters: $\gamma = 1.5h, \lambda = 1, \kappa = 0.05h$. Taken from Ref. [Kop15a].

averages for fixed values of τ ($t_2 > t_1$ and with t_1 big enough to become a stationary solution). Figure 4.9 shows the results of this calculation and compares them with the closed and dissipative cases without feedback. The (orange) rhombi shows the $(\bar{J}_z, \bar{J}_x^2)$ time averages in stationary limit cycle phase of the dissipative LMG system, the black curve shows the ESQPT-signal of a closed system without control. Each rhombus has its own time delay and corresponds to a limit cycle with special size. We see a very good overlap between the control caused and the original signals, thus our feedback schema compensates the dissipative smoothing (unfilled green squares) of the ESQPT-signal very well. Fig. 4.10 shows the τ-dependence of the averaged values (solid lines). Up to $\tau \approx 0.2/h$ the fixed point is stable and the averaged values are the values of the fixed point. For $\tau \gtrsim 0.2/h$ this dependency is qualitatively the same as the energy dependency of the corresponding expectation values in eigenstates with the energy E in the closed system without time delay, see dotted lines in the same figure. However, a direct comparison between the energy and τ representation might not be applicable, as there is no direct linear correspondence between the both scales. To overlay them, one could try to stretch and linear resize the τ or the energy axis manually, which would give rather similar curves. To get a better overlay, one has to resize different areas of the x-axis by different factors. That's why, the τ or energy independent representation which is generated from the data shown in the Fig. 4.10 and plotted in Fig. 4.9 is much better suitable for comparison of the goodness between different data.

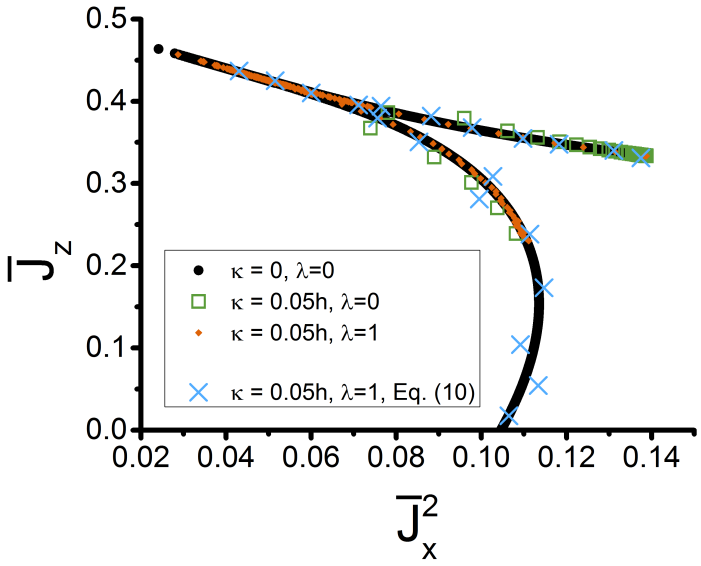

Figure 4.9.: (a) Time delayed feedback undo the dissipative effects to the ESQPT signal. The orange (light-colored)rhombus shows averaged system values $\bar{J}_z, \bar{J}_x^2$ in the stationary state for fixed τ with $\tau \in [0.1, 0.6]h$, which matches to the signal of the closed system (black curve) very well. Unfilled squares represent the ESQPT-signal under dissipation. The blue crosses shows the ESQPT-signal obtain from a dynamical evolution of the system for one big τ-value using Eq. (4.24). Parameters: $\gamma = 1.5h, \lambda = 1h$. Taken from Ref. [Kop15a].

4.5.3. Chaotic Behaviour

For $\tau \gg 1$ the stationary dynamics can become much more complex than just limit cycles. Oscillations with more than one maximum and minimum appear, which is known as a way to chaos by period doubling [Str01, Hoh99]. In Fig. 4.11 (left) we plot all local maxima and minima between which $J_x(t)$ can oscillate in the stationary state (for $t \gg 1$) for fixed values of time delay τ. Note that the steady state of the system can depend on the initial condition, too, which has to be changed, to get all possible end states. First, we show an example how to obtain the data-points which are located on the vertical dash-dotted line in the bifurcation diagram. Figure 4.11 (right) shows possible end states of the system in the (J_x, J_y) plane for different initial conditions. The maxima and minima of the J_x oscillation (arrows) are lying on the dash-dotted line in the bifurcation diagram. Next, we discuss the systems dynamic as a function of τ, therefore we mark different areas in the bifurcation diagram by capital letters A-E. In the inset we show a zoom for the area A, which contains three parts A1-A3. Increasing τ from zero, both stable fixed points (arrow, orange line, part A1) loses their stability (orange dotted line, part A2) at the first boundary condition in Fig. 4.7 and a Hopf-bifurcation appears (part A). There are two limit cycle possible, for positive and negative J_x values, however both limit cycles grow with τ and merge

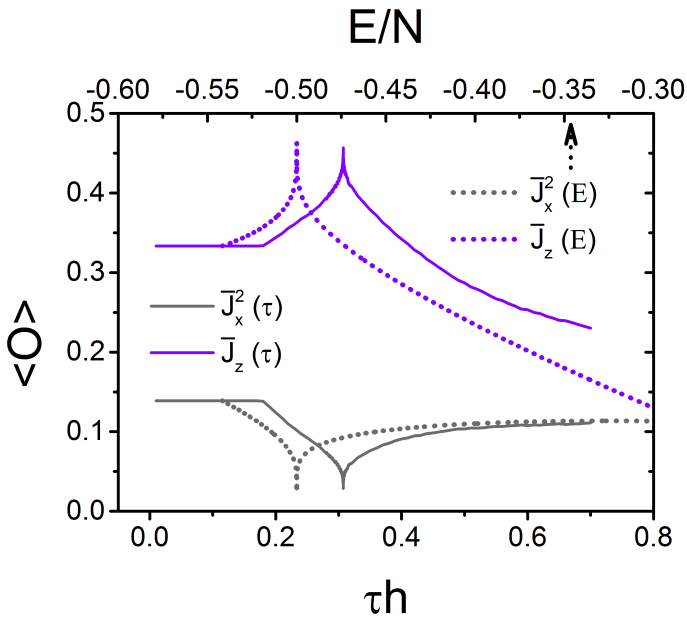

Figure 4.10.: (a) $\bar{J}_z, \bar{J}_x^2$ as a function of τ in a steady state (solid) and for comparison the dependency of the same averages as a function of energy in a closed LMG system (dotted). Please note the different scaling of the upper and lower x-axis. We see that the corresponding averages are qualitatively similar. Parameters: $\gamma = 1.5h, \lambda = 1h$.

to one big limit cycle which covers both J_x sides on the Bloch sphere, part A3 (see also Fig. 4.8 for visualization). In part B, the fixed points become stable again. But there exist still a stable limit cycle solution with rather big J_x-amplitude. Thus, in area B two stable solutions are possible, which is not in contradiction to the stability of the fixed point, as the initial condition is not chosen in a way to fulfill the linearized assumption. The system will then converge either to the fixed point or to the limit cycle, depending on the initial condition. For $4 \lesssim \tau \lesssim 5$ this limit cycle disappears. Further increase of time delay leads to a creation of a period doubling structure (area C), which is separated by windows where the solution converges to a limit cycle. In the region D the fixed point becomes stable again and the double period structure is gone, whereas in the Region E it appears again. Note that the dotted line at $J_x^{\max} = 0$ represents the unstable trivial fixed point.

Such chaotic behavior can also be used to obtain the ESQPT signal, see blue crosses in Fig. 4.9. Fixing the time delay in the chaotic area of the bifurcation diagram (Fig. 4.11, left), one can use the integration method with effective period (Eq. (4.16)) to obtain the shown curve. Therefore we solve the corresponding equation of motion (4.13) and use Eq. (4.16) starting from $t = 0$ till $t \gg 1$. We see that also this result matches pretty well with the original ESQPT signal.

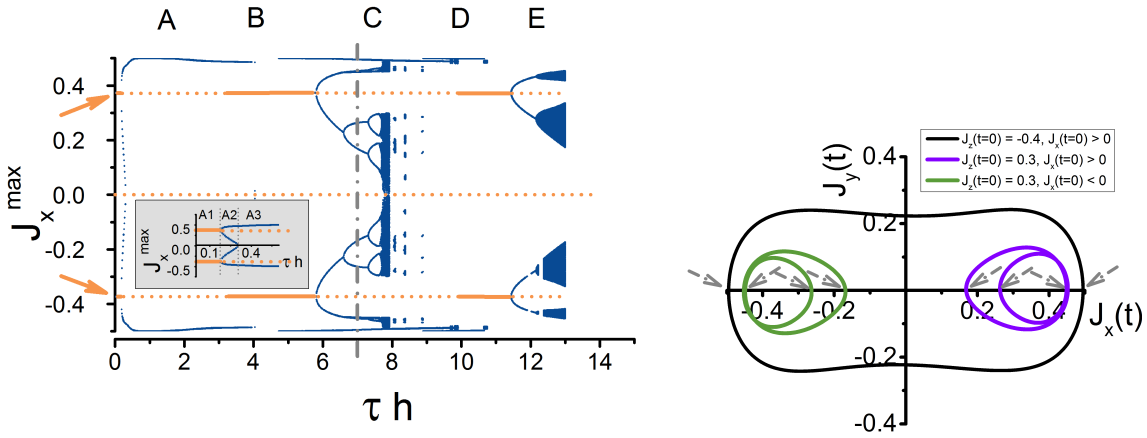

Figure 4.11.: (left) Bifurcation and period doubling for different time delays τ. For each τ-values the values of local maxima and minima of $J_x(t)$-value are plotted in stationary case. The dashed orange lines shows the unstable fixed points. The arrows points to the non-trivial fixed points. The phase diagram is divided the regions A-E with different properties. The inset shows shows a zoom of area A which contains three Areas A1-A3 with different dynamic. (right) Steady state of the system for $\tau h = 7$ and different initial condition in the (J_x, J_y) plane. The maxima and minima of J_x oscillations (dash-dotted arrows) are shown in the bifurcation diagram (left) and are located at a vertical dash-dotted line. Parameters: $\gamma = 1.5h, \lambda = 1h$. Taken from Ref. [Kop15a].

4.6. Discussion

In this paper we have demonstrated the effect of dissipation on the ESQPT signal for the LMG model and showed how to compensate it using time-delayed Pyragas feedback modulating the interaction parameter between the atoms. Our results show that the ESQPT is encoded in the spectral properties of the effective Hamiltonian as well as it is visible in the measured averaged values of the spin components. In the last case, smoothing effects appear which can be undone by our feedback scheme.

We think that an experimental measurement of an ESQPT signal using the time-delayed method is easier than in an ideal, closed system. Using time delay one has only to measure the system values for different time delays τ, instead of preparing the system in eigenstates or coherent superpositions to obtain the same information [Eng15].

We also checked the interaction strength γ_x depending on other operator differences instead of J_z^2, or a modulated magnetic field h instead of γ_x. However, in both cases the general dynamical properties remains the same. The LMG system has still limit cycles close to the separatrix for some fixed time-delayed values and has a parameter range with chaotic behavior. Both effects might be interesting from an experimental point of view. On the one hand, it is easier to control the magnetic field h, on the

other hand, choosing another feedback loop can shift the appearing effects to other τ values, which could be easier to realize.

We also tried to find ESQPT signatures in the correlation function [Car09] $C_t(z) \equiv \left\langle \hat{J}^+(t+z)\hat{J}^-(t) \right\rangle$, which we have calculated using the quantum regression theorem [Sch14a] and in a waiting time distribution $w(z)$. A correlation function of type $C_t(z)$ shows maxima in the Fourier space (the width of which scales with the dissipation rate κ) at the energy differences between a reference level (which is set by an initial condition) and two neighbouring levels. Thus, the vanishing level spacing around the ESQPT should lead to a peak of a correlation function around the zero value in frequency space. This peak is usually accompanied then by two additional peaks. The macroscopic occupation always leads to an offset of a correlation function $C_t(z)$ as a function of z which results in a peak at the origin in the Fourier space. Furthermore, the energies below the ESQPT energy are degenerated, this property is also accountable for a peak at the origin, if the corresponding energies are not negligible in the initial condition. Due to these disruptive effects, we have not found the ESQPT signal in the correlation function. However one possible way to detect the ESQPT in the correlation function could be to drive the LMG system additionally with an external laser and calculate the resonance fluorescence spectrum. This would require a re-derivation of the master equation under the effect of additional driving. Note that such spectra have been already calculated for an LMG system, but only in the linearized version [Mor08a].

The waiting time distribution $w(z)$ shows oscillations in the normal phase which frequency can be linked to the energy difference of two levels which are energetically the closest ones to the ground state. In the symmetry broken regime this oscillations are absent. However, we could not find any signatures of the ESQPT. We subscribe the absence of any signatures to the structure of the density matrix in the steady state which is used for calculation of waiting times. The density matrix contains only information about the first two levels with the lowest energy, which is not enough to get into the ESQPT region.

Similar to the Dicke model with feedback in the previous chapter, the Pyragas controlled LMG model has stable limit cycle phases. In contrast to the Dicke model, it shows chaotic dynamics for bigger time delay. This is surprisingly as one would expect such behavior especially from the Dicke system, which is chaotic in nature [Ema03a]. However, the Dicke model has an additional bosonic mode which is not bounded by a conservation law like the spin components. This could be a reason, why no chaotic behavior appears there.

We think that the feedback-induced limit cycles are a hidden property of the LMG model. On the one hand limit cycles are a natural property of the closed system. On the other hand, the time dependent limit cycles describe the ESQPT signal pretty well. Though the chaotic behavior is an artefact of the time delay feedback, as it was neither a part of a closed LMG system.

The feedback scheme is applied at a semiclassical level, thus we have neglected the influence of fluctuations in the thermodynamic limit, which could be important

[Nag11]. Nevertheless, we think that the fluctuations have not dramatic contributions to the described effects for $N \gg 1$ as they should scale with $1/\sqrt{N}$ and the used feedback scheme does not modify γ in a strong way. Furthermore, the semiclassical LMG model predicts in many cases the same results [PF11b, Bra13, Eng15]. But the full quantum version of the considered feedback type still remains an open issue. However, a recently published article [Gri15] shows a way to go beyond mean field for a coherent type of feedback where the author describes feedback action via mapping to a bigger system. This would be one possible way to study the role of oscillations in quantum systems with one special feedback type.

4.7. Summary

In this chapter we investigated the properties of the ESQPT signal in the open Lipkin-Meshkov-Glick model which is described by the master equation

$$\dot{\hat{\rho}} = -i[\hat{H}, \hat{\rho}] - \frac{\kappa}{2N}\mathcal{D}[\hat{J}^+]\hat{\rho},$$

with the Hamiltonian

$$\hat{H} = -h\hat{J}_z - \frac{\gamma_x}{N}\hat{J}_x^2 - \frac{\gamma_y}{N}\hat{J}_y^2,$$

and the Lindblad dissipator $\mathcal{D}$.

We found that the ESQPT signal is still imprinted in the spectral properties of the non-hermitian Hamiltonian $H_{eff} = H - i\frac{\kappa}{2N}J^-J^+$. It is directly visible in its - due to dissipation - complex spectrum as a cusp Υ or as logarithmic divergence in the density of states, see Fig. 4.1. On the mean-field level the ESQPT signal is hidden in the dynamical evolution of system observables. But the signal is smoothed especially for big dissipation rates κ. To cancel the dissipative effects we introduce a time-delayed feedback control of Pyragas form

$$\gamma_x = \gamma_x(t) = \gamma + \frac{\lambda}{N^2}\left[\left\langle \hat{J}_z(t-\tau)\right\rangle^2 - \left\langle \hat{J}_z(t)\right\rangle^2\right].$$

For a certain time-delay parameters τ this feedback scheme creates a new non-equilibrium steady states in form of the limit cycles for finite dissipation rates κ. The corresponding limit-cycle paths for finite τ values are very close to the paths with fixed energy in the closed version of the LMG model. Moreover, the size of the limit cycle can be tuned by τ. In this way the limit cycles can cross the the separatrix on the semiclassical energy sphere which is responsible for the ESQPT signal. Calculations of averaged values for different τ parameters show that the ESQPT signal is restored by time-delayed feedback, see Fig. 4.9.

5. Dissipative Two-Mode Tavis-Cummings Model with Time-Delayed Feedback Control

This chapter is mainly based on the results published in Ref. [Kop15c].

5.1. Introduction

Lasers build one of the key technologies in the current world as their rich dynamical behavior and high degree of control establish a solid basis for a wide range of applications [Sie86]. Especially, time-delayed feedback control [Jus09] can effectively manipulate short and long time behavior of a laser system [Sch12]. Typical examples are the control of laser bistability [Mas07], chaos, and noise [Kik97] as well as the manipulation of the laser emission [Hop13, Sch14b].

A common description of the controlled laser dynamics, particularly in the case of a quantum dot laser, is based on the semi-classical rate equations known as the Lang-Kobayashi model [Lan80]. It provides good agreement with the experiments if the photon output power is high enough [Sor13]. However, there exists a more general microscopic quantum treatment [Sar78, Hak84], which describes successfully the photon statistics of laser light. It turned out that this microscopic laser theory also represents an essential ingredient for describing the Bose-Einstein condensation of photons [Kir13] which has been realized in dye filled microcavities in a seminal experiment in Bonn [Kla10] and recently also in London [Mar15]. Both lasing transition and Bose-Einstein condensation of light may appear in such systems under appropriate conditions, although the former reveals non-equilibrium physics, whereas the latter represents an equilibrium phenomenon. For low cavity losses and above the external pumping threshold, the modes of the cavity become thermally populated according to a Bose-Einstein distribution with the macroscopically occupied lowest mode [Kla12]. However, for higher cavity losses the system behavior switches to be laser-like, where one of the excited cavity modes becomes macroscopically occupied and all thermal properties are lost [Kir15].

Here we work out a two-mode laser model which allows to study under which conditions one of the two cavity modes becomes macroscopically occupied. To this end we extend the Tavis-Cummings model and consider N non-interacting two-level atoms in a two-mode optical cavity with incoherent pumping and decay channels. Starting from a quantum master equation for the density operator we apply a mean-field ap-

proximation and determine the equations of motion for the statistical averages of the respective system operators in the thermodynamic limit. We find an analytical solution for the steady states and obtain the resulting complex phase diagram. Under proper conditions, either the lower or the excited cavity mode can become macroscopically occupied. Hence, our model can be seen as a minimalistic precursor of the detailed model of photon condensation [Kir13, Kir15]. In this sense, the former case could be referred as condensate-like and the latter case as laser-like state of light, although a direct analogy is not applicable due to the absence of the temperature scale in our simplified approach. The richness of possible phases even within this reduced model indicates that the inclusion of realistic processes, like the thermalization via phonon dressing of the absorption and emission of the emitters, can potentially lead to an even larger variety of states.

Additionally, we design different feedback control schemes to stabilize or to select one of the two radiating modes. The two-mode laser, also known as two-color laser, with feedback was already studied both experimentally [Nad10, Vir14] and theoretically [Vir13]. However, these studies within the Lang-Koboyashi model were focused on switching between the two modes using a non-Pyragas feedback type. In contrast to that we apply here the Pyragas type of feedback that was originally designed to prevent chaos by stabilizing an unstable periodic orbit [Pyr92]. It is generally known as a powerful tool to change the stability of stationary states without modifying them. This is due to the fact that the feedback control term vanishes in the stationary state since it is proportional to the difference of the system observable at two times $t - \tau$ and t [H05, Kop15b], see Sec. 2.1 for more details .

This chapter is is structured as follows. In section 5.2 we introduce the underlying model and apply a mean-field approximation in the thermodynamic limit. In section 5.3 we calculate the fixed points, investigate their stability, and discuss the resulting phase diagram. In section 5.4 we suggest several Pyragas feedback control schemes to stabilize the unstable mode or to select the mode of interest. Section 5.5 contains the summary of the obtained results with a short outlook.

5.2. Model

We consider N non-interacting two-level atoms inside a two-mode cavity. The light-atom interaction is assumed to be of the Jaynes-Cummings type [Scu97]. Thus, the total Hamiltonian of the system is

$$\hat{H} = \sum_{i=1}^{2} \omega_i \hat{a}_i^\dagger \hat{a}_i + \Delta \hat{J}_z + \frac{g}{\sqrt{N}} \sum_{i=1}^{2} (\hat{a}_i \hat{J}^+ + \hat{a}_i^\dagger \hat{J}^-) \tag{5.1}$$

and represents an extension of the Tavis-Cummings (TC) model [Tav68, Nar73] from one to two modes. Here, we put $\hbar = 1$ and $\hat{a}_i^{(\dagger)}$ $(i \in \{1, 2\})$ is a ladder algebra of the first/second cavity mode with frequency $\omega_{1,2}$, where we assume $\omega_1 < \omega_2$ without loss of generality. The collective angular momentum operators are given by the sums $\hat{J}_z = \frac{1}{2} \sum_{k=1}^{N} \sigma_k^z$ and $\hat{J}^\pm = \sum_{k=1}^{N} \sigma_k^\pm$ over all Pauli matrices of each two-level atom with

energy level-splitting Δ. The population inversion of the atomic ensemble is directly related to $\hat{J}_z$, while its dipole moment can be expressed in terms of $\hat{J}^{\pm}$. The coupling between the atoms and the optical mode assumes rotating wave approximation (RWA) and has the strength $g/\sqrt{N}$ that is taken to be the same for both modes. In spite of RWA, the TC model for large values of g has its own physical relevance since it can be experimentally realized in an ingenious setup using Raman transitions [Bad14].

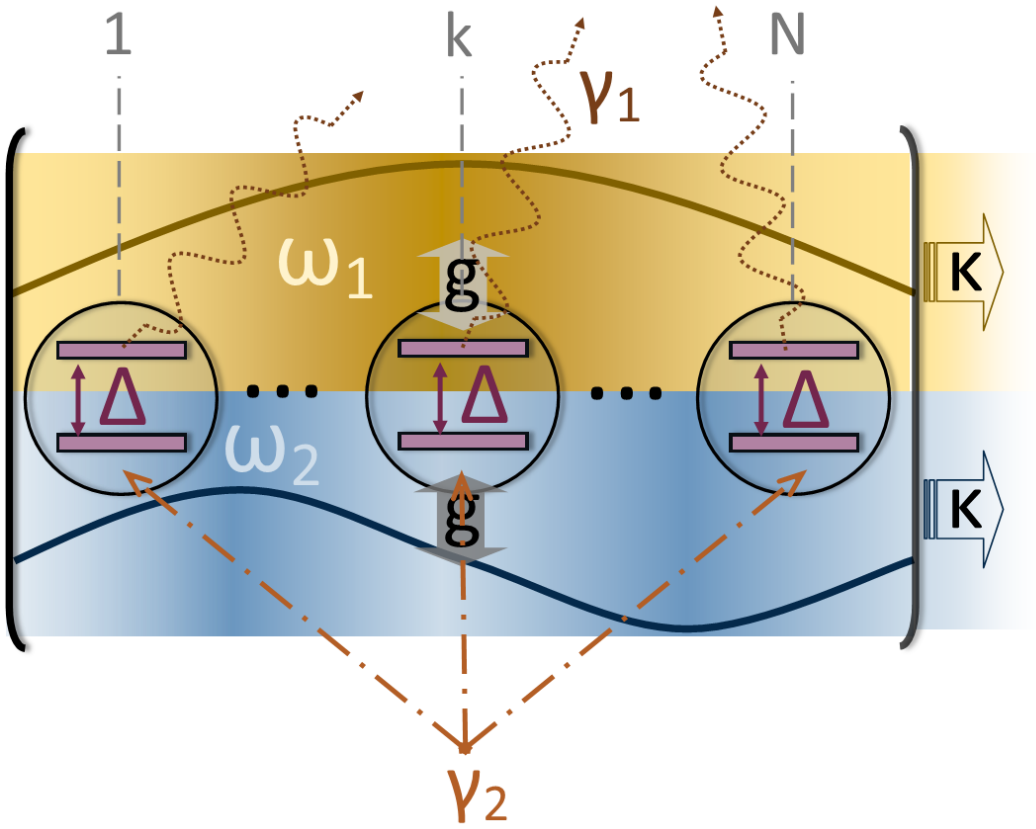

Figure 5.1.: Visualization of the used extended TC model with two different cavity modes with frequencies ω_1 and ω_2 and a decay rate κ to the environment. Δ is the atomic detuning, γ_1 and γ_2 are the pumping and losses of the atomic system, respectively. Coupling g is the field-atom-interaction strength and is assumed to be the same for both modes. N is the number of atoms in the cavity.

To generate a lasing behavior and the interesting dynamics we add decay channels and incoherent pumping to the system. We note in passing that the two-mode Jaynes-Cummings models were studied in the past either with mode degeneracy and without/with dissipation or without both mode degeneracy and dissipation [Mun10, Pra11, Wic13, Ema13a, Fan14]. Following Ref. [Chi14], we couple our system to three different baths. Both cavity fields are damped by coupling them to a zero temperature bath of harmonic modes with the characteristic decay rate κ, while the atomic system

radiates into the non-cavity modes with a rate γ_1. Additionally, the atomic system is incoherently pumped with a rate γ_2. Pumping can be formally described as coupling the atomic system to a bath of inverted harmonic oscillators [Gar04]. All these effects are captured by the following Markovian master equation of Lindblad type for the density operator $\hat{\rho}$

$$\frac{d\hat{\rho}(t)}{dt} = -i[\hat{H},\hat{\rho}] - \kappa\mathcal{L}[\hat{a}_1]\hat{\rho} - \kappa\mathcal{L}[\hat{a}_2]\hat{\rho} - \frac{\gamma_2}{2}\sum_{k=1}^{N}\mathcal{L}[\hat{\sigma}_k^+]\hat{\rho} - \frac{\gamma_1}{2}\sum_{k=1}^{N}\mathcal{L}[\hat{\sigma}_k^-]\hat{\rho},$$

with the Lindblad operator $\mathcal{L}[\hat{x}]\hat{\rho} = \hat{x}^\dagger\hat{x}\hat{\rho} + \hat{\rho}\hat{x}^\dagger\hat{x} - 2\hat{x}\hat{\rho}\hat{x}^\dagger$. Pumping effectively occurs provided that $\gamma_2 > \gamma_1$. Fig. 5.1 visualizes the model.

The dynamics of the statistical average $\left\langle \hat{A} \right\rangle = \mathrm{Tr}(\hat{A}\hat{\rho})$ of an arbitrary system operator $\hat{A}$ is described by $d\left\langle \hat{A} \right\rangle/dt = \mathrm{Tr}(\hat{A}\dot{\hat{\rho}})$. To obtain a closed set of semi-classical equations, we factorize the averages of operator products as $\left\langle \hat{A}_1\hat{A}_2 \right\rangle \approx \left\langle \hat{A}_1 \right\rangle \left\langle \hat{A}_2 \right\rangle$ and perform the thermodynamic limit where the number N of two-level atoms tends to infinity [Rib07, Bha12, Eng15], yielding the underlying mean-field equations of the two-mode laser model

$$\dot{a}_1 = (-\kappa - i\omega_1)a_1 - igJ^-, \quad \dot{a}_1^* = (-\kappa + i\omega_1)a_1^* + igJ^+, \tag{5.2a}$$
$$\dot{a}_2 = (-\kappa - i\omega_2)a_2 - igJ^-, \quad \dot{a}_2^* = (-\kappa + i\omega_2)a_2^* + igJ^+, \tag{5.2b}$$
$$\dot{J}^- = (-\Gamma_\downarrow - i\Delta)J^- + 2ig(a_1 + a_2)J_z, \tag{5.2c}$$
$$\dot{J}^+ = (-\Gamma_\downarrow + i\Delta)J^+ - 2ig(a_1^* + a_2^*)J_z, \tag{5.2d}$$
$$\dot{J}_z = \Gamma_\uparrow(z_0 - J_z) + ig(a_1^* + a_2^*)J^- - ig(a_1 + a_2)J^+, \tag{5.2e}$$

where $\Gamma_\uparrow = 2\Gamma_\downarrow = \gamma_1 + \gamma_2$, and $z_0 = \frac{\gamma_2 - \gamma_1}{2(\gamma_2 + \gamma_1)}$. Note that, by definition, one has $-1/2 \leq z_0 \leq 1/2$. Here we denote the operator averages appropriately rescaled in the thermodynamic limit by corresponding symbols without hat, i.e., $J^\pm \equiv \left\langle \hat{J}^\pm \right\rangle/N$, $J_z \equiv \left\langle \hat{J}_z \right\rangle/N$ and $a_{1,2}^{(*)} \equiv \left\langle \hat{a}_{1,2}^{(\dagger)} \right\rangle/\sqrt{N}$, where asterisk denotes complex conjugation. Note that $J^- = (J^+)^*$ and J_z is a real quantity.

In the one-mode limit, the corresponding equations similar to (5.2) represent a common example of a laser model. For the critical value of $g_\mathrm{c} = \left\{ \frac{\kappa\Gamma_\downarrow}{2z_0}\left[1 + \frac{(\omega-\Delta)^2}{(\kappa+\Gamma_\downarrow)^2}\right]\right\}^{1/2}$ the optical mode becomes macroscopically occupied, i.e., a phase transition occurs from a non-lasing to a lasing state. In the limit of vanishing atomic pumping and losses, i.e. $\Gamma_\uparrow \to 0$, Eqs. (5.2) describe the quantum phase transition in the Dicke model with RWA from a normal to a superradiant phase [Ema03a, Hay11, Bha12, BM14b]. Thus, the presence of the two modes and the pumping term allows the generation of a much more complicated dynamics, as either of the two modes can be macroscopically occupied. Moreover, we can influence the dynamical evolution of the system by applying different Pyragas time delay schemes, which allows to stabilize or destabilize the modes and to select the transition type.

5.3. Dynamics without Feedback

Equations (5.2) describe the dynamical evolution of the two-mode system depending on decay rates and pumping strength. Steady state of these equations can be either a stable fixed point or an oscillating state , i.e. a limit cycle. In the following we provide an analytical description of the possible steady states.

5.3.1. Steady States

The system (5.2) has a trivial fixed point $a_1^0 = a_2^0 = (a_1^*)^0 = (a_2^*)^0 = 0$, $(J^+)^0 = (J^-)^0 = 0$, and $J_z^0 = z_0$, where no cavity mode is occupied and the atomic ensemble has a stationary population inversion with zero dipole moment. Due to the $U(1)$ symmetry of the equations (5.2), there also exist non-trivial solutions that can oscillate in time with some characteristic frequency, so that the observables, like the mode occupation $a_1^* a_1$, reach a fixed value. To find such steady state solutions, we have to determine the frame where also $a_{1,2}^{(*)}$, and $J^\pm$ reach a fixed value. Therefore, we switch into a frame rotating with frequency ω, which has to be determined, i.e. we put $a_i \to a_i e^{-i\omega t}$, $a_i^* \to a_i^* e^{i\omega t}$, $J^\pm \to J^\pm e^{\pm i\omega t}$. Note that this transformation shifts the natural frequencies of both the cavity modes and the atoms by ω, i.e.,

$$\omega_i \to \omega_i - \omega \equiv \omega_{i,s},\ \Delta \to \Delta - \omega \equiv \Delta_s, \tag{5.3}$$

but does not change the observables like $a_1^* a_1$. Setting $\dot{a}_{1,2}^{(*)}$ in the transformed equations (5.2a-d) to zero, we can express these cavity quantities in terms of $J^\pm$. Next, setting $\dot{J}^\pm$ to zero in the transformed equations (5.2e,f) with the cavity quantities being eliminated, we find the requirement

$$0 \overset{!}{=} J^\pm \Big\{ \pm 2g^2 J_z \big[\mp 2\kappa + i(\omega_{1,s} + \omega_{2,s}) \big] + (\Gamma_\downarrow \mp i\Delta_s)(\kappa \mp i\omega_{1,s})(\kappa \mp i\omega_{2,s}) \Big\}. \tag{5.4}$$

For $J^\pm \overset{!}{\neq} 0$ the previous equation determines the value of the stationary atomic inversion

$$J_z^0 = \frac{(\Gamma_\downarrow - i\Delta_s)(\kappa - i\omega_{1,s})(\kappa - i\omega_{2,s})}{2g^2(2\kappa - i\omega_{1,s} - i\omega_{2,s})}. \tag{5.5}$$

However, since J_z^0 has to be real on physical grounds, its imaginary part has to be zero. This condition enforces the characteristic frequency ω to solve the equation

$$\Gamma_\downarrow(\omega_{1,s} + \omega_{2,s}) \left(\kappa^2 + \omega_{1,s}\omega_{2,s}\right) + \kappa\Delta_s \left(2\kappa^2 + \omega_{1,s}^2 + \omega_{2,s}^2\right) = 0. \tag{5.6}$$

Note that, due to Eq. (5.3), (5.6) is a cubic equation in ω and has up to 3 real solutions. For each real solution ω, the real part of the expression for J_z^0 in (5.5) gives the steady state expectation value

$$J_z^0 = \frac{\kappa(\Gamma_\downarrow^2 + \Delta_s^2) \left(2\kappa^2 + \omega_{1,s}^2 + \omega_{2,s}^2\right)}{2g^2\Gamma_\downarrow \left[4\kappa^2 + (\omega_{1,s} + \omega_{2,s})^2\right]}. \tag{5.7}$$

The remaining transformed equation (5.2g) can be solved for J^+J^- in the steady state, yielding

$$(J^+J^-)^0 = \frac{\Gamma_\uparrow(z_0 - J_z^0)\left(\kappa^2 + \omega_{1,s}^2\right)\left(\kappa^2 + \omega_{2,s}^2\right)}{2g^2\kappa\left(2\kappa^2 + \omega_{1,s}^2 + \omega_{2,s}^2\right)}. \tag{5.8}$$

Since J^+J^- has to be positive, the obtained steady state values are physical iff $J_z^0 \leq z_0$. If that is the case, the previous equation fixes $J^\pm$ up to the phase factor. Therefore, we may choose $(J^+)^0 = (J^-)^0 = \sqrt{(J^+J^-)^0}$ as a steady state expectation. Finally, the corresponding expressions for a_i^0 and $(a_i^*)^0$ ($i \in \{1,2\}$) in terms of $(J^\pm)^0$ follow from their transformed equations

$$a_i^0 = -\frac{ig(J^-)^0}{\kappa + i\omega_{i,s}}, \quad (a_i^*)^0 = \frac{ig(J^+)^0}{\kappa - i\omega_{i,s}}. \tag{5.9}$$

With this we have found a complete set of steady state solutions for our two-mode model. Each physical solution for a characteristic frequency ω corresponds to a different non-trivial fixed point. Thus, together with the trivial fixed point, the laser model possesses up to 4 different steady state configurations, whose stability properties we are going to study in more detail in the next subsection.

5.3.2. Stability of Steady States

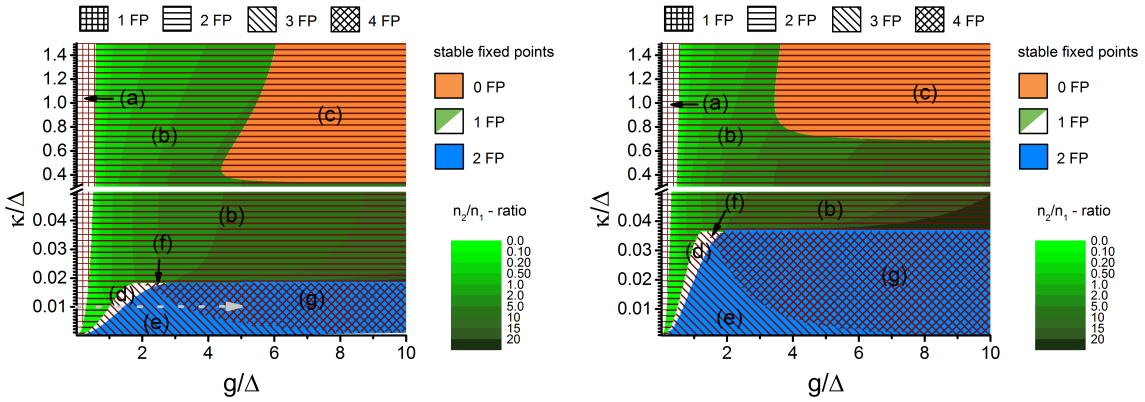

Figure 5.2.: The phase diagram shows the total number of fixed points and the number of stable fixed points in the g-κ plane. For small κ, there exist up to 4 physical fixed points, 2 of which are stable. In the region (c) all fixed points are unstable. Table I sums up the main properties of the regions (a)-(g). The green color gradient encodes the mode population ratio n_1/n_2, where $n_i = a_i^* a_i$. The right part shows the effect of increased pumping. Parameters: $\omega_1 = 2\Delta, \omega_2 = 4\Delta, \gamma_1 = 0.1\Delta, \gamma_2 = 0.2\Delta$ (left), $\gamma_2 = 0.5\Delta$ (right). Taken from Ref. [Kop15c].

First, we investigate the stability of the fixed points. This is checked as usual by linearizing the mean-field Eqs. (5.2) in the rotated frame around the fixed point and

Area	(a)	(b)	(c)	(d)	(e)	(f)	(g)
#(FP)	1	2	2	3	3	4	4
#(SFP)	1	1	0	1	2	1	2

Table 5.1.: Overview of the total number of fixed points #(FP) and the number of stable fixed points #(SFP) within different regions of the phase diagram in Fig. 5.2. Taken from Ref. [Kop15c].

by determining the eigenvalues of the linearized system. An eigenvalue with positive (negative) real part would support the solution divergence (convergence) from (to) the fixed point, which is then unstable (stable).

Figure 5.2 shows the main result in form of a complex phase diagram in the g-κ plane for two different pumping rates γ_2, encoding the total number and the number of stable fixed points. We see that, if the atom-field coupling is too small, only one trivial solution exists which corresponds to region (a). By overcoming some critical value for g, at least one non-trivial solution appears, thus the ω_1 and ω_2 modes become macroscopically occupied. For smaller κ-rates, we see a rich structure in the phase diagram. One can have different combinations of possible and stable fixed points, which are represented by a combination of color and dashing in figure 5.2. For example, the region (d) has two non-trivial physical solutions, but only one is stable. Table I provides the corresponding overview. For larger κ and g-values, the phase diagram contains region (c) without any stable fixed points. Here the system observables, like the mode occupation, oscillate with fixed frequency and amplitude, thus a limit cycle represents the only stable solution in this area. Note that we have found no stable limit cycles except in region (c). The coloring in the (b)-region shows the ratio n_1/n_2 of occupation of both modes, where $n_i = a_i^* a_i$. We observe that the occupation ratio and thus the dominating mode changes with the dissipation rate κ and the coupling strength g. Note that in the regions (e) and (g), where we have two stable fixed points, both ratios $n_1/n_2 \gtrless 1$ for fixed κ and g values exist. Especially in this region one of the modes is much more occupied and vice versa, thus the emitted radiation comes here mainly from one mode.

The lower part of Fig. 5.2 shows the effect of increased pumping. We see that the region with more than two fixed points (d)-(g) becomes larger, while the limit cycle region (c) is shifted to higher κ values.

Figure 5.3 shows the occupation of both modes as a function of coupling strength g for a fixed value of κ, along the horizontal gray arrow in the phase diagram of Fig. 5.2. We plot all possible stationary solutions including the unstable ones. The unstable fixed points are dashed, the occupations, which belong to the same fixed point, have the same color and the same thickness. The curves of the second mode are additionally marked with crosses. We see different types of bifurcations while increasing g. First, at $g = 0.3\Delta$ a pitchfork bifurcation occurs, where the trivial solution becomes unstable and a new stable solution occurs. Afterwards, an additional bifurcation takes place at $g = \Delta$, where an unstable solution splits up from the trivial one and becomes stable

at $g = 1.5\Delta$. Later, at $g = 3.2\Delta$, a third bifurcation with an unstable solution splits up. For the used parameter values Eq. (5.6) has three real roots, nevertheless at least one of the observables in Eqs. (5.7)-(5.8) is unphysical, for instance a negative mode population n_i or an imaginary J^+J^- value. Thus we have only two non-trivial solutions for $g > 1.5\Delta$. The two solutions allow the lower or the upper mode to have a high occupation, respectively. Note that the solution depends crucially on the chosen initial condition. Figure 5.4 shows an example of this behavior where we vary the initial state of the cavity modes $n_1(0), n_2(0)$. In the light blue area (diagonal lines) the system converges to the fixed point FP 1, in the dark blue area (vertical lines) to the fixed point FP 2 from Fig. 5.3.

In the next section we present different Pyragas feedback schemes. They allow to switch between a macroscopic occupation of the two cavity modes irrespective of the chosen initial condition and also to change further dynamical properties like the fixed point attraction region of the considered model.

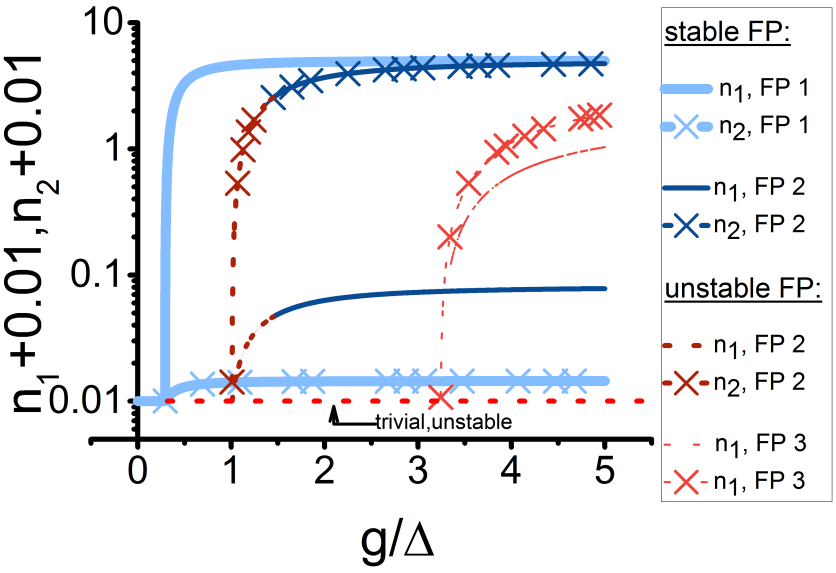

Figure 5.3.: All stationary solutions of the mean-field equation (5.2) for the occupation of both modes (n_1, n_2) are plotted as a function of g for fixed κ-value along the horizontal dashed arrow in Fig. 5.2 (left). The unstable solutions are dashed, the solution set is marked by the same color and the same thickness. The trivial solution with zero-mode occupation is always present but unstable beyond a critical g. Note that all occupations in the plot are shifted by 10^{-2} due to the log-scaling. Parameters: $\kappa = 0.01\Delta, \omega_1 = 2\Delta, \omega_2 = 4\Delta, \gamma_1 = 0.1\Delta, \gamma_2 = 0.2\Delta$. Taken from Ref. [Kop15c].

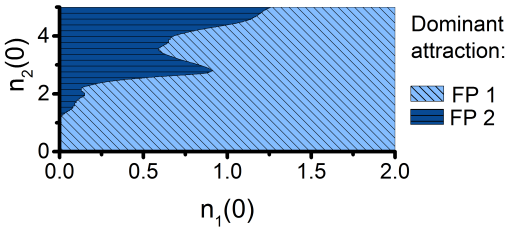

Figure 5.4.: Attraction region of two stable fixed points from Fig. 5.3 depending on the initial population of the cavity modes $n_1(0)$ and $n_2(0)$. Used parameters: $J^+(0) = J^-(0) = 0.185$, $J_z(0) = 0.076$, $g = 2\Delta$, $\kappa = 0.01\Delta$, $\omega_1 = 2\Delta$, $\omega_2 = 4\Delta$, $\gamma_1 = 0.1\Delta$, $\gamma_2 = 0.2\Delta$. Taken from Ref. [Kop15c].

5.4. Dynamics with Feedback

We now demonstrate the impact of time-delayed feedback control on the system. As a feedback signal we always use one of the system properties and restrict ourselves only to Pyragas feedback type [Pyr92]. Therefore, we insert into the mean-field equations (5.2) an additional control term, which is conditioned on the difference of a system property at two different times $t - \tau$ and t, where τ represents a time delay between the signal determination and the feedback into the system. Due to the rich phase diagram even without feedback in Fig. 5.2, it seems impossible to engineer one feedback scheme which works in every part of the phase diagram. Hence, we have to find for each part of the phase diagram a scheme which produces the desired results like mode selection or stabilization. However, the chosen feedback may not work in other parts of the phase diagram or will have other influences onto the system dynamics. In the following, we present three feedback schemes for different purposes and parts of the phase diagram, give a possible implementation picture for each scheme and demonstrate exemplary their influence onto the system evolution.

5.4.1. Stabilization of Fixed Points

The phase diagram in Fig. 5.2 has regions with non-trivial unstable steady states, which do not attract the solution. If no stable point exists, the solution oscillates periodically. This occurs only in region (c), see grey dotted curve in Fig. 5.5 (left). To stabilize the unstable non-trivial fixed point we suggest the following feedback scheme of Pyragas type [Pyr92]

$$\dot{J}_z \to \dot{J}_z - \lambda\big[J_z(t-\tau) - J_z(t)\big], \tag{5.10}$$

thus we modify the population inversion by a difference of the J_z spin component at two different times $t - \tau$ and t, where τ denotes the time delay parameter. Addition-

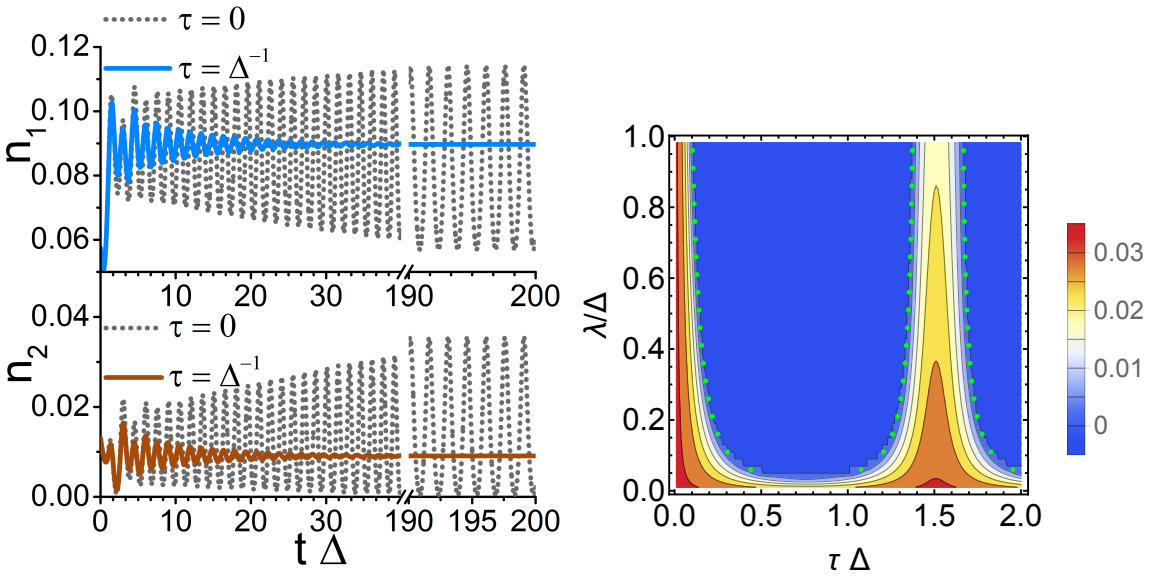

Figure 5.5.: (left) Pyragas feedback control of J_z (5.10) stabilizes the non-trivial fixed point in region (c) of phase diagram, figure 5.2. Without feedback the stationary solution is a limit cycle (gray dotted curves). With feedback the solution converges to a fixed point (solid curves). Parameters: $\tau = \Delta$, $\lambda = 0.4\Delta$. (right) Control diagram in τ-λ-plane. Vertical scale bar gives the largest real part of the eigenvalues of the linearized equations. In blue region fixed point becomes stable. Green dots show the boundaries from an analytical expression, see Eq. (5.16). Parameters: $\kappa = 0.5\Delta$, $g = 5\Delta$, $\omega_1 = 2\Delta$, $\omega_2 = 4\Delta$, $\gamma_1 = 0.1\Delta$, $\gamma_2 = 0.2\Delta$. Taken from Ref. [Kop15c].

ally, this difference is scaled by λ. The feedback term in Eq. (5.10) can be realized, for instance, by extra pumping of the atomic system or by opening additional decay channels, depending on the value of the feedback signal $\lambda[J_z(t-\tau) - J_z(t)]$.

The solid lines in Fig. 5.5 (left) show feedback actions for a point in the region (c). We see that for $t \gg 1/\Delta$ the mode occupations become constant, thus the fixed point is stabilized and the feedback signal vanishes. In contrast, without feedback the oscillations with finite amplitude are always present (gray dotted line). The right part of figure 5.5 shows the control diagram [Sch08] in the τ-λ plane. The color encodes the largest real part of all existing eigenvalues, obtained from the linearized equation of motion [HÖ5]. The fixed point is stable if this value is negative, which is the case in the blue area (figure 5.5, right). For the boundaries (green dots in figure 5.5, right) an analytical expression can be derived, as follows.

5.4.1.1. Auxiliary Calculation: Linearization Procedure

Here we show how to determine the boundary condition in the stability diagram Fig. 5.5 (right) in the presence of time-delayed Pyragas feedback control term (5.10).

Linearizing the equation of motion (5.2) together with the feedback condition (5.10)

we obtain the equation

$$\delta\dot{\mathbf{v}}(t) = \mathbf{A}\,\delta\mathbf{v}(t) + \mathbf{B}\,\delta\mathbf{v}(t-\tau), \tag{5.11}$$

where $\mathbf{v} = (a_1, a_1^*, a_2, a_2^*, J^+, J^-, J_z)$, $\delta\mathbf{v}$ gives a deviation from the fixed point $\mathbf{v}^0$ determined via the procedure given in Section 5.3.1 and we have introduced the matrices

$$\mathbf{A} = \begin{pmatrix}
-i\omega_{1,s}-\kappa & 0 & 0 & 0 & 0 & -ig & 0 \\
0 & i\omega_{1,s}-\kappa & 0 & 0 & ig & 0 & 0 \\
0 & 0 & -i\omega_{2,s}-\kappa & 0 & 0 & -ig & 0 \\
0 & 0 & 0 & i\omega_{2,s}-\kappa & ig & 0 & 0 \\
0 & -2igJ_z^0 & 0 & -2igJ_z^0 & i\Delta_s-\Gamma_\downarrow & 0 & -2ig((a_1^*)^0+(a_2^*)^0) \\
2igJ_z^0 & 0 & 2igJ_z^0 & 0 & 0 & -i\Delta_s-\Gamma_\downarrow & 2ig(a_1^0+a_2^0) \\
-ig(J^+)^0 & ig(J^-)^0 & -ig(J^+)^0 & ig(J^-)^0 & -ig(a_1^0+a_2^0) & ig((a_1^*)^0+(a_2^*)^0) & -\Gamma_\uparrow
\end{pmatrix},$$

$$\mathbf{B} = \lambda\cdot(0,0,0,0,0,0,1)^T \otimes (0,0,0,0,0,0,1).$$

The stability condition is then [HÖ5]

$$0 = \det\left[(\mathbf{A}-\mathbf{B}) - \mathbf{B}\cdot e^{-\Lambda\tau} - \Lambda\mathbf{1}\right]. \tag{5.12}$$

The fixed point is stable if all possible solutions for Λ have negative real part. From equation (5.12) the equation for phase boundaries can be obtained as follows. At the phase boundaries, Λ has vanishing real part. Thus, replacing $\Lambda \to i\Omega$ ($\Omega \in \mathbb{R}$) in Eq. (5.12) and calculating the determinant, we obtain

$$0 = e^{-i\Omega\tau}\sum_{j=0}^{6} c_j A_j \Omega^j + \sum_{j=0}^{7} c_j B_j \Omega^j, \quad c_j = \begin{cases} 1, & j \text{ even}, \\ i, & j \text{ odd}, \end{cases} \tag{5.13}$$

where A_i, B_i, $i \in \{1, 2, \ldots .7\}$ are real coefficients which depend on the system parameters both explicitly and implicitly via the fixed point solution, and on the feedback strength λ. However, the corresponding expressions are too long for showing them here.

Splitting the equation in real and imaginary part, we obtain the following two equations

$$\begin{aligned} 0 &= C_1 + C_2\cos(\Omega\tau) + C_3\sin(\Omega\tau), \\ 0 &= C_4 + C_3\cos(\Omega\tau) - C_2\sin(\Omega\tau), \end{aligned} \tag{5.14}$$

where

$$\begin{aligned} C_1 &= B_0 + B_2\Omega^2 + B_4\Omega^4 + B_6\Omega^6, \\ C_2 &= A_0 + A_2\Omega^2 + A_4\Omega^4 + A_6\Omega^6, \\ C_3 &= A_1\Omega + A_3\Omega^3 + A_5\Omega^5, \\ C_4 &= B_1\Omega + B_3\Omega^3 + B_5\Omega^5 + B_7\Omega^7. \end{aligned} \tag{5.15}$$

Squaring and summing the equations (5.14), we can eliminate the τ dependence and obtain a 14th order polynomial equation in Ω. This provides up to 14 solutions for Ω,

but only two of them turn out to be real. Next, we sum both of the equations (5.14) together in a suitable way in order to eliminate the sin term. The resulting equation can then be solved for τ as

$$\tau = \frac{1}{\Omega} \arccos\left(-\frac{C_3C_4 + C_1C_2}{C_2^2 + C_3^2}\right) + \frac{2\pi}{\Omega} z,\ z \in \mathbb{Z}. \tag{5.16}$$

This yields the boundaries in figure 5.5 (right), which perfectly agree with the corresponding numerical calculations. Two valid solutions for Ω build the $\bigcup$-shaped structure in the diagram, whereas z is responsible for its periodic structure.

5.4.2. Selection of the Dominantly Occupied Mode

We now focus onto the region (e), which features two stable non-trivial fixed points. The main interest in this region is the occupation of the respective cavity modes. In each of both solutions one mode has a high occupation, whereas the other one has a low occupation, see figure 5.3. In that way, the light leaking out from a cavity is generated by mostly one of the two modes. Without feedback the dominating mode is selected by the initial condition, see figure 5.4, which is usually hard to control. Interestingly, we found a feedback scheme, which allows to select the mode of interest, i.e. to select the frequency of the radiated light, which was also achieved for a quantum dot laser in [Vir13] with a non-Pyragas feedback type. We argue that our feedback type can switch the system behavior between a macroscopic occupation of the higher or the lower cavity mode.

To select the lower mode ω_1 we modify its frequency in Eqs. (5.2) as

$$\omega_1 \to \omega_1 + \lambda\big[n_2(t-\tau) - n_2(t)\big], \tag{5.17}$$

where $n_2 = a_2^* a_2$ represents the occupation of the second mode. This feedback type is also measurement based as the mean photon flux is proportional to the mean occupation of the photonic modes [Özt12, Kop13]. Thus, the frequency of the first mode has to be changed according to the difference of mean photon fluxes of the second mode at times $t - \tau$ and t.

However, the previous (or similar) feedback scheme does not work well for selecting the upper mode ω_2. For that purpose we modify the feedback scheme according to [Gri14]

$$\dot{a}_1 \to \dot{a}_1 - \lambda\big[a_1(t-\tau) - a_1(t)\big], \tag{5.18}$$

which is now a coherent type of feedback, as one can interpret it as a direct control without measurement [Gri14]. One possible realization is the back coupling of emitted photons by a mirror, where the mirror distance fixes the time delay τ [Kab15]. This scheme works for a properly chosen τ-parameter [HÖ5] as, for instance, $\tau = 2\pi/\omega$ (or multiples of it), where ω denotes the characteristic frequency of the rotated frame determined by Eq. (5.6). This choice guarantees that the feedback term in equation (5.18) vanishes for $t \gg 1/\Delta$.

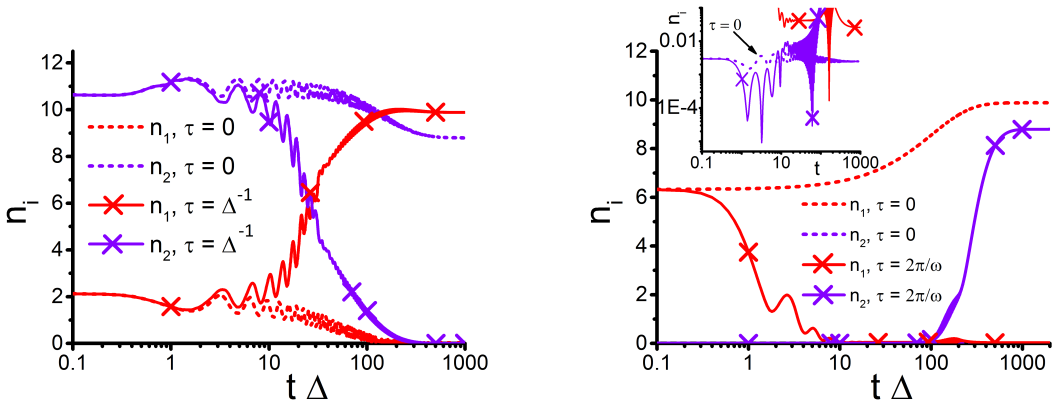

Figure 5.6.: Usage of feedback schemes in region (e) of figure 5.2 for driving the system toward a macroscopic occupation of the lower (left) or higher cavity mode (right). (left) Feedback scheme (5.17) selects highly populated ground mode (red line with markers), whereas (right) control type (5.18) selects highly populated excited mode (violet line with markers). The inset (right) shows the zoom for small photon numbers. Without feedback the other modes have a macroscopic population (dashed violet and red lines in both figures). Parameters: $\lambda = 0.01\Delta$ (left), $\lambda = \Delta$ (right), $\kappa = 0.005\Delta$, $g = 2\Delta$, $\omega_1 = 2\Delta$, $\omega_2 = 4\Delta$, $\gamma_1 = 0.1\Delta$, $\gamma_2 = 0.2\Delta$. Taken from Ref. [Kop15c].

The action of both feedback types is shown in figure 5.6. Solid marked curves show the cavity mode occupations with feedback, dashed curves without feedback. Both feedback schemes destabilize only one fixed point in the region (e) of figure 5.2, thus the system converges to the other one. In the left figure we see the action of feedback equation (5.17). Without the feedback, the excited mode ω_2 has a dominant population (dashed violet line), whereas with control its occupation becomes low (violet line with markers) and instead the ground mode ω_1 (red line with markers) is macroscopically occupied. The right figure shows the opposite behavior. Instead of the lower mode (red, dashed), the higher mode is macroscopically occupied (violet line with markers). Note that both stable steady states exist without feedback in the region (e) of figure 5.2. However, their attraction regions depend on the initial condition, as is shown without feedback in figure 5.4. We emphasize that with feedback the selection of modes works independently of the chosen initial condition for the tested parameter values.

Figure 5.7 shows the control diagram in the τ-λ space for the feedback type Eq. (5.17) obtained from a linear stability analysis. We see that there are parameter regions where only one of the fixed points becomes unstable and also where both fixed points become unstable. In the blue-dotted area the fixed point with $n_2 \gg n_1$ becomes unstable, whereas in the green-dashed region another fixed point with $n_1 \gg n_2$ is destabilized. The boundaries are calculated analytically (see last part of this section). In order to reach the fixed point with a macroscopic occupation of the lower cavity mode we have to choose the parameters in the region having only blue dots. Fixing the feedback parameter in the region having only green dashes (arrow in the diagram) should select the

fixed point with a macroscopic population of the higher cavity mode. However, there are some exceptions. The fixed point with $n_2 \gg n_1$ attracts the solution if the initial condition is rather close to it, otherwise the solution converges to a limit cycle which appears in this case in presence of Pyragas control [Kop15b]. Limit cycle solutions are also present in the parameter area where both fixed points become unstable due to the time-delayed feedback control.

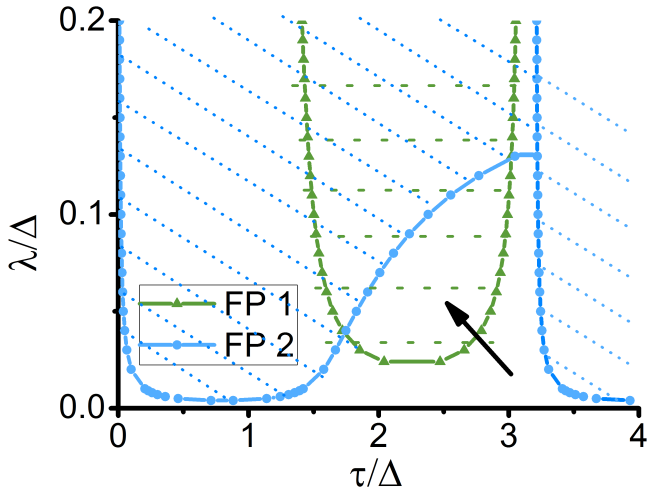

Figure 5.7.: Stability diagram for Pyragas feedback type (5.17). In the dashed (dotted) region the first (second) fixed point (FP), related to a macroscopic population of the lower (higher) cavity mode as in Fig. 5.3, becomes unstable. Parameters: $\kappa = 0.005\Delta$, $g = 2\Delta$, $\omega_1 = 2\Delta$, $\omega_2 = 4\Delta$, $\gamma_1 = 0.1\Delta$, $\gamma_2 = 0.2\Delta$. Taken from Ref. [Kop15c].

5.4.2.1. Auxiliary Calculation: Linearization Procedure

Here we show how to determine the boundary condition in the stability diagram Fig. 5.7 in the presence of time-delayed Pyragas feedback control term Eq. (5.17).

The procedure is similar to the one in the previous section , but the feedback condition is given now by the Eq. (5.17). The matrix $\mathbf{B}$ is then redefined as

$$\mathbf{B} = -i\lambda \begin{pmatrix} 0 & 0 & (a_2^*)^0 a_1{}^0 & (a_2^*)^0 a_1{}^0 & 0 & 0 & 0 \\ 0 & 0 & -a_2{}^0 (a_1^*)^0 & -a_2{}^0 (a_1^*)^0 & 0 & 0 & 0 \\ 0 & 0 & 0 & 0 & 0 & 0 & 0 \\ 0 & 0 & 0 & 0 & 0 & 0 & 0 \\ 0 & 0 & 0 & 0 & 0 & 0 & 0 \\ 0 & 0 & 0 & 0 & 0 & 0 & 0 \\ 0 & 0 & 0 & 0 & 0 & 0 & 0 \end{pmatrix}.$$

The further procedure is the same. First we calculate the determinant Eq. (5.12) and

write it in a similar form of Eq. (5.13)

$$0 = e^{-i\Omega\tau}\sum_{j=0}^{4} c_j \tilde{A}_j \Omega^j + \sum_{j=0}^{7} c_j \tilde{B}_j \Omega^j, c_j = \begin{cases} 1, & j \text{ even}, \\ i, & j \text{ odd}. \end{cases} \tag{5.19}$$

As the parameters $\tilde{A}_j, \tilde{B}_j$ are real, Eq. (5.19) can be split in real and imaginary parts, which yields

$$\begin{aligned} 0 &= \tilde{C}_1 + \tilde{C}_2 \cos(\Omega\tau) + \tilde{C}_3 \sin(\Omega\tau), \\ 0 &= \tilde{C}_4 + \tilde{C}_3 \cos(\Omega\tau) - \tilde{C}_2 \sin(\Omega\tau), \end{aligned} \tag{5.20}$$

where

$$\begin{aligned} \tilde{C}_1 &= \tilde{B}_0 + \tilde{B}_2\Omega^2 + \tilde{B}_4\Omega^4 + \tilde{B}_6\Omega^6, \\ \tilde{C}_2 &= \tilde{A}_0 + \tilde{A}_2\Omega^2 + \tilde{A}_4\Omega^4, \\ \tilde{C}_3 &= \tilde{A}_1\Omega + \tilde{A}_3\Omega^3, \\ \tilde{C}_4 &= \tilde{B}_1\Omega + \tilde{B}_3\Omega^3 + \tilde{B}_5\Omega^5 + \tilde{B}_7\Omega^7. \end{aligned} \tag{5.21}$$

From the upper equations one can then eliminate the τ dependence to determine possible Ω values. With this τ can be calculated as in Eq. (5.16), but C_i is then replaced by $\tilde{C}_i$. The resulting (Ω, τ) combinations are the boundaries in Fig. 5.7.

5.5. Discussion

In this paper we have investigated the mean-field dynamics of a two-mode laser model based on an extended Tavis-Cummings model in the thermodynamic limit without and with time-delayed feedback. The corresponding mean-field equations can be solved analytically in the steady state. Even without feedback control this model exhibits a complex phase diagram with multiple stable fixed points. Our Pyragas feedback schemes allow to drive the system to different phases, by selecting or stabilizing one preferred stationary solution.

We studied also other feedback schemes of the Pyragas type, but they led to similar results as already shown. However, especially in phases with a combination of unstable and stable non-trivial fixed points it is difficult to design a feedback scheme which stabilizes or selects one stable configuration for a wide range of initial conditions. The reason for this is that the Pyragas control type affects the stability of all fixed points. For example, the stabilization succeeds only close to the corresponding fixed point in the sense of the linear stability analysis. Farther away from the fixed point, we have often observed the appearance of limit cycles with large attraction regions or even chaotic solutions, which is a known feature in laser systems with feedback [Ott10] and also occurs for other non-linear dynamical systems with time delay [Wis94, Gri99, Sch03b, Sch03a].

Since our calculations were done at a semi-classical level, we expect that the results should hold in the thermodynamic limit, where the number N of two-level atoms tends to infinity. On the one hand, the fluctuations scale like $1/\sqrt{N}$ with the number of atoms N [Gar04]. On the other hand, the laser dynamics or a condensation is usually studied at this level. Furthermore, the semi-classical regime of the quantum-optical models like Dicke [Dic54] or Lipkin-Meshkov-Glick [Lip65] predicts correctly their main properties, like observable averages or occurrence of a quantum phase transition [Bha12, Rib08, Eng15]. It would be certainly interesting to analyze the impact of control on the quantum fluctuations. This could be investigated with other approaches to feedback [Wis09, Ema13b], which usually requires a high numerical effort. In this respect a promising feedback scheme was introduced in [Nau14, Hei15], which allows to control the entanglement and light bunching by structured environment and converges to a Pyragas control type in the one excitation limit. However, the general quantum version of Pyragas control type remains an unsolved question. A new, conceptually significant approach has been recently introduced in [Gri15], although it appears to be numerically demanding.

Finally, we note that it would be worthwhile to extend our two-mode laser model with the thermalization mechanism along the lines of [Kir13, Kir15]. This would yield a minimal model to study the transition between a condensate- and a laser-like state which originate from a macroscopic occupation of the lower and higher cavity mode, respectively. Adding Pyragas feedback control terms as suggested here should, thus, allow to switch the system behavior between condensate- and laser-like.

5.6. Summary

In this chapter we theoretically investigated the properties of the 2-mode Laser system with and without Pyragas feedback. The model is a two mode version of the Tavis-Cummings model with the Hamiltonian H. The atomic system is driven with the rate γ_1 and decays incoherently with the rate γ_2. The cavity decays to the environment with the rate κ. The dynamic is then captured by the following master equation

$$\frac{d\hat{\rho}(t)}{dt} = -i[\hat{H},\hat{\rho}] - \kappa\mathcal{L}[\hat{a}_1]\hat{\rho} - \kappa\mathcal{L}[\hat{a}_2]\hat{\rho} - \frac{\gamma_2}{2}\sum_{k=1}^{N}\mathcal{L}[\hat{\sigma}_k^+]\hat{\rho} - \frac{\gamma_1}{2}\sum_{k=1}^{N}\mathcal{L}[\hat{\sigma}_k^-]\hat{\rho}.$$

We derive a close set of mean-field equations using the factorizing assumption in the thermodynamic limit and found analytically up to four different stationary states which properties are summarized in the phase diagram Fig. 5.2. Thus we have for example areas, we only one of both bodes are macroscopically occupied or the stationary state is unstable. Then we applied different feedback schemes to the model, assuming that a frequency of the first mode ω_1, the inversion derivative $\dot{J}_z$ or the optical mode derivative $\dot{a}_1$ is changed due to feedback action. Such schemes lead to the selection of the macroscopically occupied mode irrespectively of the initial condition or to a sta-

bilization. We investigate the conditions, when the schemes are working and discuss them in more general context.

6. Conclusion

In this thesis we have studied theoretically the application of time-delayed Pyragas control to various many-body quantum systems with quantum criticality. The Dicke system, Lipkin-Meshkov-Glick system and an extended version of a Tavis-Cummings laser act as a testbed for application of control. All systems are coupled to a dissipative environment. We have shown that the Pyragas control affects the system dynamic and system stationary state in a very unexpected and interesting way. For example, our simulations show the creation of non-equilibrium steady states in form of limit-cycles in the presence of dissipative environment or a stabilization of unstable steady states.

The starting point in all studied cases with a system Hamiltonian $\hat{H}$ is the master equation for a system density matrix $\hat{\rho}$, see Eq. (2.15)

$$\dot{\hat{\rho}} = -i\left[\hat{H}, \hat{\rho}\right] + \sum_k \frac{\kappa}{2}\mathcal{D}[\hat{O}_k]\hat{\rho}.$$

We describe the dissipative effects in a usual way by Lindblad Operators $\mathcal{D}[\hat{O}_k]\rho$, where $\hat{O}_k$ is a system operator and κ_k is a decay rate. Due to the form of assumed dissipation, all considered systems are effectively driven and have a non-equilibrium steady state in absence of control. Next, we derive a equations of motion for the averages of system operators. Assuming the factorization of averages over operator products in the thermodynamic limit, we obtain a closed set of coupled equations. We use them to include the feedback and analyze its action on the system. The feedback controls either a system parameter or a system property like the inversion. Therefore we include the Pyragas form $\left\langle \hat{O}_k(t-\tau) - \hat{O}_k(t) \right\rangle$ as a control therm with time delay τ into the system where t and $t-\tau$ are two different times.

In the Dicke model we modify the system coupling g between the atoms and the cavity mode by the difference of the mean photon flux out of the cavity at two different times t and $t-\tau$. Without feedback the dissipative Dicke model has two different phases, a normal one and a superradiant one. Only in the superradiant regime our feedback scheme works. Our numerical simulation show that the feedback scheme can speed up or slow down the convergence time till the stationary state in the superradiant phase. Moreover, a sequence of Hopf- and Saddle-Node bifurcations occur as a function of time delay τ. This is accompanied by the creation of a limit-cycle phase in the superradiant regime as a new steady state. All system averages oscillate then with a fixed frequency and finite amplitude which depend on τ. We found parameter regions, where both the steady state without time delay and the new limit cycle phase are coexisting for the same system parameter values.

Lipkin-Meshkov-Glick (LMG) model we modify - similar as in the Dicke case - the system coupling γ between the atoms by a difference of the squared inversion $J_z^2(t)$

at two different times t and $t-\tau$. Our feedback scheme works only in the symmetry broken phase and vanishes in the normal case. Our investigation was focused on the ESQPT signal in presence of damping. Without feedback, the ESQPT signal is still present in the spectrum of effective Hamiltonian, but its imprint in the semiclassical dynamic is smoothed. However, our feedback scheme is able to create new limit-cycle phases as a function of τ whose stationary dynamic is very close to the dynamic of a closed system prepared in eigenstates. This fact allows us to remove the dissipative smoothing of the ESQPT signal. Furthermore, for higher values of time delay τ we observed the doubling structure in the bifurcation diagram which is a known way to chaos.

We showed the two-mode Tavis-Cummings (TC) laser has a rather complex phase diagram with up to tree non-trivial fixed points. The complexity of the phase diagram allows more possibilities in taking influence. Therefore, we applied three different time delay schemes to achieve sundry effects, namely to stabilize an unstable state and to populate either the lower or the higher lasing mode macroscopically. On top of this, we discussed briefly the last effect in connection with condensation and lasing behavior.

In all cases we derive analytical expressions in the linearized regime which determines the boundaries of the control effect in the configuration space.

The Pyragas type of feedback turned out to be a very powerful tool to modify the system end state. We applied other feedback schemes of Pyragas type to all studied systems. We think that its potency is hidden in its form. Thus, it usually prevents the system from the non-physical behaviour, it is of non-invasive type and does not change or modify the fixed point position. Moreover it lets the hidden oscillating properties of a system appear. However, our last model shows that it is hard to control the systems with multiple fixed points. Every fixed point notices the presence of feedback and changes its basin of attraction or repulsion and the corresponded strength. This increases the effort in finding a feedback scheme witch lead to desired effect.

Although all three systems originate from the quantum optic, Pyragas control can have a very different impact on each one of them. Surprisingly, we have not found chaotic solutions in presence of time-delayed control for tested parameter values in the Dicke system, in contrast to the LMG model and TC Laser, although the Dicke model is chaotic in nature. This can be connected to the absence of additional pumping channels and - simultaneously - to the presence of the cavity mode which occupation is not limited by a conservation law. The LMG has only dissipative spin dynamic which is restricted by a conservation of the spin length. Thus, the additional energy added by feedback may in some cases not be effectively given to the environment and the system then becomes chaotic. In the TC laser chaotic solutions in presence of feedback seems to be seldom. In spite of presented conservation law for the dissipative spin system with a spin pumping term, the TC laser has a dissipative cavity mode, which could prevent the creation of chaotic behavior in most cases.

All calculations have been performed at the mean-field level in thermodynamic limit, thus we have neglected all fluctuation effects. We think that such effects play an important role for the small number of atoms N. In the thermodynamic limit the fluctuations should scale with $1/\sqrt{N}$ and are then negligible. The main properties of the consid-

ered systems agree on the mean field level with the corresponding quantum mechanical calculations for $N \gg 1$. Moreover, different phase transitions like condensation or laser have a semiclassical explanation. However, a general feedback of Pyragas type on the quantum level is still an open question. Grimsmo showed a possible way of implementation [Gri15]. Other non-Pyragas feedback types exist, too [Wis09]. However, all of them are usually numerically high demanding. But the application of the control scheme in a quantum regime keeping the fluctuations may open new control possibilities, e.g. control of quantum chaos, phase transition control via shift of the critical coupling or control of fluctuations.

Appendix

A. Overview of Used Symbols and Abbreviations

Abbreviations

QPT	Quantum Phase Transition
ESQPT	Excited State Quantum Phase Transition
LMG	Lipkin-Meshkov-Glick
TC	Tavis Cummings
Fig.	Figure
Sec.	Section
Eq.	Equation

Symbols

The following symbols are usually used as follows.

Symbol	Explanation
$\hat{O}$	An arbitrary Operator O.
O	Average over Operator O, $O = \left\langle \hat{O} \right\rangle$, usually calculated using the factorization assumption.
$\mathbf{A}, \mathbf{B}$	Matrices for linearized system with time delay
τ	Time delay.
λ	Feedback strength.
Λ	Eigenvalue of the characteristic equation.
z	Some time.
ω	Frequency of the cavity mode.
n	Occupation of the optical mode.
Δ,ω_0	Frequency of the two-level atom.
g, g_0	Atom-Field coupling.
$\gamma, \gamma_x, \gamma_y$	Spin coupling constant.
γ_c, λ_c	Critical coupling.
κ	Decay rate to the environment.

Symbol	Explanation
$\Gamma_\uparrow, \Gamma_\downarrow, \gamma_1, \gamma_2$	Pumping rates.
N	Number of atoms.
j	Pseudo spin.
θ, ϕ	Angels.
t_{ij}	Coefficients.
$\bar{O}$	Time average.
$\hat{H}$	Hamiltonian.
H	Semiclassical Hamiltonian.
$\hat{H}_{eff}$	Effective non-hermitian Hamiltonian of a dissipative system.
E	Energy.
$\hat{\rho}$	System density matrix
$\hat{a}$	Destruction operator ov the cavity mode.
$\hat{a}^\dagger$	Creation operator of the cavity mode.
$\hat{J}_{+,-,x,y,z}$	Collective spin operator.
$\hat{J}^2$	Spin length, $\hat{J}^2 = \hat{J}_x^2 + \hat{J}_y^2 + \hat{J}_z^2$.
$\sigma_{+,-,x,y,z}$	Pauli matrices.
$\hat{M}$	Excitation number, $\hat{M} = \hat{J}_z + \hat{a}^d a g \hat{a}$.
$\|n\rangle$	Eigenstate of a bosonic mode.
$\|lm\rangle$	Eigensate of $\hat{J}^2$.
$\|\theta, \phi\rangle$	Spin-Coherent state.
$\|\alpha\rangle$	Bosonic coherent state.

Connections

Pseudo spin $J_i = \frac{1}{2}\sum_k^N \sigma_i^k$, $i \in \{x, y, z\}$.
$J_\pm = \sum_k^N \sigma_i^\pm$.

Pauli Matrix $\sigma_\pm = \frac{1}{2}(\sigma_x \pm \sigma_y)$,

Averaged Value $\left\langle \hat{O} \right\rangle = \mathrm{Tr}\left(\hat{O}\hat{\rho}\right)$.

B. Time Delayed Control of Photon Condensation

B.1. Introduction

In chapter 5 we studied a two-mode laser model with feedback and demonstrated that the Pyragas scheme allows to switch between the states where the lower or upper cavity mode is macroscopically occupied. We argued that such states have an analogy with a condensate-like or lasing-like states but due to the absences of the temperature scale a direct correspondence is not justified. The model of a photon condensation introduced in Ref. [Kir13, Kir15] by Kirton et al. does not have such weak point. Our model in chapter 5 can be then seen as a minimalistic model of Ref. [Kir13]. We assumed two cavity modes interacting with N two-level atoms inside a cavity, which are pumped and have incoherent losses. Keeling at al. add on top an interaction with dye molecules, which generate a temperature bath.

Here we rederive the master equation by Kirton et al. [Kir13] of the photon condensate and recapitulate the main results. Then we apply the time delayed control of Pyragas type and show its affect on the system.

B.2. Model of Photon Condensation

Kirten et al. assumes following Hamiltonian (here and later we skip the $\hat{}$ symbol)

$$H = \sum_m \omega_m a_m^\dagger a_m + \sum_i \frac{\Delta}{2}\sigma_i^z + \Omega(b_i^\dagger b_i + \sqrt{S}\sigma_i^z(b_i + b_i^\dagger) + g\sum_{m,l}(a_m\sigma_i^+ + a_m^\dagger\sigma_i^-), \quad \text{(B.1)}$$

where a_m is the destruction operator of the mth cavity mode, $\sigma_i^{(z,\pm)}$ denotes Pauli matrices of the ith two-level atom with the energy separation Δ, b_i is a destruction operator of the ith phonon which is coupled to the ith atom by S. The coupling g describes the interaction strength between cavity modes and atoms, see Fig. B.1(a). Cavity modes decay to the environment with a rate κ, atoms gets pumped and decays into non-cavity modes with the rates $\Gamma_\uparrow$, $\Gamma_\downarrow$, respectively.

B.3. Re-derivation of the Master Equation

First, we recapitulate the form of a master equation in Born-Markov approximation. Later, we can use this formula do derive the master equation starting with the Hamil-

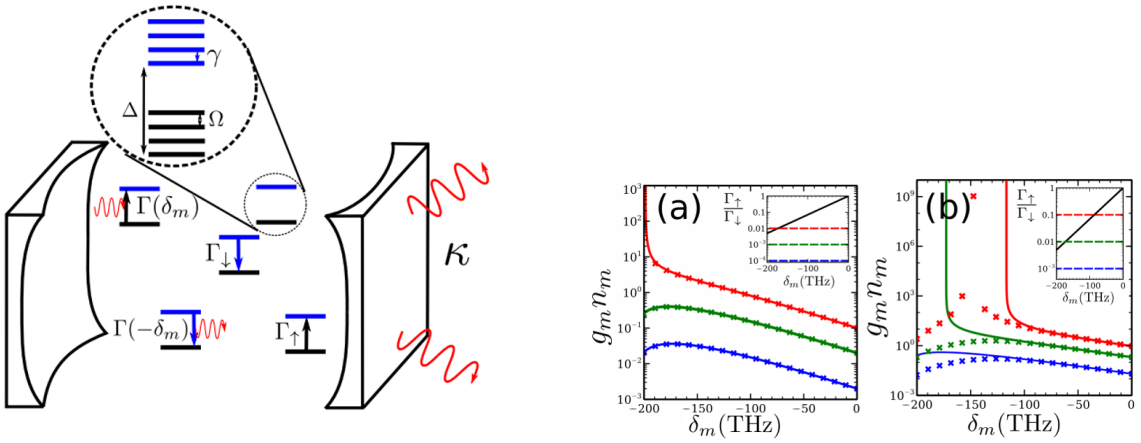

(a) Model (b) Occupation

Figure B.1.: Take (and reprinted with permission) from Ref. [Kir13], ©American Physical Society. a) Schema for a model which describes a photon condensation. b) The corresponding mean mode occupation in different parameter regimes: the condensate (left, κ small) and laser states (right, *kappa* big).

tonian Eq. (B.1).

B.3.1. General Form of the Master Equation with Born-Markov Approximation

We assume the Hamiltonian of the Form $H = H_0 + H_1$. H_1 describes the coupling between the system and the bath and has the form $\sum_k S_k \times B_k$, S_k are the System and B_k the Bath operators respectively. In this case the general form of the Born-Markov master equation is:

$$\boxed{\frac{d}{dt}\rho(t) = -i[H,\rho(t)] - \sum_k \left(S_k D_k \rho(t) - D_k \rho(t) S_k + \rho(t) E_k S_k - S_k \rho(t) E_k\right)} \tag{B.2}$$

with

$$D_k = \int_0^\infty d\tau \sum_l C_{kl}(\tau)\tilde{S}_l(-\tau)\,, \tag{B.3}$$
$$E_k = \int_0^\infty d\tau \sum_l C_{lk}(-\tau)\tilde{S}_l(-\tau)\,,$$

and the Bath-correlation function

$$C_{kl}(t) = Tr_B \rho_B \tilde{B}_k(t)\tilde{B}_l(t=0)\,. \tag{B.4}$$

Tilde denotes the operators in the interaction picture.

B.3.1.1. Additional term $\sim$ coupling strength

The term which is linear in System-Bath-coupling is absent in the Eq. (B.2), because of the general assumption what $\langle B_k \rangle = 0$. However, if it is not the case, the master equation would have an additional term

$$\begin{aligned}\frac{d}{dt}\rho(t) = -i[H,\rho(t)] - \sum_k \left(S_k D_k \rho(t) - D_k \rho(t) S_k + \rho(t) E_k S_k - S_k \rho(t) E_k\right) \\ - i\sum_k [S_k, U_0 \tilde{\rho}(t=0) U_0^\dagger] \langle B_k \rangle (t=0),\end{aligned} \tag{B.5}$$

where $U_0 = \exp(-iH_0 t)$ is a time evolution operator of the free system. This additional linear term connects the evolution with the initial condition of the system $\rho(t=0)$.

B.3.2. Polaron Transformation and System-Bath Identification

To get rid of the phonon interaction, we make first a Polaron transformation [Kir13] of Eq. (B.1): $H \to U^\dagger H U$ with $U = \exp\left(\sum_i \sqrt{S}\sigma_i^z (b_i - b_i^\dagger)\right)$, yielding

$$H = \sum_m \omega_m a_m^\dagger a_m + \sum_i \left(\frac{\Delta}{2}\sigma_i^z + \Omega b_i^\dagger b_i\right) + g\sum_{m,i}\left(a_m \sigma_i^+ e^{2\sqrt{S}(b_i^\dagger - b_i)} + a_m^\dagger \sigma_i^- e^{-2\sqrt{S}(b_i^\dagger - b_i)}\right), \tag{B.6}$$

where the atomic operators in the cavity-atom interaction are dressed by a phonon-term $e^{\pm 2\sqrt{S}(b_i^\dagger - b_i)}$. This is typical for a application of a Polaron transformation.

Hamiltonian (B.6) is a starting point for the derivation of the master equation. We identify the b_i-phonon-modes with a Bath and the interaction H_1 with

$$\begin{aligned}H_1 &= g\sum_{m,i}\left(a_m \sigma_i^+ e^{2\sqrt{S}(b_i^\dagger - b_i)} + a_m^\dagger \sigma_i^- e^{-2\sqrt{S}(b_i^\dagger - b_i)}\right) \\ &\equiv \sum_{k,i=1,2}(S_{k,i} \otimes B_{k,i}) = \sum_k (S_{k,1} \otimes B_{k,1} + S_{k,2} \otimes B_{k,2}),\end{aligned} \tag{B.7}$$

with identified system- and bath- operators

$$S_{k,1} = \sum_m a_m \sigma_k^+, \quad S_{k,2} = \sum_m a_m^\dagger \sigma_k^-, \quad B_{k,1} = e^{2\sqrt{S}(b_k^\dagger - b_k)}, \quad B_{k,2} = e^{-2\sqrt{S}(b_k^\dagger - b_k)}. \tag{B.8}$$

B.3.3. Determination of the Bath Correlation Functions

We calculate now the bath correlation functions. Using

$$C_{k,\lambda}^{i,j}(t) = Tr_B(\rho_B \tilde{B}_{k,i}(t) \cdot B_{\lambda,j}),$$

with $\rho_B = 1/Z \cdot e^{-\beta H_B}, H_B = \sum_k \Omega b_k^\dagger b_k$ i.e. the phonon bath is in thermal equilibrium. The calculation of the bath correlation functions results in (see the next sub-section for more details)

$$\begin{aligned} C_{kk}^{11} &= e^{-4S(2\coth\left(\frac{\beta\Omega}{2}\right)\cos^2\left(\frac{t\Omega}{2}\right) - i\cdot\sin(t\Omega))} \\ C_{k\lambda}^{11} &\overset{k\neq\lambda}{=} e^{-4S\coth(\frac{\beta\Omega}{2})} \\ C_{kk}^{12} &= e^{-4S(2\coth\left(\frac{\beta\Omega}{2}\right)\sin^2\left(\frac{t\Omega}{2}\right) + i\cdot\sin(t\Omega))} \\ C_{k\lambda}^{12} &\overset{k\neq\lambda}{=} e^{4S\coth(\frac{\beta\Omega}{2})} \\ C_{kk}^{22} &= C_{kk}^{11} \\ C_{kk}^{21} &= C_{kk}^{12} \end{aligned} \tag{B.9}$$

B.3.3.1. Auxiliary Calculation for C_{kk}^{11}

$$\begin{aligned} C_{kk}^{11} &= Tr_B\left(\rho_B \tilde{B}_{k,1}(t) B_{k,1}\right) = 1/Z Tr_B\left(e^{-\beta H_B} e^{\sum_j i\Omega b_j^\dagger b_j t} B_{k,1} e^{-\sum_j i\Omega b_j^\dagger b_j t} B_{k,1}\right) \\ &= 1/Z Tr_B\left(e^{-\beta H_B} e^{i\Omega b_k^\dagger b_k t} B_{k,1} e^{-i\Omega b_k^\dagger b_k t} B_{k,1}\right) \\ &= 1/Z Tr_B\left(e^{-\beta H_B} e^{2\sqrt{S}(b_k^\dagger e^{i\Omega t} - b_k e^{-i\Omega t})} \cdot e^{2\sqrt{S}(b_k^\dagger - b_k)}\right). \end{aligned} \tag{B.10}$$

using $e^{\hat{A}} e^{\hat{B}} = e^{\hat{A}+\hat{B}} e^{1/2[A,B]}$ if $[A,B]$ is a number, we obtain

$$\begin{aligned} &= 1/Z\, Tr_B\left(e^{-\beta H_B} e^{2\sqrt{S}(b_k^\dagger(1+e^{i\Omega t}) - b_k(1+e^{-i\Omega t}))}\right) \cdot e^{4iS\sin(\Omega t)} \\ &= 1/Z\, Tr_B\left(e^{-\beta H_B} e^{2\sqrt{S}(1+e^{i\Omega t})b_k^\dagger} e^{-2\sqrt{S}(1+e^{-i\Omega t})b_k}\right) \cdot e^{-4S(1+e^{-i\Omega t})}. \end{aligned} \tag{B.11}$$

Using the Fock states $|n\rangle$ to calculate the trace, we exclude the $|n_k\rangle$ sum part, insert the H_B Hamiltonian and perform a series expansion for the last two exponentials.

$$\begin{aligned} C_{kk}^{11} = \frac{e^{-4S(1+e^{-i\Omega t})}}{Z} &\sum_{n_j \neq n_k} \langle n_1 n_2 ... |\, e^{-\beta \sum_{l\neq k} \Omega b_l^\dagger b_l} \,| n_1 n_2 ... \rangle \\ &\cdot \sum_{n_k} \langle n_k |\, e^{-\beta\Omega b_k^\dagger b_k} \\ &\left(1 + \frac{2\sqrt{S}}{1!}(1+e^{i\Omega t}) b_k^\dagger + \frac{(2\sqrt{S})^2}{2!}(1+e^{i\Omega t})^2 (b_k^\dagger)^2 + ...\right) \cdot \\ &\left(1 + \frac{-2\sqrt{S}}{1!}(1+e^{-i\Omega t}) b_k + \frac{(-2\sqrt{S})^2}{2!}(1+e^{-i\Omega t})^2 (b_k)^2 + ...\right) \\ |n_k\rangle\,. \end{aligned} \tag{B.12}$$

$$\tag{B.13}$$

In the second sum only the products with the same number of creation and annihilation operators survives, other combinations are zero due to the orthogonality of the Fock state $\{|n_k\rangle\}$. Defining $n_l = b_l^\dagger b_l$, the upper equation results in

$$C_{kk}^{11} = \frac{e^{-4S(1+e^{-i\Omega t})}}{Z} \sum_{n_j \neq n_k} e^{-\beta \sum_{l\neq k} n_l} \tag{B.14}$$

$$\cdot \sum_{n_k} e^{-\beta\Omega n_k} \left[1 + \frac{-4S}{1!\cdot 1!}(1+e^{i\Omega t})(1+e^{-i\Omega t}) n_k \right.$$

$$\left. + \frac{(-4\sqrt{S})^2}{2!\cdot 2!}(1+e^{i\Omega t})^2(1+e^{-i\Omega t})^2 \cdot n_k(n_k-1) + ... \right] \tag{B.15}$$

$$= \frac{e^{-4S(1+e^{-i\Omega t})}}{Z} \sum_{n_j \neq n_k} e^{-\beta \sum_{l\neq k} n_l} \cdot \sum_{n_k} e^{-\beta\Omega n_k}$$

$$\sum_m \left[\frac{(-4S)^m}{m!} \cdot \underbrace{(1+e^{i\Omega t})(1+e^{-i\Omega t})}_{=2^m(1+\cos(\Omega t))^m} \cdot \underbrace{\frac{1}{m!}\frac{n_k}{(n_k-m)!}}_{=\binom{n}{k}} \right]$$

$$= \frac{e^{-4S(1+e^{-i\Omega t})}}{Z} \sum_{n_j \neq n_k} e^{-\beta \sum_{l\neq k} n_l} \cdot \sum_{n_k} e^{-\beta\Omega n_k} L_{n_k}\left(8S(1+\cos(\Omega t))\right),$$

where L_{n_k} is a Laguerre Polynomial. Using now the generating function of Laguerre Polynomials $\sum_n^\infty t^n L_n(x) = \frac{1}{1-t} e^{-\frac{tx}{1-t}}$, the upper equation becomes

$$C_{kk}^{11} = \frac{e^{-4S(1+e^{-i\Omega t})}}{Z} \underbrace{\sum_{n_j \neq n_k} e^{-\beta \sum_{l\neq k} n_l} \cdot \frac{1}{1-e^{-\beta\Omega}}}_{=Z} \cdot e^{-e^{-\beta\Omega}\cdot\frac{8S(1+\cos(\Omega t))}{1-e^{-\beta\Omega}}}$$

$$= e^{-4S(1+e^{-i\Omega t}) - e^{-\beta\Omega}\cdot\frac{8S(1+\cos(\Omega t))}{1-e^{-\beta\Omega}}}$$

$$= e^{-4S\left(2\coth\left(\frac{\beta\Omega}{2}\right)\cos^2\left(\frac{t\Omega}{2}\right) + i\cdot\sin(t\Omega)\right)}. \tag{B.16}$$

B.3.3.2. Auxiliary Calculation for C_{kk}^{12}

In the same manner we recalculate

$$
\begin{aligned}
C_{k,k}^{1,2} &= \mathrm{Tr}\left\{\tilde{B}_{k,1}B_{k,2}\right\} = \mathrm{Tr}\left\{e^{2\sqrt{S}\left(b_k^\dagger e^{i\Omega t} - b_k^{-i\Omega t}\right)}\cdot e^{-2\sqrt{S}\left(b_k^\dagger - b_k\right)}\right\} \\
&= \mathrm{Tr}\left\{e^{2\sqrt{S}\left(b_k^\dagger\left(e^{i\Omega t}-1\right)-b_k\left(e^{-i\Omega t}-1\right)\right)}\right\}\cdot e^{-4iS\sin(\Omega t)} \qquad \text{(B.17)} \\
&= \underbrace{\mathrm{Tr}\left\{e^{2\sqrt{S}b_k^\dagger\left(e^{i\Omega t}-1\right)}e^{-2\sqrt{S}b_k\left(e^{-i\Omega t}-1\right)}\right\}}_{=e^{-\frac{e^{-\beta\Omega}\cdot 4S(e^{i\Omega t}-1)(e^{-i\Omega t}-1)}{1-e^{-\beta\Omega}}}}\cdot\underbrace{e^{-4iS\sin(\Omega t)}\cdot e^{-2S(e^{i\Omega t}-1)(e^{-i\Omega t}-1)}}_{=e^{4S(e^{-i\Omega t}-1)}} \\
&= e^{-4S\left(2\coth\left(\frac{\beta\Omega}{2}\right)\sin^2\left(\frac{t\Omega}{2}\right)-i\cdot\sin(t\Omega)\right)}. \qquad \text{(B.18)}
\end{aligned}
$$

B.3.4. Putting the Master Equation together

Since we have an additional index in the definition of system and bath operators, thus $S_{k_i}$and B_{k_i}, $i \in 1,2$, we have to change the summation in the upper defined master equation (B.2) to

$$
\frac{d}{dt}\rho(t) = -i[H,\rho(t)] - \sum_{k,j}\left(S_{k,j}D_{k,j}\rho(t) - D_{k,j}\rho(t)S_{k,j} + \rho(t)E_{k,j}S_{k,j} - S_{k,j}\rho(t)E_{k,j}\right), \qquad \text{(B.19)}
$$

with

$$
\begin{aligned}
D_{k,j} &= \int_0^\infty d\tau \sum_{l,i} C_{kl}^{ji}(\tau)\tilde{S}_{l,i}(-\tau)\,, \qquad \text{(B.20)} \\
E_{k,j} &= \int_0^\infty d\tau \sum_{l,i} C_{lk}^{j,i}(-\tau)\tilde{S}_{l,i}(-\tau)\,, \\
C_{kl}^{ij}(t) &= Tr_B\rho_B\tilde{B}_{k,i}(t)\tilde{B}_{l,j}(t=0) \text{ die Bath-correlation functions}\,.
\end{aligned}
$$

B.3.4.1. Calculation in Parts

We are going to calculate now the expressions appearing in the $\sum_{k,i}$.

$$
\begin{aligned}
D_{k,1} &= \int_0^\infty d\tau \sum_l C_{kl}^{11}(\tau)\tilde{S}_{l,1}(-\tau) + C_{kl}^{12}(\tau)\tilde{S}_{l,2}(-\tau) \qquad \text{(B.21)}\\
&= \int_0^\infty d\tau \Big\{ \sum_{l\neq k} \Big(C_{kl}^{11} \sum_m a_m \sigma_l^+ e^{i\overbrace{(\omega_m - \Delta)}^{=\delta_m}\tau} + C_{kl}^{12} \sum_m a_m^\dagger \sigma_l^- e^{-i\delta_m\tau} \Big)\\
&\quad + C_{kk}^{11} \sum_m a_m \sigma_k^+ e^{i\delta_m\tau} + C_{kk}^{12} \sum_m a_m \sigma_k^+ e^{-i\delta_m\tau} \Big\}\\
&= C_{kl}^{11} \sum_{l\neq k,m} a_m \sigma_l^+ \int_0^\infty d\tau\, e^{i\delta_m\tau} + C_{kl}^{12} \sum_{l\neq k,m} a_m^\dagger \sigma_l^- \int_0^\infty d\tau\, e^{-i\delta_m\tau}\\
&\quad + \sum_m a_m \sigma_k^+ \int_0^\infty d\tau\, C_{kk}^{11} e^{i\delta_m\tau} + \sum_m a_m^\dagger \sigma_k^- \int_0^\infty d\tau\, C_{kk}^{12} e^{-i\delta_m\tau}.
\end{aligned}
$$

$$
\begin{aligned}
D_{k,2} &= \int_0^\infty d\tau \sum_l C_{kl}^{21}(\tau)\tilde{S}_{l,1}(-\tau) + C_{kl}^{22}(\tau)\tilde{S}_{l,2}(-\tau) \qquad \text{(B.22)}\\
&= \int_0^\infty d\tau \Big\{ \sum_{l\neq k} \Big(C_{kl}^{21} \sum_m a_m \sigma_l^+ e^{i\overbrace{(\omega_m - \Delta)}^{=\delta_m}\tau} + C_{kl}^{22} \sum_m a_m^\dagger \sigma_l^- e^{-i\delta_m\tau} \Big)\\
&\quad + C_{kk}^{21} \sum_m a_m \sigma_k^+ e^{i\delta_m\tau} + C_{kk}^{22} \sum_m a_m \sigma_k^+ e^{-i\delta_m\tau} \Big\}\\
&= C_{kl}^{21} \sum_{l\neq k,m} a_m \sigma_l^+ \int_0^\infty d\tau\, e^{i\delta_m\tau} + C_{kl}^{22} \sum_{l\neq k,m} a_m^\dagger \sigma_l^- \int_0^\infty d\tau\, e^{-i\delta_m\tau}\\
&\quad + \sum_m a_m \sigma_k^+ \int_0^\infty d\tau\, C_{kk}^{21} e^{i\delta_m\tau} \quad + \sum_m a_m^\dagger \sigma_k^- \int_0^\infty d\tau\, C_{kk}^{22} e^{-i\delta_m\tau}.
\end{aligned}
$$

We can evaluate now

$$
\begin{aligned}
\sum_{k,i} S_{k,i} D_{k,i}\rho(t) &= \sum_k S_{k,1} D_{k,1}\rho(t) + S_{k,2} D_{k,2}\rho(t)\\
&= \sum_k \left(\sum_{m'} a_{m'} \sigma_k^+ \right) \cdot D_{k,1}\rho(t) + \sum_k \left(\sum_{m'} a_{m'}^\dagger \sigma_k^- \right) D_{k,2}\rho(t). \qquad \text{(B.23)}
\end{aligned}
$$

Inserting the upper relation for D and using that $\sigma_i^{(\pm)}\sigma_j^{(\pm)} = 0, \sigma_i^+\sigma_j^- = \delta_{i,j}\sigma_i^+\sigma_i^-$ leads to

$$\sum_{k,i} S_{k,i}D_{k,i}\rho(t) = \sum_k \sum_{m,m'} a_{m'}\sigma_k^\dagger a_m^\dagger \sigma_k^- \underbrace{\int_0^\infty d\tau \underbrace{C_{kk}^{12}}_{\equiv f(t)} \cdot e^{-i\delta_m\tau}\,\rho}_{=K(-\delta_m)} + \sum_k \sum_{m,m'} a_{m'}^\dagger \sigma_k^- a_m \sigma_k^+ \underbrace{\int_0^\infty d\tau \underbrace{C_{kk}^{21}}_{\equiv f(t)} \cdot e^{i\delta_m\tau}\,\rho}_{=K(\delta_m)} \tag{B.24}$$

We use now a rotating wave approximation, neglecting the terms $a_m^\dagger a_{m'}$ with different $m \neq m'$. We get then

$$\sum_{k,i} S_{k,i}D_{k,i}\rho(t) = \sum_k \sum_m a_m\sigma_k^\dagger a_m^\dagger \sigma_k^- K(-\delta_m)\rho + \sum_k \sum_m a_m^\dagger \sigma_k^- a_m \sigma_k^+ K(\delta_m)\rho. \tag{B.25}$$

$$\begin{aligned} E_{k,1} &= \int_0^\infty d\tau \sum_l C_{lk}^{11}(-\tau)\tilde{S}_{l,1}(-\tau) + C_{lk}^{21}(-\tau)\tilde{S}_{l,2}(-\tau) \\ &= \int_0^\infty d\tau \Bigg\{ \sum_{l\neq k} \left[C_{lk}^{11} \sum_m a_m\sigma_l^+ e^{i\delta_m\tau} + C_{lk}^{21} \sum_m a_m^\dagger \sigma_l^- e^{-i\delta_m\tau} \right] \\ &\qquad + C_{kk}^{11}(-\tau) \sum_m a_m\sigma_k^+ e^{i\delta_m\tau} + C_{kk}^{21}(-\tau) \sum_m a_m\sigma_k^+ e^{-i\delta_m\tau} \Bigg\} \\ &= C_{k\lambda}^{11} \sum_{l\neq k,m} a_m\sigma_l^+ \int_0^\infty d\tau\, e^{i\delta_m\tau} + C_{k\lambda}^{21} \sum_{l\neq k,m} a_m^\dagger \sigma_l^- \int_0^\infty d\tau\, e^{-i\delta_m\tau} \\ &+ \sum_m a_m\sigma_k^+ \int_0^\infty d\tau\, C_{kk}^{11}(-\tau) e^{i\delta_m\tau} + \sum_m a_m^\dagger \sigma_k^- \int_0^\infty d\tau\, C_{kk}^{21}(-\tau) e^{-i\delta_m\tau}. \end{aligned} \tag{B.26}$$

$$\begin{aligned} E_{k,2} &= \int_0^\infty d\tau \sum_l C_{lk}^{12}(-\tau)\tilde{S}_{l,1}(-\tau) + C_{lk}^{22}(-\tau)\tilde{S}_{l,2}(-\tau) \\ &= \int_0^\infty d\tau \Bigg\{ \sum_{l\neq k} \left[C_{lk}^{12} \sum_m a_m\sigma_l^+ e^{i\delta_m\tau} + C_{lk}^{22} \sum_m a_m^\dagger \sigma_l^- e^{-i\delta_m\tau} \right] \\ &\qquad + C_{kk}^{12}(-\tau) \sum_m a_m\sigma_k^+ e^{i\delta_m\tau} + C_{kk}^{22}(-\tau) \sum_m a_m\sigma_k^+ e^{-i\delta_m\tau} \Bigg\} \\ &= C_{k\lambda}^{12} \sum_{l\neq k,m} a_m\sigma_l^+ \int_0^\infty d\tau\, e^{i\delta_m\tau} + C_{k\lambda}^{22} \sum_{l\neq k,m} a_m^\dagger \sigma_l^- \int_0^\infty d\tau\, e^{-i\delta_m\tau} \\ &+ \sum_m a_m\sigma_k^+ \int_0^\infty d\tau\, C_{kk}^{12}(-\tau) e^{i\delta_m\tau} + \sum_m a_m^\dagger \sigma_k^- \int_0^\infty d\tau\, C_{kk}^{22}(-\tau) e^{-i\delta_m\tau}. \end{aligned} \tag{B.27}$$

This allows the evaluation of

$$\sum_{k,i} \rho(t) E_{k,i} S_{k,i} = \sum_{k} \rho(t) E_{k,1} S_{k,1} + \rho(t) E_{k,2} S_{k,2} \tag{B.28}$$

$$= \sum_{k} \rho(t) E_{k,1} \left(\sum_{m'} a_{m'} \sigma_k^+ \right) + \sum_{k} \rho(t) E_{k,2} \left(\sum_{m'} a_{m'}^\dagger \sigma_k^- \right)$$

$$= \sum_{k} \rho \sum_{m,m'} a_m^\dagger \sigma_k^- a_{m'} \sigma_k^+ \underbrace{\int_0^\infty d\tau \underbrace{C_{kk}^{21}(-\tau)}_{\equiv f(-t)} \cdot e^{-i\delta_m \tau}}_{=K(-\delta_m)}$$

$$+ \sum_{k} \rho \sum_{m,m'} a_m \sigma_k^+ a_{m'}^\dagger \sigma_k^- \underbrace{\int_0^\infty d\tau \underbrace{C_{kk}^{12}(-\tau)}_{\equiv f(-t)} \cdot e^{i\delta_m \tau}}_{=K(\delta_m)} \tag{B.29}$$

$$\overset{\text{RWA}}{=} \sum_{k} \rho \sum_{m} a_m^\dagger \sigma_k^- a_m \sigma_k^+ K(-\delta_m) + \sum_{k} \rho \sum_{m} a_m \sigma_k^+ a_m^\dagger \sigma_k^- K(\delta_m). \tag{B.30}$$

Remark: for the real part is valid $f(t) = f(-t)$.

The last two sums of the master equation can now be evaluated. We use on this stage the RWA two times, one for the $\sigma_i^\pm$ and one for the a_j operators. We get then

$$\sum_{k,i} D_{k,i} \rho S_{k,i} = \sum_{k,m} a_m^\dagger \sigma_k^- \rho a_m \sigma_k^+ K(-\delta_m) + \sum_{k,m} a_m \sigma_k^+ \rho a_m^\dagger \sigma_k^- K(\delta_m), \tag{B.31}$$

$$\sum_{k,i} S_{k,i} \rho E_{k,i} = \sum_{k,m} a_m^\dagger \sigma_k^- \rho a_m \sigma_k^+ K(-\delta_m) + \sum_{k,m} a_m \sigma_k^+ \rho a_m^\dagger \sigma_k^- K(\delta_m). \tag{B.32}$$

B.3.4.2. Putting all together

We insert all calculated terms into the master equation

$$\begin{aligned}
\dot{\rho} &= -i \left[H_0, \rho \right] \\
&\quad - \sum_{k,m} \Big[K(-\delta_m) a_m \sigma_k^\dagger a_m^\dagger \sigma_k^- \rho + K(\delta_m) a_m^\dagger \sigma_k^- a_m \sigma_k^+ \rho - 2K(-\delta_m) a_m^\dagger \sigma_k^- \rho a_m \sigma_k^+ \\
&\quad - K(\delta_m) 2 a_m \sigma_k^+ \rho a_m^\dagger \sigma_k^- + K(-\delta_m) \rho a_m^\dagger \sigma_k^- a_m \sigma_k^+ + K(\delta_m) \rho a_m \sigma_k^+ a_m^\dagger \sigma_k^- \Big] \\
&= -i \left[H_0, \rho \right] - \sum_{m,k} \left[K[-\delta_m] \mathcal{L}[a_m^\dagger \sigma_k^-] - K[\delta_m] \mathcal{L}[a_m \sigma_k^+] \right].
\end{aligned} \tag{B.33}$$

B.3.4.3. Additional Damping in the Master Equation

Till now the derived master equation does not describe the damping of the photonic modes a_m, the fluorescence and pumping of the dye molecules. Assuming that this process is also modelled by a master equation of Lindblad-form, we simply add them to the master equation:

$$\dot{\rho} = -i\,[H_0, \rho] - \sum_{m,k}\left[\frac{\Gamma[-\delta_m]}{2}\mathcal{L}[a_m^\dagger \sigma_k^-] + \frac{\Gamma[\delta_m]}{2}\mathcal{L}[a_m \sigma_k^+]\right] - \sum_m \kappa/2\mathcal{L}[a_m] - \sum_k \frac{\Gamma_\uparrow}{2}\mathcal{L}[\sigma_k^+] - \sum_k \frac{\Gamma_\downarrow}{2}\mathcal{L}[\sigma_i^-]. \tag{B.34}$$

Here we have also redefined $\Gamma(\omega) = 2K(\omega)$.

B.3.5. Comparison of Derived $K(\omega)$ With Ref. [Kir13]

Our definition (with reinstalled g) for $K(\omega)$ is
$K(\omega) = g^2 \int_0^\infty dt f(t) e^{i\omega t}$.
It differs from Eq. 3 in Ref. [Kir13]:

- in Eq. 3 is $e^{-i\omega t}$ instead of $e^{i\omega t} \rightarrow$ is a typo.
- in Eq. 3 an additional $e^{-(\Gamma_\uparrow+\Gamma_\downarrow)t/2}$ is added

Our definition for $f(t)$ is

$$e^{-4S(2\coth\left(\frac{\beta\Omega}{2}\right)\sin^2\left(\frac{t\Omega}{2}\right)+i\cdot\sin(t\Omega))} = \exp\Big[-4S\int_{-\infty}^{\infty} d\nu\delta(\Omega-\nu)(2\coth\left(\frac{\beta\nu}{2}\right)\sin^2\left(\frac{t\nu}{2}\right) + i\cdot\sin(t\nu))\Big]. \tag{B.35}$$

In comparison to Eq. 4 of the Ref. [Kir13], δ-Function was replayed by some spectral density of the form

$$\frac{\gamma}{2\pi}\cdot\frac{1}{(\Omega-\nu)^2+\gamma^2/4}.$$

This replacement can be justified assuming that one have more general form of coupling to the phonon bath, like $\sqrt{S_{i,j}}\sigma_i^z(b_j + b_j^\dagger)$. This should lead to a change in the bath-correlation-function like: $f(t) \rightarrow \exp(...\sum_j(\sin^2()\coth()...))$. Introducing now the δ-function a spectral density function can be defined as $\sum_j \sqrt{S_{i,j}}\delta(\omega_n u - \nu)$.

B.3.6. Master Equation with Linear Coupling Term

The

$$\langle B\rangle = e^{-2S\coth(\frac{\beta\Omega}{2})}$$

term does not disappear. However for the in Ref. [Kir13] used values it is of order 10^{-35}. But for lower temperature this value increase strong.

B.4. Semiclassical Rate Equation

Using the master equation, we re-derive the semiclassical equations of motions for the mode population.

B.4.1. Equation for $\langle \hat{n}_m \rangle \equiv a_m^\dagger a_m$

Define

$$n_m(t) \equiv \langle \hat{n}_m \rangle \equiv \mathrm{Tr}\rho(t)\hat{n}_m,$$

where $\rho(t)$ obeys Eq. (2) in Ref. [Kir13]

We derive the terms on the r.h.s. of the differential equation $\dot{n}_m(t)$.

- Commutator term $-i[H_o, \rho]$ yields zero after tracing over since $[H_0, \hat{n}_m] = 0$.
- Term $-\sum_m \frac{\kappa}{2}\mathcal{L}[a_m]$: yields usual $-\kappa n_m(t)$ as for single damped harmonic oscillator.
- Term $-\sum_{im} \frac{\Gamma(-\delta_m)}{2}\mathcal{L}[a_m^\dagger \sigma_i^-]$ yields

$$\begin{aligned}
\dot{n}_m(t) &= ... - \sum_{in} \frac{\Gamma(-\delta_n)}{2} \mathrm{Tr}\hat{n}_m \left(\sigma_i^+ a_n a_n^\dagger \sigma_i^- \rho + \rho \sigma_i^+ a_n a_n^\dagger \sigma_i^- - 2 a_n^\dagger \sigma_i^- \rho \sigma_i^+ a_n\right) \\
&= ... - \sum_{in} \frac{\Gamma(-\delta_n)}{2} \left(\langle \sigma_i^+ \sigma_i^- \hat{n}_m a_n a_n^\dagger \rangle + \langle \sigma_i^+ \sigma_i^- a_n a_n^\dagger \hat{n}_m \rangle - 2\langle \sigma_i^+ \sigma_i^- a_n \hat{n}_m a_n^\dagger \rangle\right) \\
&= ... - \sum_{in} \frac{\Gamma(-\delta_n)}{2} \left(2\langle \sigma_i^+ \sigma_i^- \hat{n}_m (\hat{n_n} + 1)\rangle - 2\langle \sigma_i^+ \sigma_i^- a_n (a_n^\dagger \hat{n}_m + [\hat{n}_m, a_n^\dagger])\rangle\right) \\
&= ... - \sum_{in} \frac{\Gamma(-\delta_n)}{2} \left(-2\langle \sigma_i^+ \sigma_i^- a_n a_m^\dagger \delta_{nm}\rangle\right) \qquad \text{(B.36)} \\
&= ... + \sum_i \Gamma(-\delta_m) \langle \sigma_i^+ \sigma_i^- (\hat{n}_m + 1)\rangle \\
&\approx ... + \sum_i \Gamma(-\delta_m) \langle \sigma_i^+ \sigma_i^- \rangle \langle \hat{n}_m + 1\rangle, \qquad \text{(B.37)}
\end{aligned}$$

where we used cyclic invariance of the trace, the commutativity of the $a_n, a_n^\dagger$ with the $\sigma_i^\pm$ and the definition $\left\langle \hat{O} \right\rangle = Tr(\hat{O}\rho)$. In the last step, we employed the factorization assumption $\langle AB \rangle \approx \langle A \rangle \langle B \rangle$ between photonic operators A and atomic operators B. Here, this is introduced more or less ad hoc, but can be formalized via projection methods or similar.

Using the representation with atomic states bras and kets for atom i,

$$\sigma_i^- \equiv |0\rangle_i\langle 1|, \quad \sigma_i^+ \equiv |1\rangle_i\langle 0| \rightsquigarrow \sigma_i^- \sigma_j^- = 0, \quad \sigma_i^+ \sigma_j^- = \delta_{ij}|1\rangle_i\langle 1|, \qquad \text{(B.38)}$$

we obtain a simple interpretation of the above expression

$$\sum_i \Gamma(-\delta_m)\langle\sigma_i^+\sigma_i^-\rangle\langle\hat{n}_m+1\rangle = N\Gamma(-\delta_m)p_1(t)\langle\hat{n}_m+1\rangle$$

with

$$p_1(t) \equiv \langle\sigma_i^+\sigma_i^-\rangle$$

being the occupation of the upper level of one of the N equivalent two-level systems i - thus the factor N. This describes the temporal change of the photon mode occupation due to a (spontaneous plus induced) decay of the upper levels, each at rate $\Gamma(-\delta_m)$.

Similarly, there has to be the opposite process of excitation from the lower level by absorption of photons, leading to a reduction of photon occupation as

$$\dot{n}_m = ... - N\Gamma(\delta_m)p_0(t)\langle\hat{n}_m\rangle$$

with

$$p_0(t) \equiv \langle\sigma_i^-\sigma_i^+\rangle = 1 - p_1(t),$$

where the last equality follows from conservation of probability. This should also follow directly from the term $-\sum_{im}\frac{\Gamma(\delta_m)}{2}\mathcal{L}[a_m\sigma_i^+]$ in Eq. (2) Ref. [Kir13]

- Term $-\sum_i\frac{\Gamma_\uparrow}{2}\mathcal{L}[\sigma_i^+]$: yields no contribution

$$\dot{n}_m(t) = ... - \sum_i\left(\langle\hat{n}_m\sigma_i^-\sigma_i^+\rangle + \langle\hat{n}_m\sigma_i^-\sigma_i^+\rangle - 2\langle\hat{n}_m\sigma_i^-\sigma_i^+\rangle\right) = ... - 0 \qquad \text{(B.39)}$$

  owing to commutativity of the $a_n, a_n^\dagger$ with the $\sigma_i^\pm$.

- In a similar way, the term with $-\sum_i\frac{\Gamma_\downarrow}{2}\mathcal{L}[\sigma_i^-]$ yields no contribution.

These are all terms from Eq. (2) Ref. [Kir13]. Summing them up, we obtain the first main set of equations

$$\dot{n}_m(t) = -\kappa n_m(t) + N\Gamma(-\delta_m)p_1(t)(n_m(t)+1) - N\Gamma(\delta_m)\left(1-p_1(t)\right)n_m(t). \qquad \text{(B.40)}$$

We recognize that in order to close these equations, we need the equation of motion for $p_1(t)$.

B.4.2. Equation for $p_1(t) \equiv \langle\sigma_i^+\sigma_i^-\rangle$

Note that $p_1(t)$ does not depend on the index i if we assume all two-level systems i to be equivalent.

- Commutator term $-i[H_o, \rho]$ yields zero after tracing over since $[H_0, \sigma_i^+\sigma_i^-] = 0$.

- Term $-\sum_i \frac{\Gamma_\uparrow}{2}\mathcal{L}[\sigma_i^+]$ yields

$$\begin{aligned}\dot{p}_1(t) =& ... - \sum_j \frac{\Gamma_\uparrow}{2}\mathrm{Tr}\sigma_i^+\sigma_i^-\left(\sigma_j^-\sigma_j^+\rho + \rho\sigma_j^-\sigma_j^+ - 2\sigma_j^+\rho\sigma_j^-\right)\\ =& ... + \Gamma_\uparrow\langle\sigma_i^-\sigma_i^+\rangle = ... + \Gamma_\uparrow p_0(t).\end{aligned} \tag{B.41}$$

- Similarily, the term $-\sum_i \frac{\Gamma_\downarrow}{2}\mathcal{L}[\sigma_i^-]$ yields

$$\dot{p}_1(t) = ... - \Gamma_\downarrow p_1(t). \tag{B.42}$$

- The term $\propto \kappa$ in Eq. (2) Ref. [Kir13] yields zero as the atomic and photonic operators commute.

- The term $\propto \Gamma(-\delta_m)$ in Eq. (2) Ref. [Kir13] yields

$$\begin{aligned}\dot{p}_1(t) =& ... - \sum_{jm} \frac{\Gamma(-\delta_m)}{2}\mathrm{Tr}\sigma_i^+\sigma_i^-\left(\sigma_j^+ a_m a_m^\dagger\sigma_j^-\rho + \rho\sigma_j^+ a_m a_m^\dagger\sigma_j^- - 2a_m^\dagger\sigma_j^-\rho\sigma_j^+ a_m\right)\\ =& ... - \sum_{jm} \frac{\Gamma(-\delta_m)}{2}\delta_{ij}2\langle\sigma_j^+\sigma_j^- a_m a_m^\dagger\rangle \approx ... - \sum_m \Gamma(-\delta_m)\langle\sigma_i^+\sigma_i^-\rangle\langle a_m a_m^\dagger\rangle\\ =& ... - p_1(t)\sum_m \Gamma(-\delta_m)\langle a_m a_m^\dagger\rangle,\end{aligned} \tag{B.43}$$

  where we again used the bra-ket representation of the σ operators and factorized.

- In an analogous fashion, the term $\propto \Gamma(\delta_m)$ in (2) Ref. [Kir13] yields

$$\begin{aligned}\dot{p}_1(t) =& ... - \sum_{jm} \frac{\Gamma(\delta_m)}{2}\mathrm{Tr}\sigma_i^+\sigma_i^-\left(\sigma_j^- a_m^\dagger a_m\sigma_j^+\rho + \rho\sigma_j^- a_m^\dagger a_m\sigma_j^+ - 2a_m\sigma_j^+\rho\sigma_j^- a_m^\dagger\right)\\ =& ... + \sum_{jm} \frac{\Gamma(\delta_m)}{2}\delta_{ij}2\langle\sigma_j^-\sigma_j^+ a_m^\dagger a_m\rangle \approx ... + \sum_m \Gamma(\delta_m)\langle\sigma_i^-\sigma_i^+\rangle\langle a_m^\dagger a_m\rangle\\ =& ... + (1-p_1(t))\sum_m \Gamma(\delta_m)\langle a_m^\dagger a_m\rangle,\end{aligned} \tag{B.44}$$

  where again we used $\langle\sigma_i^-\sigma_i^+\rangle \equiv p_0(t) = 1 - p_1(t)$ in the last step.

These are all terms from Eq. (2) Ref. [Kir13] Summing them up, we obtain

$$\dot{p}_1(t) = \Gamma_\uparrow(1-p_1(t)) - \Gamma_\downarrow p_1(t) - p_1(t)\sum_m \Gamma(-\delta_m)\langle a_m a_m^\dagger\rangle + (1-p_1(t))\sum_m \Gamma(\delta_m)\langle a_m^\dagger a_m\rangle. \tag{B.45}$$

Here, an issue arises now concerning the **degeneracy** g_m of the photonic levels m. Apparently, Ref. [Kir13] use

$$\sum_m \Gamma(-\delta_m)\langle a_m a_m^\dagger\rangle = \sum_m \Gamma(-\delta_m) g_m (n_m(t)+1), \quad \sum_m \Gamma(\delta_m)\langle a_m^\dagger a_m\rangle = \sum_m \Gamma(\delta_m) g_m n_m(t). \tag{B.46}$$

This leads to our main equation for $p_1(t)$,

$$\begin{aligned}\dot{p}_1(t) = \Gamma_\uparrow(1-p_1(t)) - \Gamma_\downarrow p_1(t) - p_1(t)\sum_m \Gamma(-\delta_m) g_m (n_m(t)+1) \\ + (1-p_1(t))\sum_m \Gamma(\delta_m) g_m n_m(t).\end{aligned} \tag{B.47}$$

B.4.3. Adiabatic Elimination

This consists in solving the $\dot{p}_1(t)$ equation with fixed n_m for its stationary value at $t \to \infty$, leading to

$$\begin{aligned} p_1(t\to\infty) = \frac{\tilde{\Gamma}_\uparrow}{\tilde{\Gamma}_\uparrow + \tilde{\Gamma}_\downarrow}, \quad 1 - p_1(t\to\infty) = \frac{\tilde{\Gamma}_\downarrow}{\tilde{\Gamma}_\uparrow + \tilde{\Gamma}_\downarrow} \\ \tilde{\Gamma}_\uparrow \equiv \Gamma_\uparrow + \sum_m \Gamma(\delta_m) g_m n_m, \quad \tilde{\Gamma}_\downarrow \equiv \Gamma_\downarrow + \sum_m \Gamma(-\delta_m) g_m (n_m+1). \end{aligned} \tag{B.48}$$

Here, the n_m are assumed as time-independent. When re-introducing the time-dependence into the n_m and inserting these results into the $\dot{n}_m$ equation, we obtain

$$\dot{n}_m(t) = -\kappa n_m(t) + N\Gamma(-\delta_m)(n_m(t)+1)\frac{\tilde{\Gamma}_\uparrow}{\tilde{\Gamma}_\uparrow + \tilde{\Gamma}_\downarrow} - N\Gamma(\delta_m) n_m(t)\frac{\tilde{\Gamma}_\downarrow}{\tilde{\Gamma}_\uparrow + \tilde{\Gamma}_\downarrow}, \tag{B.49}$$

which is Eq. (5) of Ref. [Kir13].

B.4.4. Contribution of Linear Term in the Master Equation

The linear coupling term adds to the equation $\dot{n}_m$ and $\dot{p}_1$ an additional term of the form

$$i\langle B\rangle\left(\langle a_m\rangle(t=0)\sum_k\left\langle\sigma_k^+\right\rangle(t=0) - \left\langle a_m^\dagger\right\rangle(t=0)\sum_k\left\langle\sigma_k^-\right\rangle(t=0)\right)$$

for the $\dot{n}_m$-Equation (and similar for $\dot{p}_1$ equation). At the begin $t=0$, the system is assumed to be in thermal equilibrium. In this way $\langle a_m\rangle = 0$ and the linear term of the master equation is not important.

B.4.5. Solution of the Mean-Field Equation

Fig. B.1(b) shows solution of the mode occupation Eq. (B.49) in the steady state in two very different cases. For lower dissipation rate κ the Bose-Einstein distribution fits perfectly the occupation of different modes (left). Thus, the non-equilibrium steady state of the system behaves as a condensate. If the pumping strength $\Gamma_\uparrow$ overgrows a critical value, the ground mode becomes macroscopically occupied. In contrast, for higher dissipation rate κ the equilibrium distribution does not match any more (left). The system is in a lasing state, for higher pumping strength $\Gamma_\uparrow$ an excited mode becomes macroscopically occupied.

In the following, we want to influence the system dynamic by time delayed control.

B.5. Time-Delayed Feedback Control Applied to Photon Condensation Model

Here we sketch the assumed feedback types, the correspondent results and discuss them in context of feedback and model properties.

B.5.1. Feedback Types

The idea of the feedback control is to measure the mean photon flux out of the cavity, which should be simple proportional to the occupation of the corresponding cavity mode and to couple this information back into the system.

We considered following types of feedback

A. Based only on the Eq. (B.49) for the occupation of the mth optical mode

$$\dot{n}_m(t) = -\kappa n_m(t) + N\Gamma(-\delta_m)(n_m(t)+1)\frac{\tilde{\Gamma}_\uparrow}{\tilde{\Gamma}_\uparrow+\tilde{\Gamma}_\downarrow} - N\Gamma(\delta_m)n_m(t)\frac{\tilde{\Gamma}_\downarrow}{\tilde{\Gamma}_\uparrow+\tilde{\Gamma}_\downarrow},$$

with the plugged in stationary solution of the p-Equation. We introduce then different types of feedback in the following ways

1) Adding the control operation C to the equation for $\dot{n}_m$, with

$$C = \lambda \sum_k g_k[n_k(t-\tau) - n_k(t)]. \tag{B.50}$$

The new equation with the control term becomes then

$$\dot{n}_m = ... + C.$$

2) Adding the control operation C_m to the equation for $\dot{n}_m$, with

$$C_m = \lambda g_m[n_m(t-\tau) - n_m(t)] \tag{B.51}$$

and the new equation with the control term becomes

$$\dot{n}_m = ... + C_m.$$

3) Modulating the number of active molecules by the control operation C_m.

$$C_m = \lambda / N g_m [n_m(t-\tau) - n_m(t)] \tag{B.52}$$

and we have to replace in the equation for n_m

$$N \to N = N_0 + C_m.$$

4) Modulating the number of active molecules by the control operation C_m

$$C_m = \lambda / N g_m [n_m(t-\tau) - n_m(t)] \tag{B.53}$$

and we have to replace in the n_m-equation

$$N \to N = N_0 + \sum_m C_m.$$

5) Modulating the coupling g between field modes and atoms by C_m

$$C_k = \lambda g_k [n_k(t-\tau) - n_k(t)] \tag{B.54}$$

and we have to replace in the n_m equation

$$g \to g = g_0 + C_k.$$

B. Based on the equations, where n and p are still coupled, thus the corresponding equations are

$$\dot{n}_m(t) = -\kappa n_m(t) + N\Gamma(-\delta_m) p_1(t)(n_m(t)+1) - N\Gamma(\delta_m)\left(1 - p_1(t)\right) n_m(t), \tag{B.55}$$

$$\begin{aligned} \dot{p}_1(t) = {} & \Gamma_\uparrow(1 - p_1(t)) - \Gamma_\downarrow p_1(t) - p_1(t) \sum_m \Gamma(-\delta_m) g_m (n_m(t)+1) \\ & + (1 - p_1(t)) \sum_m \Gamma(\delta_m) g_m n_m(t). \end{aligned} \tag{B.56}$$

1) Adding to the p_1 equation

$$C_k = \lambda g_k [n_k(t-\tau) - n_k(t)] \tag{B.57}$$

$$\dot{p}_1 = ... + C_k, \tag{B.58}$$

where k is one of the modes.

2) Adding to the p_1 Equation

$$C_m = \lambda(p_1(t-\tau) - p_1(t)) \tag{B.59}$$

$$\dot{p}_1 = ... + C_m. \tag{B.60}$$

C. Non-invasive feedback type. The outgoing photons are coupled back into a cavity with some time delay τ, defined for example by geometry of the system. It is done by a following control operation

$$C_m = \lambda n_m(t-\tau) \tag{B.61}$$

and the equation with control becomes

$$\dot{n}_m = ... + C_m.$$

In all cases, τ is the time delay and λ is a coupling strength. We will analyze the results for the feedback B1 and then briefly sum up the results of other coupling possibilities. It will turn out that the A-case has areas with unphysical behavior but all feedback types leads to a similar evolution.

B.5.2. Coupling of Type B

In the following we use different number of modes in a cavity and a positive and negative coupling strength λ. B1 feedback changes the inversion of the atoms. Thus, in the real experimental setup the inversion of the atoms could be additionally manipulated depending on the feedback signal. We allow the feedback strength λ to be as positive as also negative. The $\lambda < 0$ case would then correspond to the lowering of the atom inversion and leads to more interesting results.

B.5.2.1. Dynamical Evolution

Fig. B.2 shows the typical system dynamics in presence of time delayed feedback. Whereas the $\lambda > 0$ case slows down the system equilibration time (green curves), the $\lambda < 0$ case may induce oscillating behavior (blue curves). At some critical feedback coupling strength λ_{cr} (red curves) the system observables show non damped oscillating behavior. In this case the feedback balances the system losses. For $\lambda < \lambda_{cr}$ the feedback input is so strong that the observables grow instantaneous. From the inversion p_1 Fig. B.2(c) we see that the $\lambda < 0$ can also speed up the dynamics. This however depends on parameter values.

B.5.2.2. Stability Analysis

This findings maintains the linear stability analysis (not shown here explicitly). The stability equation shows that $\lambda > 0$ case indeed never destabilize the system and slows down the relaxation time. Fig. B.3 shows the critical λ as a function of time delay for different values of Γ. An interesting finding is that for the used parameter vales λ_{cr} is independent from the modes number. Additionally Fig. B.3(b) shows the behaviour of the system in the $n_0 - p_1$-plane.

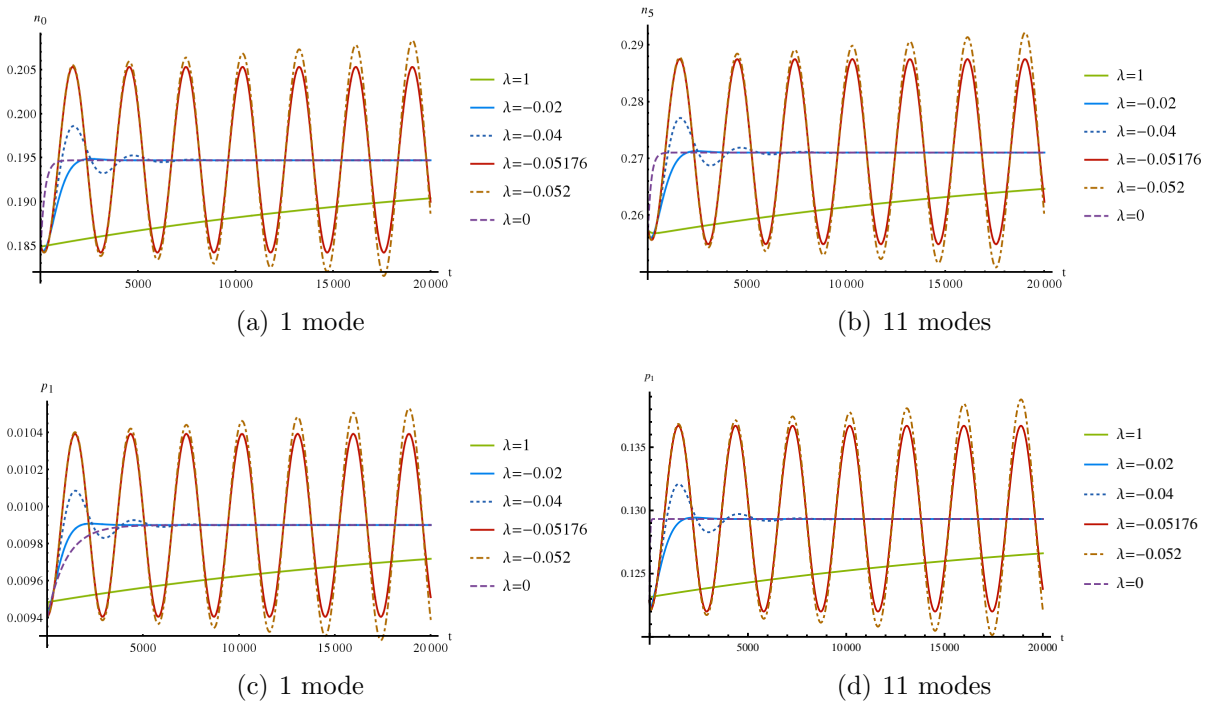

(a) 1 mode (b) 11 modes

(c) 1 mode (d) 11 modes

Figure B.2.: The time evolution of the optical mode occupation and of the inversion for $\tau = 1$ ps and different coupling strength λ. Whereas $\lambda > 0$ leads only to the increase of the characteristic time scale (green curve) of the system, $\lambda < 0$ may prevent the system to reach equilibrium (red curve) and can destabilize it at all. The system in the left figures has 1 optical mode, the system in the right figures has 11 optical modes. Parameters: $\kappa = 5GHz, \Gamma_\uparrow = 0.01\Gamma_\downarrow$ other like in Fig. 2 in Ref. [Kir13].

B.5.2.3. Summing-up/Discussion

The B1-control slows down the dynamical evolution for $\lambda > 0$, but the negative feedback strength leads to the oscillating behavior for fixed value of λ. The dynamical evolution of this system (see Fig. B.3(b)) is equivalent to the harmonic oscillator with time delayed feedback, see the Theory part Sec. 2.2, or of two coupled equations with feedback [HÖ5]. It is also interesting from the mathematical point of view: The structure of our equations differs (especially for one mode) from Eq. (4) in Ref. [HÖ5] by the non-linear coupling term. But the non-linear term seems not to change the general dynamics by application of the time delay.
The system with B1-control remains also for $\lambda < \lambda_{cr}$ physical, for example the mode occupation is positive for tested parameter values.
Only in one case, where the feedback operation couples back the occupation of the macroscopically occupied mode to the p_1 equation, leads to a diverging and unphysical behavior of the whole system. Due to macroscopic values, the back coupled signal is very strong if compared to the value of p_1 and blows up the whole system after a very

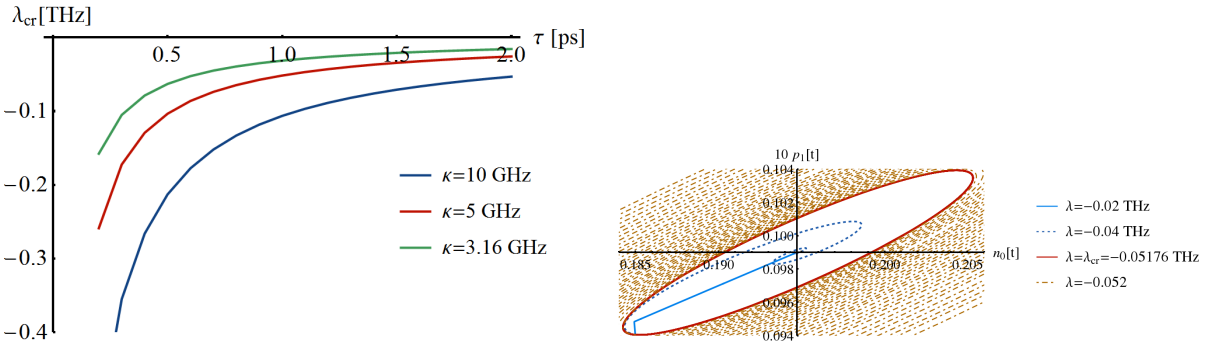

(a) 1 or 11 modes

(b) $\kappa = 5GHz, \tau = 1ps$

Figure B.3.: (left) The critical λ_c, where the oscillating behavior occurs, and the system losses are balanced by successful feedback application. For $\lambda < \lambda_c$ the system shows diverging behavior, whereas for $\lambda > \lambda_c$ the system tends to its fixed point. (right) Visualization in the $n_0 - p_1$-plane of different feedback strength λ for fixed κ, τ values. Parameters: $\Gamma_\uparrow = 0.01\Omega$, other like in Fig. 2 in Ref. [Kir13].

short time.

B.5.3. Coupling of Type A

B.5.3.1. Similar Behaviour as in Case B1

In general, all couplings of type A lead to the behavior described in the previous chapter. For $\lambda > 0$ the system dynamics slow down. For $\lambda < 0$ there is a critical value, where an oscillation occurs, followed by the blow up of the whole system. But for some configuration setups especially in the region $\lambda \approx \lambda_c$ or $\lambda < \lambda_c$, the occupation of some modes can became negative at some time values (due to the oscillating behavior), which is not physical any more. Note that by the A type of coupling, as in B1 case, one should couple the macroscopic occupation only to the mode, which is macroscopic occupied. Otherwise the numerical solution diverges and becomes unphysical.

B.5.3.2. Change the Number of Active Atoms

The A3 and A4 coupling modulates the number of active molecules. One have to pay attention that during the control the number of active particles remains positive. In Fig. B.4 we demonstrate the A3/A4 control operation and plot the number of active particles. But to achieve the effects as with the B1 feedback scheme, the values of λ should be quite large: $\lambda \approx -10\Omega$ for 11 modes in case of A4 type and $\lambda \approx -500\Omega$ for 1 mode. In both cases, for $\lambda > \lambda_{cr}$ the number of particles becomes negative. A4 type of coupling can produce even for $\lambda \lesssim \lambda_{cr}$ negative particle number values. In contrast, $A3$ type of coupling conserves the positivity of the particle number N till the feedback parameter λ gets smaller than λ_{cr}, see Fig. B.4(d). However, our numeric shows that

the increase of $\Gamma_\uparrow$ up to 10 times, so that the system gets one macroscopically occupied mode, lowers λ_{cr} approximately at 10 times. Note, in this case we should not couple the macroscopically occupied mode, otherwise we overdrive the whole system, as in schemas A and B. Note that the coupling A5 is equivalent to the coupling A4.

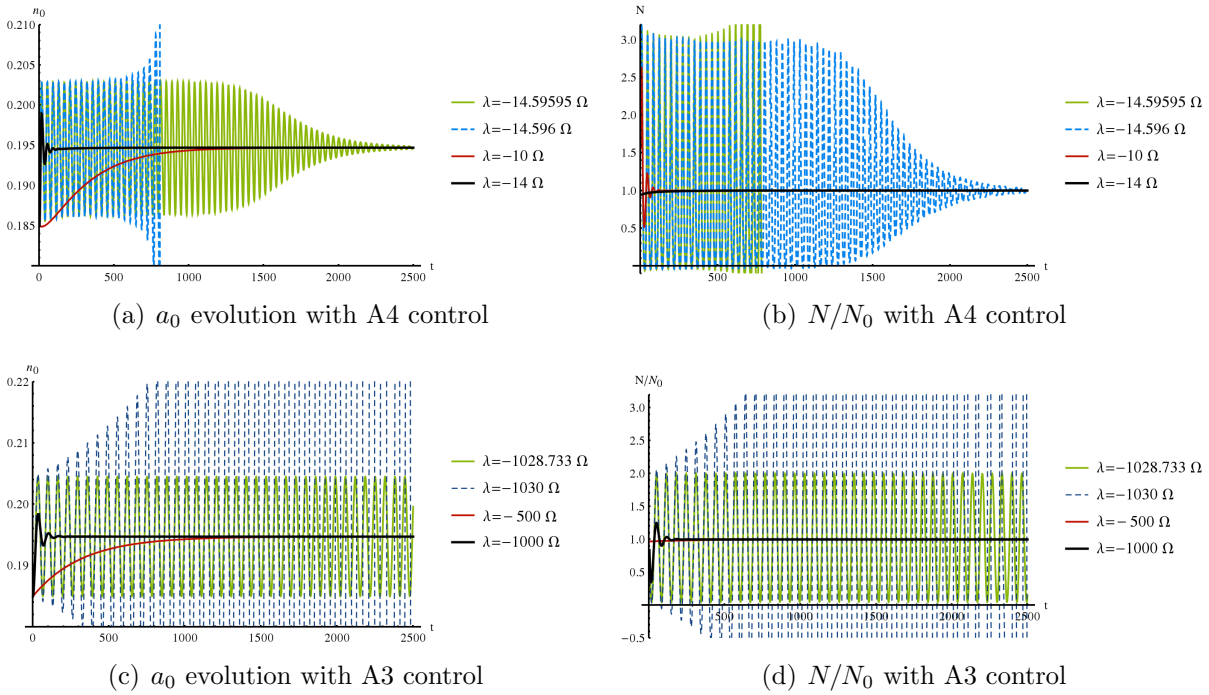

(a) a_0 evolution with A4 control

(b) N/N_0 with A4 control

(c) a_0 evolution with A3 control

(d) N/N_0 with A3 control

Figure B.4.: Occupation of the 1. optical mode with A3 (upper) /A4 (lower) control-type for different feedback strength λ (left). We see the transition from non-oscillating behaviour via oscillating to divergence for $\lambda > \lambda_{cr}$ for decreasing λ values. The dynamical evolution is typical for the A/B control types. (right) The number of active particle N as a function of time. The calculation was done for 11 modes. In A3-case we couple to the a_0-mode. Parameters: $\Gamma_\uparrow = 0.01\Omega$, $\tau\Omega = 1$.

B.5.4. Coupling of Type C

The invasive coupling can be interpreted as a modulation of the dissipation rate κ. The performed stability analysis shows that this kind of coupling can not destabilize the existing fixed points. But due to the non-Pyragas form, the feedback of type C can shift them. Indeed, the new stable point depends now on the value of effective $\tilde{\kappa} = \kappa - \lambda$. This shrinks the λ to its maximum value to prevent negative $\tilde{\kappa}$. This offers a possibility to shift the macroscopically occupied mode by increasing the λ -value. To tune through a lot of modes, one should start with a big dissipation rate κ and then increase the λ value. This effect should appear for arbitrary time delays τ, which

influence only the system dynamics. Fig. B.5.4 visualizes this effect. The increase of λ shifts the macroscopic occupation to the lower mode.

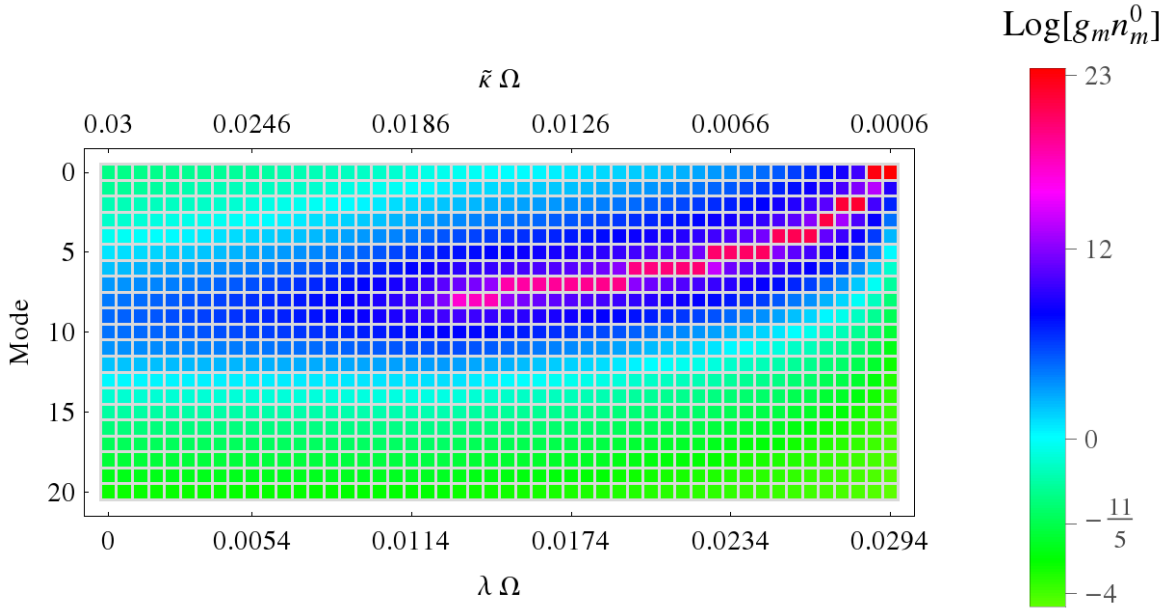

Figure B.5.: The mean occupation n_m of 20 modes depending on the feedback strength λ or effective dissipation rate κ. The macroscopic occupation (red) is shifted to the lower modes with increasing λ. Parameters: $\Gamma_\uparrow = 0.1\Gamma_\downarrow$.

B.6. Discussion

We applied different types of the Pyragas control (A,B types) and the invasive time delayed control (C) to the mean-field equations which describe a photon condensation. In general, all Pyragas feedback types have in this case in common that

- Positive feedback ($\lambda > 0$) only slows down the system dynamic and does not affect the fixed point stability
- Negative feedback ($\lambda < 0$) can destabilize the system:
  - there exist (at least one) $\lambda_{cr} < 0$, where the system observables oscillate undamped. The system is then in a new non-equilibrium oscillating phase, where the losses are covered by feedback.
  - For $\lambda > \lambda_{cr}$ the values of observables are diverging.
  - For $\lambda < \lambda_{cr}$ the observables tend to the stationary state.
- Some feedback types lead to an unphysical behavior even for $\lambda < \lambda_c r$.

- If the macroscopically occupied mode is coupled back to the system, it fixes the modes at initial values in most cases (from numerics).
- The described behavior is valid for different number of optical modes.

The Pyragas feedback is non-invasive, thus it can not add additional fixed points or shift the fixed points in a useful way. Interestingly - and in contrast to our model in chapter 5 - the mean field equations (B.49) have only one fixed point for all possible physical configurations. We subscribe it to the presence of the additional phonon damping which is included in this model. Even in our case, see chapter 5, multiple stable fixed points are only present for a small damping rate κ. For bigger κ values, only one non-trivial fixed point survives, see Fig. 5.2. The change between the condensate and a laser occurs for different system parameter values. That's why Pyragas type of feedback can not be used to switch between this states, as it vanishes in the steady state. In contrast the non-invasive coupling C does not disappear in a steady state, moreover it changes the fixed points and can be used to choose a mode, which is macroscopically occupied.

C. ESQPT Signal from Periodic Dynamic in Dicke and Tavis-Cummings Models

In this chapter we show how to get an ESQPT signal which is hidden in the periodic dynamic of the closed Dicke and Tavis-Cummings models. First, we extract the ESQPT signal from the periodic dynamic which is based on the mean-field equations of both models. Later, we show that this signal can be extracted from the time evolution of a coherent state. The results in the last case are mostly based on Ref. [Eng15].

C.1. Dicke Model

C.1.1. Semiclassical Equations

The Dicke Hamiltonian, see Eq. (3.1) for more information, is

$$H = \omega \hat{a}^\dagger \hat{a} + \omega_0 \hat{J}_z + \frac{g}{\sqrt{2j}}(\hat{a}^\dagger + \hat{a})(\hat{J}_+ + \hat{J}_-). \tag{C.1}$$

We obtain the corresponding equations of motion setting the decay rate κ in Eq. (3.11) to zero

$$\begin{aligned}
\partial_t a &= -i\omega a + i\frac{g}{\sqrt{N}}\left(J_+ + J_-\right), & \partial_t a^* &= i\omega a^* - i\frac{g}{\sqrt{N}}\left(J_+ + J_-\right), \\
\partial_t J_- &= -i\omega_0 J_- + 2i\frac{g}{\sqrt{N}}(aJ_z + a^* J_z), & \partial_t J_+ &= i\omega_0 J_+ - 2i\frac{g}{\sqrt{N}}(aJ_z + a^* J_z), \\
\partial_t J_z &= i\frac{g}{\sqrt{N}}(a^* + a)(J_- - J_+).
\end{aligned} \tag{C.2}$$

C.1.2. Energy Landscape

The Dicke Hamiltonian preserves the spin length j, which we assume to be at a maximum value $j = N/2$. Additionally, in absence of dissipation the energy is fixed for a given system configuration. Using in Eq. (C.1) the polar representation of the angular momentum part with the angels φ and θ, splitting the mode variable a in its real and imaginary parts $a = x + iy$ and normalizing with respect to N, we obtain the energy landscape in the thermodynamic limit

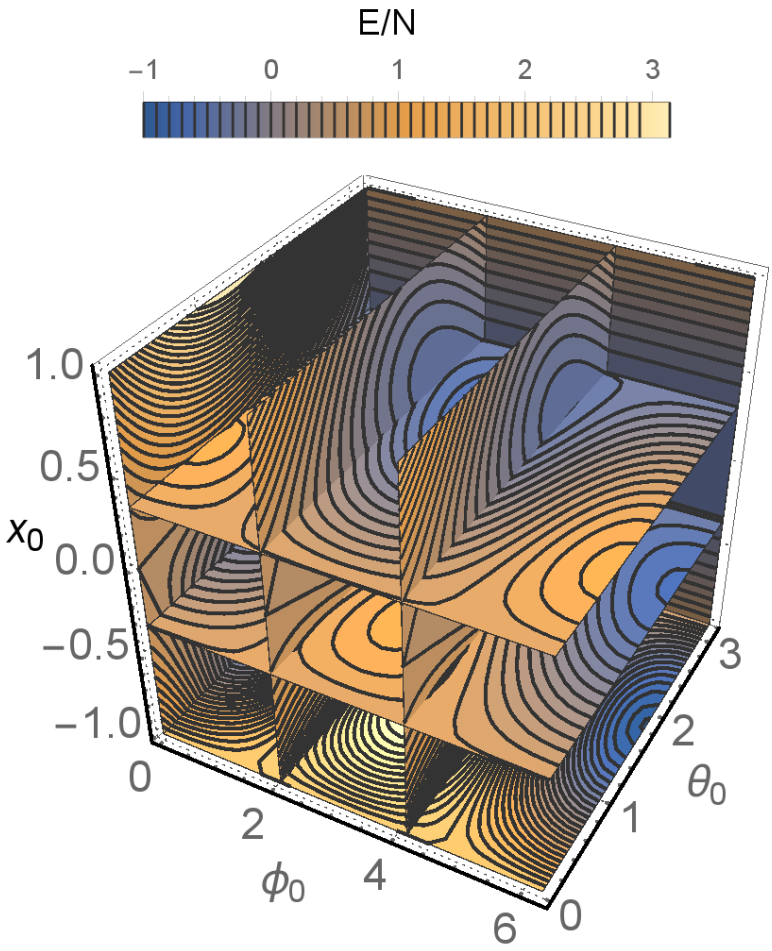

Figure C.1.: Cuts through an energy landscape, Eq. (C.3). Coloring represents the normalized energy for a given system configuration $(x/N, y/N, \phi, \theta) = (x_0, 0, \phi_0, \theta)$. Contour lines represent cuts through a regions with equal energy. Parameters: $\omega = \omega_0, g = \omega_0$.

$$E = (x^2 + y^2)\omega + \frac{1}{2}N\omega_0 \cos(\theta) + 2\sqrt{N}gx \cos(\varphi)\sin(\theta). \tag{C.3}$$

However, due to a four dimensional space of initial conditions, there are various combinations leading to the same energy. Figure C.1 shows cuts through the energy space. Black contour lines have the same energy and represent only a cut through a four-dimensional manifold of points with equal energy within.

C.1.3. Averaged Dynamics

We solve the equations of motion Eq. (C.2) in the superradiant regime for different initial conditions $J_z/N \in \{-0.5, 0.5\}$ and $x/N \in \{-6.5, 1.5\}$, keeping $J_y = y = 0$. The trajectory is chaotic [Ema03a, BM14b]. However, averaged over time from zero

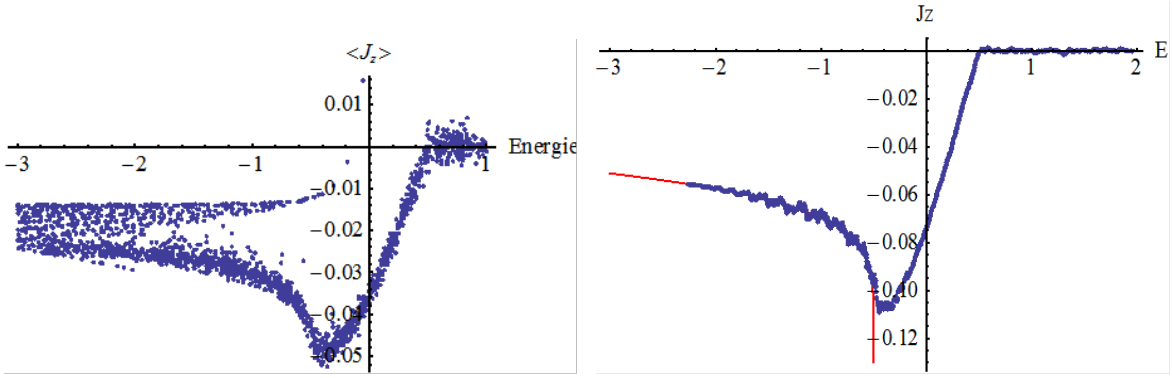

(a) (b)

Figure C.2.: (a) Averaged J_z value for different initial condition as a function of energy. (b) Additional average over 30 points and an exponential fit. The divergence at $E = -0.5N$ is due to the ESQPT. Parameters: $\omega = \omega_0, g = 1.5\omega_0$.

to $t_1 \gg 0$ converges to a fixed value. Figure C.2 shows an averaged value for the J_z component.

In the left part of Fig. C.2(a) we see an averaged value for each chosen initial condition. For $E < 0$ there are two different branches. Averaging over 30 data points sorted by energy we obtain only one branch C.2(b) which has a minimum around the ESQPT energy $E = -0.5N$. Note that both figures are qualitatively the same as in Refs. [PF11b, BM14b], where the data was obtained from a quantum mechanical calculation for finite lattice size. Moreover, the left part can be fitted with an power-law function $A + B|E + 0.5|^c$ with a critical exponent $c = 0.15$, which is in the rage of a critical exponent discussed in Ref. [PF11b].

C.2. Tavis-Cummings model

In this section we consider a rotating wave approximation (RWA) of the Dicke model, known as the Tavis-Cummings Model. We show that its mean-field description predicts correctly results for the time-averaged system observables in the thermodynamic limit as the corresponding quantum calculation. We emphasizing the role of the excitation number

$$\hat{M} = \hat{J}_z + \hat{a}^\dagger \hat{a}$$

which is conserved in this model in contrast to the non-RWA case. In the last part of this section we consider a coherent state and show how to obtain an ESQPT signal from its quantum mechanical evolution.

The Tavis-Cummings Model [Tav68] is a quantum optical model, where the N two-level atoms, described by collective angular momentum operators $\hat{J}_i = \frac{1}{2}\sum_{j=1}^{N} \sigma_i^j$, $\hat{J}_\pm = \frac{1}{2}\sum_{j=1}^{N} \sigma_\pm^j$, $i \in \{x, y, z\}$ are interacting with one bosonic mode a. The corresponding Hamiltonian has the form

$$\hat{H}_{TC} = \omega \hat{a}^\dagger \hat{a} + \omega_0 \hat{J}_z + \frac{g_0}{\sqrt{2j}} \left(\hat{a} \hat{J}_+ + \hat{a^\dagger} \hat{J}_- \right) \tag{C.4}$$

and corresponds to a Dicke Hamiltonian Eq. (C.1) where the non-counter rotating terms aJ_- and $a^\dagger J_+$ are skipped due to RWA. Besides the energy conservation, this model has two additional conserved quantities. The length of the collective spin $\hat{J}^2$ and the excitation number $\hat{M} = \hat{a}^\dagger \hat{a} + \hat{J}_z$ commutes with H_{TC} and are therefore conserved [Tav68]. A quantum mechanical state of the TC model can be described in a basis build by photon number states $|n\rangle$ and the Dicke states of the atomic system $|jm\rangle$, which are the eigenstates of $\hat{a}^\dagger \hat{a}$ and $\hat{J}^2$ operators, respectively. The $\hat{J}^2$-conservation divides the Hilbert space in independent blocks with a fixed quantum number j. Each block can be described with only two quantum numbers using the basis $\langle nm|$, where the quantum number j is fixed between 0 and $N/2$. We consider only states with the maximum spin length and set $l = N/2$. The $\hat{M}$ conservation implies $M = n + m$ and restricts the still infinite Hilbert space $|nm\rangle$ to a finite one, $|nm\rangle \to |n, M - m\rangle$. Especially this fact allows to perform an exact numerical diagonalization at the quantum level. Its basis contains $M + j + 1$ states if $M \leq j$ or $2j + 1$ states if $M \geq j$ [Nar73].

Even the TC model has a quantum phase transition which occurs, if the coupling g overgrows the critical coupling $g_c = \frac{|\omega - \omega_0|}{2}$ [PF11b]. The existing exact or approximated quantum mechanical solutions of this model [Tav68, Nar73, Bog00, Bra13] round off the existing numerical and semiclassical studies. The numerics was often used to calculate the expectation values especially to identify the ESQPT-signal [PF11a, BM14b], whereas the semiclassics allows to determine a potential or the density of states [PF11b, BM14a, Bra13]. However, the obtained results depend strongly on the quantum number M and on the usage of this additional quantum number in the calculations.
We show that also the mean-field-description of the Tavis-Cummings-Model coincides with the quantum-mechanical result in the thermodynamic limit for arbitrary M .

C.2.1. Mean-Field Equations

First, we derive the equations of motion for the Tavis-Cummings model using

$$d_t \left\langle \hat{O} \right\rangle = i \left\langle [\hat{H}_{TC}, \hat{O}] \right\rangle \equiv d_t O$$

and denote now the averaged values without a hat. Then, we factorize the averaged operator products like $\left\langle \hat{O}_1 \hat{O}_2 \right\rangle \to O_1 O_2$ obtaining a closed set of semiclassical equations of motion:

$$
\begin{aligned}
x'(t) &= \omega \cdot y(t) - \frac{g_0}{\sqrt{N}} \cdot J_y(t), \\
y'(t) &= -\omega \cdot x(t) - \frac{g_0}{\sqrt{N}} \cdot J_x(t), \\
J_x'(t) &= -\Omega_0 \cdot J_y(t) - 2 \cdot \frac{g_0}{\sqrt{N}} \cdot y(t) \cdot J_z(t), \\
J_y'(t) &= \Omega_0 \cdot J_x(t) - 2 \cdot \frac{g_0}{\sqrt{N}} \cdot x(t) \cdot J_z(t), \\
J_z'(t) &= 2\frac{g_0}{\sqrt{N}} \cdot (x(t) \cdot J_y(t) + y(t) \cdot J_x(t),
\end{aligned}
\tag{C.5}
$$

where we redefine $x = \Re(a), y = \Im(a)$ and use the known connection $J_\pm = J_x \pm iJ_y$. This semiclassical version fulfills all at quantum mechanical level conserved quantities, e.g. energy, spin length and excitation number. At the semiclassical level they become:

$$
\begin{aligned}
\hat{H} \to E_{TC} &= \omega(x^2 + y^2) + \omega_0 J_z + \frac{g_0}{\sqrt{N}} \left(xJ_x - yJ_y\right), \\
\hat{J}^2 \to J^2 &= J_x^2 + J_y^2 + J_z^2 = N^2/4, \quad \hat{M} \to M = x^2 + y^2 + J_z,
\end{aligned}
\tag{C.6}
$$

respectively.

Note that in the resonant case $\Omega = \Omega_0$ exist a known real valued solution (that means $y(t) = J_y(t) = 0$) in a closed form [Bon70]. In this case the conservation laws for H and M coincide.

The energy in Eq. C.6 can be written in a very compact way [Eng15]. First, we use the M conservation law to eliminate the x^2+y^2 term. Then, we parametrize the optical mode as $x = \alpha\cos(\vartheta), y = a\sin(\vartheta), a \in \mathcal{R}$. Finally we change into a rotated frame introducing rotated spin variables $\tilde{J}_x = J_x\cos(\vartheta) - J_y\sin\vartheta, \tilde{J}_y = J_x\sin(\vartheta) + J_y\cos(\vartheta), \tilde{J}_z = J_z$. The Last transformation introduces mixed variables for spin and cavity modes. The energy becomes then [Eng15]

$$
E_{TC} = \omega M + (\omega_0 - \omega)\tilde{J}_z + \frac{g_0}{\sqrt{N}}\sqrt{(M - \tilde{J}_z)}\tilde{J}_x. \tag{C.7}
$$

The advantage of such a representation is that the complete energy surface can then be visualized on a Bloch sphere, as the rotated spin variables still fulfill the spin length conservation law.

C.2.2. Numerical Procedure

We solve now Eq. (C.5) numerically. Without damping all observables remain oscillating with finite amplitude. We get the average of means, performing the time integration numerically.

Solving the system of coupled first order differential equation, we have to choose the initial condition $x(0) = x_0$, $y(0) = y_0$, $J_i(0) = J_{0,i}$, which have to agree with the conserved quantities. Typically we set $J_y(0) = 0$ and choose $J_z(0) \in \{-N/2, N/2\}$. We

choose for $x(0)$ some real value, in general out of the interval $[-5,5]\sqrt{N}$. The fixed number M determines then $y(0)$. The known initial conditions allow also the calculation of the classical energy H.
To obtain the time average $\bar{O}(t)$ for one observable $O(t)$, we calculate

$$1/n \cdot \sum_{n=0}^{n=n_{max}} (O(t_0 + \Delta t \cdot n)),$$

where n_{max}, Δt is chosen in a way that the convergence occurs. This is also the way one would determine it in the experiment.

C.2.3. Averages and ESQPT Signal

C.2.3.1. Observable as a Function of Energy

We calculate the time averages $\bar{J}_z$ for various initial conditions that belongs to various M-values. Figure C.4 shows $\bar{J}_z$ as a function of energy, which encodes the initial

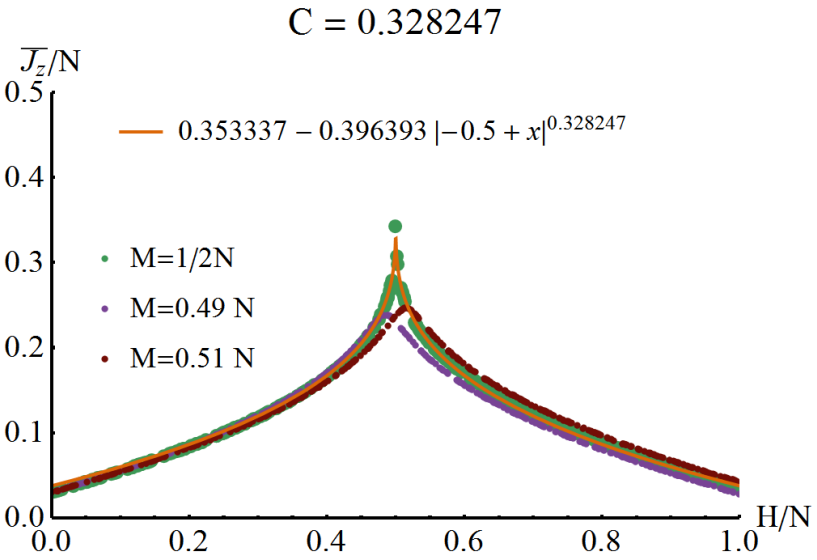

Figure C.3.: The peak in the restricted TC-Model exists only for $M = 1/2$N and can be fitted by a power law $A + B|x - 0.5|^C$ (orange solid line). Parameters: $M = 1/2N, g_0 = 2\omega_0$.

condition. Gray dots in the upper part show $\bar{J}_z$ for different initial conditions, each point can have different H and M values. The colored curves connect the points with the same M values and make the underlying structure visible. Whereas the upper-left part shows the normal phase (Fig. C.4(a)), the upper-right part presents the results after the phase transition (Fig. C.4(b)) for $g > g_c$. First, we recognize that not all values of $\bar{J}_z$ are possible and they strongly depend on the value of M. For $g < g_0$ the approximately linear structure is visible. Each of this gray-dotted lines correspond to some fixed value of M. The black dash-dotted lines refers to the maximal values of

$\bar{J}_z = N/2$. We note that the maximum value of $\bar{J}_z$ can be reached only for $M \geq 1/2N$ with the minimal possible energy value $\omega M - (\omega - \omega_0)N/2$ for a given M. The system is then trapped in the minimum of the classical potential (see Fig. C.6(a)).

However, this is not the case for $g_0 > g_c$ and the dependence of $\bar{J}_z$ on H and M changes completely, Fig. C.4(b). We see that the ESQPT (here visible as a peak) appears only for $M = N/2$, which coincide with the literature [Nar73]. The more M deviates from this value the more this peak smooths, until it is not visible any more. The $\times$ shows the corresponding QM-Results for 500 particles which coincide with semi-classical results very good. Furthermore, the green dotted curve of the ESQPT scenario in Fig. C.3 can be fitted by a power law, the exponent of 0.33 coincides with the literature [PF11b]. All this demonstrates a very good agreement between the semiclassical and quantum long-spin dynamics.

We can switch from the so called restricted Tavis-Cummings-Model to the unrestricted one [Bra13] averaging additionally over the M number (Fig. C.4, lower part). We see that for both g_0 values persist a sharp bend at $H/N = 0.5$ and the phase transition shifts to $H/N = -0.5$ (Fig. C.4(d)) in accordance with the semiclassical density of states calculation [BM14a].

C.2.3.2. Energy Independent Representation of ESQPT

Whereas $\overline{a^*a}$,$\bar{x^2}$, $\bar{y^2}$,$\bar{J_x^2}$,$\bar{J_y^2}$,$\bar{J_z^2}$ show the ESQPT-divergence for M = N/2 and $g_0 > g_c$ as well, the time averages of single operators except of J_z is zero for arbitrary values of H, as known from the quantum mechanical calculations and has its origin in the symmetry of H. Plotting then $\overline{J_+a} + \overline{J_-a^*}$ vs. $\bar{J}_z$ we obtain the energy independent representation, where the ESQPT is visible as a peak. Figure C.5 shows the results for two phases. The gray underlying structure results from the arbitrary values of H and M, fixed by an arbitrary chosen initial condition. The fixed values of M indicate an underlying structure (colored curves). For $g_0 < g_c$ the positive values of $\bar{J}_z$ can be only reached for $M > 0$. Otherwise, the $M = J_z + a^*a$ conservation law can not be satisfied, as a^*a is only positive. For $g > g_c$ we see a cusp at (0,0.5) position which is due to the ESQPT existence only for $M = 1/2N$.

C.2.3.3. Classical Potential

Especially the occurrence of an ESQPT for $M = 1/2N$ can be explained and understood deriving the semiclassical potential for this model, as was performed by P. Perez-Fernandez et al. [PF11a]. After the Holstein-Primakoff transformation they obtain the transformed Hamiltonian

$$H_{TC,2} = -M \cdot \frac{\omega_0}{2} + \frac{\omega_0}{2} \cdot (d^2 + p^2) + \frac{\omega}{2} \cdot (x^2 + y^2) + \frac{g_0}{\sqrt{2}} \cdot \sqrt{2M - (d^2 + p^2)}(x * d + y * p) \quad \text{(C.8)}$$

in thermodynamic limit, where $c = d + ip$ represent a bosonisation of the spin components $J_+ = c^\dagger \sqrt{2j - c^\dagger c}$, $J_- = \sqrt{2j - c^\dagger c}c$, $J_z = c^\dagger c - j$ and the conservation of M

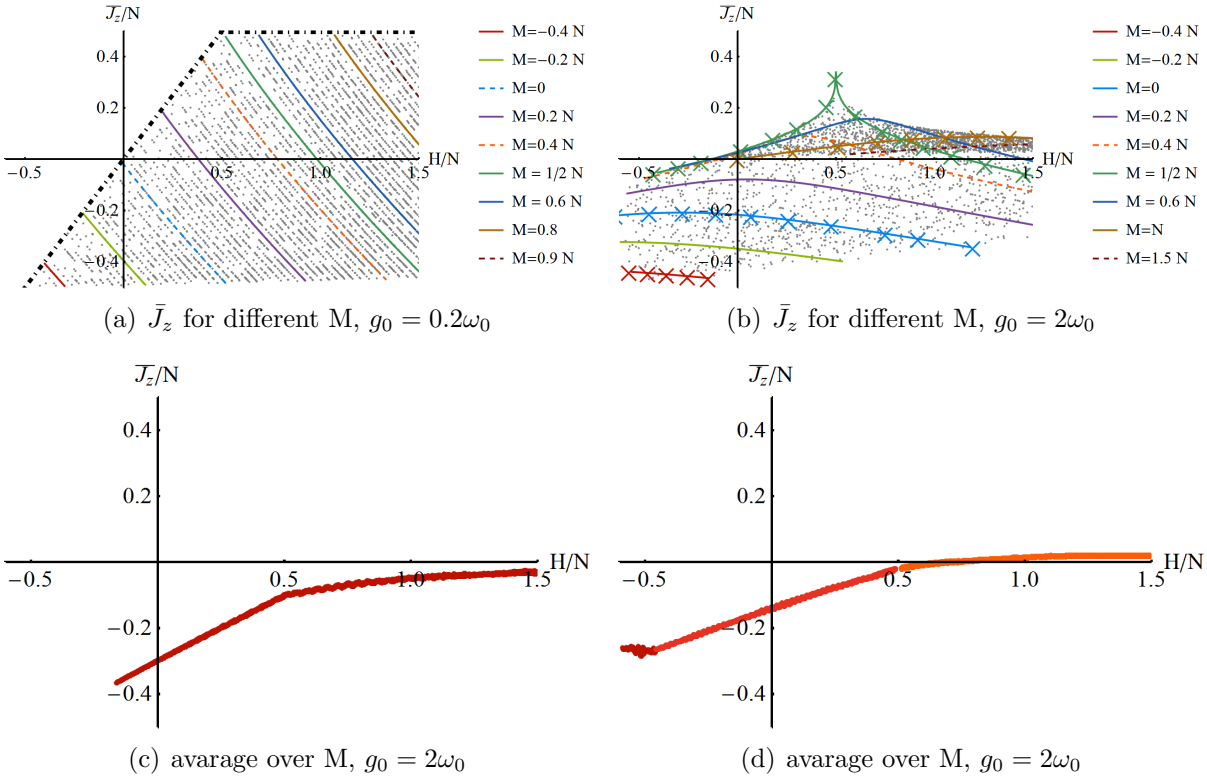

(a) $\bar{J}_z$ for different M, $g_0 = 0.2\omega_0$

(b) $\bar{J}_z$ for different M, $g_0 = 2\omega_0$

(c) avarage over M, $g_0 = 2\omega_0$

(d) avarage over M, $g_0 = 2\omega_0$

Figure C.4.: $\bar{J}_z$-Time average for different energies H and different M numbers (gray points, upper) and an additional average over the M numbers (lower) for $g_0 < g_c$ (left) and $g_0 > g_c$ (right). The colored curves (upper) represent the fixed values of M. The ESQPT-Peak exists only for $M = N/2$ and $g_0 > g_c$ (colored curves, (b)) and $H = 1/2N$. Averaging over all M-numbers (lower) leads to the unrestricted TC-Model. For $g_0 > g_c$ an additional discontinuity in the derivative at $H = -0.5N$ appears. Parameters: $\omega = 2\omega_0$

becomes

$$x^2 + y^2 + a^2 + b^2 = 1.$$

Due to the separation of a and c in position x, d and momentum y, p operators, setting $p = x = 0$ the semiclassical potential can be obtained [PF11a]

$$V_{TC} = -M \cdot \frac{\omega_0}{2} + \frac{\omega_0}{2} \cdot d^2 + \frac{\omega}{2} \cdot x^2 + \frac{g_0}{\sqrt{2}} \cdot \sqrt{2M - d^2} x \cdot d. \tag{C.9}$$

Using now the transformation $x = cos\vartheta, d = sin\vartheta$, which fulfills the M-restriction, V_{TC} becomes

$$V_{TC}(\vartheta) = (1 - M)\frac{\omega_0}{2} + \frac{|\omega_0 - \omega|}{2} \sin^2\vartheta + \frac{g_0}{8} \sin(2\vartheta)\sqrt{2M - \cos^2\vartheta}. \tag{C.10}$$

The plot of this potential reveals the presence of ESQPT-signal only for $M = 1/2N$ and $g_0 > g_c$: The saddle point, which is necessary for this signal, exists only for

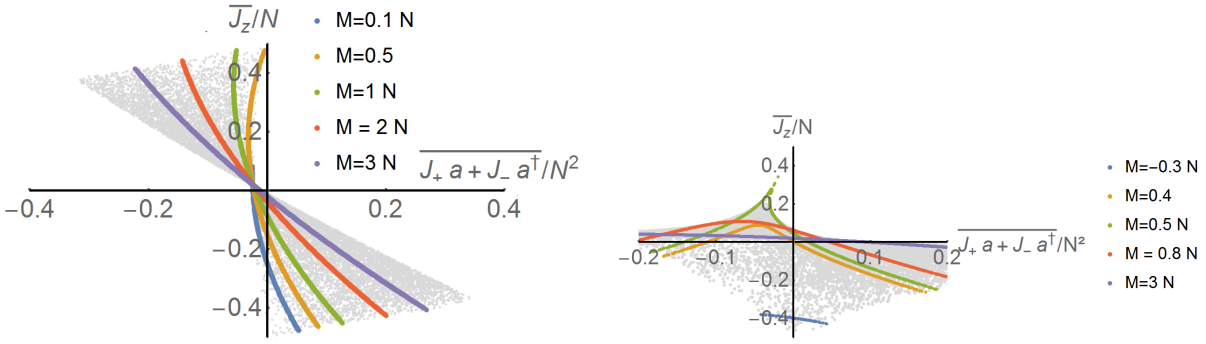

(a) for different M values, $g_0 = 0.2\omega_0$ (b) for different M values, $g_0 = 2\omega_0$

Figure C.5.: Energy independent representation of J_z as a function of $J_+a + J_-a^*$ for different M-values (upper). The gray points denote M-values in the range from $-0.5N$ to $2N$. We see the typical ESQPT-peak only for $M = N/2$ (left). Lower part shows the average over many M-values. Parameters: $\omega = 2\omega_0$

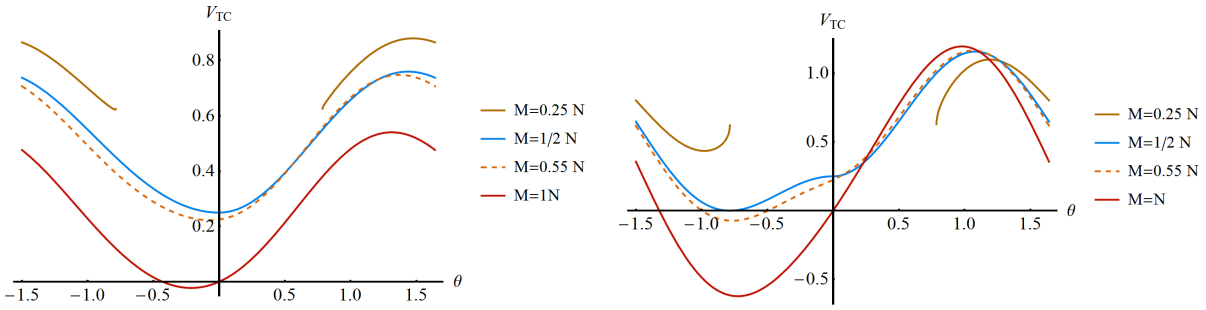

(a) $g_0 = 0.2\omega_0$ (b) $g_0 = 2\omega_0$

Figure C.6.: Semiclassical potential plots for different M for both phases. We observe only for $M = 0.5N$ the saddle point in the potential, which leads to the ESQPT. Parameters: $\omega = 2\omega_0$.

$M = 1/2N$ at $\theta = 0$ and disappears for other M, see Fig. C.6(b). It is also interesting that in the normal phase the potential minimum is shifted from $\theta = 0$ with growing M, see Fig. C.6(a), but the analogous shift of the saddle-point is absent for $g_0 > g_c$.

C.2.4. ESQPT Signal from Coherent State Dynamics

This part is mainly based on Ref. [Eng15].

In this part we assume that the TC system is prepared in a coherent state $|\psi(t = 0)\rangle$. These states are the closest ones to classical states and can be realized in many systems [Are72]. The expectation value $\left\langle \hat{O} \right\rangle$ of an operator $\hat{O}$ is measured then in the state $|\psi(t)\rangle$ after the time t. Repeating such measurements multiple times the temporal average can be defined as

$$\overline{\langle O \rangle} = \frac{1}{T} \int_0^T \langle \psi(t) | \hat{O} | \psi(t) \rangle \, , \tag{C.11}$$

where T is the evolution time.

C.2.4.1. Coherent State in Finite Hilbert Space

The state $|\alpha\rangle$ with $\hat{a}|\alpha\rangle = \alpha|\alpha\rangle$ is the well-known bosonic coherent state. For a spin system a coherent state $|\theta, \phi\rangle$ can be expressed in the basis of Dicke states $|j, m\rangle$ as [Dow94, Zha90]

$$|\theta, \phi\rangle = \sum_{m=-j}^{j} t_m |j, m\rangle \, , \tag{C.12}$$

with

$$t_m = \sqrt{\binom{2j}{j+m}} \left[\sin\left(\frac{\theta}{2}\right)\right]^{j-m} \left[\cos\left(\frac{\theta}{2}\right)\right]^{j+m} e^{-i(j+m)\phi}. \tag{C.13}$$

A coherent state for the TC model is then

$$|\Psi(t=0)\rangle = |\alpha\rangle \otimes |\theta, \phi\rangle \tag{C.14}$$

with the mean photon number $|\alpha|^2$. The Dynamic of such a state distributes over many different M values in general, covering the whole Hilbert space. However, to see the ESQPT signal the condition $M = N/2$ has to be fulfilled, as we have showed previously. Thus, the initial coherent state $|\Psi\rangle$ has to fulfill

$$\left\langle \hat{M} \right\rangle \equiv M = N/2 = x^2 + y^2 + J_z = N/2\cos(\theta) + |\alpha|^2 \tag{C.15}$$

on average. The averaged value is conserved for time evolved states, too, because $\hat{M}$ and $\hat{H}$ commute. The variance of $\hat{M}$ scales with $\frac{1}{N}$ and vanishes in the thermodynamic limit.

For faster numerical calculation one can express the initially coherent state as a sum over the sub-Hilbert spaces with fixed excitation numbers M

$$|\Psi(t=0)\rangle = \sum_{M=M_{Min}}^{M_{max}} \sum_{m=-N/2}^{min(j,M)} a_{M-m} t_m |M-m\rangle \otimes |j, m\rangle \, , \tag{C.16}$$

where $(M_{min}, M_{max}) = (-j, \infty)$ and $a_n = e^{-|\alpha|^2/2} \frac{\alpha^n}{\sqrt{n!}}$.

The advantage of such a representation is that the time evolution of the whole state can be performed for each subspace with fixed M separately, as the different subspaces do not couple. This decreases the matrix size of the Hamiltonian and the computation time. Moreover, the state can be truncated at

$$(M_{min}, M_{max}) = (j - \Delta M, j + \Delta M),$$

ΔM being chosen in a way that the time evolution of expectation values converges. Especially for higher atomic number N, in our simulation ΔM is in the order of 10.

C.2.4.2. Results

As initial condition we choose the phase of α to be $\vartheta = 0$. The rotated frame is then equivalent to the lab frame for $t = 0$, see Eq. (C.7). The initial condition for α is then fixed by the constrain $\alpha = \sqrt{N/2 - N/2\cos(\theta)}$. The initial condition for θ is varied between $(0, \pi)$ and ϕ is chosen to be either $\phi = 0$ or $\phi = \pi$. For each initial condition we calculate the temporal average for the operators $\hat{O}_1 = \hat{J}_z$ and $\hat{O}_2 = \hat{J}_+\hat{a} + \hat{J}_-\hat{a}^\dagger$ using Eq. (C.11) and plot $(\overline{\hat{O}_1}, \overline{\hat{O}_2})$ in Fig. C.7.

In Fig. C.7(a) we see the cusp structure (circles, arrow) which matches very good to semiclassical calculation (crosses). Surprisingly, we see an additional smoothed peak which is marked by $*$. The initial condition is decisive, which result we measure. The color of the circles encodes the initial condition, see the plot legend. The chosen θ and ϕ values are marked by he same color on the Bloch sphere, see Fig. C.7(b) as the results in (a). Comparing both parts of Fig. C.7 we see that the ESQPT cusp is generated if the initial condition was chosen closed to the saddle point (S). In contrast, we obtain the smoothed peak for initial condition on the other side of the Bloch sphere. This peak is completely absent in the semiclassical mean-field calculation and can be connected to the participation ratio [Eng15].

C.2.5. Discussion/Conclusion

In this section we have shown, how to obtain the ESQPT signal from a periodic dynamic in the Dicke and TC models in the thermodynamic limit. Whereas in the first case, we used only the mean-field equations for the calculations, in the second case we showed additionally how to extract the ESQPT signal form an evolution of coherent states. The semiclassical time averages agrees with the averaged values obtained from the evaluation in eigenstates. In contrast, the dynamics of coherent states can lead to a smoothed peak instead of the ESQPT cusp. This feature depends on the initial condition of the coherent state. TC model has an additional constrain $\left\langle \hat{M} \right\rangle$ - a total excitation number. We visualized the role of M especially in context of the ESQPT appearance, thus only for $M = N/2$ the semiclassical energy landscape has a saddle point. Therefore, the coherent state has to be prepared in a way to fulfill this equality, thus $\left\langle \hat{M} \right\rangle = N/2$. Additionally we showed, the connection between the unrestricted and restricted TC model, averaging over the M number.

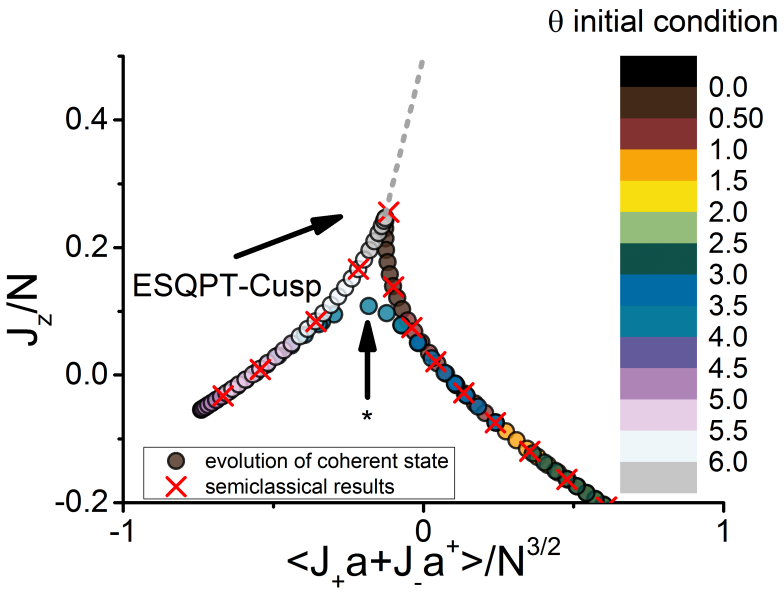

(a) ESQPT cusp

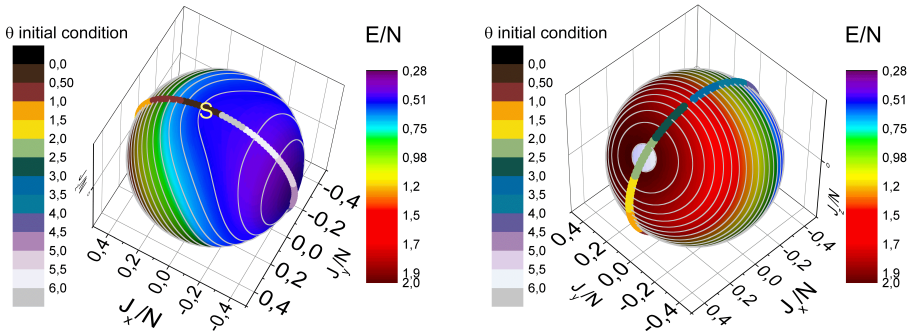

(b) Bloch sphere from both sides

Figure C.7.: (a) ESQPT cusp obtained by averaging over time evolved coherent states for different initial conditions (colored circles). Crosses denotes averaged values obtained from a semiclassical calculation. The smoothed peak marked by * depends on the chosen initial condition which are visualized in part (b) on the Bloch sphere. Bloch sphere colors show the rescaled energy Eq. (C.7). The colored line on the Bloch sphere indicates the initial condition for the coherent state $\Psi(t=0)$ in the same colors as the results in (a). Parameters: $\omega = 2\omega_0, g = 2\omega_0, M = 0.5(b), N = 60(a)$.

Danksagung

In diesem besonderen Abschnitt möchte ich versuchen möglichst alle zu würdigen, die mich auf dem PhD-Weg begleiten.

Vom ganzen Herzen möchte ich mich bei meinem Betreuer Prof. Dr. Tobias Brandes bedanken. Für seine exzellente Betreuung, seine inspirierende Art, seine Zeit, seine ganz viele ausgeklügelten Ideen, für seine kontinuierliche Unterstützung während der PhD Phase (und davor).

Ein besonderer Dank gilt Dr. Clive Emary für die innovativen Vorschläge und Ideen sowie konstruktive Diskussionen.

Ich bedanke mich bei Milan Radonić, Antun Balaž und Axel Pelster für eine sehr effektive und konstruktive Zusammenarbeit. Bei Milan Radonić und Antun Balaž bedanke ich mich auch für den warmen Empfang in Belgrad und für ihre Zeit, die sie mit mir dort verbrachten. Und bei Milan Radonić noch extra für unzählige Diskussionsstunden in Deutschland oder via Skype.

Ein besonderer Dank gilt Georg Engelhard, Alexander Sorokin und Javier Cerrillo, die geholfen haben diese Arbeit lesbarer und fehlerfreier zu gestalten.

Ich bedanke mich auch bei unserer Arbeitsgruppe, insbesondere bei Georg Engelhard, Victor Bastidas, Mathias Hayn, Philipp Strasberg, Christian Nietner, Javier Cerrillo für hilfreiche Diskussionen und Gespräche.

Auch Entspannungsphasen sind wichtig. Daher ein Dank an alle meine Freunde. Insbesondere an Familien Bekalskij, Stelwag, Frick und Frizon; an Emely Wiegland, Georg Engelhard, Alexander Sorokin, Javier Cerrillo, Christian Fräßdorf, Felix Kramer – auch für die schönen Kaffe- und Kakao-Pausen und witzige Gespräche; an Alex Schreider, Igor Derr und Michael Lewkowski; an Mischa Kondrakhin – er weiß warum.

Last but not least, ein ganz besonderer Dank gilt meinen Eltern, meiner Oma und meinem kleineren Bruder für die ständige Unterstützung im Lern- und Arbeitsprozess und vor allem im Leben insgesamt.

Bibliography

[Ace15] O. L. Acevedo, L. Quiroga, F. J. Rodrguez and N. F. Johnson. *Robust quantum correlations in out-of-equilibrium matterlight systems*. New Journal of Physics **17**(9), 093005 (2015).

[Alc12] M. A. Alcalde, M. Bucher, C. Emary and T. Brandes. *Thermal phase transitions for Dicke-type models in the ultrastrong-coupling limit*. Phys. Rev. E **86**, 012101 (2012). doi:10.1103/PhysRevE.86.012101.

[Are72] F. T. Arecchi, E. Courtens, R. Gilmore and H. Thomas. *Atomic Coherent States in Quantum Optics*. Phys. Rev. A **6**, 2211–2237 (1972). doi:10.1103/PhysRevA.6.2211.

[Arm06] M. A. Armen and H. Mabuchi. *Low-lying bifurcations in cavity quantum electrodynamics*. Phys. Rev. A **73**, 063801 (2006). doi:10.1103/PhysRevA.73.063801.

[Bad14] M. P. Baden, K. J. Arnold, A. L. Grimsmo, S. Parkins and M. D. Barrett. *Realization of the Dicke Model Using Cavity-Assisted Raman Transitions*. Phys. Rev. Lett. **113**, 020408 (2014). doi:10.1103/PhysRevLett.113.020408.

[Bas12] V. M. Bastidas, C. Emary, B. Regler and T. Brandes. *Nonequilibrium Quantum Phase Transitions in the Dicke Model*. Phys. Rev. Lett. **108**, 043003 (2012). doi:10.1103/PhysRevLett.108.043003.

[Bas14a] V. M. Bastidas, G. Engelhardt, P. Pérez-Fernández, M. Vogl and T. Brandes. *Critical quasienergy states in driven many-body systems*. Phys. Rev. A **90**, 063628 (2014). doi:10.1103/PhysRevA.90.063628.

[Bas14b] V. M. Bastidas, P. Pérez-Fernández, M. Vogl and T. Brandes. *Quantum Criticality and Dynamical Instability in the Kicked-Top Model*. Phys. Rev. Lett. **112**, 140408 (2014). doi:10.1103/PhysRevLett.112.140408.

[Bau10] K. Baumann, C. Guerlin, F. Brennecke and T. Esslinger. *Dicke quantum phase transition with a superfluid gas in an optical cavity*. Nature (London) **464**(1301-1306) (2010). doi:doi:10.1038/nature09009.

[Bau11] K. Baumann, R. Mottl, F. Brennecke and T. Esslinger. *Exploring Symmetry Breaking at the Dicke Quantum Phase Transition*. Phys. Rev. Lett. **107**, 140402 (2011). doi:10.1103/PhysRevLett.107.140402.

[Bha12] M. J. Bhaseen, J. Mayoh, B. D. Simons and J. Keeling. *Dynamics of nonequilibrium Dicke models*. Phys. Rev. A **85**, 013817 (2012). doi:10.1103/PhysRevA.85.013817.

[BM14a] M. A. Bastarrachea-Magnani, S. Lerma-Hernández and J. G. Hirsch. *Comparative quantum and semiclassical analysis of atom-field systems. I. Density of states and excited-state quantum phase transitions*. Phys. Rev. A **89**, 032101 (2014). doi:10.1103/PhysRevA.89.032101.

[BM14b] M. A. Bastarrachea-Magnani, S. Lerma-Hernández and J. G. Hirsch. *Comparative quantum and semiclassical analysis of atom-field systems. II. Chaos and regularity*. Phys. Rev. A **89**, 032102 (2014). doi:10.1103/PhysRevA.89.032102.

[Bog00] N. Bogolyubov. *Algebraic bethe anzatz and the tavis-cummings model*. Journal of Mathematical Sciences **100**(2), 2051–2060 (2000).

[Bon70] R. Bonifacio and G. Preparata. *Coherent Spontaneous Emission*. Phys. Rev. A **2**, 336–347 (1970). doi:10.1103/PhysRevA.2.336.

[Bra08] T. Brandes. *Waiting times and noise in single particle transport*. Annalen der Physik **17**(7), 477–496 (2008).

[Bra13] T. Brandes. *Excited-state quantum phase transitions in Dicke superradiance models*. Phys. Rev. E **88**, 032133 (2013). doi:10.1103/PhysRevE.88.032133.

[Bre02] H.-P. Breuer and F. Petruccione. *The theory of open quantum systems*, (Oxford university press2002).

[Bre08] F. Brennecke, S. Ritter, T. Donner and T. Esslinger. *Cavity optomechanics with a Bose-Einstein condensate*. Science **322**(5899), 235–238 (2008).

[Cap08] M. Caprio, P. Cejnar and F. Iachello. *Excited state quantum phase transitions in many-body systems*. Annals of Physics **323**(5), 1106 – 1135 (2008). doi:http://dx.doi.org/10.1016/j.aop.2007.06.011.

[Car09] H. J. Carmichael. *Statistical Methods in Quantum Optics 1*, vol. 2, (Springer Science & Business Media2009).

[Chi14] A. Chiocchetta and I. Carusotto. *Quantum Langevin model for nonequilibrium condensation*. Phys. Rev. A **90**, 023633 (2014). doi:10.1103/PhysRevA.90.023633.

[Der03] C. Deransart, V. Riban, L. Vercueil, K. Nail-Boucherie, C. Marescaux and A. Depaulis. *Control of Epileptic Seizures*. In A. Graybiel, M. Delong and S. Kitai, editors, *The Basal Ganglia VI*, vol. 54 of *Advances in Behavioral Biology*, pages 169–178, (Springer US2003). doi:10.1007/978-1-4615-0179-4_17.

[Dic54] R. H. Dicke. *Coherence in Spontaneous Radiation Processes*. Phys. Rev. **93**, 99–110 (1954). doi:10.1103/PhysRev.93.99.

[Die13] B. Dietz, F. Iachello, M. Miski-Oglu, N. Pietralla, A. Richter, L. von Smekal and J. Wambach. *Lifshitz and excited-state quantum phase transitions in microwave Dirac billiards*. Phys. Rev. B **88**, 104101 (2013). doi:10.1103/PhysRevB.88.104101.

[Dim07] F. Dimer, B. Estienne, A. S. Parkins and H. J. Carmichael. *Proposed realization of the Dicke-model quantum phase transition in an optical cavity QED system*. Phys. Rev. A **75**, 013804 (2007). doi:10.1103/PhysRevA.75.013804.

[DL09] S. De Liberato, D. Gerace, I. Carusotto and C. Ciuti. *Extracavity quantum vacuum radiation from a single qubit*. Phys. Rev. A **80**, 053810 (2009). doi:10.1103/PhysRevA.80.053810.

[Dow94] J. P. Dowling, G. S. Agarwal and W. P. Schleich. *Wigner distribution of a general angular-momentum state: Applications to a collection of two-level atoms*. Phys. Rev. A **49**, 4101–4109 (1994). doi:10.1103/PhysRevA.49.4101.

[Dus05] S. Dusuel and J. Vidal. *Continuous unitary transformations and finite-size scaling exponents in the Lipkin-Meshkov-Glick model*. Phys. Rev. B **71**, 224420 (2005). doi:10.1103/PhysRevB.71.224420.

[Ema03a] C. Emary and T. Brandes. *Chaos and the quantum phase transition in the Dicke model*. Phys. Rev. E **67**, 066203 (2003). doi:10.1103/PhysRevE.67.066203.

[Ema03b] C. Emary and T. Brandes. *Quantum Chaos Triggered by Precursors of a Quantum Phase Transition: The Dicke Model*. Phys. Rev. Lett. **90**, 044101 (2003). doi:10.1103/PhysRevLett.90.044101.

[Ema13a] C. Emary. *Dark-states in multi-mode multi-atom JaynesCummings systems*. J. Phys. B: At. Mol. Opt. Phys. **46**, 224008 (2013).

[Ema13b] C. Emary. *Delayed feedback control in quantum transport*. Philos. Trans. R. Soc. A-Math. **371**(1999), 20120468 (2013).

[Eng13] G. Engelhardt, V. M. Bastidas, C. Emary and T. Brandes. *ac-driven quantum phase transition in the Lipkin-Meshkov-Glick model*. Phys. Rev. E **87**, 052110 (2013). doi:10.1103/PhysRevE.87.052110.

[Eng14] G. Engelhardt, V. Bastidas and T. Brandes. *Excited-state quantum phase transitions and periodic dynamics*. arXiv 1405.3514v1 (2014).

[Eng15] G. Engelhardt, V. M. Bastidas, W. Kopylov and T. Brandes. *Excited-state quantum phase transitions and periodic dynamics*. Phys. Rev. A **91**, 013631 (2015). doi:10.1103/PhysRevA.91.013631.

[Fan14] J. Fan, Z. Yang, Y. Zhang, J. Ma, G. Chen and S. Jia. *Hidden continuous symmetry and Nambu-Goldstone mode in a two-mode Dicke model.* Phys. Rev. A **89**, 023812 (2014). doi:10.1103/PhysRevA.89.023812.

[Gar04] C. Gardiner and P. Zoller. *Quantum noise: a handbook of Markovian and non-Markovian quantum stochastic methods with applications to quantum optics*, (Springer, Berlin2004).

[Gri99] E. Grigorieva, H. Haken, S. Kashchenko and A. Pelster. *Travelling wave dynamics in a nonlinear interferometer with spatial field transformer in feedback.* Physica D **125**(1), 123–141 (1999).

[Gri14] A. Grimsmo, A. Parkins and B. Skagerstam. *Rapid steady-state convergence for quantum systems using time-delayed feedback control.* New J. Phys. **16**(6), 065004 (2014).

[Gri15] A. L. Grimsmo. *Time-Delayed Quantum Feedback Control.* Phys. Rev. Lett. **115**, 060402 (2015). doi:10.1103/PhysRevLett.115.060402.

[Gro10] C. Gross, T. Zibold, E. Nicklas, J. Esteve and M. K. Oberthaler. *Nonlinear atom interferometer surpasses classical precision limit.* Nature (London) **464**(7292), 1165–1169 (2010).

[Gut81] A. H. Guth and E. J. Weinberg. *Cosmological consequences of a first-order phase transition in the SU_5 grand unified model.* Phys. Rev. D **23**, 876–885 (1981). doi:10.1103/PhysRevD.23.876.

[HÖ5] P. Hövel and E. Schöll. *Control of unstable steady states by time-delayed feedback methods.* Phys. Rev. E **72**, 046203 (2005). doi:10.1103/PhysRevE.72.046203.

[Hak84] H. Haken. *Laser theory*, vol. xxv/2c of Encyclopedia of Physics (Berlin, 1970); reprint, (Springer1984).

[Hay11] M. Hayn, C. Emary and T. Brandes. *Phase transitions and dark-state physics in two-color superradiance.* Phys. Rev. A **84**, 053856 (2011). doi:10.1103/PhysRevA.84.053856.

[Hei15] S. M. Hein, F. Schulze, A. Carmele and A. Knorr. *Entanglement control in quantum networks by quantum-coherent time-delayed feedback.* Phys. Rev. A **91**, 052321 (2015). doi:10.1103/PhysRevA.91.052321.

[Hep73a] K. Hepp and E. H. Lieb. *Equilibrium Statistical Mechanics of Matter Interacting with the Quantized Radiation Field.* Phys. Rev. A **8**, 2517–2525 (1973). doi:10.1103/PhysRevA.8.2517.

[Hep73b] K. Hepp and E. H. Lieb. *On the superradiant phase transition for molecules in a quantized radiation field: the dicke maser model.* Annals of Physics **76**(2), 360 – 404 (1973). doi:10.1016/0003-4916(73)90039-0.

[Hoh99] A. Hohl and A. Gavrielides. *Bifurcation Cascade in a Semiconductor Laser Subject to Optical Feedback*. Phys. Rev. Lett. **82**, 1148–1151 (1999). doi:10.1103/PhysRevLett.82.1148.

[Hop13] C. Hopfmann, F. Albert, C. Schneider, S. Höfling, M. Kamp, A. Forchel, I. Kanter and S. Reitzenstein. *Nonlinear emission characteristics of quantum dot–micropillar lasers in the presence of polarized optical feedback*. New J. Phys. **15**(2), 025030 (2013).

[Jun99] C. Jung, M. Müller and I. Rotter. *Phase transitions in open quantum systems*. Phys. Rev. E **60**, 114–131 (1999). doi:10.1103/PhysRevE.60.114.

[Jus09] W. Just, A. Pelster, M. Schanz and E. Schöll. *Delayed complex systems: an overview*. Phil. Trans. R. Soc. A-Math. **368**(1911), 303–304 (2009). doi:10.1098/rsta.2009.0243.

[Kab15] J. Kabuss, D. O. Krimer, S. Rotter, K. Stannigel, A. Knorr and A. Carmele. *Analytical Study of Quantum Feedback Enhanced Rabi Oscillations*. arXiv:1503.05722 (2015).

[Kik97] N. Kikuchi, Y. Liu and J. Ohtsubo. *Chaos control and noise suppression in external-cavity semiconductor lasers*. IEEE J. Quantum Electron. **33**(1), 56–65 (1997).

[Kir13] P. Kirton and J. Keeling. *Nonequilibrium Model of Photon Condensation*. Phys. Rev. Lett. **111**, 100404 (2013). doi:10.1103/PhysRevLett.111.100404.

[Kir15] P. Kirton and J. Keeling. *Thermalization and breakdown of thermalization in photon condensates*. Phys. Rev. A **91**, 033826 (2015). doi:10.1103/PhysRevA.91.033826.

[Kla10] J. Klaers, J. Schmitt, F. Vewinger and M. Weitz. *Bose-Einstein condensation of photons in an optical microcavity*. Nature (London) **468**(7323), 545–548 (2010). doi:10.1038/nature09567.

[Kla12] J. Klaers, J. Schmitt, T. Damm, F. Vewinger and M. Weitz. *Statistical Physics of Bose-Einstein-Condensed Light in a Dye Microcavity*. Phys. Rev. Lett. **108**, 160403 (2012). doi:10.1103/PhysRevLett.108.160403.

[Kle85] P. Kleinwachter and I. Rotter. *Spectroscopic properties of highly excited states*. Phys. Rev. C **32**, 1742–1744 (1985). doi:10.1103/PhysRevC.32.1742.

[Kli15] J. Klinder, H. Keler, M. Wolke, L. Mathey and A. Hemmerich. *Dynamical phase transition in the open Dicke model*. Proceedings of the National Academy of Sciences **112**(11), 3290–3295 (2015). doi:10.1073/pnas.1417132112.

[Kop13] W. Kopylov, C. Emary and T. Brandes. *Counting statistics of the Dicke superradiance phase transition.* Phys. Rev. A **87**, 043840 (2013). doi:10.1103/PhysRevA.87.043840.

[Kop15a] W. Kopylov and T. Brandes. *Time delayed control of excited state quantum phase transitions in the Lipkin-Meshkov-Glick model.* arXiv:1505.02060 (2015).

[Kop15b] W. Kopylov, C. Emary, E. Schöll and T. Brandes. *Time-delayed feedback control of the DickeHeppLieb superradiant quantum phase transition.* New J. Phys. **17**(1), 013040 (2015).

[Kop15c] W. Kopylov, M. Radonjić, T. Brandes, A. Balaž and A. Pelster. *Dissipative Two-Mode Tavis-Cummings Model with Time-Delayed Feedback Control.* arXiv preprint arXiv:1507.01811 (2015).

[Lan80] R. Lang and K. Kobayashi. *External optical feedback effects on semiconductor injection laser properties.* IEEE J. Quantum Electron. **16**(3), 347–355 (1980).

[Lax68] M. Lax. *Quantum Noise. XI. Multitime Correspondence between Quantum and Classical Stochastic Processes.* Phys. Rev. **172**, 350–361 (1968). doi:10.1103/PhysRev.172.350.

[Lee14] T. E. Lee, C.-K. Chan and S. F. Yelin. *Dissipative phase transitions: Independent versus collective decay and spin squeezing.* Phys. Rev. A **90**, 052109 (2014). doi:10.1103/PhysRevA.90.052109.

[Lip65] H. J. Lipkin, N. Meshkov and A. Glick. *Validity of many-body approximation methods for a solvable model:(I). Exact solutions and perturbation theory.* Nucl. Phys. **62**(2), 188–198 (1965).

[LL70] E. L. L.D. Landau. *Lehrbuch der Theoretischen Physik V, Statische Physik*, (Akademie Verlag1970).

[Mac86] S. Machida and Y. Yamamoto. *Observation of sub-poissonian photoelectron statistics in a negative feedback semiconductor laser.* Opt. Commun. **57**(4), 290 – 296 (1986). doi:http://dx.doi.org/10.1016/0030-4018(86)90100-8.

[Mar15] J. Marelic and R. A. Nyman. *Experimental evidence for inhomogeneous pumping and energy-dependent effects in photon Bose-Einstein condensation.* Phys. Rev. A **91**, 033813 (2015). doi:10.1103/PhysRevA.91.033813.

[Mas07] C. Masoller, T. Sorrentino, M. Chevrollier and M. Oria. *Bistability in semiconductor lasers with polarization-rotated frequency-dependent optical feedback.* IEEE J. Quantum Electron. **43**(3), 261–268 (2007).

[Mor08a] S. Morrison and A. S. Parkins. *Collective spin systems in dispersive optical cavity QED: Quantum phase transitions and entanglement.* Phys. Rev. A **77**, 043810 (2008). doi:10.1103/PhysRevA.77.043810.

[Mor08b] S. Morrison and A. S. Parkins. *Dynamical Quantum Phase Transitions in the Dissipative Lipkin-Meshkov-Glick Model with Proposed Realization in Optical Cavity QED.* Phys. Rev. Lett. **100**, 040403 (2008). doi:10.1103/PhysRevLett.100.040403.

[Mun10] P. P. Munhoz and F. L. Semio. *Multipartite entangled states with two bosonic modes and qubits.* Eur. Phys. J. D **59**(3), 509–519 (2010). doi:10.1140/epjd/e2010-00188-2.

[Nad10] N. A. Naderi, F. Grillot, K. Yang, J. B. Wright, A. Gin and L. F. Lester. *Two-color multi-section quantum dot distributed feedback laser.* Opt. Express **18**(26), 27028–27035 (2010).

[Nag10] D. Nagy, G. Kónya, G. Szirmai and P. Domokos. *Dicke-Model Phase Transition in the Quantum Motion of a Bose-Einstein Condensate in an Optical Cavity.* Phys. Rev. Lett. **104**, 130401 (2010). doi:10.1103/PhysRevLett.104.130401.

[Nag11] D. Nagy, G. Szirmai and P. Domokos. *Critical exponent of a quantum-noise-driven phase transition: The open-system Dicke model.* Phys. Rev. A **84**, 043637 (2011). doi:10.1103/PhysRevA.84.043637.

[Nar73] L. M. Narducci, M. Orszag and R. A. Tuft. *Energy Spectrum of the Dicke Hamiltonian.* Phys. Rev. A **8**, 1892–1906 (1973). doi:10.1103/PhysRevA.8.1892.

[Nau14] N. L. Naumann, S. M. Hein, A. Knorr and J. Kabuss. *Steady-state control in an unstable optomechanical system.* Phys. Rev. A **90**, 043835 (2014). doi:10.1103/PhysRevA.90.043835.

[Ott10] C. Otto, K. Lüdge and E. Schöll. *Modeling quantum dot lasers with optical feedback: sensitivity of bifurcation scenarios.* Phys. Status Solidi B-Basic Solid State Phys. **247**(4), 829–845 (2010).

[Özt12] B. Öztop, M. Bordyuh, Ö. E. Müstecaplıoğlu and H. E. Türeci. *Excitations of optically driven atomic condensate in a cavity: theory of photodetection measurements.* New J. Phys. **14**(8), 085011 (2012).

[PÏ1] C. Pöltl, C. Emary and T. Brandes. *Feedback stabilization of pure states in quantum transport.* Phys. Rev. B **84**, 085302 (2011). doi:10.1103/PhysRevB.84.085302.

[Pan99] F. Pan and J. Draayer. *Analytical solutions for the {LMG} model.* Phys. Lett. B **451**(12), 1 – 10 (1999). doi:http://dx.doi.org/10.1016/S0370-2693(99)00191-4.

[Pau93] T. Paul and A. Uribe. *A construction of quasi-modes using coherent states.* In *Annales de l'IHP Physique théorique*, vol. 59, pages 357–381 (1993).

[PF09] P. Pérez-Fernández, A. Relaño, J. M. Arias, J. Dukelsky and J. E. García-Ramos. *Decoherence due to an excited-state quantum phase transition in a two-level boson model.* Phys. Rev. A **80**, 032111 (2009). doi:10.1103/PhysRevA.80.032111.

[PF11a] P. Pérez-Fernández, P. Cejnar, J. M. Arias, J. Dukelsky, J. E. García-Ramos and A. Relaño. *Quantum quench influenced by an excited-state phase transition.* Phys. Rev. A **83**, 033802 (2011). doi:10.1103/PhysRevA.83.033802.

[PF11b] P. Pérez-Fernández, A. Relaño, J. M. Arias, P. Cejnar, J. Dukelsky and J. E. García-Ramos. *Excited-state phase transition and onset of chaos in quantum optical models.* Phys. Rev. E **83**, 046208 (2011). doi:10.1103/PhysRevE.83.046208.

[Pit03] L. P. Pitaevskii and S. Stringar. *Bose-Einstein Condensation*, (Oxford2003).

[Pra11] F. O. Prado, F. S. Luiz, J. M. Villas-Bôas, A. M. Alcalde, E. I. Duzzioni and L. Sanz. *Atom-mediated effective interactions between modes of a bimodal cavity.* Phys. Rev. A **84**, 053839 (2011). doi:10.1103/PhysRevA.84.053839.

[Pyr92] K. Pyragas. *Continuous control of chaos by self-controlling feedback.* Phys. Lett. A **170**(6), 421–428 (1992).

[Rib07] P. Ribeiro, J. Vidal and R. Mosseri. *Thermodynamical Limit of the Lipkin-Meshkov-Glick Model.* Phys. Rev. Lett. **99**, 050402 (2007). doi:10.1103/PhysRevLett.99.050402.

[Rib08] P. Ribeiro, J. Vidal and R. Mosseri. *Exact spectrum of the Lipkin-Meshkov-Glick model in the thermodynamic limit and finite-size corrections.* Phys. Rev. E **78**, 021106 (2008). doi:10.1103/PhysRevE.78.021106.

[Rit09] S. Ritter, F. Brennecke, K. Baumann, T. Donner, C. Guerlin and T. Esslinger. *Dynamical coupling between a Bose–Einstein condensate and a cavity optical lattice.* Appl. Phys. B **95**(2), 213–218 (2009).

[Rit13a] H. Ritsch, P. Domokos, F. Brennecke and T. Esslinger. *Cold atoms in cavity-generated dynamical optical potentials.* Rev. Mod. Phys. **85**, 553–601 (2013). doi:10.1103/RevModPhys.85.553.

[Rit13b] H. Ritsch, P. Domokos, F. Brennecke and T. Esslinger. *Cold atoms in cavity-generated dynamical optical potentials.* Rev. Mod. Phys. **85**, 553–601 (2013). doi:10.1103/RevModPhys.85.553.

[Ros04] M. Rosenblum and A. Pikovsky. *Delayed feedback control of collective synchrony: An approach to suppression of pathological brain rhythms.* Phys. Rev. E **70**, 041904 (2004). doi:10.1103/PhysRevE.70.041904.

[Sac07] S. Sachdev. *Quantum phase transitions*, (Wiley Online Library2007).

[San15] L. F. Santos and F. Pérez-Bernal. *Structure of eigenstates and quench dynamics at an excited state quantum phase transition.* arXiv preprint arXiv:1506.06765 (2015).

[Sar78] M. Sargent, M. Scully and W. Lamb. *Laser Physics.* Advanced book program, (Perseus Books Group, New York City1978).

[Sch03a] M. Schanz and A. Pelster. *Analytical and numerical investigations of the phase-locked loop with time delay.* Phys. Rev. E **67**, 056205 (2003). doi:10.1103/PhysRevE.67.056205.

[Sch03b] M. Schanz and A. Pelster. *Synergetic system analysis for the delay-induced Hopf bifurcation in the Wright equation.* SIAM J. Appl. Dyn. Syst **2**(3), 277–296 (2003).

[Sch08] E. Schöll and H. G. Schuster. *Handbook of chaos control*, (John Wiley & Sons, Weinheim2008), 2nd ed.

[Sch09] E. Schöll, G. Hiller, P. Hövel and M. A. Dahlem. *Time-delayed feedback in neurosystems.* Philosophical Transactions of the Royal Society A: Mathematical, Physical and Engineering Sciences **367**(1891), 1079–1096 (2009).

[Sch10] E. Schöll, P. Hövel, V. Flunkert and M. A. Dahlem. *Time-delayed feedback control: from simple models to lasers and neural systems.* In *Complex time-delay systems*, pages 85–150, (Springer2010).

[Sch12] H. G. Schuster and K. Lüdge. *Nonlinear laser dynamics: from quantum dots to cryptography*, (John Wiley & Sons, Weinheim2012).

[Sch14a] G. Schaller. *Open Quantum Systems Far from Equilibrium*, (Springer2014).

[Sch14b] F. Schulze, B. Lingnau, S. M. Hein, A. Carmele, E. Schöll, K. Lüdge and A. Knorr. *Feedback-induced steady-state light bunching above the lasing threshold.* Phys. Rev. A **89**, 041801 (2014). doi:10.1103/PhysRevA.89.041801.

[Scu97] M. O. Scully. *Quantum optics*, (Cambridge University Press, Cambridge1997).

[Sie86] A. E. Siegman. *Lasers*, (University Science Books, Mill Valley1986).

[Sor13] M. C. Soriano, J. García-Ojalvo, C. R. Mirasso and I. Fischer. *Complex photonics: Dynamics and applications of delay-coupled semiconductors lasers.* Rev. Mod. Phys. **85**, 421–470 (2013). doi:10.1103/RevModPhys.85.421.

[Str01] S. H. Strogatz. *Nonlinear dynamics and chaos: with applications to physics, biology, chemistry, and engineering (studies in nonlinearity)*, (Westview Press2001).

[Str14] P. Strnsk, M. Macek and P. Cejnar. *Excited-state quantum phase transitions in systems with two degrees of freedom: Level density, level dynamics, thermal properties.* Annals of Physics **345**(0), 73 – 97 (2014). doi:http://dx.doi.org/10.1016/j.aop.2014.03.006.

[Tav68] M. Tavis and F. W. Cummings. *Exact Solution for an N-Molecule¯Radiation-Field Hamiltonian.* Phys. Rev. **170**, 379–384 (1968). doi:10.1103/PhysRev.170.379.

[Vac12] G. Vacanti, S. Pugnetti, N. Didier, M. Paternostro, G. M. Palma, R. Fazio and V. Vedral. *Photon Production from the Vacuum Close to the Superradiant Transition: Linking the Dynamical Casimir Effect to the Kibble-Zurek Mechanism.* Phys. Rev. Lett. **108**, 093603 (2012). doi:10.1103/PhysRevLett.108.093603.

[Val13] V. M. B. Valencia. *AC-Driven Quantum Phase Transitions : Nonequilibrium aspects of criticality.* Ph.D. thesis, TU Berlin (2013).

[Vir13] M. Virte, K. Panajotov and M. Sciamanna. *Mode competition induced by optical feedback in two-color quantum dot lasers.* IEEE J. Quantum Electron. **49**(7), 578–585 (2013).

[Vir14] M. Virte, S. Breuer, M. Sciamanna and K. Panajotov. *Switching between ground and excited states by optical feedback in a quantum dot laser diode.* Appl. Phys. Lett. **105**(12), 121109 (2014). doi:http://dx.doi.org/10.1063/1.4896576.

[Wan73] Y. K. Wang and F. T. Hioe. *Phase Transition in the Dicke Model of Superradiance.* Phys. Rev. A **7**, 831–836 (1973). doi:10.1103/PhysRevA.7.831.

[Wic13] A. Wickenbrock, M. Hemmerling, G. R. M. Robb, C. Emary and F. Renzoni. *Collective strong coupling in multimode cavity QED.* Phys. Rev. A **87**, 043817 (2013). doi:10.1103/PhysRevA.87.043817.

[Win05] B. P. Winnewisser, M. Winnewisser, I. R. Medvedev, M. Behnke, F. C. De Lucia, S. C. Ross and J. Koput. *Experimental Confirmation of Quantum Monodromy: The Millimeter Wave Spectrum of Cyanogen Isothiocyanate NCNCS.* Phys. Rev. Lett. **95**, 243002 (2005). doi:10.1103/PhysRevLett.95.243002.

[Wis94] W. Wischert, A. Wunderlin, A. Pelster, M. Olivier and J. Groslambert. *Delay-induced instabilities in nonlinear feedback systems*. Phys. Rev. E **49**, 203–219 (1994). doi:10.1103/PhysRevE.49.203.

[Wis09] H. M. Wiseman and G. J. Milburn. *Quantum measurement and control*, (Cambridge University Press, Cambridge2009).

[Yi06a] S. Yi, P. W. Nelson et al. *Solution of systems of linear delay differential equations via Laplace transformation*. In *Decision and Control, 2006 45th IEEE Conference on*, pages 2535–2540, (IEEE2006).

[Yi06b] S. Yi and A. G. Ulsoy. *Solution of a system of linear delay differential equations using the matrix Lambert function*. In *American Control Conference, 2006*, pages 6–pp, (IEEE2006).

[Zha90] W.-M. Zhang, D. H. Feng and R. Gilmore. *Coherent states: Theory and some applications*. Rev. Mod. Phys. **62**, 867–927 (1990). doi:10.1103/RevModPhys.62.867.

[Zib10] T. Zibold, E. Nicklas, C. Gross and M. K. Oberthaler. *Classical Bifurcation at the Transition from Rabi to Josephson Dynamics*. Phys. Rev. Lett. **105**, 204101 (2010). doi:10.1103/PhysRevLett.105.204101.